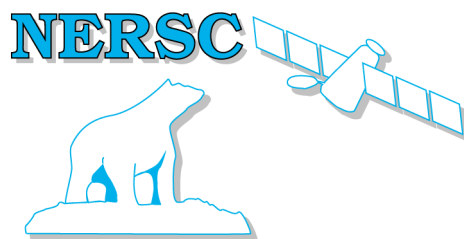


# Nansen Environmental and Remote Sensing Center

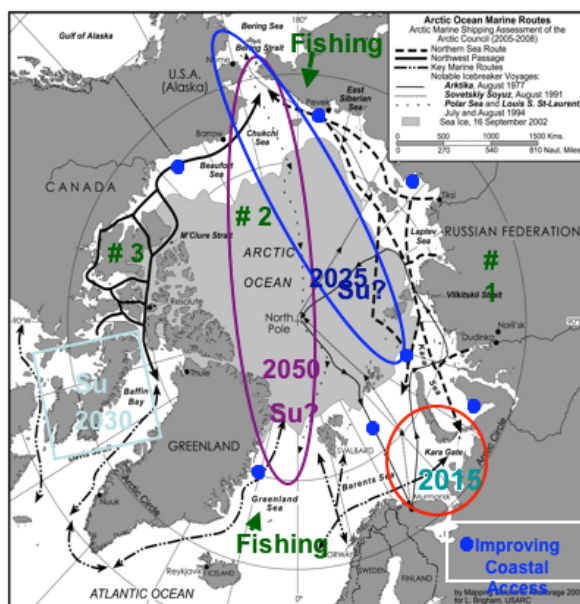
A non-profit  
Research institute affiliated  
With the University of  
Bergen



Thormøhlensgate 47  
N-5006 Bergen,  
Norway  
<http://www.nersc.no>

## NERSC Technical Report no. 277

# Impact of changing ice and met-ocean conditions on offshore design and operations in Arctic regions



Map provided by Lawson Brigham


## Project for Shell Technology Norway AS

Contract no. SC06020

Authors:

Stein Sandven, Helge Drange, Knut Arild Lisæter, Laurent Bertino, Lena Shalina

June 2007

	<p><b>Nansen Environmental and Remote Sensing Center (NERSC)</b></p> <p>Thormøhlensgate 47  N-5006 Bergen, Norway  Phone: + 47 55 20 58 00  Fax: + 47 55 20 58 01  E-Mail: <a href="mailto:Stein.Sandven@nersc.no">Stein.Sandven@nersc.no</a>  <a href="http://www.nersc.no">http://www.nersc.no</a></p>
---	--

<p><b>TITLE:</b>  Impact of changing ice and metocean conditions on offshore design and operations in the Arctic regions</p>	<p><b>REPORT IDENTIFICATION</b></p> <p><b>NERSC Technical report no. 277</b></p>
<p><b>CLIENT</b>  Shell Technology Norway AS</p>	<p><b>CONTRACT</b>  Contract no. SC06020</p>
<p><b>CLIENT REFERENCE</b>  Hans Jørgen Sætre</p>	<p><b>AVAILABILITY</b>  Customer report</p>
<p><b>INVESTIGATORS</b></p> <p>Stein Sandven,  Helge Drange,  Knut Arild Lisæter,  Laurent Bertino,  Lena Shalina</p>	<p><b>AUTHORISATION</b></p> <p>Bergen, 22 June 2007</p> <p>Stein Sandven</p>



## Contents

<b>EXECUTIVE SUMMARY .....</b>	<b>3</b>
<b>1. INTRODUCTION .....</b>	<b>4</b>
<b>2. REVIEW OF SEA ICE AND MET-OCEAN CONDITIONS IN THE ARCTIC .....</b>	<b>6</b>
2.1 ATMOSPHERIC CONDITIONS .....	6
2.1.1 Air Pressure in the Arctic.....	6
2.1.2 The Arctic Energy Budget and north-south flows .....	7
2.1.3 The Arctic Oscillation and the North Atlantic Oscillation .....	10
2.1.4 Surface air temperature .....	12
2.1.5 Polar Lows .....	15
2.1.6 Clouds.....	16
2.1.7 Precipitation .....	18
2.1.8 Snow cover .....	20
2.1.9 Feedback Loops: Interactions that Influence Arctic Climate.....	21
2.1.10 Meteorological conditions of importance for operations and navigation .....	23
2.2 PHYSICAL OCEANOGRAPHY .....	29
2.2.1 Bathymetry and circulation patterns.....	29
2.2.2 Forcing the ocean circulation.....	34
2.2.3 Heat and freshwater content.....	35
2.2.4 Sea level.....	39
2.2.5 Waves.....	42
2.3 SEA ICE.....	44
2.3.1 General sea ice conditions .....	44
2.3.2 Sea ice conditions of importance for operation and navigation.....	48
2.4 ICEBERGS .....	52
2.5 FRESHWATER FLUXES .....	57
2.6 PERMAFROST .....	61
<b>3. SEA ICE MODEL SIMULATIONS AND SATELLITE ANALYSIS FOR THE ARCTIC REGIONS .....</b>	<b>65</b>
3.1 INTRODUCTION .....	65
3.2 MODEL DESCRIPTION AND SETUP .....	66
3.2.1 Ice thickness distribution.....	66
3.2.2 Thermodynamic model.....	67
3.2.3 Coupling with HYCOM and the EVP rheology.....	70
3.3 MODEL VALIDATION .....	71
3.3.1 Comparison with ULS data.....	72
3.3.2 SSM/I comparison.....	76
3.4 ICE COVER STATISTICS .....	76
3.4.1 Barents Sea region.....	77
3.4.2 Beaufort Sea region.....	79
3.4.3 Chukchi Sea region.....	81
3.4.4 East Siberian Sea region.....	83
3.4.5 Eastern Arctic region .....	85
3.4.6 Fram Strait region.....	87
3.4.7 Greenland Sea region.....	89
3.4.8 Kara Sea region.....	91
3.4.9 Laptev Sea region.....	93
3.4.10 Western Arctic region.....	95
3.5 REGIONAL ANALYSIS OF SATELLITE DATA 1978-2005 .....	97
3.5.1 Satellite data description.....	97
3.5.2 Algorithm for sea ice concentration.....	98
3.5.3 Trend analysis of ice area in each region.....	98
3.6 CONCLUSIONS.....	107

<b>4. REVIEW OF RECENT CLIMATE MODEL PROJECTIONS.....</b>	<b>109</b>
4.1 GLOBAL WARMING UNDER DIFFERENT EMISSION SCENARIOS .....	109
4.2 CHANGES IN ARCTIC SEA ICE COVER .....	112
4.3 SEA ICE REDUCTION IS FASTER THAN THE IPCC MODELS .....	113
4.4 PRECIPITATION .....	114
4.5 ATLANTIC MERIDIONAL OVERTURNING CIRCULATION .....	115
4.6 GREENLAND ICE SHEET MELTING .....	116
4.7 SEA LEVEL RISE .....	117
4.8 SNOW COVER AND FROZEN GROUND .....	118
4.9 SEA LEVEL PRESSURE AND ATMOSPHERIC CIRCULATION .....	119
4.10 EXTREME WEATHER AND CLIMATE EVENTS.....	119
<b>5. CONCLUSIONS AND IMPACT ON ARCTIC DESIGN AND OPERATIONS.....</b>	<b>122</b>
<b>6. REFERENCES.....</b>	<b>126</b>

## Executive Summary

The objective of the project has been to 1) review sea ice and related met-ocean conditions of importance for Arctic offshore operations, 2) quantify regional and interannual variability of the sea ice in different regions of the Arctic, and 3) assess future outlook for Arctic met-ocean conditions of importance for offshore design and operations based on climate model simulations.

The project has made a state-of-the-art review of scientific results regarding ice and met-ocean conditions in different parts of the Arctic Ocean. Results from new publications and studies are synthesised, with focus on sea ice and iceberg conditions as well as atmospheric and ocean processes with impact on the ice conditions. Analysis of satellite data and model simulations have been performed to study variability of the ice conditions in the Barents Sea, Kara Sea, East Siberian Sea, Chukchi Sea, Beaufort Sea and Greenland waters over the last 50 years. Scenarios for future changes of the Arctic climate by use of climate models have been investigated. Possible impact of projected changes in ice and metocean conditions on offshore design and operations in different Arctic regions is discussed.

Results of recent sea ice model simulation in the Arctic from 1958 to present based on ERA40 forcing fields from European Centre for Medium-range Weather Forecasting (ECMWF) are presented. This is the best reanalyzed atmospheric forcing fields available for the Arctic, extending back to 1958. These fields have been used to run the North-Atlantic model at NERSC, which consists of a Multi-Category ice model coupled to the HYCOM ocean circulation model. The Multi-Category ice model treats the ice cover as a collection of ice floes in different thickness categories. This makes it possible to model the ice thickness probability density function for each grid cell. Ice thickness distribution gives a description of how much of the thickest ice generated by ridges is present in each grid cell. The model simulations from 1958 contains also ice drift and ice concentration in every grid cell. The simulations have been analysed to retrieve regional, seasonal and interannual variability in the sea ice fields in response to the atmospheric forcing fields. Analysis of satellite data from 1979 to present shows a decrease in sea ice extent in all regional seas of the Arctic, although the interannual variability is the dominant feature in the ice extent data.

The recently published Fourth Assessment Report from IPCC has reinforced the conclusions on global warming as a consequence of increasing greenhouse gas emissions into the atmosphere. For the Arctic regions observations in the last decades shows that the sea ice cover decreases, the glaciers and ice sheets reduce their masses, the snow cover has decreased, and so have permafrost areas. Air temperatures are increasing in most areas and ocean temperatures have been observed to increase in areas such as the Fram Strait and the Barents Sea. However, long-term observations of the ocean are scarce, and we are lacking data to determine changes in the ocean water masses and circulation in the Arctic. Available data from the world oceans show increasing temperature over the last decades, with thermal expansion leading to sea level rise. Also melting of ice sheets, ice caps and glaciers contribute to the sea level change, but much less than the thermal expansion. IPCC states that the projections in the 21st century will be:

- The Arctic is very likely to warm during this century in most areas, and the annual mean warming is very likely to exceed the global mean warming. Warming is projected to be largest in winter and smallest in summer.
- Annual arctic precipitation is very likely to increase. It is very likely that the relative precipitation increase will be largest in the winter and smallest in summer.
- Arctic sea ice is very likely to decrease in extent and thickness. It is uncertain how the Arctic Ocean circulation will change.

In addition to the long-term trend it is important to be aware of decadal variability in the Arctic climate system. The understanding of the polar climate system and its variability is still incomplete due to its complex atmosphere-land-cryosphere-ocean interactions. The models used to simulate the global climate are not representing processes such as clouds, planetary boundary layer processes and sea ice. Planning of offshore operations in the Arctic need to consider that there is considerable uncertainty in the predictions of atmosphere, sea ice and ocean changes for the different regions of Arctic for the next decades.

## 1. Introduction

Instrumental observations, particularly from the former Soviet Union, show a pronounced warming in the Arctic between 1920 and into the 1940s, known as the early 20<sup>th</sup>-century warming (Bengtson et al., 2004) and a marked cooling in the following decades, with corresponding changes in the sea ice cover (Johannessen et al., 2004). Recent synthesis reviews (Serreze et al., 2000; SEARCH, 2001; Moritz et al., 2004) based on available observational evidence provide a reasonably coherent portrait of Arctic climate change, indicating that the last 2-3 decades have experienced unusual warming over northern Eurasia and North America, reduced Arctic sea ice (Johannessen et al., 1999; Rothrock et al., 1999; Serreze et al., 2003; Yu et al., 2004; Kvingedal, 2005; Lindsay and Chang, 2005) marked changes in Arctic Ocean hydrography (Morison et al., 1998; Dickson, 1999; Swift et al., 2005) increased runoff into the Arctic (Peterson et al., 2002), increased tree growth in northern Eurasia (Nymeni et al., 1997), and reduced tundra areas (Serreze et al., 2000; Wang and Overland, 2004) and thawing permafrost.

The Arctic glaciers have, in general, retreated over the same period (Dyrgerov and Meier, 2000; Rignot et al., 2004), whereas less is known about the Greenland ice sheet, one of the wildcards of the climate system. The latter has been the subject of increased attention for two important reasons: Melting of the Greenland ice sheet will add fresh water to the North Atlantic Ocean which have been theorized to weaken or even destruct the Atlantic MOC (Stouffer et al., 2006). Secondly, the Greenland ice sheet stores a freshwater amount equivalent to an increase of the global sea level of 7 meters, implying that even partial melting will influence the global sea level in dramatic ways. Recent observation-based studies of the surface elevation of the Greenland ice sheet diverge; reporting that the interior of the Greenland ice sheet has increased during 1992-2003 (Johannessen et al., 2005), that there is a net positive mass balance for the whole ice sheet for the same period (Zwally et al., 2005), and that there has been a dramatic glacier acceleration between 1996-2005 (Rignot and Kanagaratnam, 2006). The fresh water discharges create the East Greenland Coastal Current (Wilkinson and Bacon, 2005), corresponding to at least 30 % of the total Arctic freshwater gain. Clearly, both the fresh water from the Greenland Ice Sheet and the freshwater transport out of the Arctic are of key importance for the Arctic and global climate system.

The sea ice cover has over the last 2-3 decades decreased by ~10% (Johannessen et al., 1999, 2004; whereas the ice thickness has decreased up to 40% during summer (Rothrock et al., 1999). Other observed changes include a warming of the Atlantic water in the Arctic Ocean (Bobylev et al., 2003; Morison et al., 1998) increased precipitation in the Arctic regions and higher river discharge into the Arctic ocean (Peterson et al., 2002). During the last decades detected changes include a significant freshening of the deep North Atlantic Ocean (Dickson, 1999), warming in the deep water of the Nordic Seas (Bobylev et al, 2003) and a decrease of deep overflow in the Faeroe Bank Channel. The Arctic Ocean plays a major role concerning the surface energy and freshwater budgets, because it is a large and effective heat sink, and it exports a significant amount of freshwater into the North Atlantic and into areas of deep water formation like the Greenland, Irminger and Labrador Seas, from where the global oceanic thermohaline circulation is driven. Improved monitoring systems are needed to provide consistent and long-term data on the ice-ocean circulation in the Arctic Ocean including the Fram Strait and Nordic Seas. Monitoring systems should have a central role in detection and verification of climate variability and trends. Monitoring and forecasting of the environmental conditions on daily to seasonal scale is also needed to support all types of marine operations to secure sustainable and safe development in high latitudes.

A consensus from coupled atmosphere–ocean modelling studies of increasing greenhouse-gas (GHGs) scenarios is that anthropogenic global warming will be enhanced in the northern high latitudes (IPCC, 2001, 2007; Raisanen, 2002; CIMP2; 2003; ACIA, 2005) due to complex feedback mechanisms in the atmosphere–ocean–ice system. The predicted warming in the Arctic over the next 50 years is ~3-5°C, or more than twice the global average (IPCC, 2001, 2007; ACIA,

2005): This suggests that the Arctic may be where the most rapid and dramatic climate changes (e.g., a shrinking sea ice cover and reduced glacier and ice sheet volumes) may take place during the 21<sup>st</sup> century.

The polar climate involves large natural variability on interannual, decadal and longer time scales, which is an important source of uncertainty. Both instrumental observations (like the early 20<sup>th</sup>-century warming) and modelling show that the Arctic is a region of large natural climate fluctuations (Sorteberg et al., 2005; Bengtson et al., 2006). In depth analyses of the Arctic climate's signal-to-noise ratio is therefore a prerequisite for both proper quantification of the human-induced contribution to existing and future changes in the Arctic climate system, and to quantify the capabilities and reduce the uncertainty of climate predictions for the Arctic. The understanding of the polar climate system is still incomplete due to its complex atmosphere-land-cryosphere-ocean-ecosystem interactions involving a variety of distinctive feedbacks. Processes that are not particularly well represented in the models are clouds, planetary boundary layer processes and sea ice. Additionally, the resolution of global models is still not adequate to resolve important processes in the polar seas. All this contributes to a rather large range of present-day and future simulations, which may reduce confidence in the future projections. A serious problem is the lack of observations against which to assess models, and for developing process knowledge, particularly over Antarctica.

The report contains the following chapters:

Chapter 2: Overview of atmospheric conditions, physical oceanography, sea ice, icebergs, freshwaterfluxes and permafrost conditions in the Arctic. This chapter gives a synthesis of recent studies of the Arctic climate variability based on observation sea ice and met-ocean conditions.

Chapter 3: Regional and interannual variability of the sea ice in different regions of the Arctic based on results of sea ice model simulation from 1958 to present. based on ERA40 forcing fields from European Centre for Medium-range Weather Forecasting (ECMWF). The simulations have been used to retrieve regional, seasonal and interannual variabilities in the sea ice fields in response to the atmospheric forcing fields. Satellite ice concentration data from 1979 have been used to compare and validate the model results.

Chapter 4: Review of recent climate model assessment based on the recent IPCC 2007 report. Results from Atmosphere-Ocean General Circulation Models (AOGCMs) published in the IPCC 2007 report have been extracted to assess the expected changes for the Arctic regions in the 21st century. These models have very little regional information for the different parts of the Arctic Ocean, so the results can only be used to assess climate change for the Arctic region as a whole.

Chapter 5: Conclusions and discussion of impact on Arctic design and offshore operations.

## 2. Review of sea ice and met-ocean conditions in the Arctic

### 2.1 Atmospheric conditions

#### 2.1.1 Air Pressure in the Arctic

Several fronts and semi-permanent high and low pressure systems characterize the Arctic. The "polar front" marks the boundary between cold polar air masses and warm tropical air masses. The polar front is intermittent rather than continuous around the globe. The strength of the polar front depends on the magnitude of the horizontal temperature gradient across the front. Where the temperature gradient is steep, the front is strong and is a potential site for cyclone or low pressure system development. Where temperature contrast is small, the polar front is weak. Like the polar front, the "arctic front" is discontinuous and depends on the temperature contrast between two air masses. The arctic front is the boundary between polar and arctic air masses and lies to the north of the polar front. The arctic front can be as strong as the polar front. It is particularly prominent during summer in northern Eurasia.

Semi-permanent high and low pressure systems ("highs" and "lows") are identified with particular regions and have seasonal characteristics. In winter, the Icelandic Low extends from near Iceland north into the Barents Sea, and is associated with frequent cyclone activity. The Aleutian Low is present in the Gulf of Alaska. An example of winter pressure situation is shown in Fig. 2.1, where Low-pressure storm tracks (blue) dominate the picture. Here Atlantic cyclonic systems, spawned as far upwind as the northern Pacific, reach from middle latitudes northward, high into the Arctic. The guiding upper tropospheric standing wave pattern is plotted with contours.

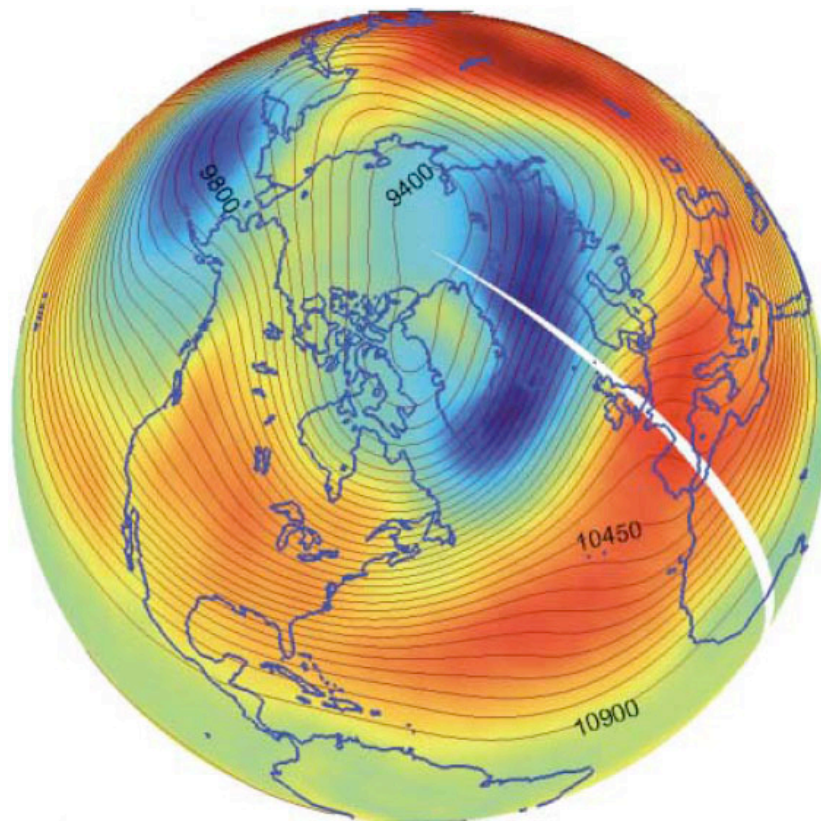


Figure 2.1. Mean sea-level pressure (colours) and 250mbar dynamic height (contours) are plotted for Jan.–Mar. 1993. Blue is low pressure reaching 993 mbar south-east of Greenland, red is high pressure, reaching 1023 mbar in the subtropical Atlantic. The 250 mbar dynamic height (m) is labelled along contours. Greenwich meridian is shown in white. (Rhines, 2006).

The Beaufort-Chukchi Sea region is dominated by a ridge of high pressure linking the Siberian High and high pressure over the Yukon of Canada. In April and May arctic pressure gradients decrease. The Icelandic and Aleutian lows weaken. The Siberian High disappears, and is replaced by a wide but shallow low. The Arctic High is centered over the Canadian Arctic Archipelago. In summer, pressure gradients are generally weak. Intermittently, however, cyclones enter the Arctic from northern Eurasia and the north Atlantic, and tend to persist over the Canadian Basin. By October the pattern has almost returned to the winter configuration. The Icelandic and Aleutian lows strengthen, as does the Siberian High.

**The Polar vortex:** The polar vortex is a persistent large-scale cyclonic circulation pattern in the middle and upper troposphere and the stratosphere, centered generally in the polar regions of each hemisphere. In the Arctic, the vortex is asymmetric and typically features a trough (an elongated area of low pressure) over eastern North America. It is important to note that the polar vortex is not a surface pattern. It tends to be well expressed at upper levels of the atmosphere (that is, above about five kilometers).

**Aleutian Low:** This semi-permanent low pressure center is located near the Aleutian Islands. Most intense in winter, the Aleutian Low is characterized by many strong cyclones. Traveling cyclones formed in the subpolar latitudes in the North Pacific usually slow down and reach maximum intensity in the area of the Aleutian Low.

**Icelandic Low:** This low pressure center is located near Iceland, usually between Iceland and southern Greenland. Most intense during winter, in summer, it weakens and splits into two centers, one near Davis Strait and the other west of Iceland. Like its counterpart the Aleutian Low, it reflects the high frequency of cyclones and the tendency for these systems to be strong. In general, migratory lows slow down and intensify in the vicinity of the Icelandic Low.

**Siberian High:** The Siberian High is an intense, cold anticyclone that forms over eastern Siberia in winter. Prevailing from late November to early March, it is associated with frequent cold air outbreaks over east Asia.

**Beaufort High:** The Beaufort High is a high pressure center or ridge over the Beaufort Sea present mainly in winter.

**North American High:** The North American High is a relatively weak area of high pressure that covers most of North America during winter. This pressure system tends to be centered over the Yukon, but is not as well-defined as its continental counterpart, the Siberian High.

### **2.1.2 The Arctic Energy Budget and north-south flows**

The energy that drives the circulating atmosphere and ocean comes largely from the sun, which strikes the low latitudes most directly. Thermal radiation is trapped by the atmosphere, absorbed by the ocean and redistributed by the combined atmosphere/ ocean circulation. Figure 2.2 schematically represents the mean annual energy budget of the Arctic ocean and atmosphere. The arrow  $T, q$  represents the advection of heat and moisture into the arctic atmosphere from lower latitudes. Solar and thermal (shortwave and longwave) radiation fluxes are represented by "S" and "L". "O" represents the flux of heat from the ocean to the atmosphere through openings in the ice (leads and polynyas). This flux is significant in winter, when the ocean is much warmer than the air. "P" represents precipitation, "M" represents the melting of snow and ice, and "R" represents the input of freshwater runoff. The "Ice" arrow symbolizes net ice production and export (export of ice from the Arctic occurs primarily through the Fram Strait along the east coast of Greenland), while the "Water" arrow symbolizes the influx of relatively warm Atlantic water into the Arctic Ocean. All of the elements in the figure represent processes that release or consume energy (such as precipitation and melting), or fluxes of energy. Over the course of a year, the net radiation balance at the top of the atmosphere (a net loss of heat energy) roughly balances the advection of heat northward into the Arctic.



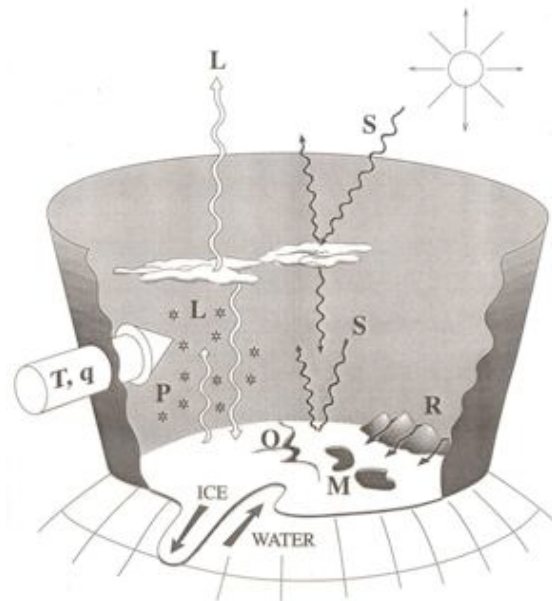


Figure 2.2. Arctic energy budget components: R = Runoff (freshwater); L = Longwave radiation; S = Shortwave radiation; O = Ocean heat; M = Melt (snow and ice); P = Precipitation; T = Temperature (heat transfer); q = moisture. (From "SHEBA, a research program on the Surface Heat Budget of the Arctic Ocean", NSF Arctic System Science Report No. 3, August 1993, by N. Untersteiner.)

Analyses of atmospheric observations by the major weather centres and oceanic observations from ships, satellites and autonomous undersea vehicles continue to home in on values for the net north-south flow of thermal energy, mass and salt. An intriguing aspect of this energy flow is that the air's 'sensible heat', the warmth we measure with a thermometer, carries only about one-third of the total. From the excess solar heating in low latitudes, just over two petawatts ( $2 \times 10^{15}$  watts) of thermal energy is carried as sensible heat by the oceanic meridional overturning circulation (MOC). Of this total energy flow, about 1.2 petawatts occurs in the North Atlantic, peaking at about  $20^{\circ}\text{N}$  latitude. The atmosphere moves a peak value of about five petawatts northward and it is often pointed out that the oceanic contribution is the smaller of the two (these numbers vary with latitude of course, and are reported here as peak values). However, a more balanced view is that there are three forms of north-south energy transport rather than just the two oceanic and atmospheric contributions (from Rhines, 2006).

First is the basic 'warm south wind, cold north wind', or dry static energy transport in the atmosphere; second is the corresponding 'warm Gulf Stream, cold deep western boundary current', or thermal energy transport of the ocean. The third form of heat transport is shared jointly by atmosphere and ocean. Water vapour enters the atmosphere through evaporation from the warm sub-tropical ocean (thus increasing the salinity there). This vapour represents latent heat and moves poleward in the atmosphere finally releasing sensible heat as it precipitates out. The amplitude of each of the three forms of thermal energy transport is comparable, with peak values of roughly two petawatts (Bryden et al. 2001).

Delivery of heat from the sub-tropical oceans to the sub-polar atmosphere through water vapour transport has a crucial secondary effect in delivering water to form snow, ice and a buoyant, floating layer of low salinity on top of the sub-polar oceans. The return circuit for poleward-flowing atmospheric moisture is the equatorward flow of the ocean. There is a growing awareness of the importance of the hydrologic cycle, which encompasses many facets of fresh water movement on Earth. The acceleration of fresh water movement is one of the keystone predictions related to global warming (IPCC 2001, 2007).



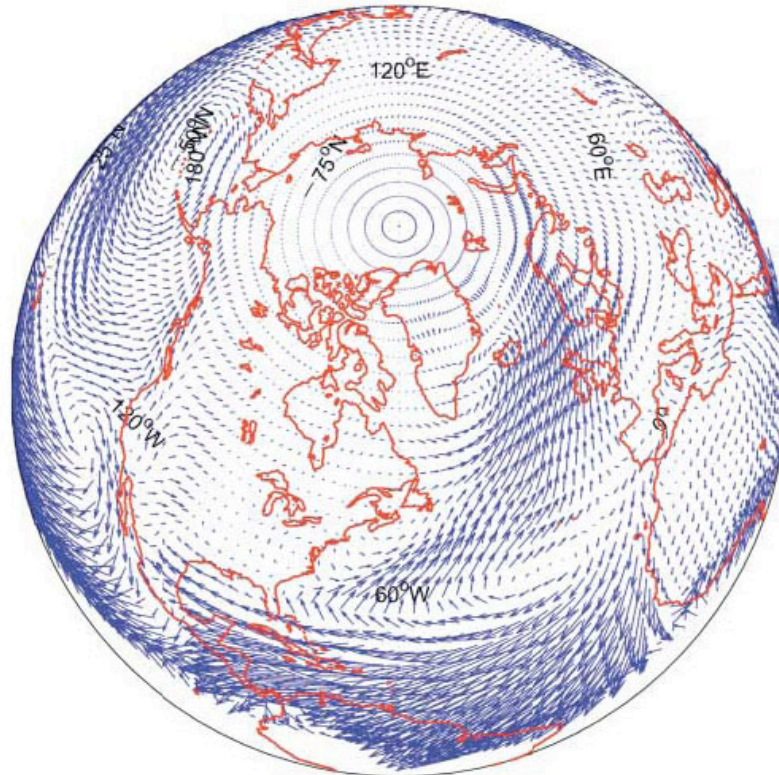


*Fig. 2.3 The transport of fresh water by the atmosphere, averaged over the same period in winter 1993 as in Fig. 2.1. The total transport across latitude 60°N ranges between 0.12 and 0.18 Sverdrups. The eastern flank of the two oceanic low-pressure centres dominates this transport which involves synoptic cyclonic systems along these storm tracks. The Pacific moisture conduit rains out on the slopes of Alaskan mountains, freshening the waters of the North Pacific Ocean, while the Atlantic moisture track continues well into the Arctic basin (Rhines, 2006).*

The co-operative flow of heat and moisture emphasizes how tightly bound these two physical properties are. Condensation of water vapour into droplets or freezing of liquid water, involves great heat release. The winds and currents themselves can be compared quantitatively. Oceanographers measure water flow in Sverdrups, or megatonnes of mass per second. The Amazon river (the world's largest river) flows with about 0.1 Sverdrup, while the Gulf Stream ranges from 30 to 150 Sverdrups at different locations. The ocean's global MOC has an amplitude of roughly 20 Sverdrups. The atmospheric circulation can also be expressed in these same terms; the wintertime westerly winds carry about 500 Sverdrups, while the average northerly and southerly winds carry about 100 Sverdrups in the tropics, 30 Sverdrups in the middle latitudes and 5 Sverdrups in the subpolar regions.

This meridional overturning, involving just over two petawatts of latent-heat transport, corresponds to about one Sverdrup of fresh water transport. While there is much recycling of moisture in the global hydrologic system, one Sverdrup is a good amplitude estimate for fresh water movement in the global atmospheric MOC. Where does this flow of energy actually occur? Can it be seen? Summing up the transports around circles of latitude is the traditional way to describe these cogs in the solar-driven climate heat-engine. As one moves further north, we find that the system becomes dominated by the Atlantic sector. The shape and strength of these flows is strongly influenced by the standing waves in the westerly winds (Fig. 2.1) and the veins and arteries of ocean circulation.

The atmospheric circulation pattern in the Northern Hemisphere owes its origin to the topography of the Rocky Mountains, to Greenland and to the Himalayan Plateau. In addition, forcing by contrasting thermal properties of continents and oceans contributes to the standing wave pattern (this is seen, for example in the contrast between winter and summer in the Northern Hemisphere, with sub-tropical high-pressure cells dominating over oceans in summer, while sub-polar low pressure dominates above the oceans in winter). In the Atlantic sector, the mean winds lie south-west/north-east, and as the air moves over the ocean, energy builds up in transient cyclonic systems. The Atlantic storm track, defined in this way, describes both ocean storms and climate processes. The transport of moisture (Fig. 2.3) shows concentrated conduits on the eastern sides of the oceanic low-pressure centres. In the North Pacific this moisture precipitates out before reaching the Arctic. The air collides with the Alaska Coast Range, causing enormous precipitation that contributes to the low salinity of the North Pacific Ocean (though some of this fresh water circulates through Bering Strait to freshen the waters of the Arctic). North of 60°N latitude, the Atlantic sector is left to dominate the net moisture transport. The rainfall of Scotland and coastal Norway produces both hydropower and the low salinity of the Baltic Sea. Condensation releases latent heat, warming these latitudes greatly. Perhaps the greatest monument to this moisture flux is Greenland itself. With its crest reaching greater than 3 km above sea-level, and its base depressed below sea-level by sheer weight, this ice mountain, if melted, would raise the world's ocean surface by more than 7m. A consequence of the strong northward tracking of storms and the warmth they transport is that the Labrador Sea, Greenland Sea, Norwegian Sea and Barents Sea all remain nearly ice-free through the entire year. It is the co-operation between the mutually warmed ocean and atmosphere along this track, engaging in a game of heat- and moisture leap-frog, that warms the sub-polar zone and Arctic, which neither air nor sea alone could do.

### 2.1.3 The Arctic Oscillation and the North Atlantic Oscillation

The Arctic Oscillation (AO), shown in Figs. 2.4 and 2.5, is an important Arctic climate index with positive and negative phases, which represents the state of atmospheric circulation over the Arctic. The positive phase (red bars in Fig. 2.5) brings lower-than-normal pressure over the polar region, steering ocean storms northward, bringing wetter weather to Scotland and Scandinavia, and drier conditions to areas such as Spain and the Middle East. While the value of the AO index was strongly positive in the early 1990's compared to the previous forty years, the value of the AO has been low and variable for the last nine years. The year to year persistence of positive or negative values and the rapid transition from one to the other is often referred to as "regime-like".

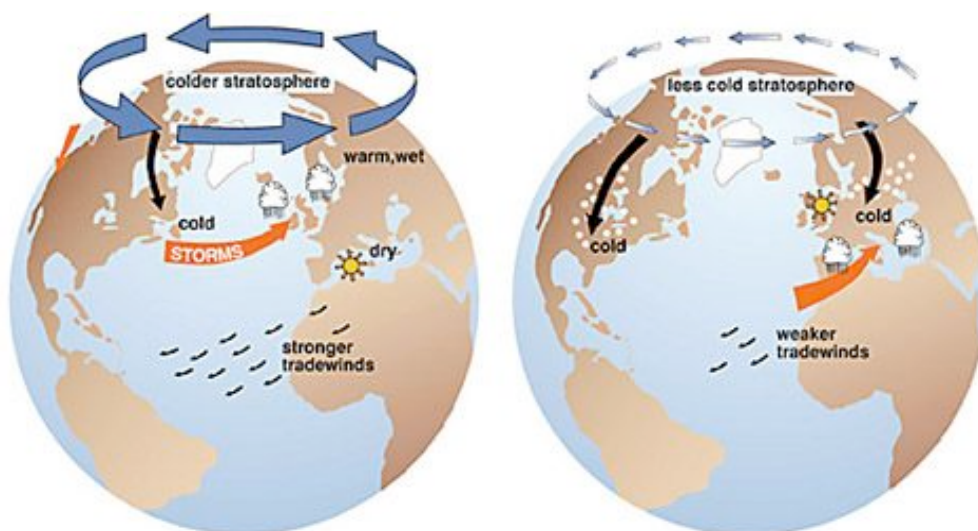


Figure 2.4 Effects of the Positive Phase (Left) and the Negative Phase (right) of the Arctic Oscillation (Figures courtesy of J. Wallace, University of Washington)

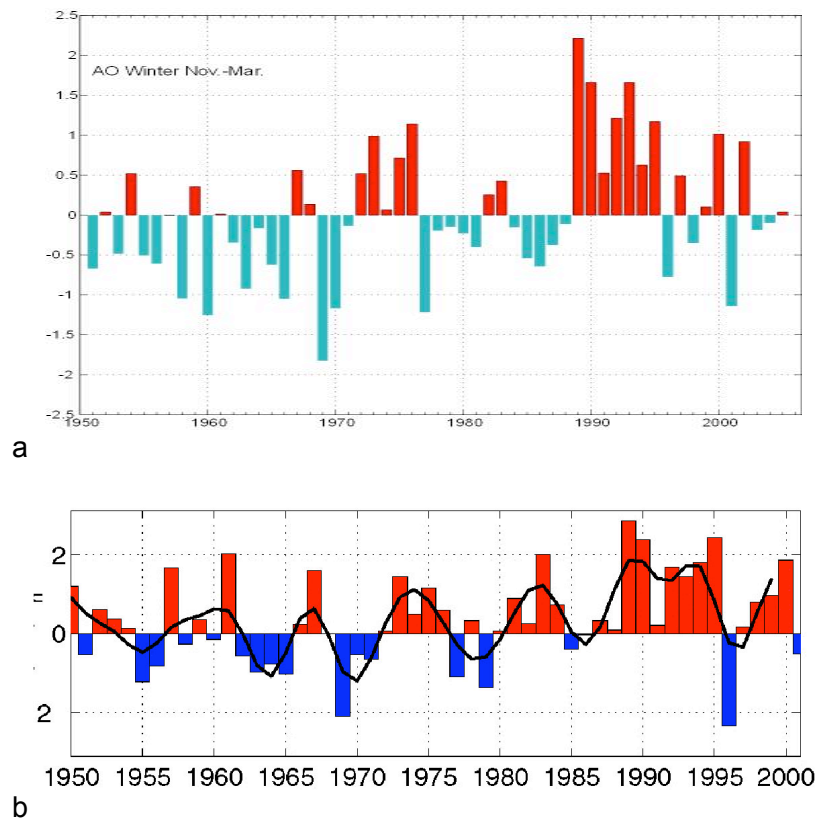


Figure 2.5. (a) Annual Arctic Oscillation (AO) index in Winter (November to March). Data from NCEP; (b) annual NAO index from 1950.

The Arctic Oscillation (AO) appears to be the cause for much of the recent changes that have occurred in the Arctic. Its effects are not restricted just to the Arctic; it also represents an important source of variability for the Northern Hemisphere as a whole. The AO has been described as "a seesaw pattern in which atmospheric pressure at polar and middle latitudes fluctuates between positive and negative phases.

The AO appears related to a well-known mode of variability for the North Atlantic called the North Atlantic Oscillation (NAO). NAO is defined as the surface pressure difference between two stations in Portugal and Iceland. The NAO has been recognized for decades and has been considered "the dominant mode of winter climate variability in the North Atlantic region ranging from central North America to Europe and much into Northern Asia. The NAO is a large scale see-saw in atmospheric mass between the subtropical high and the polar low. The corresponding index varies from year to year, but also exhibits a tendency to remain in one phase for intervals lasting several years." The positive phase of the NAO is associated with more frequent and intense storms in the North Atlantic Ocean, warmer and wetter winters in Europe, and cooler, drier winters in Greenland and northern Canada (Fig. 2.6).

A systematically positive sense to both the AO and the NAO indices since the end of the 1980s has coincided with relatively warm conditions in the Arctic and net melting of the Arctic ice pack. During the winter, the AO extends up through the stratosphere, 6 to 30 miles above the Earth's surface. When the AO changes phases, the strengthening or weakening of the circulation around the pole tends to begin in the stratosphere and work its way down through lower levels of the atmosphere. In phenomena such as El Niño in the equatorial Pacific Ocean, the changes begin in the ocean and work their way up through the atmosphere.



Stratosphere cooling in the last few decades has caused the counterclockwise circulation around the North Pole to strengthen in winter. In turn, the belt of westerly winds at the surface along 45 degrees north latitude has shifted farther north, the scientists said, sweeping larger quantities of mild ocean air across Scandinavia and Russia and bringing balmy winters over most of the United States as well.

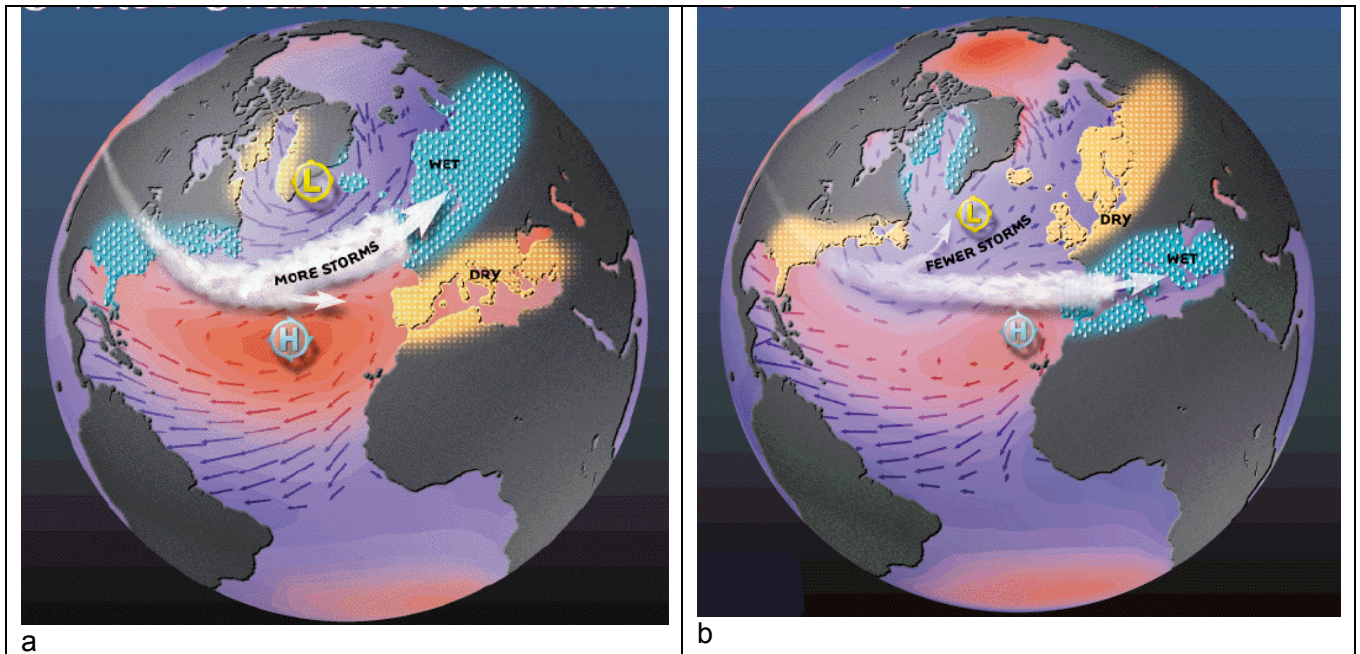


Figure 2.6 Characteristic weather patterns during positive (a) and negative (b) NAO index, and

Year-to-year fluctuations in the North Atlantic Oscillation are thought to be prompted primarily by changes in the ocean, as with El Niño. However, Thompson and Wallace (1998) argue that the North Atlantic Oscillation is in fact part of the Arctic Oscillation, which involves atmospheric circulation in the entire hemisphere. They say the trend toward a stronger, tighter circulation around the North Pole could be triggered just as well by processes in the stratosphere as by those in the ocean. The trend in the Arctic Oscillation has been reproduced in climate models with increasing concentrations of greenhouse gases.

#### 2.1.4 Surface air temperature

The huge warming of the Arctic that started in the early 1920s and lasted for almost two decades is one of the most spectacular climate events of the twentieth century (Johannessen et al., 2004). During the peak period 1930–40, the annually averaged temperature anomaly for the area 60°–90°N amounted to some 1.7°C (Fig. 2.7). After this early twentieth century warming, a colder period prevailed from the 1950s to the 1980s. The warming in recent years starting in the late 1980s, which is stronger and extends further south than in 1930–40, is illustrated in Fig. 2.7. Example of spatial distribution of air temperature anomaly for 2005 is shown in Fig. 2.8, where the highest warming is observed in the northern Barents Sea.

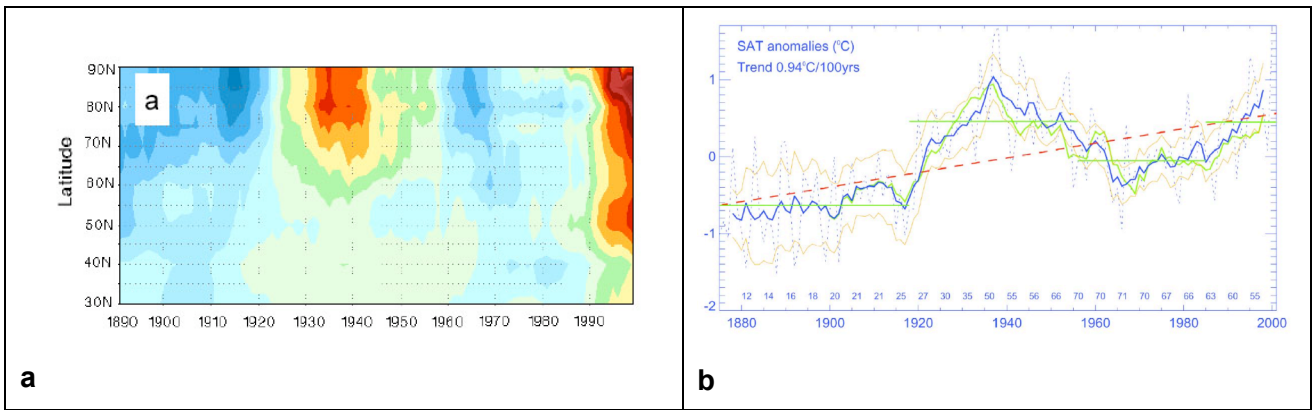


Figure 2.7 Surface air temperature (SAT) changes during the twentieth century. (a) from Johannessen et al, 2004; (b) from Polyakov et al., 2005.

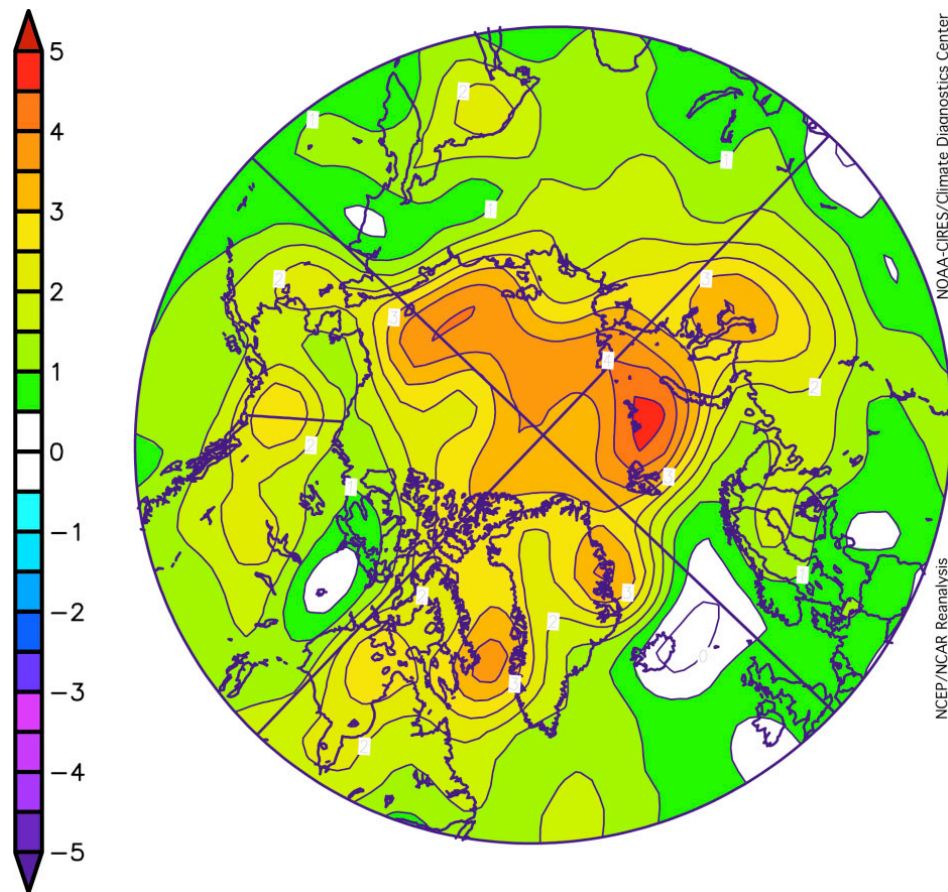
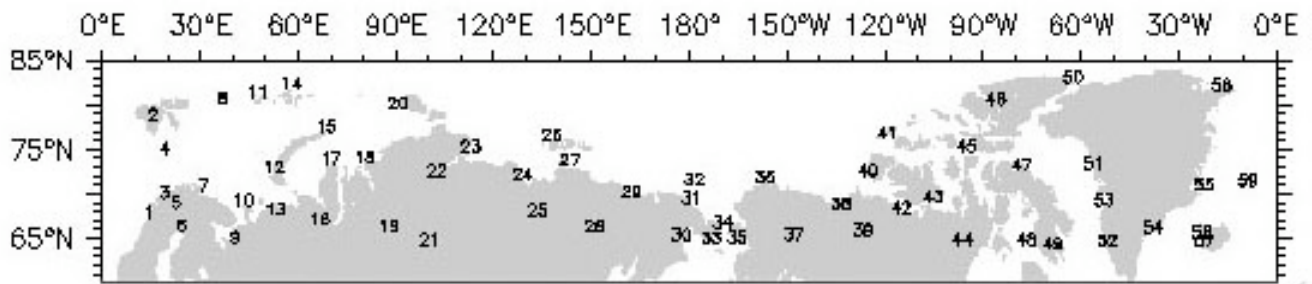


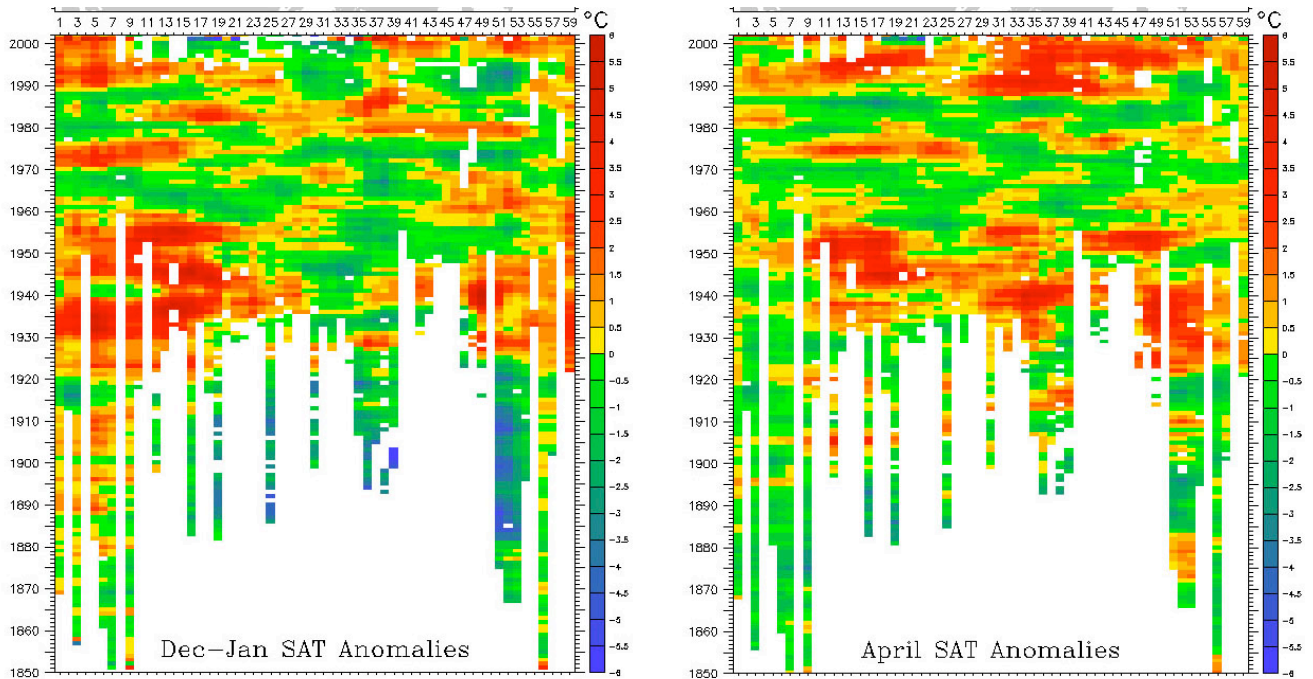
Figure 2.8 Surface air temperature (SAT) anomaly map for 2005, showing that the whole Arctic was 2-4°C warmer than the normal and that the strongest warming was found in the Northern Barents Sea. The scale is in °C (from NSIDC, 2006).

The surface temperature has been observed around the Arctic Ocean in a network of stations (Fig. 2.9.a), some of them have data records back to the 1850s. The temperature anomalies for December-January and April are presented in Fig. 2.9 b and c.





a



b

c

Figure 2.9 Circumpolar data records of surface air temperatures: (a) station map, (b) air temperature anomalies for December-January; (c) air temperature anomalies for April (from Overland et al., 2004).

Johannessen et al., (2004) suggest that natural variability is a likely cause, with reduced sea ice cover being crucial for the warming. A robust sea ice–air temperature relationship was demonstrated by a set of four simulations with the atmospheric ECHAM model forced with observed SST and sea ice concentrations. An analysis of the spatial characteristics of the observed early twentieth-century surface air temperature anomaly revealed that it was associated with similar sea ice variations. Further investigation of the variability of Arctic surface temperature and sea ice cover was performed by analyzing data from a coupled ocean–atmosphere model. By analyzing climate anomalies in the model that are similar to those that occurred in the early twentieth century, it was found that the simulated temperature increase in the Arctic was related to enhanced wind-driven oceanic inflow into the Barents Sea with an associated sea ice retreat. The magnitude of the inflow is linked to the strength of westerlies into the Barents Sea. This study proposes a mechanism sustaining the enhanced westerly winds by a cyclonic atmospheric circulation in the Barents Sea region created by a strong surface heat flux over the ice-free areas.

Observational data suggest a similar series of events during the early twentieth-century Arctic warming, including increasing westerly winds between Svalbard and Norway, reduced sea ice, and enhanced cyclonic circulation over the Barents Sea. At the same time, the North Atlantic Oscillation was weakening.

Of particular interest are atmospheric circulation contributions to the latest warm period, marked by less sea ice and changes in tundra conditions. Arctic cyclone activity (i.e., storms that bring warm, moist air to the Arctic) increased in number and intensity in the second half of the twentieth century, especially in summer, coupled with a general decrease in storminess in the mid-latitudes (Serreze *et al.*, 1997; Zhang *et al.*, 2004).

### 2.1.5 Polar Lows

Small cyclones forming over open sea during the cold season within polar or arctic air masses are called "polar lows." Typically several hundred kilometers in diameter, and often possessing strong winds, polar lows tend to form beneath cold upper-level troughs or lows when frigid arctic air flows southward over a warm body of water. In satellite imagery polar lows show characteristic spiral or comma shaped patterns of deep clouds, sometimes with an inner "eye" similar to those seen in tropical cyclones. Convective cloud bands occupy the surroundings (Fig. 2.10a and Fig. 2.11).

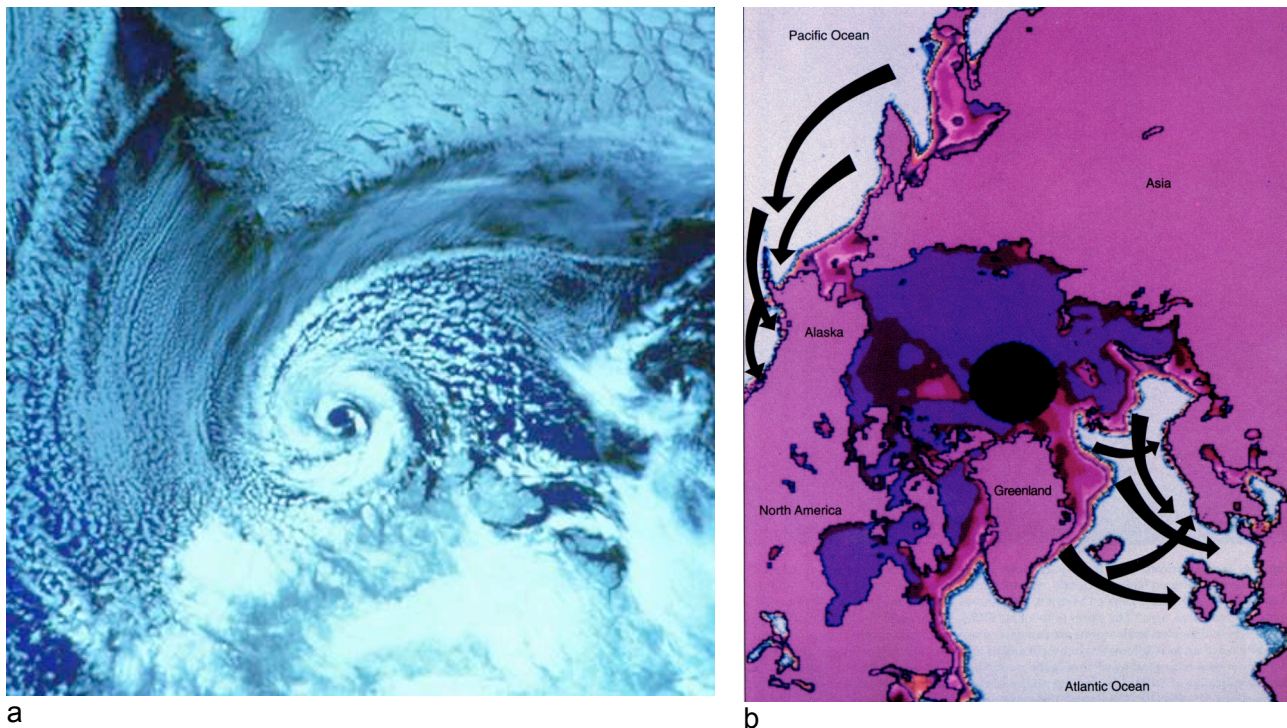


Fig. 2.10 (a) A NOAA-9 polar orbiter satellite image (visible band) of a polar low over the Barents Sea on 27 February 1987. The southern tip of Spitsbergen is visible at the top of the image. The polar low is centered just north of the Norwegian coast; (b) Map of the most common paths of Polar Lows (Courtesy: S. Businger, Department of Meteorology, University of Hawaii).

Polar lows last on average only a day or two. They can develop rapidly, reaching maximum strength within 12 to 24 hours of the time of formation. They often dissipate just as quickly, especially upon making landfall. In some instances several may exist in a region at the same time



or develop in rapid succession. They represent a specific hazard to offshore operations since they develop quickly, provide extreme wind speeds and are difficult to forecast.

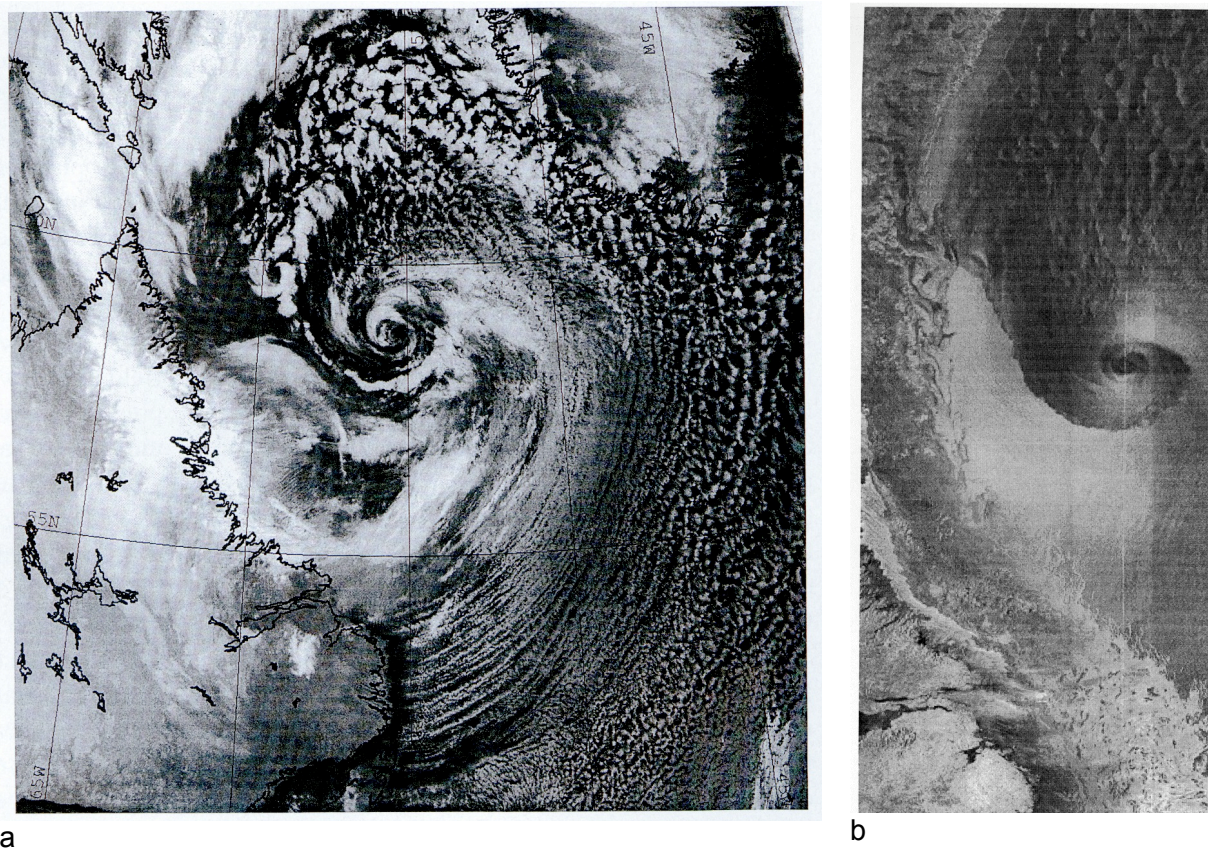


Figure 2.11. Polar lows observed in the Labrador Sea (a) from NOAA IR image, (b) from a RADARSAT ScanSAR image.

Analysis of aircraft and radiosonde data collected during field experiments reveals that polar lows may possess warm cores. This finding, coupled with their appearance in satellite imagery, has prompted some investigators to refer to polar lows as "arctic hurricanes," although they seldom, if ever, possess hurricane strength winds.

Polar lows occur most frequently in the marginal ice zones in the North Pacific and in the Greenland, Norwegian and Barents Seas (Fig. 2.10b). Polar lows are difficult to predict even with current high resolution and high performing operational numerical models, because they usually occur in remote oceanic regions where data are too sparse to define the model initial state on a sufficiently fine scale. However, present-day models can depict synoptic-scale patterns favorable to the development of the smaller scale systems, allowing forecasters to use the predictions in conjunction with satellite imagery and conventional observations to make subjective forecasts of their occurrence.

### 2.1.6 Clouds

Clouds are factors in climate that influence the radiation budget and therefore temperature. Clouds reflect a large fraction of solar radiation, resulting in surface cooling. On the other hand, clouds inhibit longwave radiation loss from the surface, which can lead to higher surface temperatures. The dominant process depends on many factors including cloud type and thickness, the magnitude of the solar radiation, and the albedo of the underlying surface. Clouds and



precipitation undergo a seasonal cycle, as shown in Fig. 2.12 a and b, and a trend of increased cloud cover over the last decades (Fig. 2.12 c and d).

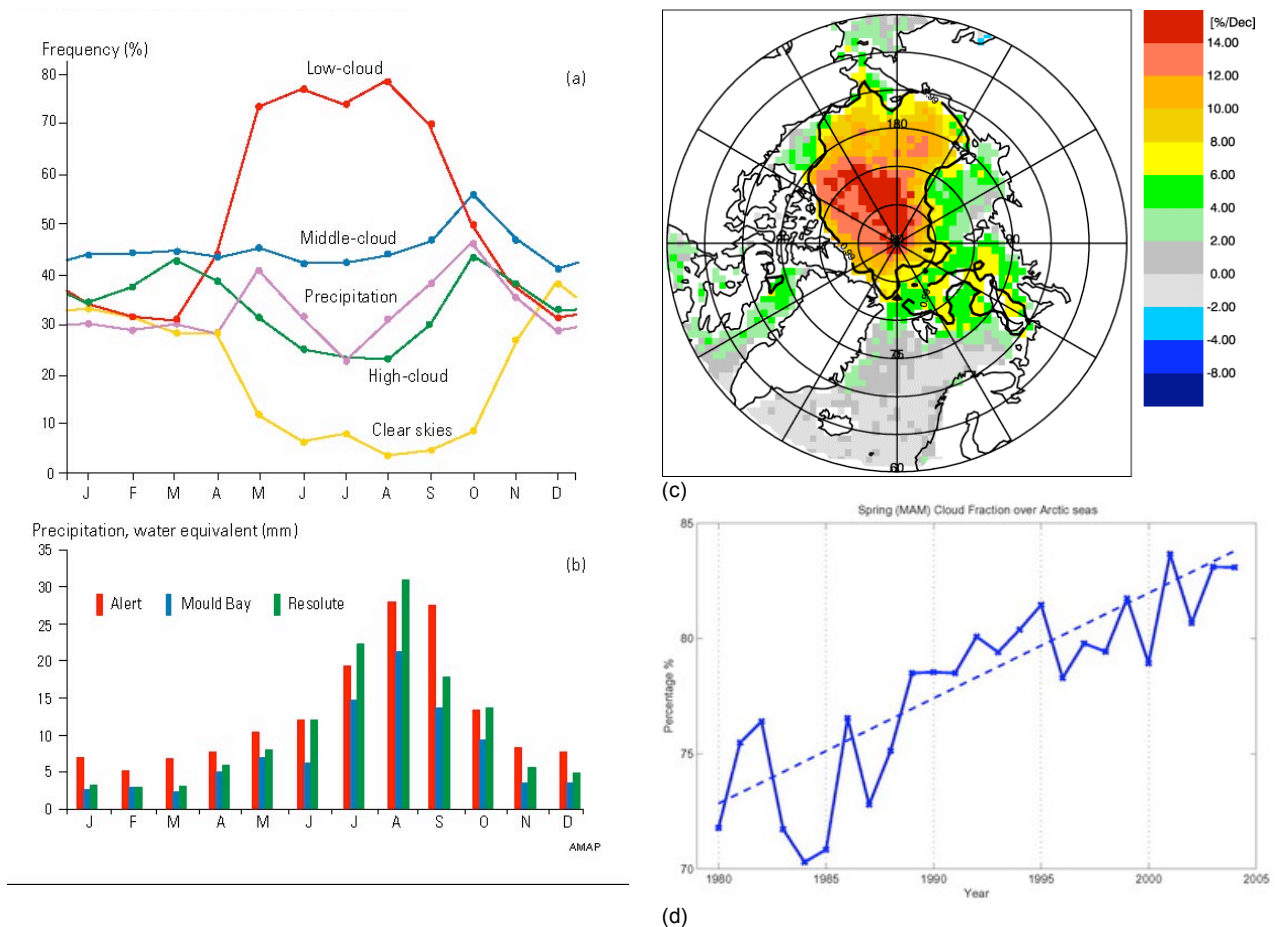


Figure 2.12. Seasonal variability of different cloud types (a) and precipitation (b) in the Arctic; Spatial distribution of trends in cloud cover over twenty years. (c); Time series of seasonally averaged cloud fraction (d) over the arctic seas in spring (March, April, May). (ref. Axel J. Schweiger for c and d).

Clouds are composed of minute water droplets, ice crystals or a combination of the two that have condensed on such atmospheric particles as airborne dust, smoke, sea salt, chemical compounds, and meteoric fragments. Condensation on nuclei occurs at relative humidities near 100 percent. Many condensation nuclei such as salts are hygroscopic, that is, they have a special chemical affinity for water molecules and promote condensation at relative humidities under 100 percent.

The most important characteristic of clouds in the Arctic is the summer stratus. From about mid-June to mid-September, the ocean area covered by sea ice is 80 to 90 percent covered with this cloud type. Summer stratus has important effects on the radiation balance of the surface.

The three main cloud layers, with approximate heights, are:

- \* low: up to 2 kilometers (cumulus and stratus)
- \* medium: 2 kilometers to 8 kilometers (altocumulus and altostratus)
- \* high: 8 kilometers to 15 kilometers (cirrus, cirrostratus and cirrocumulus)

In general, much of the arctic sky is covered by low stratus and stratocumulus clouds. Total cloud cover is least extensive in December and January. Starting in May, cloudiness increases. Warm air over the water adjacent to ice, frequent temperature inversions, and fog, cause low level stratus clouds to form and persist through the entire warm period.

The most striking feature of low cloud cover during the winter months is the frequent occurrence over the northern North Atlantic. This manifests itself as uplift of air masses by the frequent cyclone activity in this area associated with the Icelandic Low. Low cloud cover is rather limited over central and eastern Siberia because of the general subsidence (downward motion) of air in the area of the strong Siberian high. During summer, the Icelandic Low and Siberian High weaken. Low cloud cover becomes more uniform, but with a distinct increase over the Arctic Ocean. The increase reflects the dominance of low-level stratus, which form as warm air masses moving over the ocean are chilled by the cold, melting sea ice cover. The autumn months illustrate the transition back to the winter pattern. Total cloud cover combines low, middle and high clouds. While amounts of total cloud are hence greater than for only low cloud, it can be seen that most cloud cover is of the low variety.

Clouds are important to the Arctic climate because they trap high temperatures and reflect sunlight in spring and summer. There has been a nearly linear increase in the cloud cover over the central Arctic in the previous two decades. The linear trend of the time series and the western Arctic location of the major changes contrasts with the regime-like variation of the AO. The difference between the linear trend of clouds and the behavior of the AO highlights present uncertainties in understanding Arctic climate.

### ***2.1.7 Precipitation***

Precipitation, usually falling as snow, is the factor of arctic climate most important to the hydrological cycle. The principal forms of precipitation are rain, drizzle, freezing rain, snow, ice pellets (sleet), and hail. Precipitation form depends on the source cloud and the temperature of the air below the cloud. Moisture may be deposited not only by precipitation but as dew or hoar frost on a horizontal surface or on a vertical surface as rime crystals. Rain falling on a surface that is below 0 degrees Celsius forms glaze.

Cloud development is not always an indication of coming rain or snow. Although all precipitation occurs because of condensation, cloud physicists have determined that condensation alone cannot cause cloud droplets to grow into raindrops. This is because updrafts within clouds are usually strong enough to prevent cloud particles from leaving the base of a cloud and falling to the earth's surface. Even if droplets or ice crystals descend from a cloud, their downward drift is so slow that they might travel only a short distance before evaporating in the unsaturated air beneath the cloud. Cloud particles must grow large enough to counter updrafts and survive a descent to the earth's surface as raindrops or snowflakes without completely evaporating.

Once a raindrop or a snowflake leaves a cloud, it enters unsaturated air where either evaporation or sublimation can take place. In general, the longer the journey to the ground and the lower the relative humidity of the air beneath the clouds, the greater the quantity of rain or snow that returns to the atmosphere as vapor through evaporation or sublimation.

Eventually an ice crystal or water droplet becomes big enough (heavy enough) to start to fall. Often the particles will catch updrafts as they fall and circulate in the cloud a few times to pick up more water or ice. Many particles that start out as ice crystals never reach the ground. For instance, if the air is very dry, they simply evaporate, while relatively warm air will change ice into rain, and strong winds can break ice crystals into smaller fragments.

The amount of precipitation in a given region depends on the amount of available atmospheric water vapor (precipitable water), as well as on the processes that cause condensation, in particular the uplift of air associated with cyclones and fronts, as well as convection. If all the water vapor in the atmosphere were condensed, the earth's surface would be covered, on average, with

a 25 mm layer of water. However, since the amount of water vapor the atmosphere can hold decreases with decreasing temperature, the amount of water that can be condensed from the air generally decreases with latitude. In general, the amount of precipitable water in the humid tropics is more than 40 mm, while near the pole, it is often less than 5 mm.

In some parts of the Arctic, warm ocean currents bring heat and moisture to the air and frontal activity results in increased precipitation. For instance, southern Iceland, southern Alaska and parts of the Norwegian coast receive in excess of 3000 mm of precipitation per year. In contrast, inland areas of the Arctic with continental climate and lower temperatures receive less than 150 mm of precipitation per year.

The Intergovernmental Panel on Climate Change (IPCC, 1996, 2001) has consistently reported 20th-century increases in precipitation in northern high latitudes (55°–85° N) as shown in Fig. 2.13. The increase is similar to that in Karl's (1998) "Arctic region", which includes the area poleward of 65° N but excludes the waters surrounding southern Greenland. In both cases, the greatest increase appears to have occurred during the first half of the 20<sup>th</sup> century. However, the time series are based on data from the synoptic station network, which is unevenly distributed and has undergone much change.

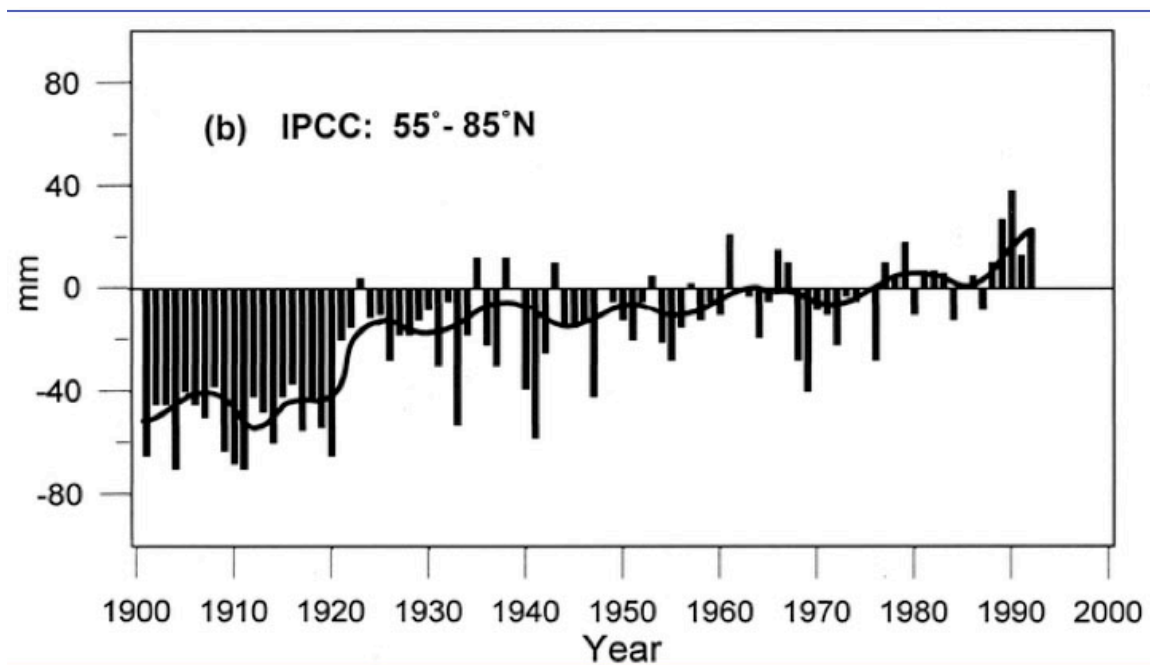


Figure 2.13 Mean annual precipitation between 55° and 85°N (IPCC, 2001).

Arctic precipitation has a characteristic the seasonal cycle (Fig. 2.12 b). During winter, precipitation is highest over the Atlantic sector. This represents the effect of frequent cyclone activity associated with the Icelandic Low. High precipitation totals are also found south of Alaska corresponding to the Aleutian Low. The lowest amounts are found over the central Arctic Ocean and land areas, where cyclone activity is uncommon and anticyclonic conditions are more the rule. From spring into summer, the pattern changes. The precipitation maxima over the Atlantic side and south of Alaska weaken, attended by increases in precipitation over the Arctic Ocean and land. The increases over the Arctic Ocean correspond to the seasonal increase in cyclone activity in this area. This is also true for the increase in precipitation over land. Perhaps surprisingly given the high latitude, the summer maximum in terrestrial precipitation is also contributed to by convective activity (that is, by thunderstorms). Autumn shows the transition back to the winter regime. The maxima associated with the Icelandic and Aleutian lows is reestablished, and precipitation decreases over land.

### 2.1.8 Snow cover

Snow cover is an important feedback mechanism in the climate system. The extent of snow cover depends on the climate e.g. on temperature and solar radiation. However it also influences the climate and climate related systems by affecting the reflection of radiation, the thermal insulation, hydrology and length of the growing season. A decrease in snow cover reduces the reflection of solar radiation, contributing to accelerated climate change. Snow cover affects river discharge, vegetation (thermal insulation) and wildlife (migration patterns). Snow cover retreat has an adverse effect on snow sports and winter tourism as well as on the generation of hydroelectric power based on melt water. On the other hand, snow cover retreat might reduce complications in winter road and rail maintenance, and improve transport. Snow data resulting from remote sensing since the mid 1960s and terrestrial measurements are available with low uncertainty. The uncertainty in projected future snow cover is greater due to incomplete knowledge of the climate system and of non-climatic parameters, e.g. landscape properties such as topography and vegetation cover

Satellite records indicate that the northern hemisphere's annual snow cover extent has decreased by about 10 % since 1966 as a consequence of higher land temperatures (IPCC, 2001a). This change mainly affects the snow cover in spring and summer, which has significantly decreased since the mid-1980s over both the Eurasian and American continents (Robinson, 1997, 1999).

The winter fields indicate greater snow depths over the North American side of the Arctic Ocean. This is because temperatures are lower in this region, so that snow falling during the autumn months tends to more readily accumulate compared to other areas. However, March shows a tendency for deeper snow cover towards the Atlantic side of the Arctic Ocean. This is because winter snowfall is comparatively high in this area due to the northward penetration of storms associated with the Icelandic Low. Moving through spring and summer, the pattern of greater snow depths on the North American side is reestablished. Again, this is because this region tends to be colder, but here the effect is to result in slower melt. Most of the snow is melted by August. The season's first snowfall tends to occur in September. Because snow densities are broadly similar across the Arctic Ocean, the seasonal cycle of snow water equivalent is similar to that of snow depth.

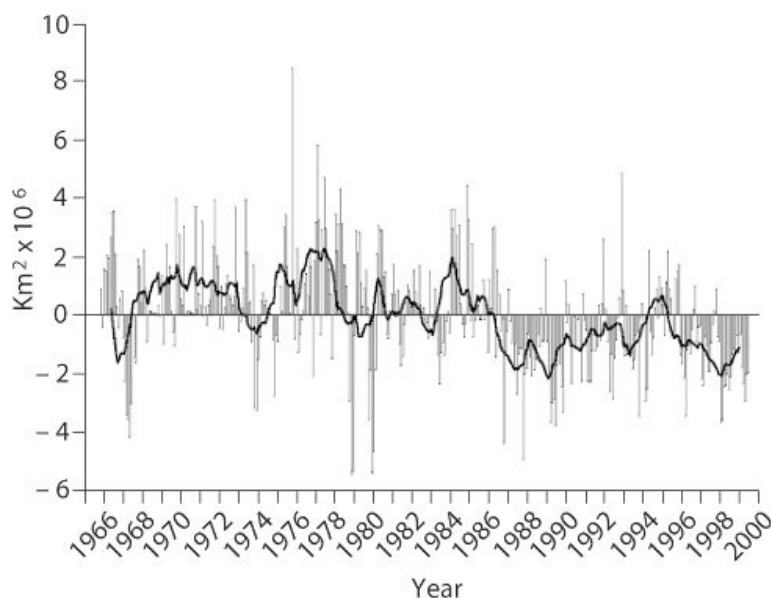


Figure 2.14. Deviations of monthly snow cover extent over the northern hemisphere lands (including Greenland). Deviations are compared to a 30 year average. 12-month running means (solid curve). From IPCC, 2001.

Land areas with high winter snow depths correspond in part to regions with fairly high elevations (for example, Alaska and parts of Siberia). This is understood in that higher-elevation areas tend to be somewhat cooler, so snow can more easily accumulate in autumn. Snowfall may also be enhanced by orographic uplift of air masses. For other areas, such as Northwestern Eurasia, large snow depths appear to be more directly a reflection of synoptic activity. Note the low winter snow depths over east-central Siberia, where the strong Siberian High suppresses precipitation. The seasonal melt of the snow cover occurs earlier over the North American side. It is estimated that, as global warming proceeds, regions currently receiving snowfall will increasingly receive precipitation in the form of rain. For every 1 °C increase in temperature, the snowline rises by about 150 metres. As a result, less snow will accumulate at low elevations. In contrast, there could be greater snow accumulation in regions above the freezing line due to increased snowfall in some of these regions.

### 2.1.9 Feedback Loops: Interactions that Influence Arctic Climate

In the climate system a "feedback loop" refers to a pattern of interacting processes where a change in one variable, through interaction with other variables in the system, either reinforces the original process (positive feedback) or suppresses the process (negative feedback). In order to model and predict arctic (and global) climate variability correctly, feedback loops must be understood. Two major feedback processes that scientists consider in studies of arctic and global climate change are described below in simple terms. In nature, the processes are considerably more complicated.

#### Temperature—Albedo Feedback

The temperature-albedo feedback mechanism is illustrated in Fig. 2.15.

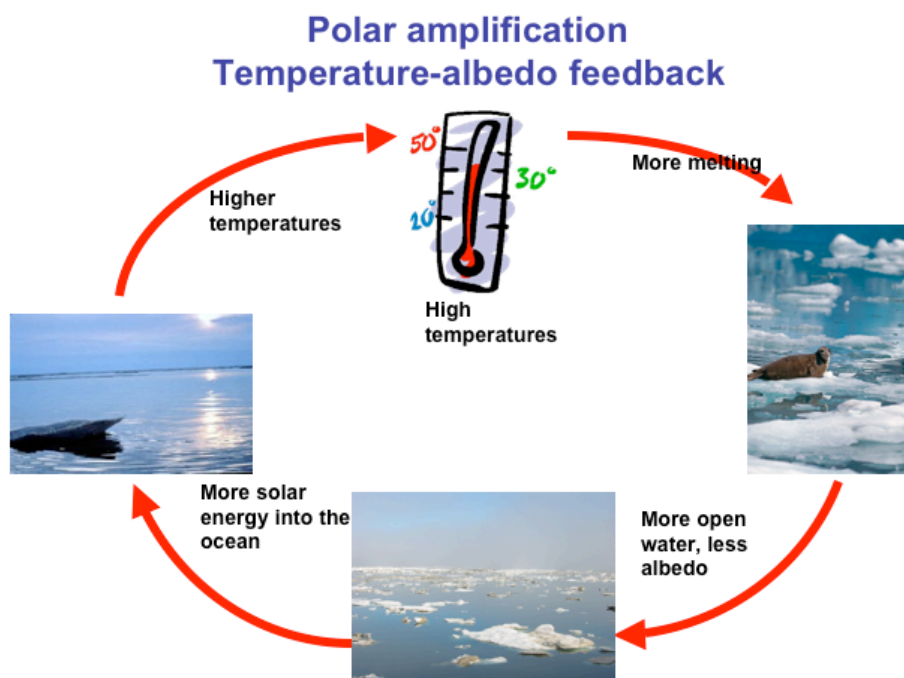


Fig. 2.15 Illustration of the temperature-albedo feedback cycle.



The figure shows that rising temperatures increase melting of snow and sea ice, reducing surface reflectance, thereby increasing solar absorption, which raises temperatures, and so on. The feedback loop can also work in reverse. For instance, if climate cools, less snow and ice melts in summer, raising the albedo and causing further cooling as more solar radiation is reflected rather than absorbed. The temperature—albedo feedback is positive because the initial temperature change is amplified.

### **Temperature—Cloud Cover—Radiation Feedbacks**

Another feedback mechanism is between temperature, cloud cover and radiation, which are potentially important agents of climate change (Fig. 2.16). However, they are not well understood but research in this area is active. It is thought that if climate warms, evaporation will also increase, in turn increasing cloud cover. Because clouds have high albedo, more cloud cover will increase the earth's albedo and reduce the amount of solar radiation absorbed at the surface. Clouds should therefore inhibit further rises in temperature. This temperature—cloud cover—radiation feedback is negative as the initial temperature change is dampened.

However, cloud cover also acts as a blanket to inhibit loss of longwave radiation from the earth's atmosphere. By this process, an increase in temperature leading to an increase in cloud cover could lead to a further increase in temperature - a positive feedback.

Knowing which process dominates is a complex issue. Cloud type plays a strong role, as do cloud water content and particle size. Another factor is whether the cloud albedo is higher or lower than that of the surface. Research indicates that the effect of this feedback in the Arctic may be different than in other latitudes. Except in summer, arctic clouds seem to have a warming effect. This is because the blanket effect of clouds tends to dominate over reductions in shortwave radiation to the surface caused by the high cloud albedo.

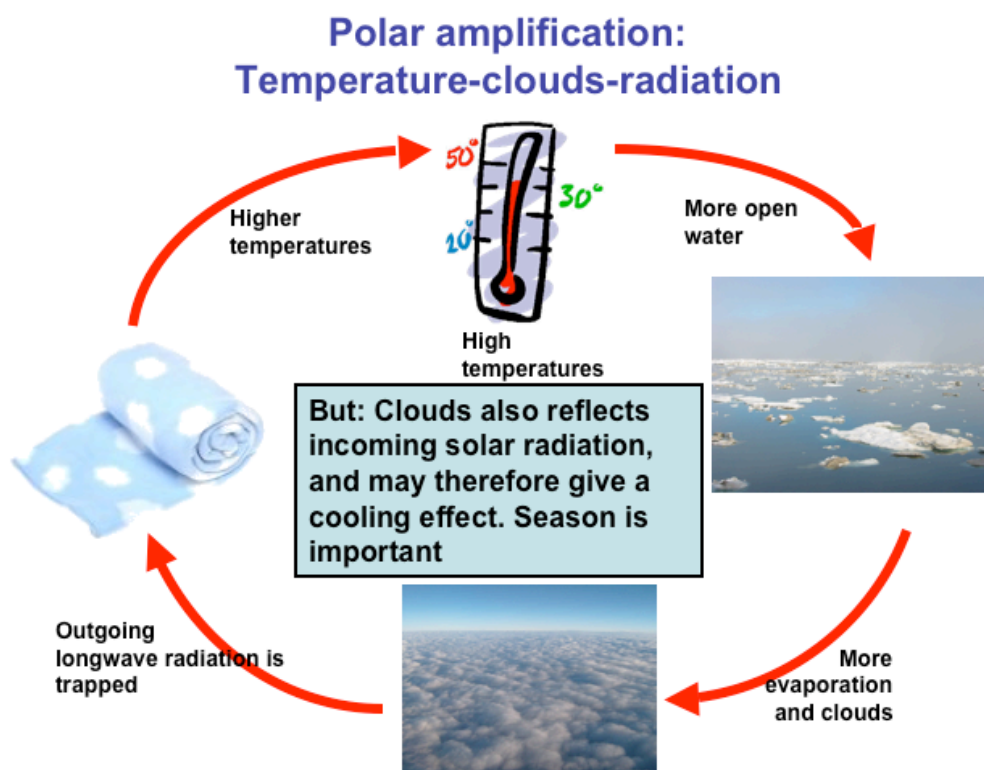


Figure 2.16 Illustration of the temperature-cloud-radiation feedback cycle.

## ***The Arctic as a "Heat Sink"***

The Arctic plays a key role in the earth's heat balance by acting as a "heat sink." The global earth-atmosphere system gains heat from incoming solar radiation, and returns heat to space by thermal radiation. Most of the heat gain occurs in low latitudes, and this gain is balanced (on average) by heat loss that takes place at latitudes north and south of about 40 degrees. Therefore the Arctic is said to act as a "heat sink" for energy that is transported from lower latitudes by ocean currents and by atmospheric circulation systems.

Heat is transported to the Arctic primarily in the following ways:

- Sensible heat is transported poleward during the exchange of air masses from the tropics to the middle and high latitudes. This transfer of heat is largely accomplished by cyclones.
- As storms travel poleward, some of the water vapor condenses as clouds, thereby releasing latent heat.
- Ocean currents bring heat from the tropics to the northern part of the Atlantic Ocean and into the Arctic.

### ***2.1.10 Meteorological conditions of importance for operations and navigation***

The meteorological conditions in the Barents Sea, Kara Sea, Laptev Sea, East Siberian Sea and Chukchi Sea have been reviewed in the INSROP project (Proshutinsky and Weingarten, 1998). The main results of this report are presented in this chapter.

There are three major meteorological factors with impact on Arctic navigation and operations: horizontal visibility (related to fog, rain, snowstorm and duration of daylight), direct influence of wind speed and wind direction, and icing (from the combined influence of air and water temperatures, direction and speed of wind, direction and speed of ship, and state of the sea).

#### ***Visibility***

Lack of visibility slows speed when a vessel is operating in conditions where the ice concentration is greater than 30%. Darkness, fog, and snowstorm are the most important factors determining the horizontal visibility in arctic waters.

The absolute air humidity in the Arctic is very low compared to sub-Arctic and mid latitude areas. Maximum mean monthly relative humidity is observed in summer (85 - 95%), while minimum is observed in winter (75 - 85%). Fog is generated by high relative humidity. In winter, the frequency of fog is low because of low absolute humidity and low number of condensation particles. In the presence of condensation particles (e.g. smoke and vehicle exhaust) frost fog can be observed.

In summer, the air is very close to saturation of water vapor, and a small decrease in temperature is enough to generate fog. In the Arctic fog often occurs during specific wind direction. In summer advective fog prevails when the temperature difference between land and open sea is large. In coastal regions fog often occurs when the wind blows from the open sea towards land. For example, on the west coast of Novaya Zemlya fog is usually generated by westerly winds. During easterly winds there is no fog. The opposite is observed on the east coast of Novaya Zemlya.

For many regions of the Arctic, there is an inverse relationship between fog and wind velocity. Maximum fog events are observed at wind velocities below about 7 m/s. But in some coastal regions and straits fog can be associated with higher winds. There is a strong relation between fog and ice edge location in the arctic seas. There is a maximum frequency of fog in the northern part

of the ice-free waters, near the ice edge. The frequency of fog increases with increasing ice concentration up to about 80-90%. The longest duration of fog periods is observed in summer in the coastal regions and around islands in the western part of the Barents Sea, where warm currents meet cold arctic air masses. Fog caused by evaporation occurs frequently in Kola Bay and other bays in the Barents Sea. From December to February up to 22 - 24 days of fog per month can occur. In Murmansk, 50% of the fog events are regular or strong fogs and about 20% are very strong fogs with visibility of less than 50 m.

A snowstorm is defined by wind velocity above 8 m/s and air temperature below 0°C, leading to visibility less than 2.5 km. In the coastal regions snowstorms occur usually from October through May. In the northern regions the snowstorm periods can be longer. The annual number of days with snowstorm is 100 - 120 days in the Barents, Kara, and Chukchi seas, and 60 - 80 days in the East Siberian and Laptev seas. Very low visibility (less than 1 km) occurs in summer due to fog and in winter due to snowstorms and darkness. In June - August, low visibility in the open sea occurs 25 - 30% of the time, decreasing to 10 % at the coast. During limited visibility there is increased risk for ships to lose their ice navigation channel, get stuck in ice, or break convoy motion.

### Wind regime

The atmospheric pressure and circulation patterns as described in this section 2.1, define the character of prevailing winds in the arctic seas. As an example of wind statistics, wind roses for January are presented in Fig. 2.17.

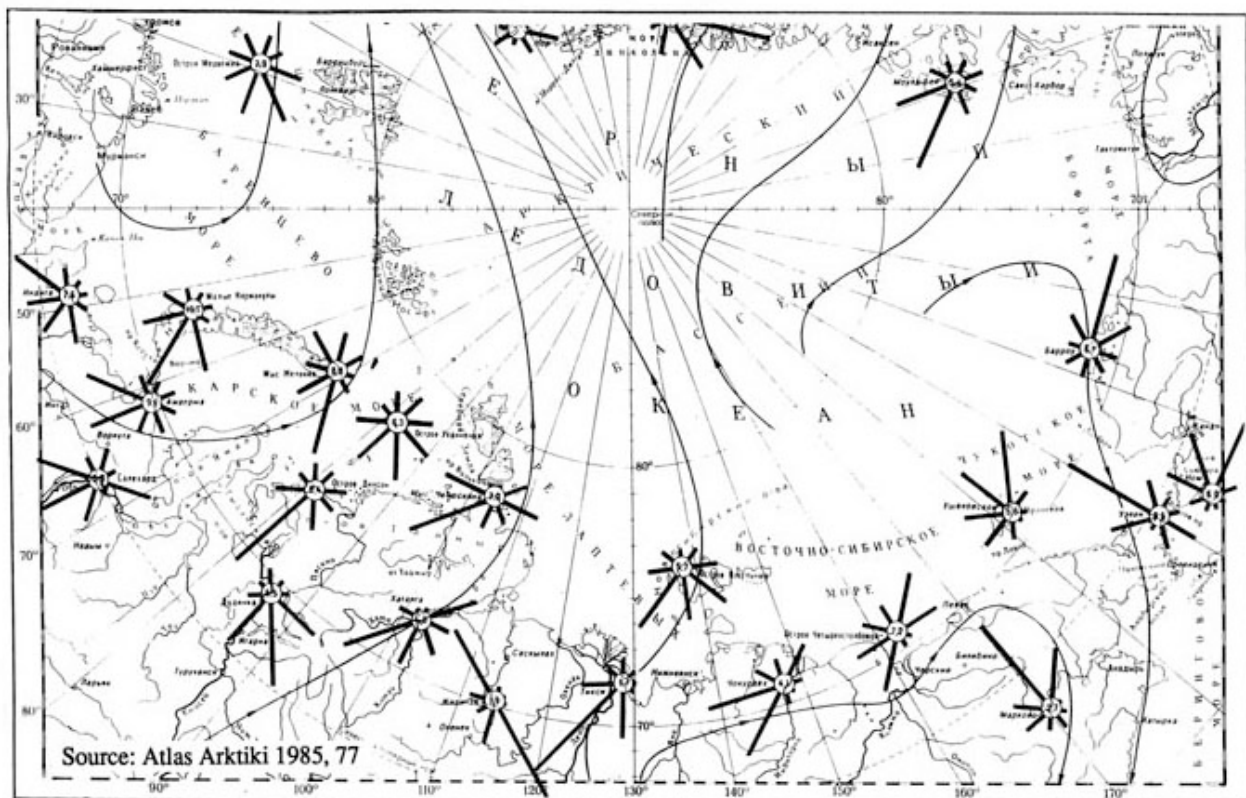


Figure 2.17. Wind roses for January in the Eurasian sector of the Arctic. The number in the center of the roses indicate mean wind speed in m/s. The length of the rays represent the probability of occurrence of wind direction in %.



In winter winds are often blowing from a south-southwesterly direction in the Barents and Kara Sea region. In the Laptev Sea, prevailing wind direction is from the south-southwest in winter. Over the New Siberian Islands and in the East Siberian Sea, the winds are ranging from westerly to southerly and easterly. Northerly winds prevail in the Chukchi Sea with directions ranging from northwest in the western part to northeast in the eastern part. In the southeastern part of the Chukchi and Bering seas, northerly winds prevail in winter. The mean wind speeds are relatively low, 4 - 5 m/s, but show significant regional variability. For example, in the western and eastern regions the velocities are higher than in the central part. In winter, the highest mean monthly wind speed is observed in the Barents Sea (8 - 9 m/s), followed by the Kara Sea (6 - 8 m/s). In the Laptev Sea and in the western part of the East Siberian Sea, the mean wind speed is less than 5 m/s. In the eastern part of the East Siberian Sea and in the Chukchi Sea, the mean wind speed is 5 - 7 m/s.

During the arctic summer, the atmospheric pressure and wind regime is often opposite to the typical winter situation. Low pressure tends to prevail over the Siberian continent, while high pressure prevails over the arctic seas. The summer monthly mean wind speed is more or less uniform (5 - 6 m/s) along the entire Russian Arctic. In both winter and summer, wind speeds typically increase near capes, in straits and in bays. High wind speeds (> 15 m/s) are observed more often in winter than in summer. In the Barents Sea, there are about 6 - 8 stormy days in January, while the Kara Sea has 4 - 6 stormy days. In the Laptev and East Siberian seas, the number of stormy days is lower, 2 - 5 days per month. In the Chukchi Sea, 6 - 10 storm days occur per month.

In summer, an average of 1-2 stormy days occur per month, but 10 - 12 stormy days can occur per month in specific places where topography enhances the wind speed. The duration of storm events for all the polar stations ranges from 6 to 24 hours. In winter, however, stormy weather can last 8-14 days in extreme cases. There are several places in the Russian Arctic where orographic effects generate increased wind speeds. Maximum catabatic wind speeds have been observed to be 50 - 56 m/s at Rudolph Island, 70 m/s at the Karmakuly, 49 m/s at Mys Stolbovoy, and more than 80 m/s at Pevek. In summer, these winds can bring warm air masses with strong temperature increase (up to 20-25 °C per day) according to (e.g. Dementev, 1985).

Wind is an important factor affecting ice conditions, especially the drift and deformation of ice. The wind conditions can be classified as "push-off" and "push-on" according to their effect on the ice drift. Push-off winds will weaken or remove the pressure in the icepack, while push-on winds will do the opposite. Along the Siberian coast, push-on winds are, with few exceptions, blowing from northerly directions. In the western Siberian coast push-on winds occur in 60 - 70% of the days in June and 33 - 35% in August. In the eastern East Siberian and Chukchi seas the occurrence rate of push-on winds increases towards the end of the navigation period (October-November). Push-on winds are usually followed by push-off winds or by low winds normally lasting for several days. The most severe push-on area is to the west and east of Vilkitsky Strait and in the vicinity of New Siberian Islands where more than 15 days of push-on winds can occur. The longest duration of push-on winds, lasting for 32 days, was observed in the western part of the Laptev Sea and in the area to the west of Vilkitsky Strait. The occurrence rate of winds with a speed of less than 12 m/s (up to 15 m/s in gusts) is greatest in the northernmost parts of the Siberian Coast, especially at the end of the navigation season. The occurrence of push-on winds varies considerably from year to year.

## Icing on vessels

There are two types of icing which can occur on vessels in cold weather regions: atmospheric icing and sea-spray icing. The most severe type is sea-spray icing, which can be a serious hazard for marine operations in polar regions.

Many lives and ships have been lost after ships sank or became disabled, after the accretion of ice on decks and superstructures (Fig. 2.18). The extra weight from ice accretion can cause capsizing, extreme rolling and pitching and topside flooding. Icing is particularly dangerous for fishing vessels and other small ships. Also navy ships with high superstructures, high speeds and low freeboard are vulnerable to icing.

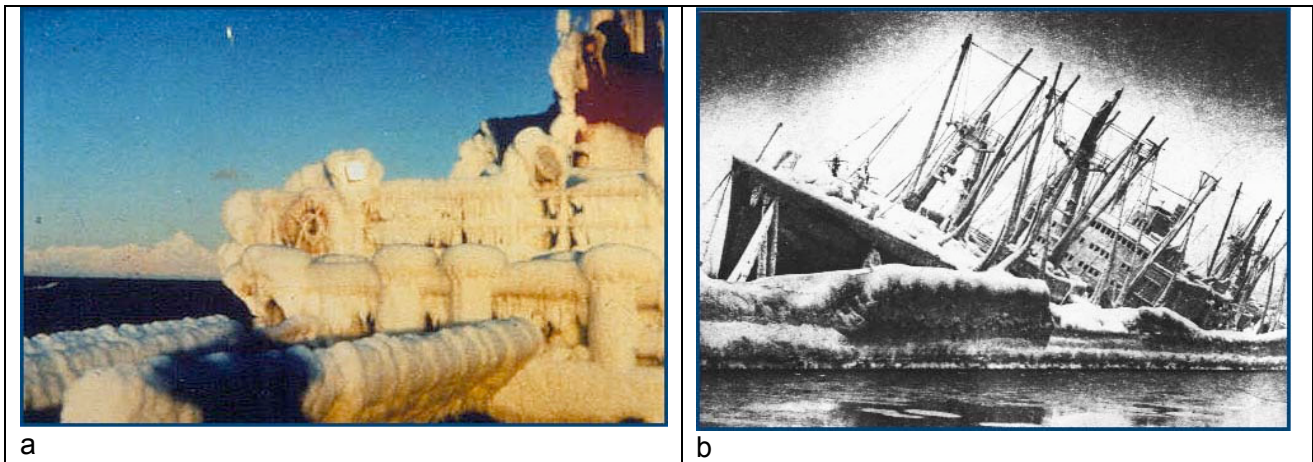


Figure 2.18. Photographs of icing on vessels operating in the Arctic (Courtesy Peter Guest).

The environmental factors determining icing include: wind speed, air temperature, water temperature, the freezing temperature of water, wind direction relative to the ship, swell and wave parameters (wave height, wave length, wave propagation direction). The main criteria for icing to occur are:

1. High Wind Speed - above 9 m/s but sometimes lower
2. Low Air Temperature - below freezing ( $-1.7\text{ }^{\circ}\text{C}$ )
3. Low Water Temperature - usually below  $7\text{ }^{\circ}\text{C}$

The first two occur during cold advection, easily observable in AVHRR images (for example during a polar low situation where wind is blowing off-ice, Fig. 2.19b).

The most important areas in the Northern Hemisphere are the Norwegian Sea, the Barents Sea, the Labrador Sea, the Bering Strait, Gulf of Alaska and Sea of Okhotsk (Fig. 2.19a). Icing can occur in all Marginal Ice Zones, in the Great Lakes, the Black Sea, the Caspian Sea and the Baltic Sea, wherever water is  $< 5\text{ }^{\circ}\text{C}$ .

The main vessel characteristics are speed, heading (with respect to wind, waves and swell), length, freeboard, handling and cold soaking. Threshold wind speeds for icing to occur on various length of ships is shown in Table 2.1.

Table 2.1 Icing as function of vessel length, wave height and wind speed

Parameter	Threshold values					
	15	30	50	75	100	150
Vessel length (m)	15	30	50	75	100	150
Significant wave height (m)	0.6	1.2	2.0	3.0	4.0	6.0
Wind speed at 200 km fetch (m/s)	5.0	7.4	9.8	12.5	15.0	20.0

The table is only a rough guide for ships steaming into the wind and waves. The actual potential for icing depends on the type, load, and handling characteristics of a particular ship. Any captain or bridge officer who is familiar with a ship should be well aware of the wind speeds which cause sea spray to reach the deck and superstructure, and should base his/her assessment on the potential for icing on this knowledge.

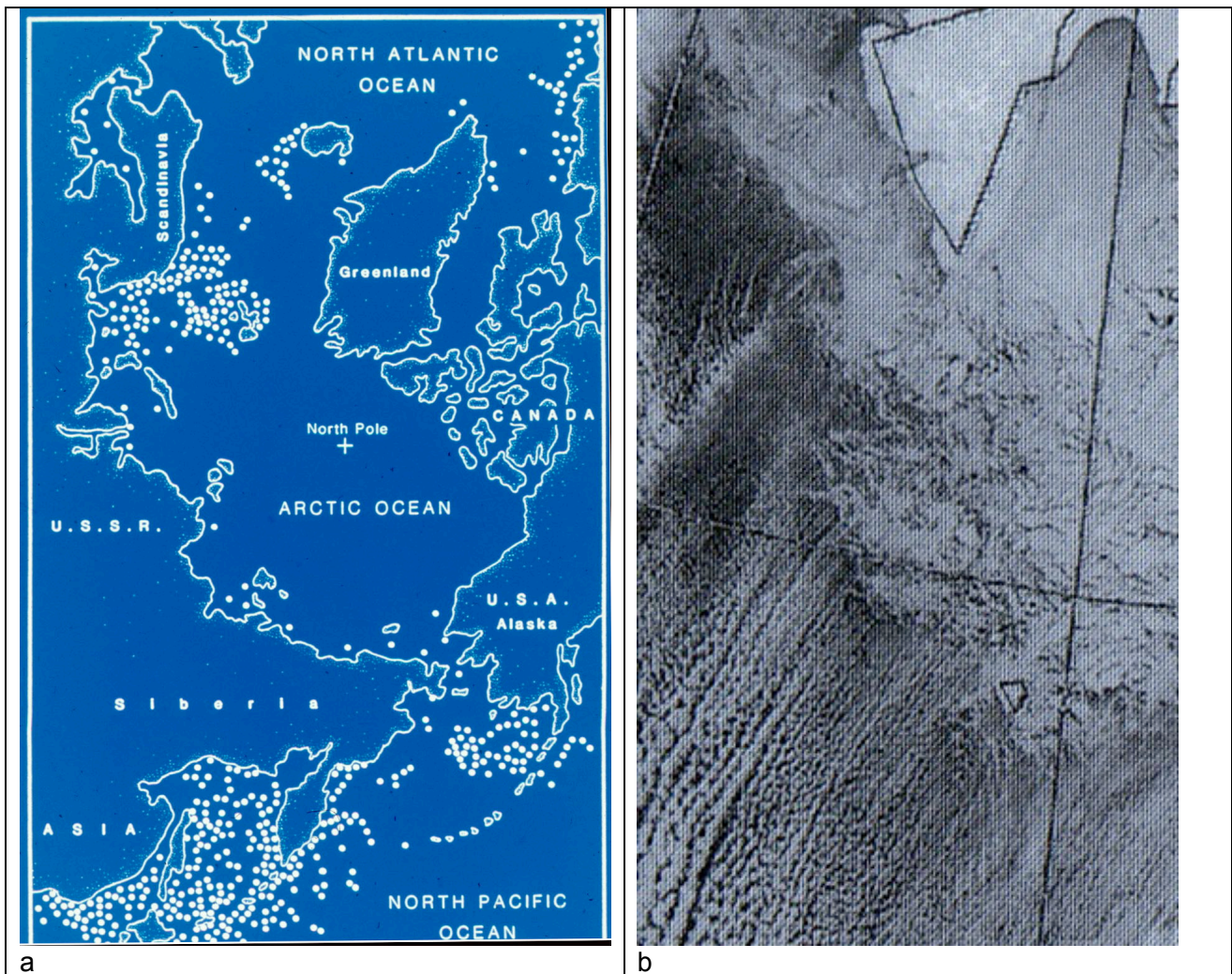


Figure 2.19. (a). Map of the areas with most frequent occurrence of icing on vessels in the Arctic areas (white dots); (b) example of cold advection observed in an NOAA AVHRR image where cold air masses flow out in open water areas generating characteristic convection cells. This example is from the western Barents Sea (courtesy P. Guest).

A forecasting algorithm for icing has been developed by Jim Overland (Overland et al., 1986). For vessels from 20 to 75 meters in length the following formula can be applied:



$$PPR = \frac{V_a(T_f - T_a)}{1 + 0.3(T_w - T_f)}$$

where

PPR = Icing Predictor ( $\text{m}^\circ\text{Cs}^{-1}$ )

$V_a$  = Wind Speed ( $\text{m s}^{-1}$ )

$T_f$  = Freezing point of seawater (usually  $-1.7^\circ\text{C}$  or  $-1.8^\circ\text{C}$ )

$T_a$  = Air Temperature ( $^\circ\text{C}$ )

$T_w$  = Sea Temperature ( $^\circ\text{C}$ )

Icing class and icing rates for different PPR are shown in Table 2.2.

Table 2.2 Icing predictor according to Overland et al. (1986)

PPR ( $\text{m}^\circ\text{Cs}^{-1}$ )	< 0	0-22.4	22.4 – 53.3	53.3 – 83.0	> 83.0
Icing class	None	Light	Moderate	Heavy	Extreme
Icing rates (cm/hour)	0	< 0.7	0.7 – 2.0	2.0 – 4.0	> 4.0

By using forecasts of wind and temperature, the algorithm by Overland can be used to predict icing class and icing rates for a given vessel. A graphical presentation of icing classes is shown in Fig. 2.20.

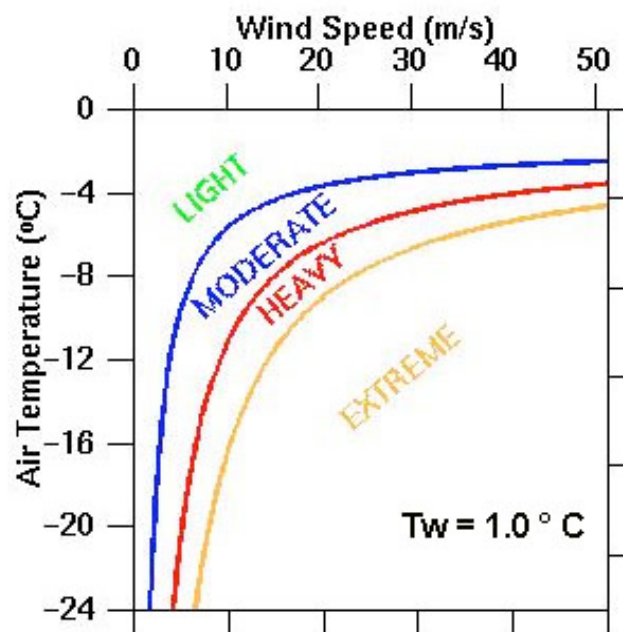


Figure 2.20. Criteria for icing according the algorithm Overland et al. (1986). The water temperature in this case is  $1.0^\circ\text{C}$ .

## 2.2 Physical Oceanography

### 2.2.1 Bathymetry and circulation patterns

The Arctic Ocean with the adjacent shelf seas are influenced by relatively warm and saline water from the Atlantic Ocean, advecting through the Fram Strait and the Barents Sea into the Arctic Ocean. Polar water masses of relatively low salinity and low temperature are supplied through Bering Strait from the Pacific. River run-off from the continents adds a significant amount of fresh water. The water of Atlantic origin circulates within the Arctic Ocean on different paths whereby it undergoes intensive modifications. The waters exiting the Arctic Ocean supply the source waters for the formation of North Atlantic Deep Water, which plays a significant role in the global thermohaline overturning circulation. Shallow water masses leave the Arctic Ocean through the Fram Strait and Canadian Archipelago into the Labrador Sea (Fig. 2.21).

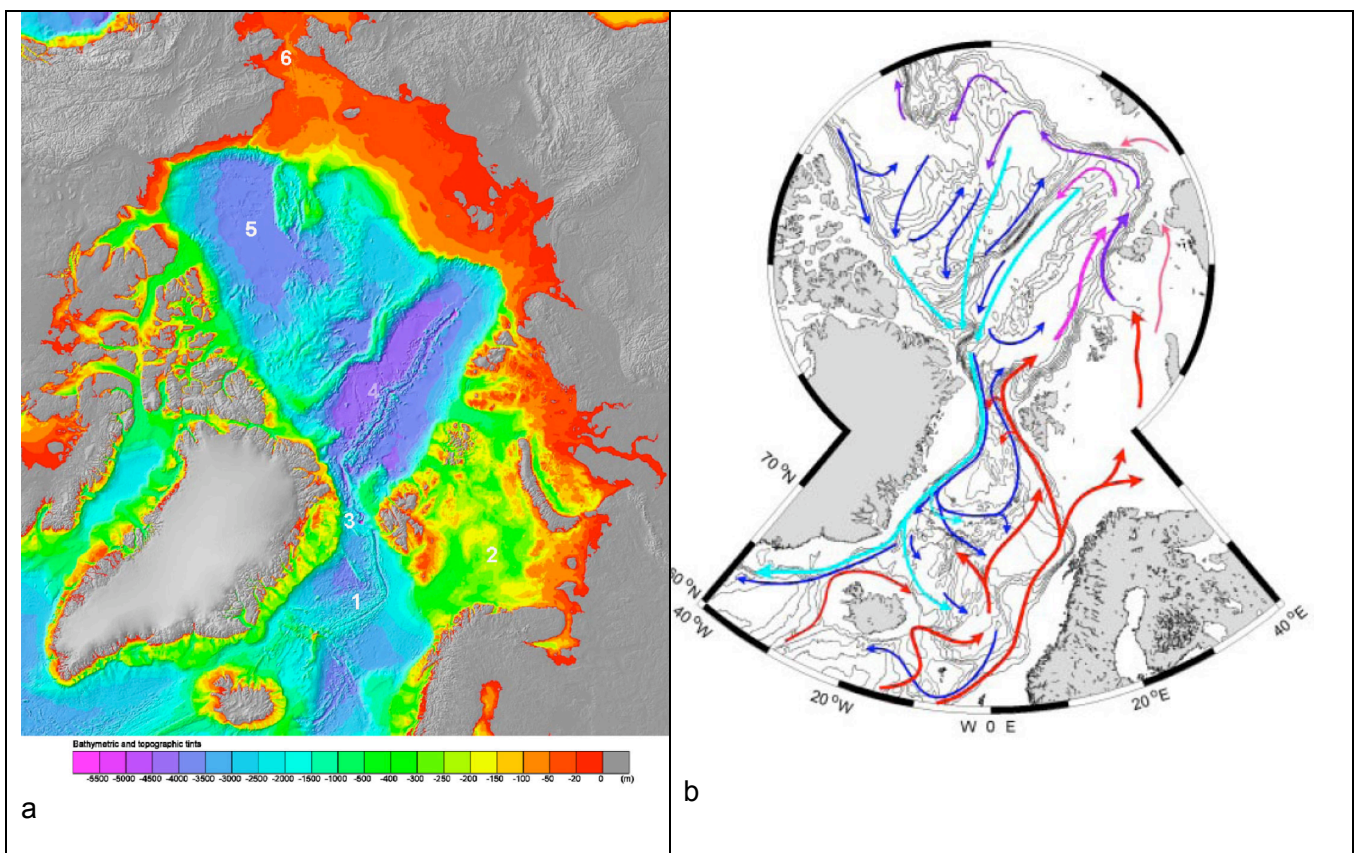


Figure 2.21. (a) Bathymetry of the Arctic Ocean and surrounding seas. 1: Nordic Seas, 2: Barents Sea, 3: Fram Strait, 4: Eurasian Basin, 5: Canadian Basin, 6: Bering Strait. (the chart is obtained from IBCAO, <http://www.ngdc.noaa.gov/mgg/bathymetry/arctic/arctic.html>) (b) Illustration of the major currents in the Arctic Ocean and the Nordic Seas: red is Atlantic water, light blue is Polar Water, dark blue/violet is Arctic Intermediate Water (Nordic Council, 2002).

The Fram Strait represents the only deep-water connection between the Arctic Ocean and the Nordic Seas. This strait is characterized by a northward flow of deep waters from the Greenland and the Norwegian Sea entering the Arctic Ocean, and deep waters from the Arctic basins flowing southward to the Nordic Seas. The source waters for the North Atlantic Deep Water formation leave the Nordic Seas as overflows between Greenland and Scotland.

The Nordic Seas comprise the Icelandic, the Norwegian and the Greenland Sea. To the south they are separated from the North Atlantic by a system of sills between Greenland and Scotland (Hansen and Østerhus, 2000). Warm and saline Atlantic water is penetrating across the sills into the Nordic Seas, as shown by the red arrows in Fig. 2.21b. Cold and dense water crosses the sills to the south and forms the overflow, which determines together with the water masses from the Labrador Sea the properties of the North Atlantic Deep Water. Within the Nordic Seas the North Atlantic Current leads the Atlantic Water at the eastern side to the north where it reaches through the Barents Sea and Fram Strait the Arctic Ocean. At the western side, the East Greenland Current transports cold and low saline Polar Water from the Arctic Ocean to the south. The two major meridional current systems are connected by cyclonic gyre flows that form several circulation branches. They are to some extent steered by bottom topography and lead waters of Atlantic origin to the west where it is incorporated into the southward flow as Atlantic Return Water and those from the East Greenland Current to the east. In the interior of the gyre water mass modifications occur affecting the properties of the recirculations and forming the Greenland Sea Deep Water, which leaks into the deep Norwegian Sea. The overflow water to the North Atlantic consists mainly of waters from intermediate depths and comprises a variety of products of water mass modifications (Rudels et al, 2002).

The oceanic circulation in the Arctic Ocean is driven by a combination of wind and thermohaline forcing. The air pressure distribution is basically determined by a high-pressure system over the Beaufort Sea and low pressure over the Nordic Seas leading to an anticyclonic circulation pattern. However, it is strongly modified by the topographical structure of the basins which gives rise to internal circulation cells (Alekseev et al., 2004). The Arctic Ocean and adjacent seas are covered by a seasonally varying ice cover, which moves by wind forcing and ocean currents. The anticyclonic circulation in the Beaufort Gyre, often called the Beaufort High, and a less well-established cyclonic counterpart over the European Arctic feed into the Transpolar Drift. The latter provides the major export of sea ice through Fram Strait into the Nordic Seas where most of it melts and affects the stability of the water column. Due to the large-scale sea level inclination there is a net flow from the Pacific Ocean into the Atlantic. In spite of a relatively small mass transports, this flow represents due to its low salinity a major control of the global fresh water cycle, maintaining the balance between the relative saline Atlantic and the fresher Pacific water.

A major shift in the atmospheric pressure system and the ice drift pattern has been observed during the 1980s and 1990s as shown in Fig. 2.22 (Steele and Boyd, 1998). The most pronounced changes are 1) the Beaufort High has decreased and shifted towards east; 2) the Transpolar Drift shifted axis counterclockwise producing more cyclonic motion in the 1990s, 3) the ice extent and thickness have decreased.

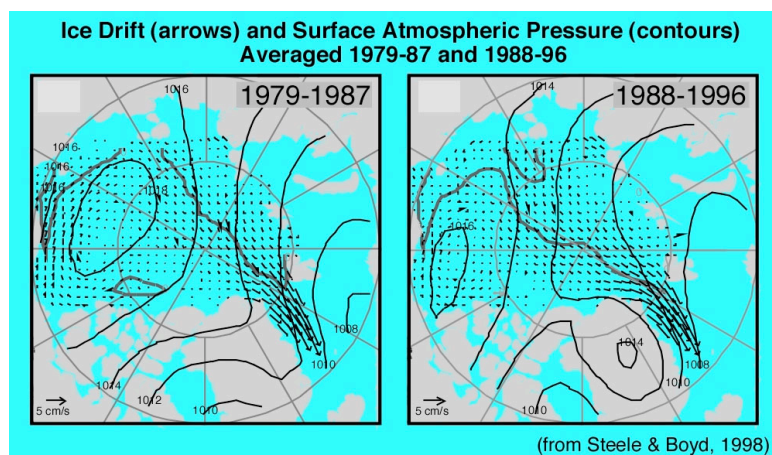
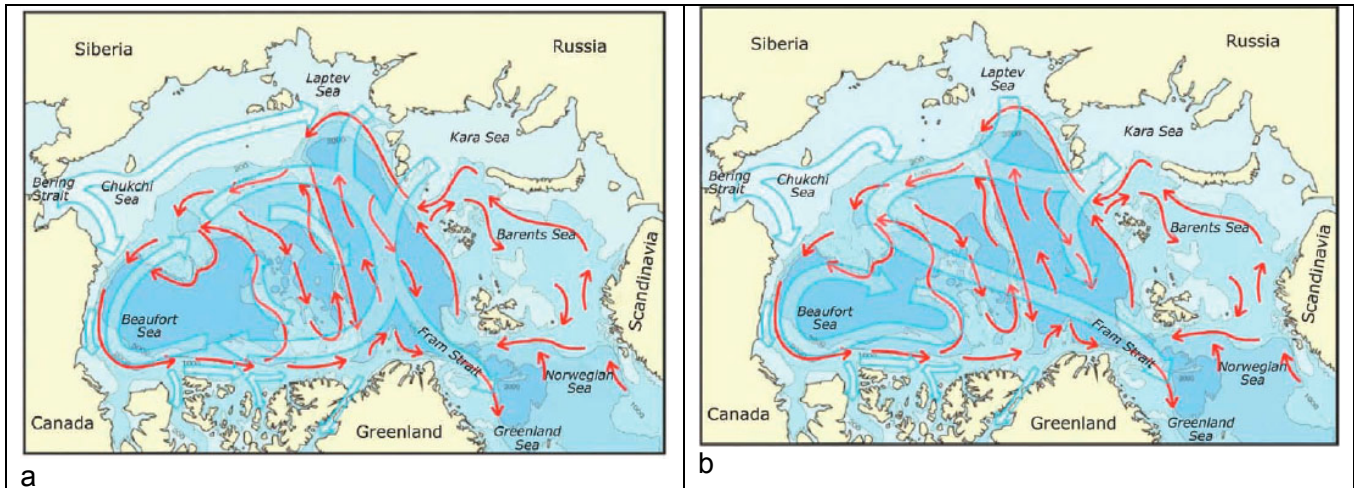


Figure 2.22. Average atmospheric surface pressure fields and sea ice drift fields for the periods 1979-1987 and 1988 – 1996, respectively (Steele and Boyd, 1998).



These changes are associated with two idealized dominant wind-driven ocean circulation regimes: anticyclonic and cyclonic. Climatological studies (e.g., Proshutinsky and Johnson, 1997) provide a foundation for understanding the significance of these ocean surface conditions. These studies indicate that the Arctic ocean surface layer motion is consistent with the Arctic atmosphere surface layer motion, alternating between cyclonic and anticyclonic circulation regimes. Each regime persists from 4 to 8 years, resulting in a period of 8–16 years. The cyclonic pattern dominated during 1989–1996. Since 1997 the dominant regime has fluctuated, with an anticyclonic pattern being slightly more prevalent (Fig. 2.23).



*Figure 2.23. Idealized patterns of the dominant circulation regimes of the Arctic Ocean. Two circulation regimes of surface waters (anticyclonic-a; cyclonic-b) are shown in wide blue arrows. In the cyclonic regime the clockwise circulation pattern in the Beaufort Sea region (the Beaufort Gyre) weakens, and the flow across the basin, from the Siberian and Russian coasts to Fram Strait (the Transpolar Drift), shifts poleward. The cyclonic pattern dominated during 1989–1996; the anticyclonic pattern has prevailed since 1997. The Atlantic water circulates cyclonically (red arrows) at approximately 200–800 m deep, independent of the circulation regime of the surface layer. (Adapted from Proshutinsky et al., 2005).*

Data from satellites and drifting buoys indicate that the circulation of the ocean surface layer has been characterized by an anticyclonic regime for the entire 2000–2005 period. The anticyclonic regime is the result of a higher sea level atmospheric pressure over the Arctic Ocean, relative to the 1948–2005 mean, and the prevalence of anticyclonic winds. The circulation of Pacific water (located at depths between 50 and 200 m) in the Arctic Ocean may be coherent with the surface currents, but its pathways are not known from direct observations

Recently our understanding of the vertical structure of this layer and its properties has been revised by Shimada *et al.* (2001, 2004) and Steele *et al.* (2004), who reported the presence of two types of summer Pacific halocline water and one type of winter Pacific halocline water in the Arctic Ocean.

According to the Environmental Working Group (EWG) analysis (EWG, 1997, 1998), the total thickness of the Pacific layer is approximately 150 m. This thickness is subject to temporal variability (McLaughlin *et al.*, 2003), depending on wind stresses and circulation modes (Proshutinsky *et al.*, 2002). Steele *et al.* (2004) found similar evidence in their examination of data from the 1980s and 1990s.

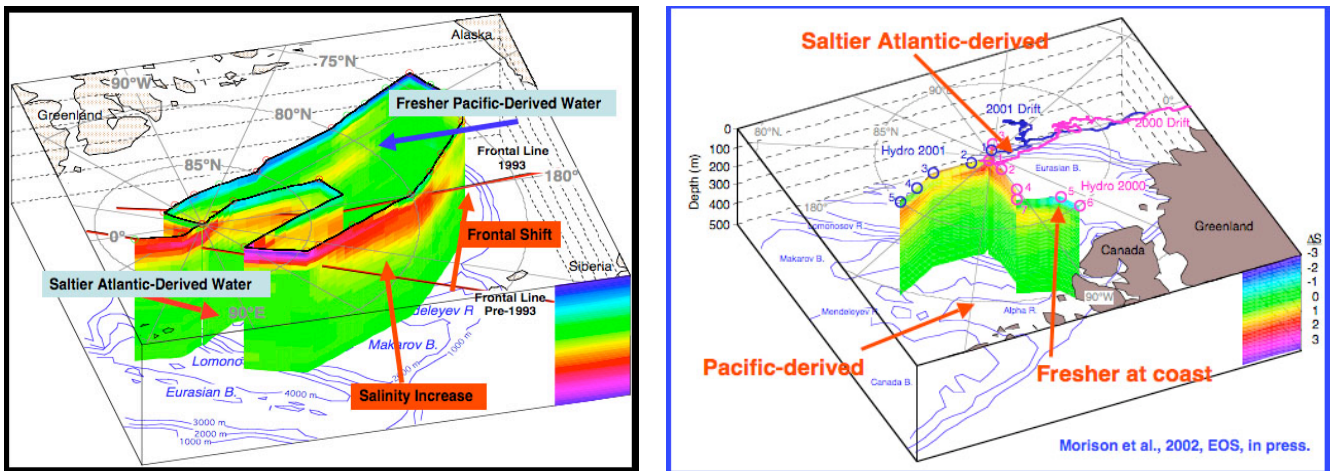


Figure 2.24. Observed changes in water mass properties and fronts in the Arctic Ocean during the 1990s (Morison, et al., 2000, 2002).

A major shift in the atmospheric pressure system and the ice drift pattern has been observed during the 1980s and 1990s as shown in Fig. 2.22 (Steele and Boyd, 1998). The most pronounced changes are 1) the Beaufort High has decreased and shifted towards east; 2) the Transpolar Drift shifted axis counterclockwise producing more cyclonic motion in the 1990s, 3) the ice extent and thickness have decreased. Furthermore, the properties of the water masses have changed in the same period. A comparison of observations during the 1990s with earlier data shows that the Atlantic Water layer was significantly warmer than during earlier decades (Alekseev et al., 2004) and the freshwater layer was significantly saltier (Fig. 2.24). A frontal shift towards east has also been observed between Atlantic and Pacific waters in the Eurasian Basin (Morison et al., 2000). These changes can have severe impacts on the heat fluxes, ice formation and melting rates and other climate related processes. To observe and quantify the changes in the Arctic water masses and circulation more systematically is an important task to be included in future monitoring systems.

The variability of the Atlantic water circulation pattern is not very well known from observations, but model results show that its circulation has a pulsating character expressed in the propagation of warm and cold events, changing from seasonal to decadal time scales. An increase of the Atlantic water temperature in Fram Strait and the Laptev Sea was observed in 2004, as illustrated in Fig. 2.25 (Polyakov *et al.*, 2005). Studies by Maslowski (2000) suggest that the amount of Atlantic Water in the Arctic Basin is linked to the AO, as shown in Fig. 2.26.

The most recent studies by Shimada *et al.* (2006) and Maslowski *et al.* (2006) indicate that the significant reduction of sea ice in the Canadian Basin observed in 2002–2005 may be attributable in part to an increase of heat flux from the Pacific water layer to the bottom of the sea ice, resulting in sea ice melt. Warming of the Pacific water is associated with an increase of heat flux via Bering Strait. In this region, preliminary observations from a mooring site, established and maintained since 1990, suggest that annual mean water temperatures have been about 1°C warmer since 2002, compared to 1990–2001 (Woodgate *et al.*, 2006). Since 2001, there has also been an increase in the annual mean water transport. Changes in the Pacific water circulation may also influence heat release from the Pacific water to the upper ocean layers. The Atlantic water circulates in the Arctic Ocean at approximately 200–800 m deep. This water penetrates to the Arctic via Fram Strait and St. Anna Trough (Barents Sea). Under extensive surface cooling, it sinks to intermediate depths and forms the warm Atlantic Layer, with water temperatures greater than 0°C. This layer is covered by low-density surface waters and is thus prevented from undergoing heat exchange with the atmosphere. The most widely accepted circulation scheme of Atlantic water (Rudels *et al.*, 1994) postulates that it circulates counterclockwise, forming several loops in the Arctic basins.



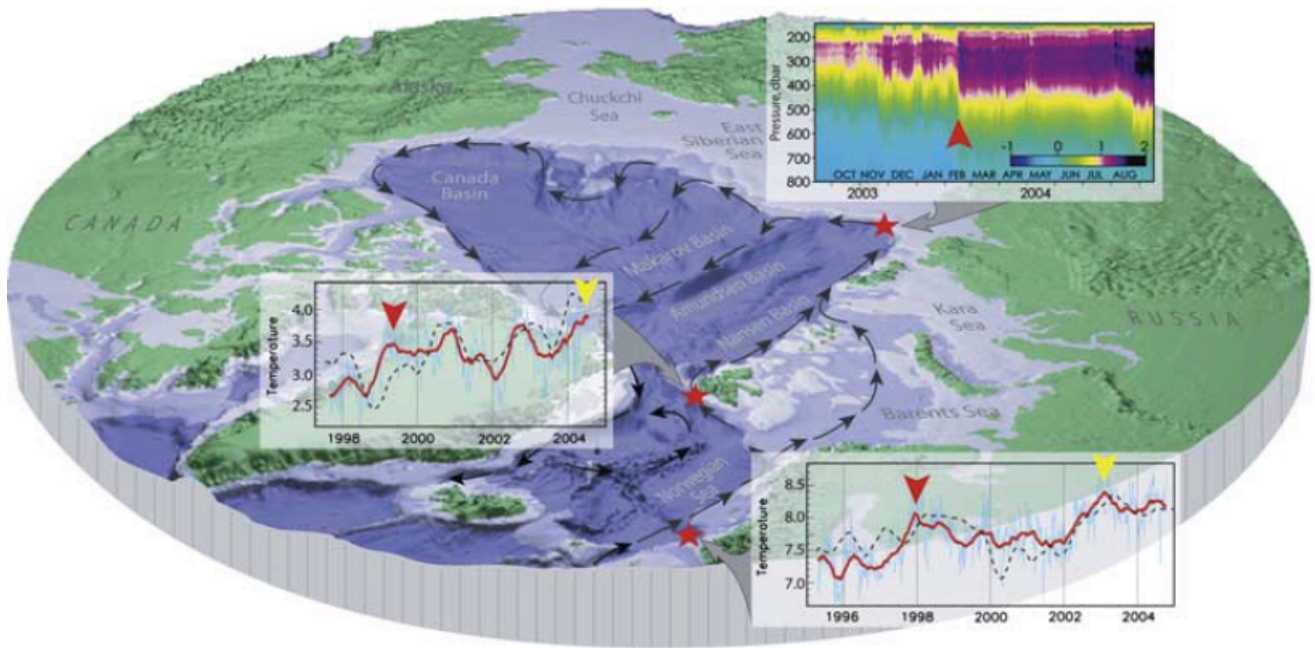


Figure 2.25. Propagation of warm temperature anomalies into the Arctic Ocean. Large red and yellow arrows indicate two pulses of warm AW. The pathways of AW are shown schematically by black arrows. Red stars show locations of moorings. (Top) Depth–time diagram of water temperature ( C) from the EEB mooring. (Middle and bottom) Time series of water temperature ( C) from Fram Strait and Svinoy moorings. Blue lines show weekly averaged temperature, red lines show sixmonth running mean temperature. Simulated [Karcher et al., 2003] de-seasoned six-month running mean water temperature anomalies are shown by black dashed lines. (Polyakov et al. 2005).

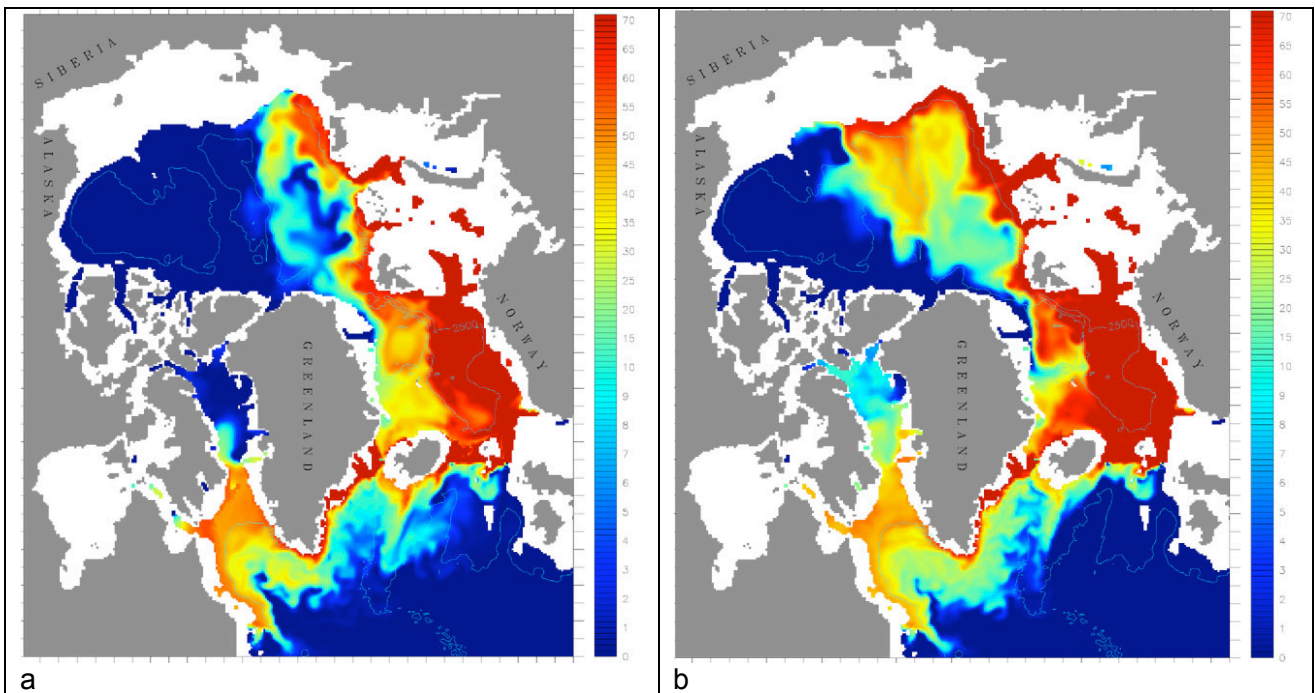


Figure 2.26. Concentration of Atlantic Water tracer (%) averaged over depth of 180-560 m for repeated forcing in 1973 (a) and 1993 (b). 1973 had a low AO while 1993 had a high AO. (Maslowski et al, 2000).

### 2.2.2 Forcing the ocean circulation

The combined heat- and fresh-water transports by the atmosphere set the stage for a dynamical 'conflict' in the ocean of massive proportions: the density of seawater is controlled both by its temperature and salinity. How do dense waters form, so as to sink and complete the globe-spanning circuit of the meridional overturning current (MOC)? Precipitation and ice-melt supply fresh water to the sub-polar ocean, reducing its salinity, and creating a buoyant surface layer which resists the sinking process. Alternating with warm, moist cyclones from the south, cold Arctic winds blowing from the continents tend to increase the density of the ocean surface waters. The winner of this battle of cooling versus freshening of the surface ocean is hard to predict. Just a very few sites in the high-latitude world have an 'open window' to the deep ocean, where surface waters gain very high density and avoid the diluting effects of buoyant fresh water. Such a site is the waters around Greenland. Figure 2.27a gives a snapshot of the low-level winds as an intense cyclone passes east of Greenland. It has a warm, moist sector to the east and yet draws exceedingly cold air off the continent in its north-western, cold sector. Greenland contributes by forming a topographic barrier that channels the winds down Baffin Bay, over the Labrador Sea, to its west, and promotes cyclone development in its wake to the east. Greenland is more than 3 km high, and extends one-quarter of the distance, north and south, between the pole and the equator. Evidently we should expect cooling of the ocean predominantly near its northwestern boundary. Indeed the Labrador and Greenland Seas are sites of significant deep convection and renewal of deep, dense water masses which then circulate about the world's oceans.

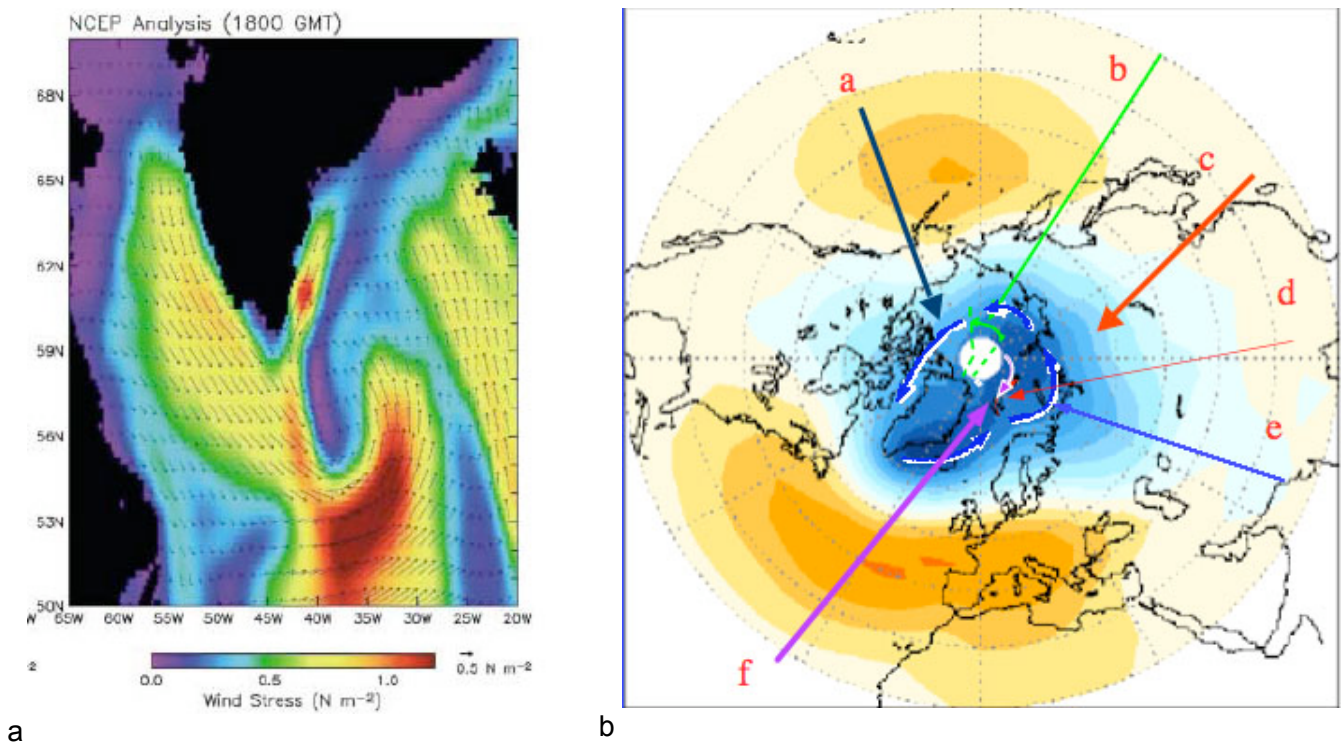


Figure 2.27. (a) Wind-stress at the ocean surface observed by satellite scatterometer in the sub-polar Atlantic, near Greenland as an intense cyclonic system moves northward and interacts with the wake of Greenland, drawing air down the topographic gap bounding the Labrador Sea (west of Greenland) on 12 January 2001. The radar scatterometer senses the surface roughness of the ocean and this is converted to wind vectors. Figure courtesy of Dr Dudley Chelton. (b) Forcing mechanisms for changing atmosphere, sea ice and ocean in the Arctic Basin (courtesy: J. Morison).



The changes of the interior of the Arctic can be synthesized as follows (Fig. 2.27 b); a strengthening of the Polar Vortex observed in the 1990s was associated with a weakening of the Beaufort High, increased advection of warm air to the Greenland Sea and Russian Arctic, increase in open water, decrease of albedo, increased radiative heating and melt and freshening of the upper Beaufort Sea (point a). The increased Polar Vortex is also associated with more cyclonic ocean circulation, shift in front and Transpolar Drift, and shift of Russian shelf water towards the Beaufort Sea (point b). Warm air advection is linked to increases SAT, warming of the soil and permafrost thawing (point c) and also warming of the Atlantic water in the Nordic Seas (point d). Finally, enhanced cyclonic circulation increases export of fresh water out of the Fram Strait and increased stratification in Greenland and Labrador Seas. This will in turn inhibit vertical convection and slow down deep water formation and the meridional overturning in these areas.

The currents of the North Atlantic and the Norwegian-Greenland sea are shown in Fig. 2.28. Warm surface currents (shown in red) cool to pink and yellow as they circulate northward and then round the sub-polar gyre of the North Atlantic Ocean. About eight Sverdrups of flow enters the Norwegian Sea; in interaction with the atmospheric storm track, the seas between Greenland, Iceland and Norway are held mostly ice-free, as is the Barents Sea in the Arctic north of Norway. Cold, deep currents return southward along the western boundary of the ocean, feeding the global meridional overturning circulation. Cold boundary currents also occur near the sea surface around Greenland, carrying low-salinity waters south out of the Arctic (McCartney and Talley 1982).

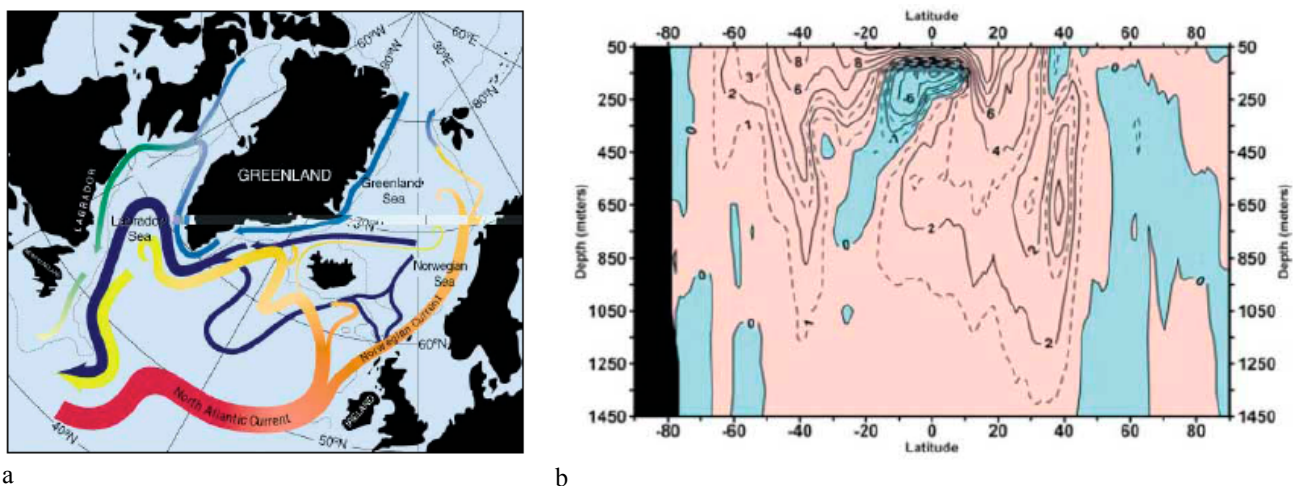


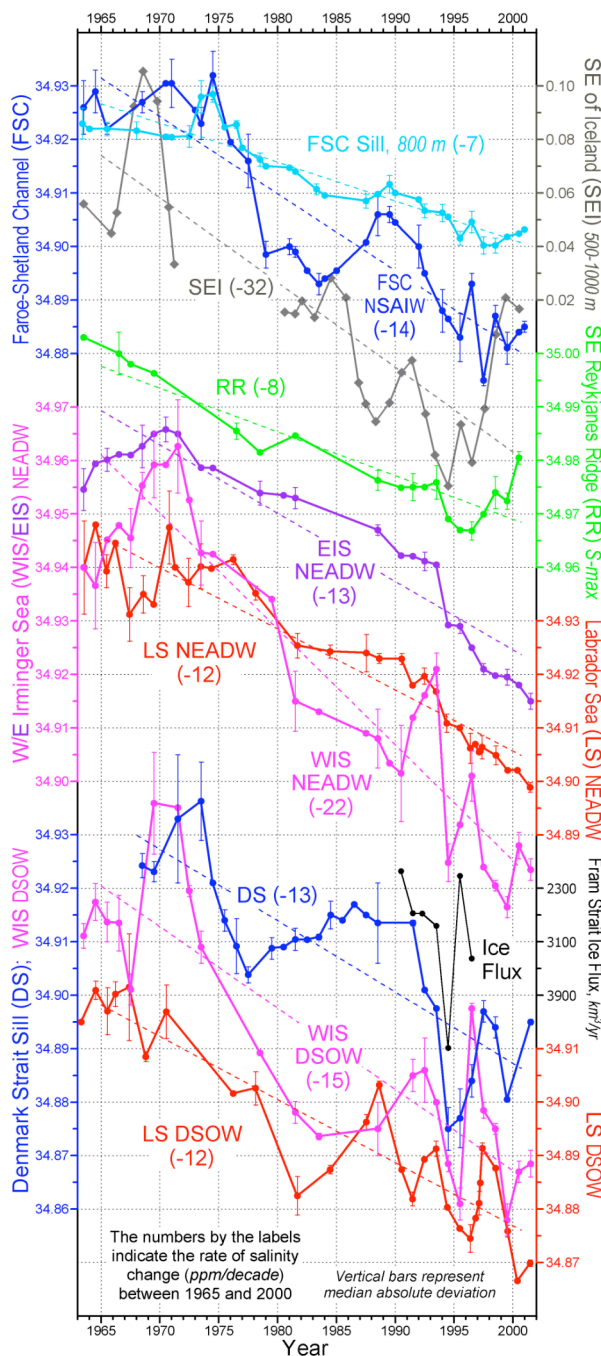
Figure 2.28 (a) Main currents in the North Atlantic (McCartney and Talley, 1982); (b) Temperature trend of the world's oceans between 1955 and 2003 (Levitus et al. 2005). Warming occurs in the sub-tropics and upper Equatorial oceans, while modest cooling occurs at high northern and southern latitudes, likely to be the result of increasing westerly winds. Contour interval is  $2 \times 10^{18} \text{ J year}^{-1}$ .

### 2.2.3 Heat and freshwater content

At the largest scale, the archive of ocean temperature shows that the oceans of the world are warming. The heat gain from 1955 to 1998 is estimated to be  $1.45 \times 10^{23}$  Joules (J.). This easily exceeds the global annual cycle of ocean heat storage, estimated at  $3.7 \times 10^{22}$  J. (Levitus et al., 2005). About 84% of the Earth's total warming of the past several decades is stored in the oceans, with the rest going into the melting of ice and warming of the solid Earth; the atmosphere accounts for a mere  $0.7 \times 10^{22}$  J. of added heat storage. This work involves the gargantuan task of collecting millions of temperature profiles from the recent past and the 'data-rescue' of older profiles archived

only on paper or decaying computer tapes. The spatial distribution of oceanic long-term temperature change is interesting: the subpolar Atlantic has, for much of the past 30 years become colder. Figure 2.28b shows cooling in both the Southern Ocean and the northern Atlantic. The origins of this cooling are very interesting, and the subject of much current dynamical research. The dominant pattern of variability of the lower atmosphere in winter is variously described as the 'annular mode', or in the northern hemisphere, the North Atlantic Oscillation (NAO, defined in the Atlantic sector) or 'Arctic Oscillation' (defined over the hemisphere).

The early 1990s was an exceptional period of strong westerly winds in the sub-polar Atlantic and cold forcing of the ocean by Arctic/continental air masses. Deep convection in the Labrador Sea was extremely intense at this time. The Atlantic storm track and Icelandic Low strengthened, sending cyclonic systems high into the Arctic. These greatly affected the wind-driven flow of sea-ice southward out of the Arctic. Conversely, the late 1960s was a warm period of strong maritime influence over key sub-polar water mass formation sites.



Even more dramatic than the cooling, which is likely to be temporary, has been a 30-year decline in the salinity of the dense waters of the sub-polar Atlantic (Fig. 2.29). Throughout much of the sub-polar gyre and Norwegian Sea to the north, the decreasing salinity has reached century-long extreme values. While it is tempting to attribute this decline to an increasing hydrologic cycle, there are other possible causes. If the MOC slows down, the normal precipitation at high-latitudes will tend to accumulate and force the salinity to decline (Häkkinen 2002). If the strong north-west winds of the positive phase of the NAO blow more ice and surface water southward out of the Arctic, then this also will reduce the salinity. Indeed, this has been happening.

Figure 2.29. Salinity records from the sub-polar Atlantic and Norwegian Sea, summarised by Dickson et al. (2003). The locations range from the Norwegian Sea (NSA/W) and Faroe-Shetland Channel (FSC, top) westward to the Labrador Sea (LS) NEADW (bottom). For three decades the deep salinity has been declining.



The heat and freshwater contents of the Arctic Ocean are important integrated parameters and are indicative of the potential role of the Arctic Ocean in the global climate system. For example, the meridional overturning circulation in the Atlantic Ocean, an important component of the global ocean circulation, is significantly influenced by freshwater fluxes from the Arctic Ocean. It is suggested that the Arctic Ocean accumulates fresh water during anticyclonic circulation regimes and releases this water to the North Atlantic during cyclonic circulation regimes. The Beaufort Gyre (illustrated in Fig. 2.23 by the closed clockwise circulation pattern in the Beaufort Sea region) is the major reservoir of fresh water in the Arctic Ocean, and its dynamics (accumulation or release) is responsible for freshwater fluxes to the Atlantic Ocean.

The heat content of the Arctic Ocean is potentially responsible for the sea ice melt and the Arctic atmosphere warm-up. However, under the existing ocean state, the direct upward loss of heat from the Atlantic water layer is greatly impeded by strong density stratification and weak temperature gradients in the upper ocean. The impact of this sensible heat reservoir on Arctic perennial ice is thought to be weak. From 2000 to 2005, the most complete observational data available to analyze changes in the freshwater and heat contents of the Arctic Ocean are the intensive investigations conducted in the vicinity of the North Pole by the North Pole Environmental Observatory (NPEO) (Morison *et al.*, 2002; <http://www.psc.apl.washington.edu/northpole/>) and in the western Arctic by the Beaufort Gyre Observing System (BGOS) ([www.whoi.edu/beaufortgyre/index.html](http://www.whoi.edu/beaufortgyre/index.html)). Hydrographic data acquired in the North Pole region in the 1990s show a strong increase in upper ocean salinity relative to the Environmental Working Group Atlas of the Arctic Ocean (EWG, 1997, 1998) climatology (Fig. 2.30, left panel), where water temperatures and salinities from observations were averaged and gridded for the decades of 1950, 1960, 1970, and 1980.

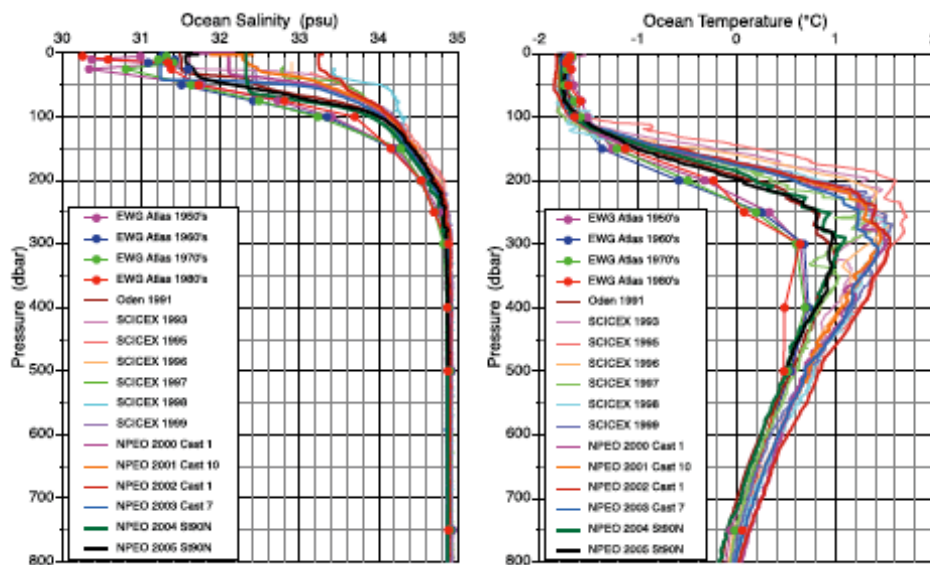


Figure 2.30. North Pole hydrography for 1991-2005 (lines) compared with EWG climatology (lines with circles); left: salinity, right: temperature. The EWG data (decadal means for 1950s–1980s) and the NPEO data (2001–2005) are for spring, and the SCICEX data (1993–1999) are for autumn. Because of summer ice melt and river runoff, the salinity of the upper ocean layer is always lower in autumn than in spring. Therefore, we expect that in the 1990s the spring water salinity was even greater than observed by SCICEX expeditions in autumn (Morison *et al.*, 2006).

This increase was associated with a more cyclonic Arctic Ocean circulation in the 1990s. Under this condition, the fresh water from river runoff tended to circulate along ocean boundaries (see Fig. 2.23, right panel, wide blue lines), resulting in a decrease of salinity along coastlines and an increase of salinity in the central Arctic (North Pole). The NPEO data also show a large increase in

Atlantic water temperature at depth relative to the EWG climatology (Fig. 2.30, right panel). This was also consistent with the cyclonic circulation regime conditions in the 1990s, when more Atlantic water penetrated to the Arctic Ocean and, correspondingly, there was an increase in Atlantic water temperature.

Hydrographic measurements made by the NPEO shows that the conditions since 2000 have relaxed toward the pre-1990 climatology, but some changes, at least partially, still persist. The hydrography of the Beaufort Gyre (the major freshwater reservoir in the Arctic Ocean) has also changed dramatically relative to the 1990s (Fig. 2.31). The results of several hydrographic surveys in this region in the 1990s, compared to the EWG data, indicate that, in contrast to the salinity increase at the North Pole, the salinity of the upper layer in the Beaufort Gyre was significantly reduced in the 1990s (Fig. 2.31, left panel). This is a consequence of both sea ice melt during Arctic warming in the 1990s and the addition of fresh water from Siberian rivers. The shift in the pattern of freshwater transport is consistent with the presence of cyclonic winds, which redirect the ocean surface flow of fresh water from the Russian and Siberian coasts along the Siberian Seas to the Beaufort Sea. Under anticyclonic winds, this fresh water flows toward Fram Strait (compare the left and right circulation patterns in Fig. 2.23, wide blue arrows). In the 2000s, relative to the 1990s, the salinity in the Beaufort Gyre increased but was still approximately one unit less than shown by the EWG climatology. There was also a very small salinity decrease in the 50- to 300-m layer of the ocean, but this change was within the range of interannual variability. Interestingly, the total freshwater content in the Beaufort Gyre in the 2000s has not changed dramatically relative to climatology, but there has been a significant change in the freshwater distribution (Fig. 2.32, panels 3 and 4). The center of the freshwater maximum has shifted toward Canada and intensified significantly relative to climatology. In the 1990s, the water temperature in the Beaufort Gyre increased significantly relative to EWG data (Fig. 2.31, right panel).

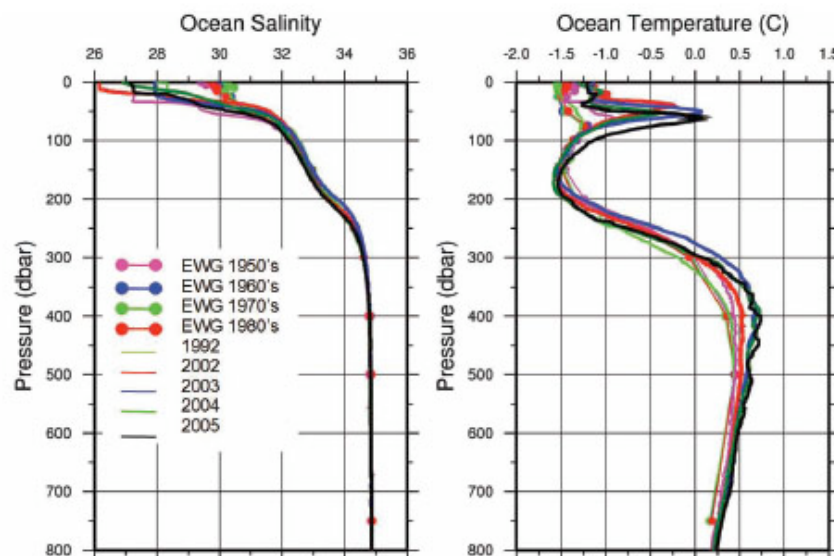


Figure 2.31. Beaufort Gyre hydrography for 1991–2005 (lines) compared with EWG climatology (lines with circles).

The most pronounced warming (up to 1°C) was observed in the Pacific water layer (50–100 m), but the maximum heat accumulation was observed in the Atlantic waters between 200 and 800 m deep. These waters, propagating cyclonically from Fram Strait (Fig. 2.23, red arrows), reached the Beaufort Sea in the late 1990s, much later than when they reached the North Pole. The combination of warming water temperatures and a change in the circulation pattern resulted in a significant increase in the heat content in the Beaufort Gyre in the 2000s relative to the EWG climatology and observations made in the beginning of the 1990s for the vicinity of 75°N and 150°W (Fig. 2.32).

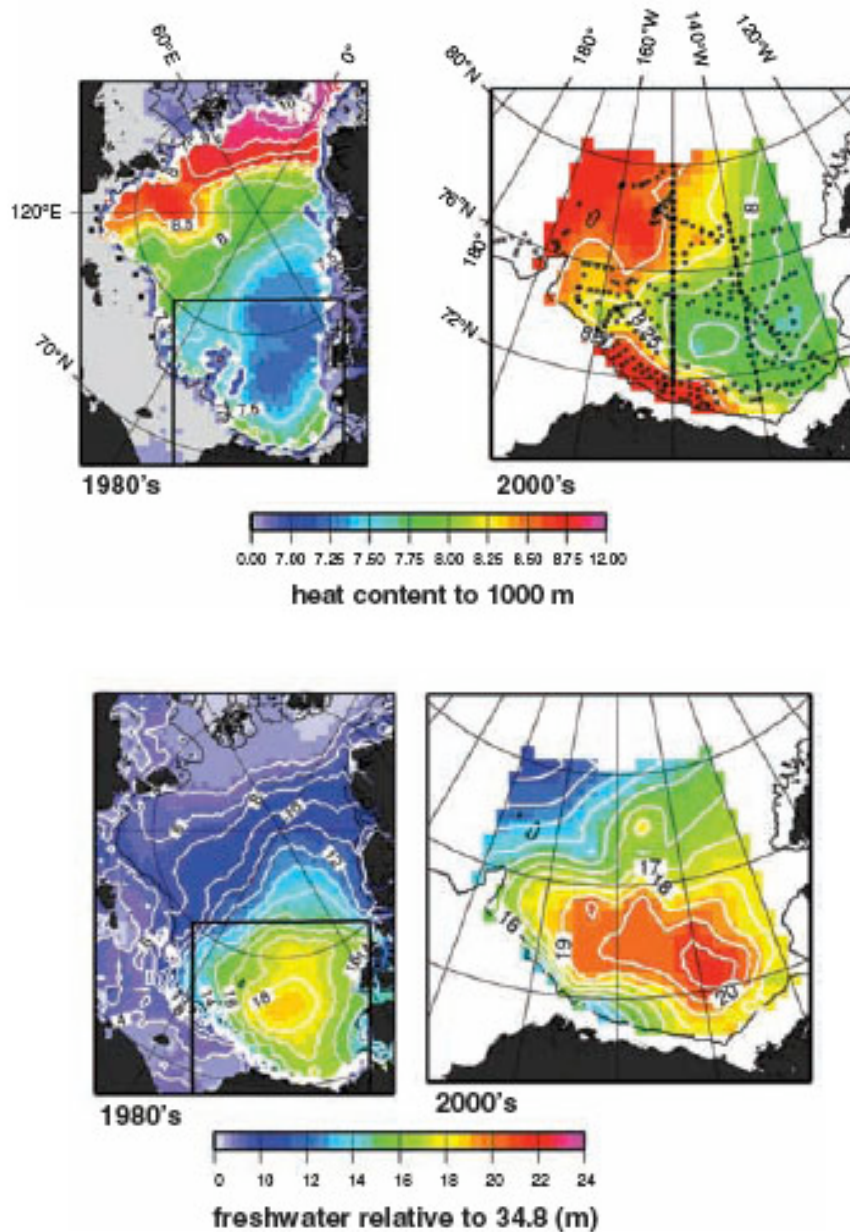


Figure 2.32. Summer heat ( $10^9 \text{ J/m}^2$ , upper graphs) and freshwater (m, lower graphs) content. Panels 1 and 3 (left side) show the heat and freshwater content in the Arctic Ocean based on 1980s climatology (EWG, 1997, 1998). Panels 2 and 4 (right side) show the heat and freshwater content in the Beaufort Gyre in 2000–2005 based on hydrographic surveys (the black dots indicate locations of hydrographic stations). For reference, this region is outlined in black in panels 1 and 3. The heat content is calculated relative to the water temperature freezing point in the upper 1000-m ocean layer. The freshwater content is calculated relative to a reference salinity of 34.8.

#### 2.2.4 Sea level

There is a positive sea level trend along the Arctic coastlines as shown in Fig. 2.33. From 1954 to 1989 the rate of sea level rise was estimated as 0.185 cm/year (Proshutinsky *et al.*, 2004). Adding 1990–2004 data increases the estimated rate to 0.191 cm/year. The sea level time series correlates relatively well with the AO index (the correlation coefficient is 0.83). Consistent with the

influences of AO-driven processes, the sea level dropped significantly after 1990 and increased after the circulation regime changed from cyclonic to anticyclonic in 1997. In contrast, from 2000 to 2004 the sea level rise rate has increased, in spite of a steady decrease in the AO index. At this point, because of the large interannual variability, it is difficult to evaluate the significance of this change.

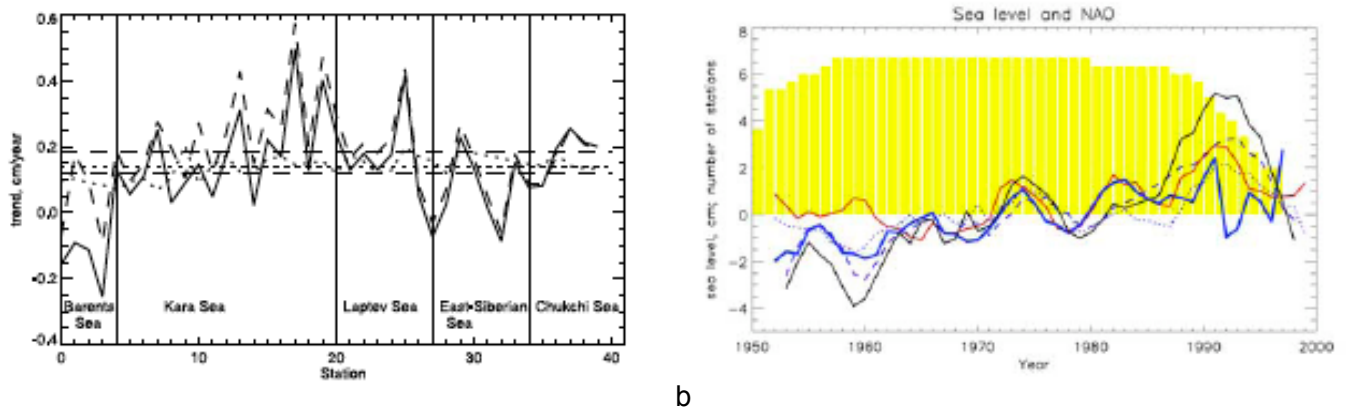


Figure 2.33 (a) Sea level trends for 1954–1989 in different regions of the Arctic. Solid line shows trends from observations. Dashed line shows observed trends corrected for GIA (Glacial Isostatic Adjustment), and dotted line depicts variability of trends associated with the inverted barometer effect, river runoff and steric effects. Thin horizontal dashed and dotted lines show mean trends for all seas. (b) Mean sea level time series for different seas. Dotted lines denote number of coastal stations used for averaging. Mean time series for all seas (thick blue line, 5-year running mean). Mean number of stations used in each sea is shown by yellow bars. Red thick line shows 5-year running mean North Atlantic Oscillation index. Thin dashed line shows sea level variability from 3-D model, and dotted blue line shows variability of sea level due to inverted barometer effect. Solid black line shows sea level from 3-D model corrected for the inverted barometer effect. (Proshutinsky *et al.*, 2004).

The conclusions of the study of Arctic sea level change by (Proshutinsky *et al.*, 2004) are the following:

1. Relative sea level monthly data from the 71 tide gauges in the Barents, Kara, Laptev, East Siberian, and Chukchi Seas have been analyzed in order to estimate the rate of sea level change and major factors responsible for this process in the Arctic Ocean. The trends for each tide gauge station are shown in Fig. 2.34.
2. The Arctic Ocean sea level time series have well pronounced decadal variability which corresponds to the variability of the North Atlantic Oscillation index. Because of the strength of this variability and the relatively short sea level time series, our assessments of sea level trends remain somewhat uncertain. In spite of this limitation, we have employed statistical methods together with numerical models and estimated the contributions of various factors to the observed sea level change. By subtracting the influence of these factors from the observed regional rate of sea level rise we have been able to estimate the rate of sea level rise due to increase of the global ocean mass that is presumably due to the melting of land ice.
3. During the period 1954–1989 the average rate of relative sea level rise over the seas of the Russian Arctic has been  $0.185 \text{ cm yr}^{-1}$ . The sea level rise at each gauge station is shown in Fig. 2.34. The sea level rise is within range of the rate that has previously been inferred using tide gauge data for the global ocean as a whole [IPCC, 2001]. It is also essentially the same as the rate for the Global Ocean recently inferred by Peltier [2002].



4. In the Arctic, the contribution to the observed rate of sea level rise from the steric effect is  $0.064 \text{ cm yr}^{-1}$ . This is smaller than the rate of ocean thermal expansion estimated for the global ocean by IPCC [2001]. In the Arctic Ocean, changes in salinity are more important for sea level variability than changes in temperature, and the combination of freshening of the Arctic seas with warming and salinization of the Atlantic layer therefore leads to the rise of sea level along coastlines and the fall of sea level in the central parts of the Arctic Basin.
5. The contribution of the inverse barometer effect to the Arctic Ocean sea level rise is  $0.056 \text{ cm yr}^{-1}$ . This is the highest rate of sea level rise among any of the estimates of this factor presented by IPCC [2001] for various regions.
6. The estimated rate of sea level rise due to the effect of wind is  $0.018 \text{ cm yr}^{-1}$ , but it varies significantly from region to region. In the Arctic, this effect is due to the gradual decrease of the sea level atmospheric pressure over the Arctic Ocean and therefore to the more strongly cyclonic atmospheric circulation.
7. The contributions of river runoff, evaporation and precipitation to sea level change in the Arctic Ocean are very small and their cumulative effect is negligible. On the other hand, the P-E estimates over the Arctic Ocean are less accurate than the other investigated factors.
8. The residual term of the sea level rise balance assessment,  $0.048 \text{ cm yr}^{-1}$ , may be due to the increasing of the Arctic Ocean and global ocean mass associated with melting of ice caps and small glaciers and with adjustments of the Greenland and Antarctica ice sheets to the observed climate change.

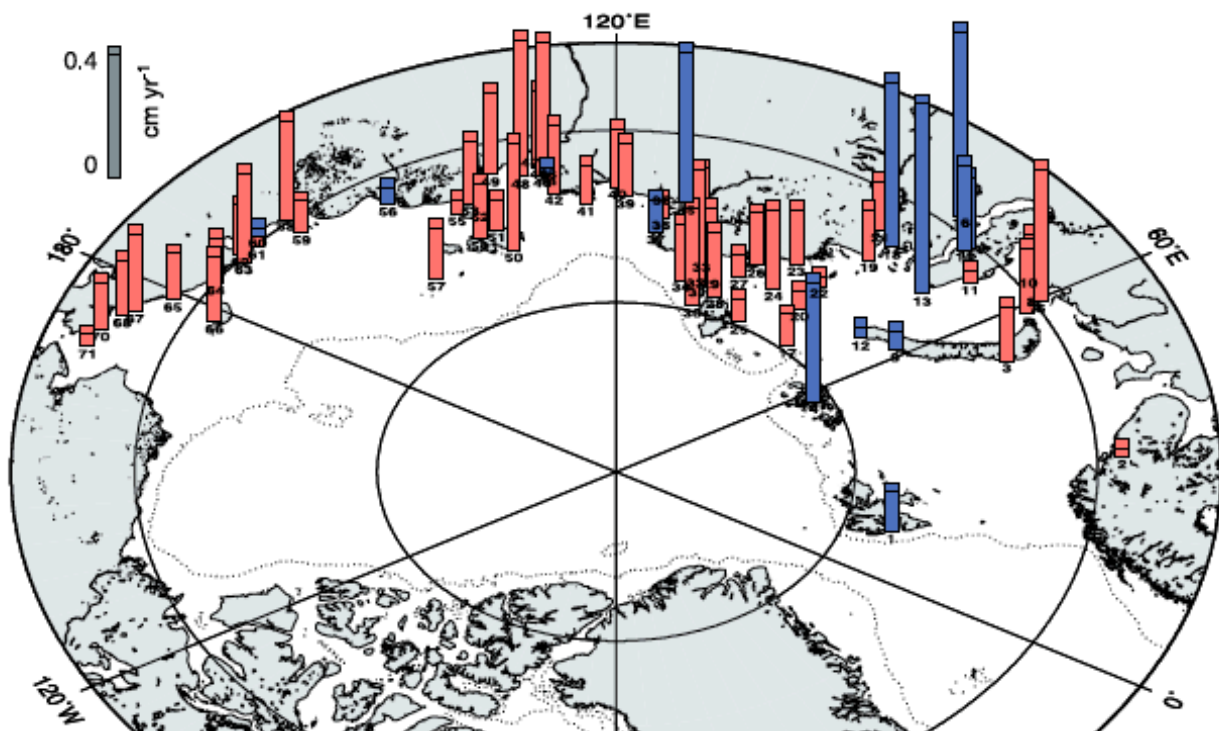


Figure 2.34 Observed sea level trends ( $\text{cm yr}^{-1}$ ) without corrections (red is positive trend, and blue is negative trend). (Proshutinsky et al., 2004).

### 2.2.5 Waves

The wave conditions and other met-ocean parameters in open waters of the Arctic Seas have been reviewed by Proshutinsky and Weingarten (1998) in a report provided as part of the INSROP project (<http://www.ims.uaf.edu/insrop-2>). The main results from the wave studies are summarized in this section.

Wave parameters in the Arctic seas are affected by both wind regime and ice conditions. Maximum significant wave heights (SWH) are observed in the arctic seas in autumn. In the Barents Sea maximum wind waves are observed in winter when SWH can reach 10 - 11 m. These waves are generated by stable west or southwesterly winds with velocities of 20 - 25 m/s and duration of 16 - 18 hours. This happens, on average, once or twice every five years. In the beginning of April, the intensity of waves in the Barents Sea decreases. The frequency of waves with SWH of 5 m or more is 4 - 5% in April compared to more than 15% in winter. The minimum SWH is found from May to August, while in September the SWH starts to increase. In November, a wave regime similar to that in winter is established. In winter, well-developed swells are observed in the southern parts of the Barents Sea. The monthly probability of the wind waves with SWH above 5 metres is shown in Fig. 2.35.

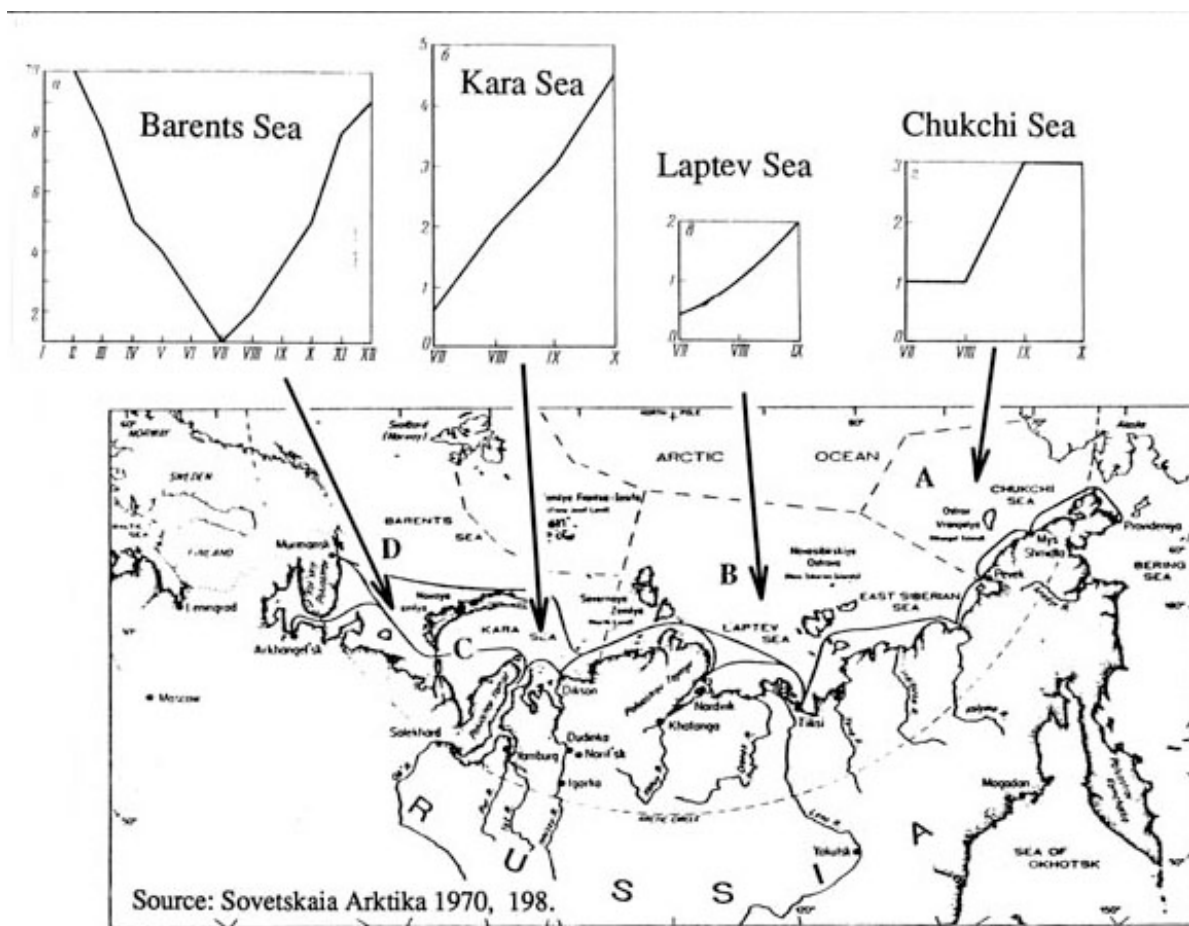


Figure 2.35. Probability of occurrence of wind waves with SWH above 5 meters for the ice-free months in different parts of the Russian Arctic. The upper graphs show SWH in meter for each month of the year in four regional seas.

In the Kara Sea, wave statistics only occur for the ice-free months July – October (Fig. 2.35). In this period the frequency of waves with SWH above 3 m increases from 8 to 15 %. Note that the

SWH for the Kara Sea is smaller compared to the Barents Sea, as shown by the different scale in diagrammes in Fig. 2.35. Occasionally, more severe waves can penetrate from north and be dangerous for small ships navigating along the Siberian coast. SWH of 1.5 - 2.5 m is most common in the Kara Sea. Also the Laptev Sea has modest SWH, with 1.5 m as the mean value. In July - August, easterly winds can generate maximum SWH reaching up to 5 m. In the southeastern Laptev Sea, the SWH does not exceed 4 m. Because of the shallow depths and large areas with ice cover, wind waves are relatively modest in the East Siberian Sea. From July to September, the ice edge moves northward and the frequency of SWH exceeding 2 m increases, reaching its maximum in September. The Chukchi Sea has similar wave regime as the East Siberian Sea. In the Bering Strait the SWH increases to 5 – 6 m during northerly winds.

## 2.3 Sea ice

### 2.3.1 General sea ice conditions

Sea ice is a sensitive component of the climate system, influenced by conditions in both the atmosphere and ocean. Variations in sea ice may in turn modulate climate by altering the surface albedo; the exchange of heat, moisture, and momentum between the atmosphere and ocean; and the upper ocean stratification in areas of deep water formation. The surface albedo effect is considered to be one of the dominant factors in the poleward amplification of global warming due to increased “greenhouse gas” concentrations simulated in many climate models (e.g., IPCC 2001; Arzel et al., 2006).

Since the late 1970s, satellite records show a decreasing linear trend in Arctic sea ice extent at a mean rate of about  $0.3 \times 10^6 \text{ km}^2$  (or about 3 % of the ice area) per decade (Cavalieri et al., 2003; Johannessen et al., 1999, 2004). Several numerical experiments display as well a thinning of the Northern Hemisphere ice pack over the last few decades (Rothrock et al., 2003). The increasing greenhouse gas concentrations associated to human activities is now considered as the main contender to explain this feature (Vinnikov et al., 1999; Houghton et al., 2001; Johannessen et al., 2004), although the role of internal variability and natural forcings (solar activity and volcanic eruptions) are still under debate (Bengtsson et al., 2004; Goosse and Holland, 2005). In contrast, observations do not reveal a similar decreasing trend in ice extent in the Southern Hemisphere over 1978–2002, but rather a slight increase of about  $0.2 \cdot 10^6 \text{ km}^2$  (Cavalieri et al., 2003). This latter trend is however not statistically significant owing to the large interannual variability. The different sea ice responses in the Northern and Southern Hemisphere were partly attributed to different oceanic heat uptakes at high latitudes in both hemispheres (Houghton et al., 2001; Flato and Boer, 2001; Goosse and Renssen, 2001).

Observational studies of sea ice extent in the Arctic indicate that variability on timescales of weeks and longer tends to be organized into large-scale geographical patterns that are closely associated with the dominant structures of atmospheric circulation variability, particularly during winter (e.g. Walsh and Johnson 1979; Prinsenberg et al. 1997). The consensus of the observational studies is that “interannual variability in sea ice conditions is caused by the variability in the large-scale atmospheric circulation which locally manifests itself as surface air temperature and wind anomalies” (Prinsenberg et al. 1997). Feedbacks or other influences of winter ice anomalies upon the atmosphere have been more difficult to detect due to the dominance of atmospheric forcing of sea ice in the observed associations, as shown by temporal asymmetries in ice–atmosphere cross-correlation functions (e.g., Lemke et al. 1980).

Over the past 3–4 decades, the dominant patterns of wintertime atmospheric circulation variability in the Northern Hemisphere, particularly the Pacific–North American and the North Atlantic oscillation (NAO) or Arctic oscillation (AO) teleconnection patterns, have exhibited trends that are unprecedented in the observational record. For the purposes of this study, the NAO may be regarded as a subset of the spatially broader AO (Thompson and Wallace 1998). Sea level pressures (SLPs) have decreased over the central Arctic and over the climatological Icelandic and Aleutian low centers, and increased farther south (Hurrell 1996; Thompson and Wallace 1998). The most pronounced SLP reductions over the central Arctic has occurred since 1988 (Walsh et al. 1996). Associated with these circulation changes, winter surface air temperatures over land (Eurasia in particular) have increased to record values while those over the oceans have cooled slightly (Hurrell 1996; Thompson et al. 2000). The latter authors hypothesize that anthropogenic forcing may be a contributing factor to the recent unprecedented strengthening of the polar vortex (reflected by the AO) and associated warming over the Northern Hemisphere continents.

During 2005, each month except May showed a record minimum sea ice extent in the northern hemisphere for the period 1979–2005. The extent of the sea ice cover is typically at or near its maximum in March and its minimum in September. The ice extent in March 2005 was 14.8 million



km<sup>2</sup>. In September 2005 the ice extent was 5.6 million km<sup>2</sup>. In comparison, the mean ice extent for March and September, for the period 1979–2005, was 15.7 million km<sup>2</sup> and 6.9 million km<sup>2</sup>, respectively (Fig. 2.36). It is notable that in March 2005 the ice extent fell within the median contour at almost every location. In September 2005, the retreat of the ice cover was particularly pronounced along the Eurasian and North American coastlines.

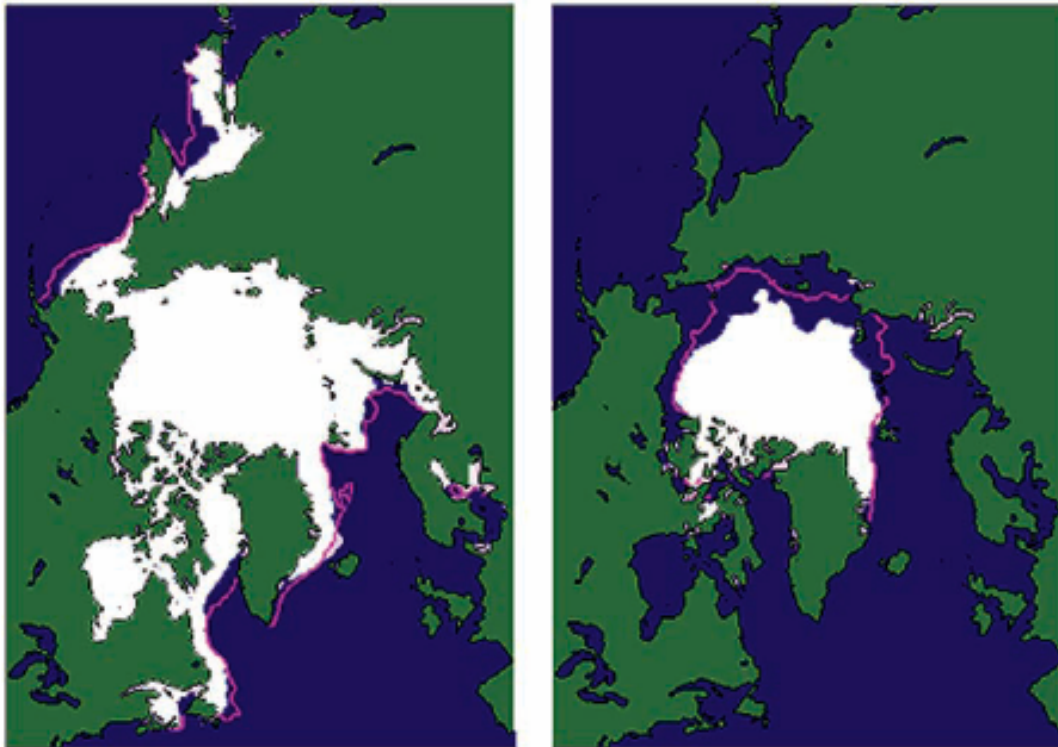


Figure 2.36 Sea ice extent in March (left) and September (right) 2005, when the ice cover was at or near its maximum and minimum extent, respectively. The magenta line indicates the median maximum and minimum extent of the ice cover for 1979–2000. In both cases, the ice extent reached a record minimum in 2005 for the period 1979–2005. (Adapted from National Snow and Ice Data Center web site, <http://nsidc.org/>.)

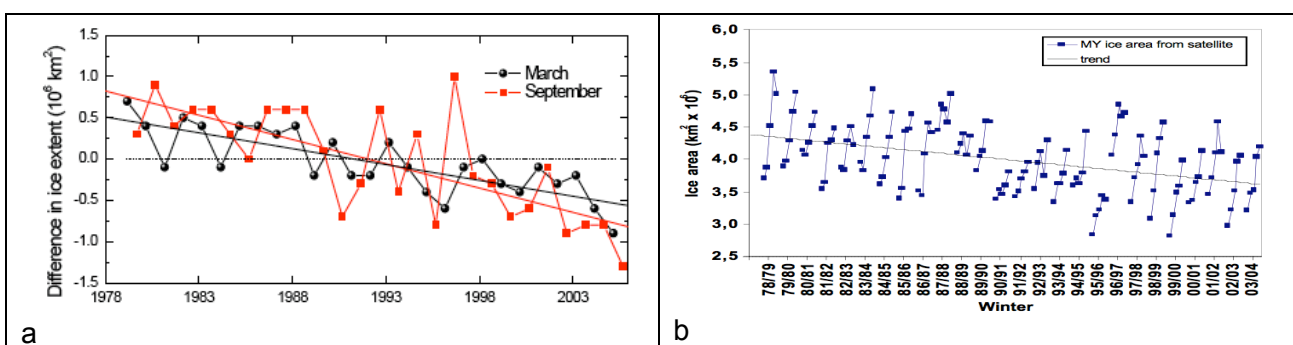


Figure 2.37: (a) Time series of the difference in ice extent in March ( maximum) and September (minimum) from the mean values for 1979–2005 from SSM/I data. Based on a least-squares linear regression, the rates of decrease in March and September were 2% per decade and 7% per decade, respectively. Recent data from March 2006 are also shown and represent a new record minimum for the period of observation (<http://nsidc.org/>). (b) Time series of multiyear ice area for the winter months derived from SSM/I data (Johannessen et al., 2004).

Recent data from winter 2006 indicate a further reduction in the maximum ice extent, reaching 14.5 million km<sup>2</sup> in March. To put the 2005 minimum and maximum ice extents into context, the time series of the variability of ice extent in March and September for 1979–2005 are presented in Fig. 2.37. In both cases, a negative trend is apparent, with a rate of 2% per decade for March and 7% per decade for September. The summers of 2002–2005 marked an unprecedented series of extreme ice extent minima (Stroeve *et al.*, 2005). The state of the sea ice cover is intrinsically linked to the state of the ocean and atmosphere. This is confirmed by the observation that during this same period (1979–2005), the annual surface temperatures over land areas north of 60°N have generally been rising and have been above the mean value for the twentieth century since the early 1990s.

Ice thickness is more difficult to monitor than ice extent. With satellite based techniques only recently introduced (Laxon *et al.*, 2003; Kwok *et al.*, 2006), observations have been spatially and temporally limited. Data from submarine based observations indicate that at the end of the melt season the permanent ice cover (the ice located toward the center of the Arctic basin that survives year round; see Fig. 2.38, right panel) thinned by an average of 1.3 m between 1956–1978 and the 1990s, from 3.1 to 1.8 m (Rothrock *et al.*, 1999).

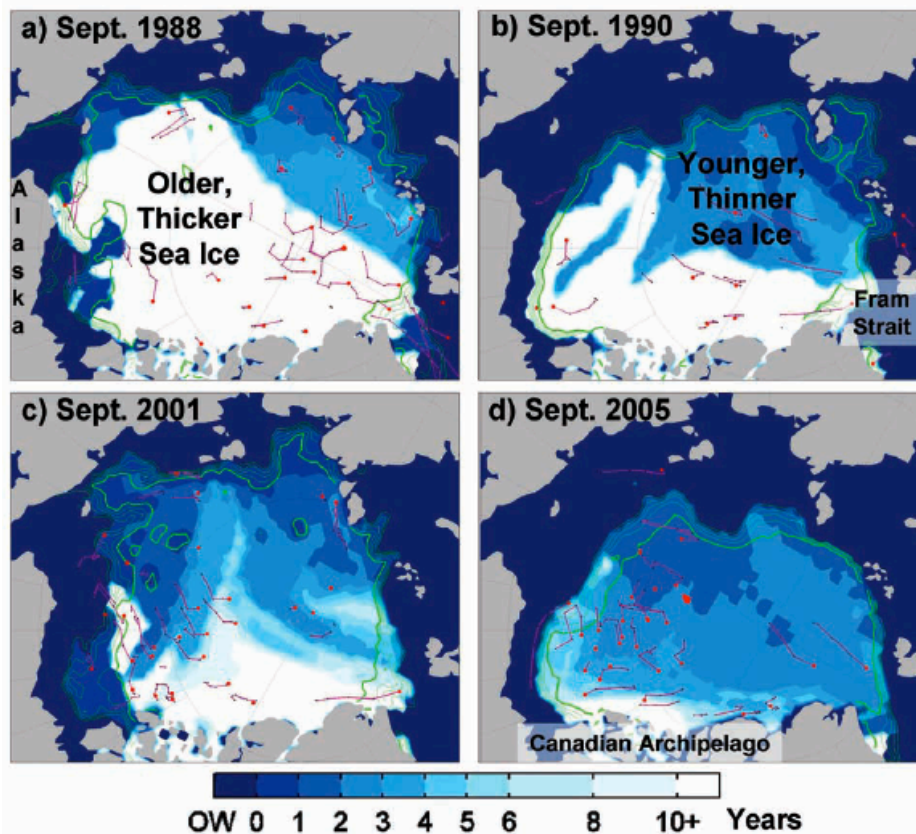


Figure 2.38: Change in the age of ice on the Arctic Ocean, compared for September and based on results from a simulation using drifting buoy data and satellite-derived ice concentration data (Rigor and Wallace, 2004). Open water (OW) is shown in dark blue, and the oldest ice is shown in white. The darker green line marks 90% ice concentration, and the lighter green lines mark ice concentrations of 80, 70, 60, and 50%. This sequence shows that (a) most of the Arctic Ocean was covered by older, thicker sea ice in September 1988; (b) coincident with a transition to high-AO conditions in 1989 (Fig. 2.5), most of the older, thicker sea ice was rapidly flushed out of the Arctic Ocean through Fram Strait, so that by 1990 only 30% of the Arctic Ocean was covered by older, thicker sea ice; (c) the relative distribution between older, thicker and younger, thinner sea ice persisted during the 1990s, in spite of a shift back towards a more neutral AO in the mid-1990s; and (d) the average ice age over the Arctic Ocean apparently continued to decrease through 2005, with older, thicker ice now limited to the area north of the Canadian Archipelago.

On the other hand, measurements of the seasonal ice cover (the ice around the periphery of the Arctic basin that melts during the summer) do not indicate any statistically significant change in thickness in recent decades (Melling *et al.*, 2005; Haas, 2004; Polyakov *et al.*, 2003). The trends in the extent and thickness of the cover are consistent with observations of a significant loss of older, thicker ice out of the Arctic via Fram Strait (e.g., Rigor and Wallace, 2004; Pfirman *et al.*, 2004; Yu *et al.*, 2004) in the late 1980s and early 1990s (Fig. 2.38). This event coincided with the strong, positive AO period that extended from 1989 to 1995 (Fig. 2.5). When the AO is positive, atmospheric and oceanic conditions favor a thinner ice cover. A younger, thinner ice cover, such as the one left behind from this event, is more susceptible to atmospheric or oceanic warming. It is of great interest to observe whether the sea ice cover will continue its decline or rebound under the recent, more-neutral AO conditions.

The Arctic sea ice variability and its association with surface air temperature (SAT) and sea level pressure (SLP) in the Northern Hemisphere has been investigated by Deser *et al.* (2000). Forty years (1958–97) of reanalysis products and corresponding sea ice concentration data were analyzed using empirical orthogonal function (EOF) analysis. The dominant mode of winter (January–March) sea ice variability exhibits out-of-phase fluctuations between the western and eastern North Atlantic, together with a weaker dipole in the North Pacific. The time series of this mode has a high winter-to-winter autocorrelation (0.69) and is dominated by decadal-scale variations and a longer-term trend of diminishing ice cover east of Greenland and increasing ice cover west of Greenland. Associated with the dominant pattern of winter sea ice variability are large-scale changes in SAT and SLP that closely resemble the North Atlantic oscillation. The associated SAT and surface sensible and latent heat flux anomalies are largest over the portions of the marginal sea ice zone in which the trends of ice coverage have been greatest, although the well-documented warming of the northern continental regions is also apparent. The temporal and spatial relationships between the SLP and ice anomaly fields are consistent with the notion that atmospheric circulation anomalies force the sea ice variations. However, there appears to be a local response of the atmospheric circulation to the changing sea ice cover east of Greenland. Specifically, cyclone frequencies have increased and mean SLPs have decreased over the retracted ice margin in the Greenland Sea, and these changes differ from those associated directly with the North Atlantic oscillation.

The dominant mode of sea ice variability in summer (July–September) is more spatially uniform than that in winter. Summer ice extent for the Arctic as a whole has exhibited a nearly monotonic decline (3 - 4% per decade) during the past 40 yr. Summer sea ice variations appear to be initiated by atmospheric circulation anomalies over the high Arctic in late spring. Positive ice–albedo feedback may account for the relatively long delay (2–3 months) between the time of atmospheric forcing and the maximum ice response, and it may have served to amplify the summer ice retreat.

The Russians started already in 1970 to measure area-averaged ice thickness derived from field-based measurements of surface elastic-gravity waves from Russian North Polar drifting stations 1970–91, when regular measurements of ice surface vibrations were made in the central Arctic Ocean (Nagurnyi *et al.*, 1994). Long elastic-gravity waves (on the order of 1 km) in the sea-ice cover arise from the interaction with ocean swells. These elastic-gravity waves can propagate for hundreds to thousands of kilometers before dampening out. Based on a linear theory of free vibrations of the sea ice cover, the measured wavelength, wave period and direction are then related to thickness through a wave-energy dispersion relation. The ice thicknesses determined from different propagation directions are averaged to provide a basin-wide mean thickness estimate (Nagurnyi *et al.*, 1994). The values compare well to those observed in the regional ice cover (Romanov, 1995) and their interannual variability correlates well with modelled arctic ice volume (see fig. 1 in Hilmer and Lemke, 2000). The thickness estimates have also been found to correlate strongly (~0.88) to the satellite-derived area of the perennial, MY ice cover in winter (Johannessen *et al.*, 1999), suggesting moreover that the decreases found in MY ice area represent a mass balance change rather than merely a peripheral effect. Figure 2.39 a shows the

20 year time series of area-averaged ice thickness, 1970–91 (Nagurny et al. 1994), from which trends for winter and summer are derived (Fig. 2.39 b). The mean thickness estimates are 2.9–3.0 m in winter and 2.5–2.6 in summer.

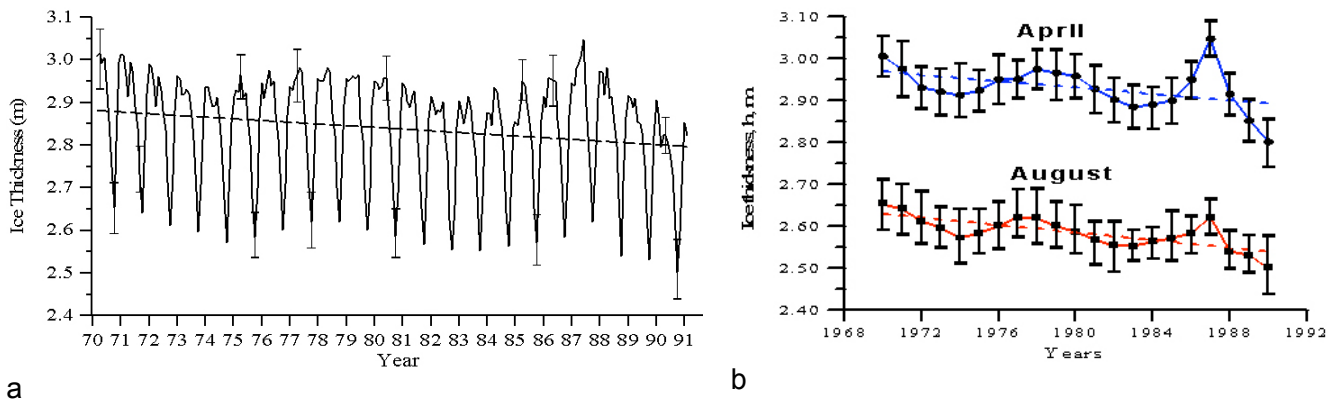


**Figure 2.39 Arctic sea-ice thickness variability from 1970-1990. (a) Monthly area-averaged thickness estimates as derived from surface-based measurements of ice-surface vibrations made from Russian North Pole drifting stations in the perennial pack ice of the Arctic Ocean (Nagurny et al., 1994). (b) Interannual variability and linear trends for winter (April) and summer (August), with error bars denoting the 95% confidence interval of the ice thickness estimates.**

The linear trend of anomalies from 1971–90 indicates a decrease of only ~10 cm (less than 4%) over 20 year. This is comparable with some observational and modelling analyses (e.g. Holloway and Sou, 2002), but is much less than the 1950s/1970s to 1990s sonar data analysis (Rothrock et al., 1999) upon which the IPCC based its statement that the arctic ice thickness has been reduced 40% during summer in recent decades. The large variability inherent in the arctic sea-ice–climate system, coupled with the problem of obtaining ice thickness data, renders the evaluation of ice thickness trends from the available observational data an open question. Further analysis of satellite-based ice extent for the period 1979 to present and sea ice model simulations using ECMWF forcing fields from 1958 are presented in Chapter 3.

### 2.3.2 Sea ice conditions of importance for operation and navigation

Ice concentration, thickness, and pressure are the major direct factors influencing ship speed. Ice pressure is one of the most important factors in slowing ship speed or even stopping an icebreaker. For offshore construction, the drift of ice as well as its thickness and mass are key parameters to estimate for ice loading calculations. In addition to the general ice conditions, it is very important to have specific data on these ice parameters in local regions where ice operations are planned. Fig 2.40 gives an overview of the fast ice areas and the main polynyas along the Siberian coast.

Starting in autumn, the fast ice is formed along the coasts of the arctic seas. Maximum development of fast ice is observed in the shallow waters, with an external boundary of about 20–25 m depth. Close to coastlines with deeper waters, the width of fast ice is only about 10–20 km. The fast ice of the arctic seas usually consists of ice generated in autumn. But in the regions of Franz Josef Land, Svalbard, and the East Siberian Sea, two-year old ice may be encountered. Sometimes fast ice can persist during the summer and become two-year or multi-year fast ice.



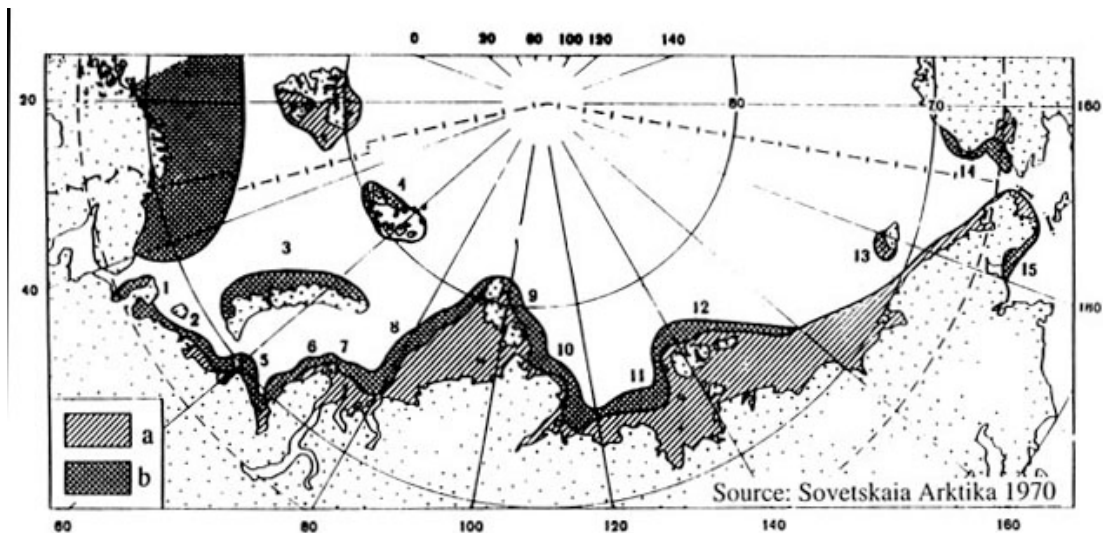
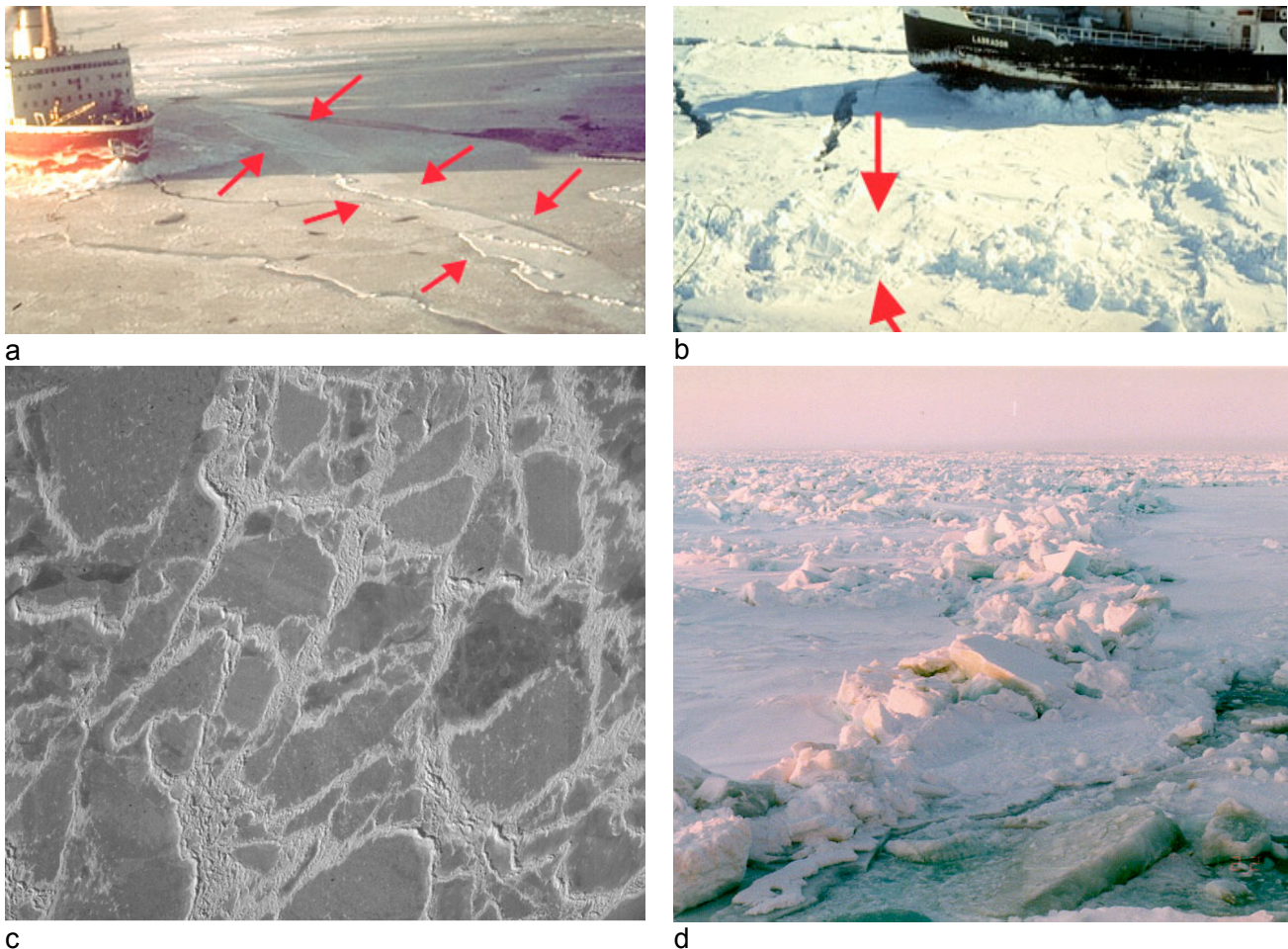


Figure 2.40. Map of fast ice (a) and coastal polynyas (b) in the Russian Arctic during the winter season. Names of the coastal polynyas include 1: Cheshkaya, 2: Pechorskaya, 3: Zapadno-Novozemelskaya, 4: More Victorii, 5: Amderminskaya, 6: Yamalskaya, 7: Ob'-Eniseyskaya, 8: Zapadno-Severozemelskaya, 9: Vostochno-Severozemelskaya, 10: Taymirskaya, 11: Lenskaya, 12: Novosibirskaya, 13: Zavragelevskaya, 14: Alaskinskaya, 15: Anadirskaya.

Two regions show the largest areas of landfast ice: the Severnaya Zemlya area and the New Siberian Islands area. These two areas account for more than 80 % of the total landfast ice area in the arctic seas. Landfast ice is usually in the range of 1.50 to 2.00 m thick. Wide leads with thinner ice, cracks, and hummocks, are frequently observed in the landfast ice. Hummocks in the landfast ice has a gradation of 1 to 2 points, according to the scale from 1 to 5 used in the Russian ice nomenclature to characterize the size of ridges. The most hummocked ice (2 to 3 points) are the narrow strips of landfast ice in the southwestern Kara Sea and along the coast of the Chukchi Sea. The landfast ice is characterized by many stamukhas, which are grounded ridges and ice keels stuck to the seafloor. Examples of ridging and rafting, which can lead to the formation of stamukhas in shallow waters, are shown in Fig. 2.41.

Along the Siberian coast it is common to have polynyas or passage ways between the fast ice and the pack ice, as shown in Fig. 2.40. The polynyas change with time under the influence of varying wind conditions. They can be very long and have variable width. During push-off winds, flaw zones of thin ice are formed beyond the landfast ice and may exist for a long time as open polynyas. Refreezing of the polynyas can occur with formations of up to 70 cm thick ice. Refrozen polynyas up to 50 km in width can occur in the Kara Sea and in areas to the west and north of New Siberian Islands. Such zones are less developed in the East Siberian and Chukchi seas where the width is less than 15 miles.

The drift ice area is located immediately beyond the zone of thin ice. Thick first-year (1.2--1.6 m) ice occupies 2/3 of the drift ice area. Perennial ice of the Arctic Basin enters into the Siberian coastal seas. Such ice is 2 to 3 m thick and is characterized by higher strength. Most of the total sea area occupied by perennial ice on the Siberian coastal shelf is concentrated in the East Siberian Sea where such ice occupies 15--20% of that area. In other Arctic shelf seas this ice normally occupies less than 5% of the areas. The ice drift responds to the wind direction within 3 to 6 hours after changes of wind direction. Ice drift results in ice exchange between the Arctic shelf seas and the Arctic Basin. In winter the ice is transported out of the Kara and Laptev seas and into the Chukchi Sea. This ice drift continues in May and June, although weaker. The ice drift to the Chukchi Sea continues, while the ice drifting from the southwestern Kara Sea almost stops. The amount of ice transported from the northwest to the East Siberian Sea increases.



*Figure 2.41. Examples of photographs of ridging and rafting of sea ice: (a) rafting where one ice sheet is pushed on top of another, (b) a ridge of about 1 m height, (c) vertical photograph of ridge pattern in firstyear ice, (d) heavily ridged area of firstyear ice.*

For offshore operations, there are two main situations which require handling of the ice. The first situation is in shallow waters (5 – 20 m ) where constructions are built on the seafloor and designed to withstand the forces of the drifting sea ice (Fig. 2.42 a). The sea ice is often attached to the seafloor and can be stationary for a long time. But stationary ice can start to drift due to strong winds and pile up ice blocks forming stamukhas. The other situation is when operations takes place in deeper water covered with ice which is freely drifting and ships can operate in the area. Drifting ice passing by a fixed construction will leave an open lead in downstream direction (Fig. 2.42 b) and ice-going vessels can operate in this lead.

Sea ice thickness is the least know of the main sea ice parameters, because data on ice thickness are scarce and systematic measurements of ice thickness do not exist in many areas. Local knowledge of thickness including ice ridges and keels are essential for design of platforms to be operated in seasonal ice-covered areas. Recently, electromagnetic (EM) sounding from helicopter flights has become a well-established technique for measuring ice thickness on local and regional scale. Large data sets representative for regional ice regimes can be gathered for determination of the of ice thickness distribution as shown in Fig. 2.43 a,b (Haas and Eicken, 2001). The EM technology is under further development and will allow repeated systematic surveys in regions where helicopters can operate and there is need for detailed measurements of sea ice thickness and ridge distribution.

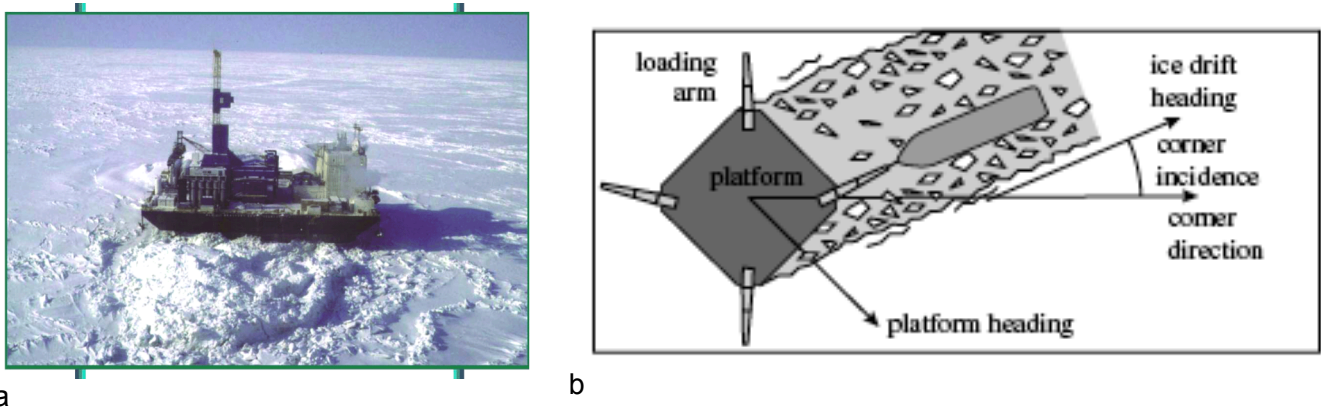


Figure 2.42. (a) photograph of a fixed bottom-mounted platform in sea ice in the Beaufort Sea, (b) illustration of drifting sea ice surrounding a fixed platform where loading to a ship takes place in the lead.

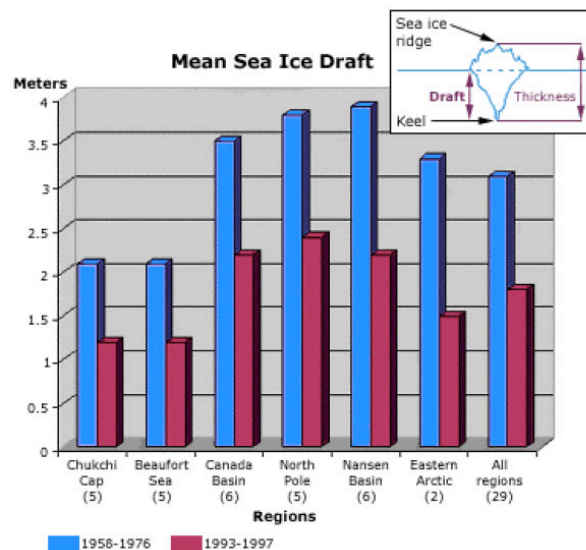
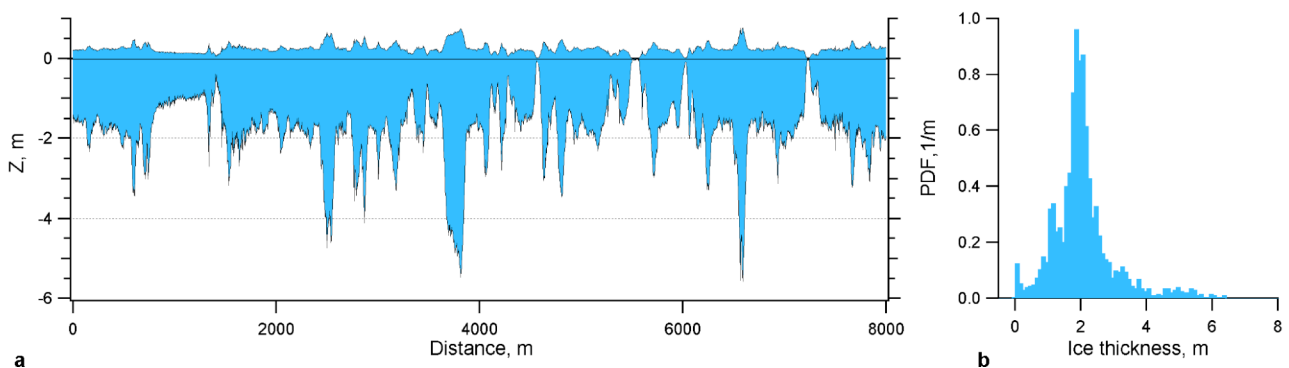


Figure 2.43. (a) Data on ice draft and ice surface height from helicopter electromagnetic induction profile, (b) ice thickness distribution function for the data presented in (a). The figures are provided by C. Haas, AWI, (c) is a comparison of mean ice draft in different Arctic seas obtained from submarine cruises from 1958 to 1997, showing a significant reduction in ice thickness over the last decades.



## 2.4 Icebergs

Icebergs, which are originating from glaciers, are commonly found off eastern Canada, around Greenland, in the Barents Sea and several places in the Russian Arctic (Fig. 2.44). They can be very dangerous for ships and oil rigs because most of the ice mass is below the surface. Smaller icebergs, with horizontal scale of typical 100 m, can be difficult to detect. Observations of sea ice and icebergs are obtained by several methods: aircraft/helicopter surveys, ship observations, reports from coastal and meteorological stations, data from drifting buoys and satellite data. The International Ice Patrol is responsible for observing and reporting icebergs in the Northwestern Atlantic (<http://www.uscg.mil/lantarea/iip/home.html>). In the European Arctic, there is a need to establish a monitoring and forecasting system for icebergs to support the offshore oil and gas exploration.

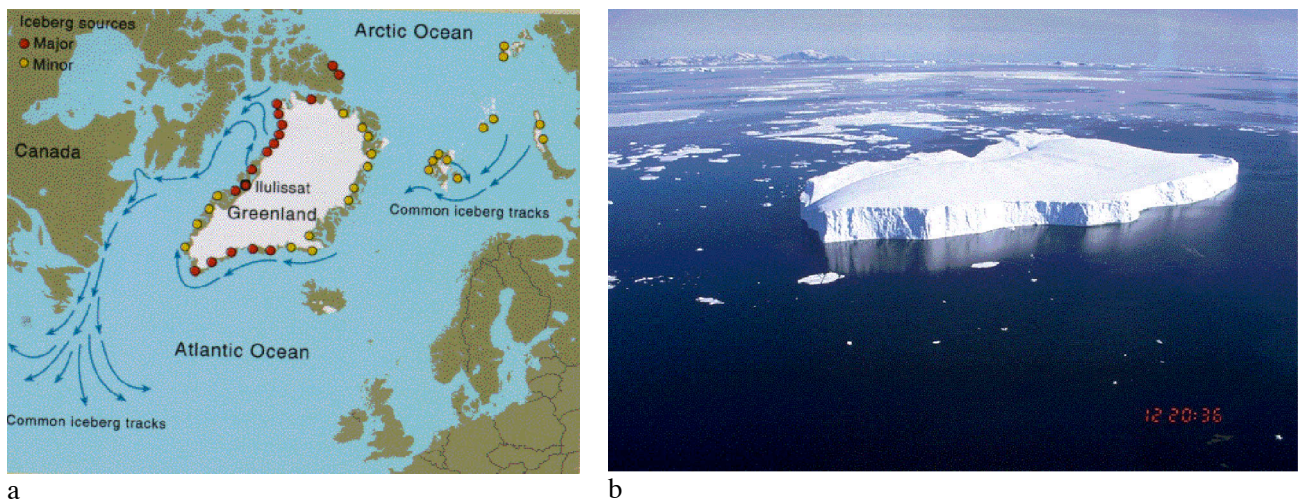


Figure 2.44. (a) Map of the main iceberg-producing areas in the European Arctic and the major drift paths for icebergs, (b) photograph of a characteristic tabular iceberg in the Barents Sea, with horizontal scale of about 100 m and freeboard height of 6 – 8 m.

Systematic monitoring of icebergs in the Arctic have been conducted by Russian aircraft surveys in previous decades, and results of these monitoring projects were presented in several reports as part of the OKN IDAP project 1988 – 1994 (Spring, 1994). Systematic observations by aircraft stopped in the 1990s. In the last 10 – 15 years, there have only been occasional observations of icebergs in connection with expeditions.

An overview of the aircraft iceberg surveys in the Barents and Kara Sea conducted by Arctic and Antarctic Research Institute in the period 1970 – 1989 has been provided by Abramov and Zubakin (1992). This report shows that more than 1500 flights were conducted in the 20 year period and icebergs were observed in more than 1000 of the flights (Table 2.3). The flight tracks are shown in Fig. 2.45a. More than 16000 icebergs were observed in total and the annual and monthly distribution of the observations are presented in Fig. 2.46. In addition to this report, the Iceberg Atlas for the Arctic by Abramov (1996) gives the best overview of icebergs from early 1900 and up to about 1993. The aircraft surveys were normally performed at a flight altitude between 100 and 500 m, with an observing range of 20 – 30 nautical miles. A main question is how much of the iceberg population is captured by this observing scheme. It is obvious that large parts of the areas that potentially can have icebergs are not covered by the surveys. The data presented in Table 2.3 is underestimating the total amount of icebergs, and the question is by how much. Another issue is the size distribution of the icebergs. Previous investigations show that most of the icebergs in the Barents Sea have size less than 100 m. This has an impact on the detection capability using aircraft surveys as well as satellite observations.



Table 2.3: Number of icebergs and aircraft surveys 1970-1989 (Abramov and Zubakin, 1992)

Year	Jan	Feb	Mar	April	May	June	July	Aug	Sept	Oct	Nov	Dec	$\Sigma$ obs	$\Sigma$ flights
1970	0 0	1 1	0 0	7 3	90 8	49 11	6 6	150 16	847 23	231 12	0 0	0 0	1381	80
1971	0 0	52 7	401 9	226 9	97 7	122 13	85 11	59 13	151 12	70 11	4 2	0 0	1267	94
1972	0 0	25 4	42 5	243 10	70 10	89 16	70 14	235 17	210 9	5 5	3 1	0 0	992	91
1973	0 0	18 4	24 3	4 1	46 5	49 7	96 12	332 9	323 13	26 6	0 0	0 0	918	60
1974	0 0	0 0	0 0	102 4	0 0	0 0	2 2	22 12	65 12	27 10	6 2	0 0	224	42
1975	0 0	11 2	55 9	64 2	119 5	0 0	0 0	9 1	31 12	0 0	0 0	0 0	289	31
1976	0 0	12 1	12 1	53 2	70 10	62 4	81 8	269 12	232 12	48 5	0 0	0 0	839	55
1977	0 0	4 1	82 5	31 6	52 5	16 4	66 7	50 10	72 16	36 5	15 3	0 0	424	62
1978	0 0	8 4	54 2	162 8	54 4	15 4	9 2	105 7	119 11	41 7	0 0	0 0	567	49
1979	0 0	20 4	11 5	261 8	306 8	9 2	15 5	184 9	125 5	65 6	3 1	11 2	1010	55
1980	0 0	5 3	19 3	177 6	22 3	219 8	4 1	1 1	48 6	26 3	72 4	0 0	593	38
1981	8 2	10 3	15 3	21 2	0 0	14 4	2 1	39 4	33 6	27 6	4 1	0 0	173	32
1982	0 0	8 2	15 4	46 6	55 3	31 3	22 5	25 3	28 2	5 3	0 0	0 0	235	31
1983	1 1	0 0	12 4	13 6	60 5	8 3	52 6	154 10	888 10	69 2	0 0	0 0	1257	47
1984	0 0	141 8	378 13	141 11	142 10	24 5	72 3	367 8	188 4	31 1	8 3	0 0	1492	66
1985	0 0	20 5	293 16	186 6	263 2	0 0	33 6	93 8	300 5	107 5	2 2	1 1	1298	56
1986	2 1	14 4	15 5	314 7	32 3	27 5	45 4	55 2	393 4	11 4	40 1	1 1	949	41
1987	0 0	23 6	25 4	107 6	1 1	0 0	0 0	186 11	68 4	0 0	0 0	0 0	410	32
1988	1 1	12 3	62 5	14 5	1 1	0 0	0 0	192 3	4 3	43 5	0 0	0 0	329	26
1989	0 0	10 4	0 0	0 0	70 1	679 4	4 1	0 0	379 7	401 8	0 0	10 2	1553	27
$\Sigma$ obs	12	394	1515	2172	1550	1413	664	2527	4504	1269	157	23	16200	
$\Sigma$ flights	5	66	96	108	91	93	94	156	176	104	20	6		1015

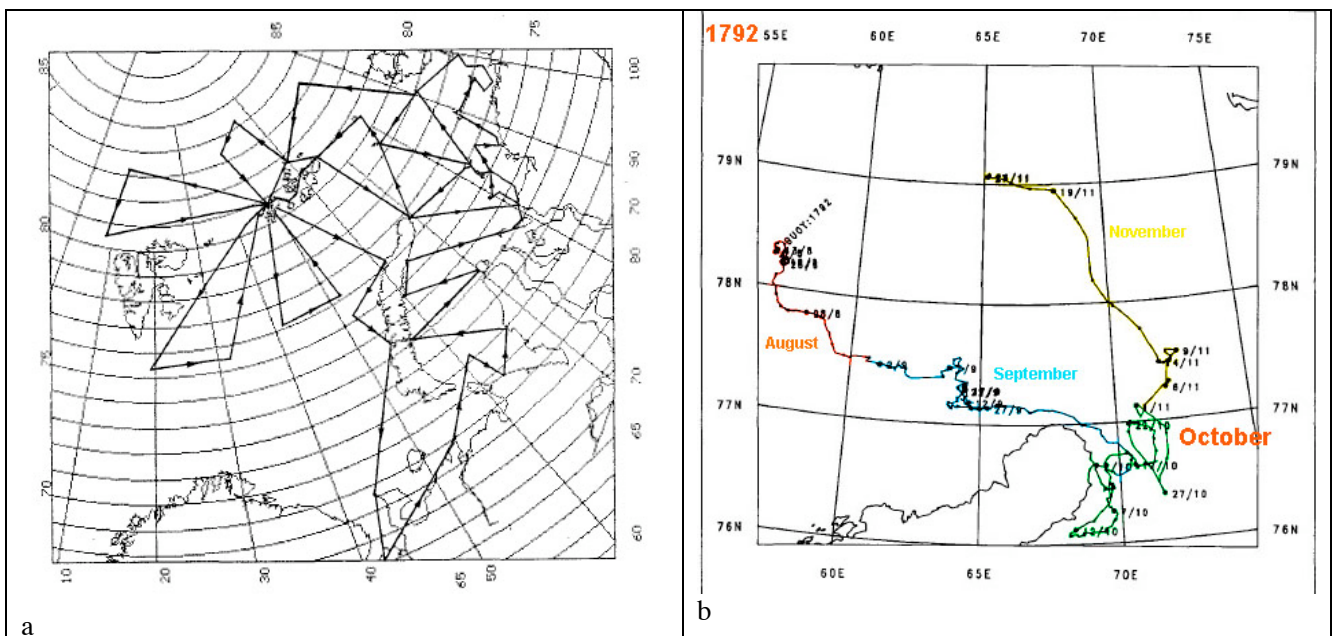


Figure 2.45. (a) Map of standard aircraft flight tracks used for icebergs surveys 1970 – 1989); (b) example of iceberg drift pattern using Argos positions during IDAP investigations (Abramov and Zubakin, 1992).

As observed in Fig. 2.46, the number flights and consequently the number of icebergs were at a minimum in the dark winter month November, December, January and February. Maximum observations in the winter season was in April, while summer observations were at maximum in August and September. Fig 2.47 shows the annual variability in total number of observed icebergs. There are noteworthy minima in 1974-75, 1981-82, and 1987-88. These minima are correlated with lower number of survey flights, as shown in Fig. 2.48.

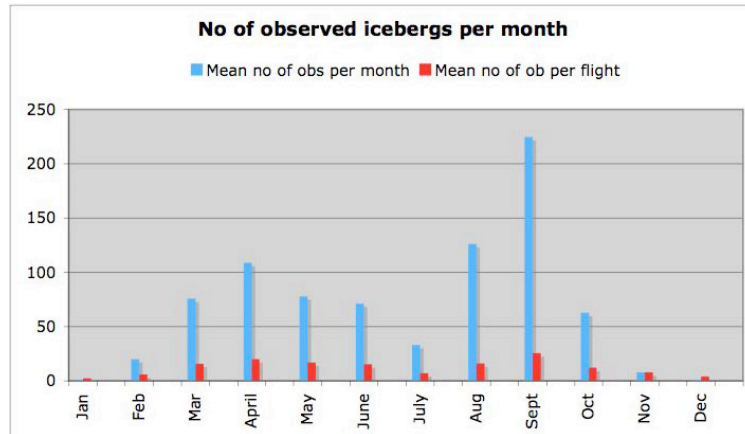


Figure 2.46 Mean number of observed icebergs per month (blue bars) and mean number of observations per flight (red bars)

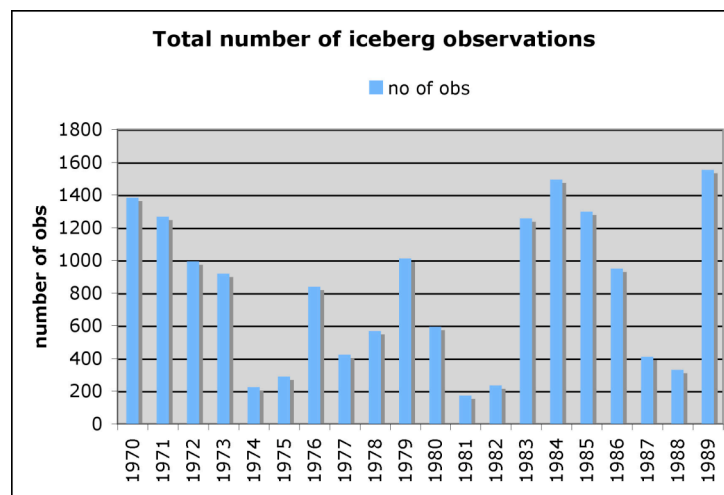


Figure 2.47 Total number of observed icebergs per year in the Barents and Kara Seas

It is noteworthy that the years with lowest number of observed icebergs in Fig 2.47 (1974-75, 1981-82 and 1987-88) also have the lowest number of flights. In addition, 1974, 1981 and 1982 had the lowest number of observations per flight. 1989 is remarkable because the number of observations per flight is significantly higher than all the other years. By comparing total number of flights with total number of observed icebergs (Fig. 38 b) is possible to assess if there has been a trend in iceberg occurrence over the 20 year period. The years 1970-73 is characterized by high number of observations and high number of flights. If we compare this with the next period of high number of observations (1983-1986), we see that relatively more icebergs were observed by a lower number of flights. Except for the extreme year 1989, it can be concluded that iceberg occurrence in the survey area showed large interannual variability and this variability is to a large extent correlated with the number of flights.

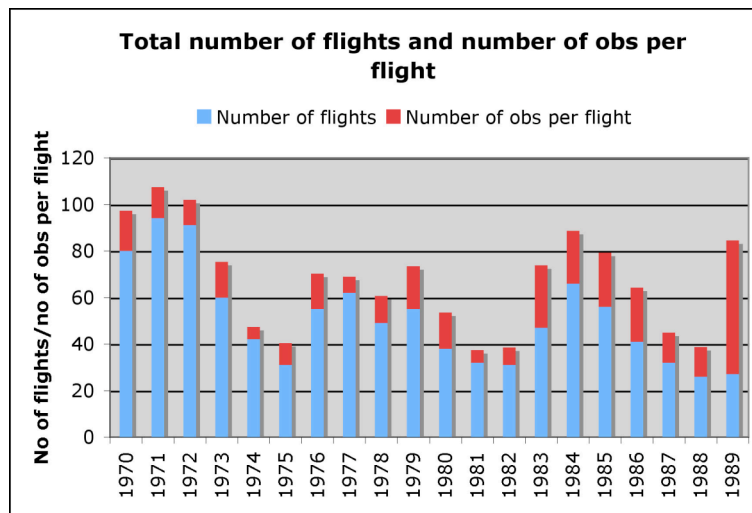


Figure 2.48 Total number of survey flights per year (blue bars) and total number of observations per flight (red bars);

The observations of icebergs from the aircraft surveys have been used to produce iceberg occurrence probability maps (e.g. Abramov and Zubakin, 1992). A more extensive compilation of iceberg data have been published in the Atlas of Arctic Icebergs by Abramov (1996). In this atlas monthly maps of iceberg distribution probability are presented. Also annual occurrence probability maps have been produced (Fig. 2.49) showing that the Northern Barents Sea, Kara Sea and part of the Laptev Sea have the highest probability of icebergs. Maximum iceberg occurrence is found around Franz Josef Land, northern Novaya Zemlya and Severnaya Zemlya.

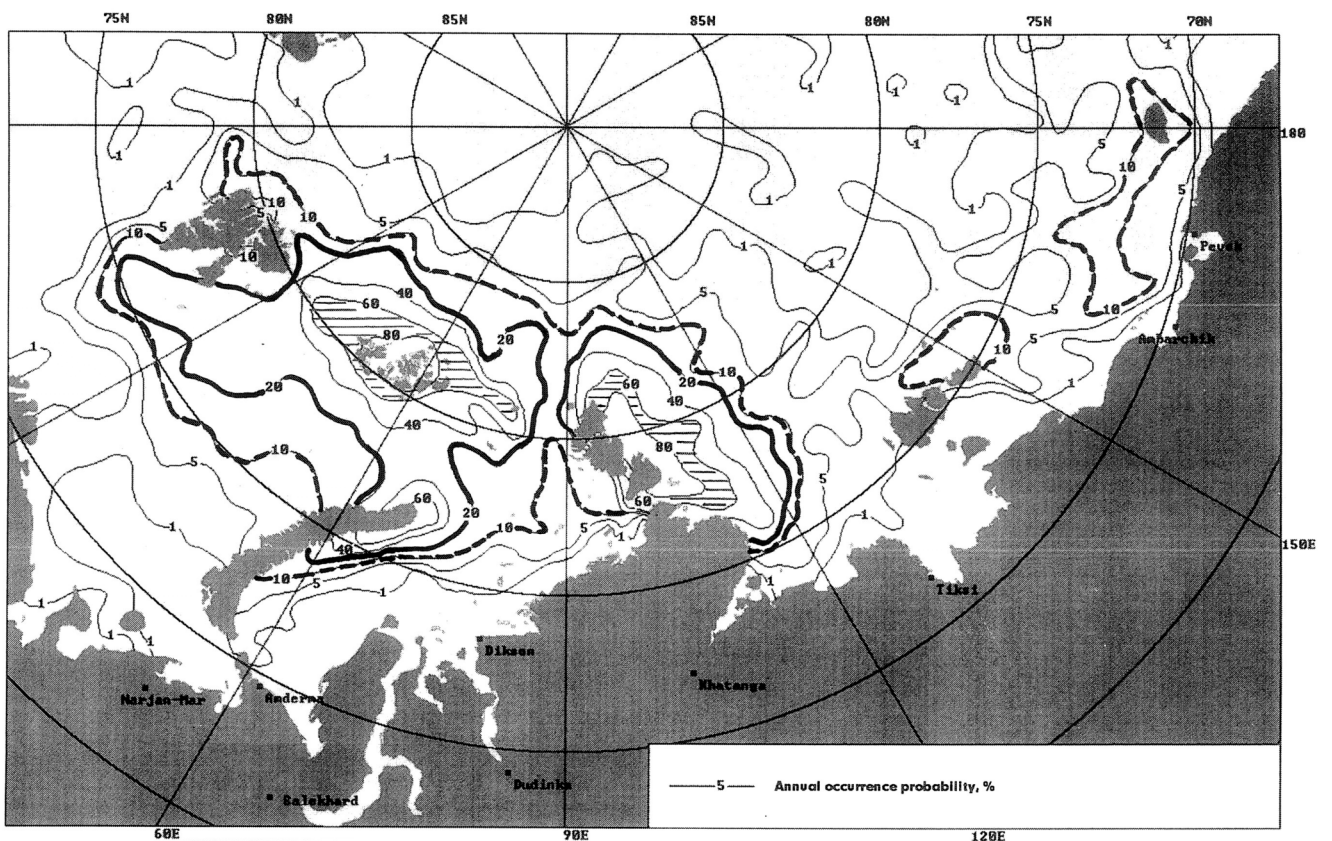


Figure 2.49. Annual iceberg occurrence probability from the Abramov Atlas (1996).

In May 2003, surprisingly many icebergs were observed in the Shtokman area south to 72 N (Zubakin et al., 2004). From ship radar observations, 109 iceberg and bergy bits were found in the area between 71 and 75 N and between 40 and 46 E. The largest iceberg was 190 by 430 m. Before this event, the iceberg occurrence probability for the Shtokman area was that 7 icebergs would occur once in ten years. After May 2003 this probability rose to 19 icebergs occurring once in ten years.

Since the iceberg distribution can vary strongly from year to year, it is important to have good monitoring and tracking systems for the icebergs. Such systems are not in operation for most parts of the Arctic today. Extreme events can happen from year to year and there is no direct method to predict when and where icebergs occur and how they drift in the ocean.



## 2.5 Freshwater fluxes

Freshwater from rivers and glaciers play an important role in the dynamics of the Arctic Ocean including sea ice freezing and melting. The river runoff into the Arctic Ocean has increased by about 7 % between 1936 and 1999 (Peterson et al., 2002). In the last two - three decades the increase has been more significant, as shown by Shiklomanov et al. (2000) and Peterson et al. (2006). Recent climate model predictions suggest that precipitation and river runoff will continue to increase in this century (ACIA, 2005).

The river discharge database R-ArcticNet ([www.R-Arcticnet.sr.unh.edu](http://www.R-Arcticnet.sr.unh.edu)) was extended up to 2004 for 48 downstream river gages. The river inflow to the ocean was computed using a hydrological analogy approach in combination with linear and multiple correlation (Shiklomanov *et al.*, 2000). For regions where no analogous site was available, additional meteorological information and water balance simulations were used (Rawlins *et al.*, 2003). The best estimates were obtained for the Asian and European seas, as well as for the Bering Strait and Beaufort Sea, because only relatively small areas there are unmonitored and data are more available.

The discharge of freshwater to the Arctic ocean has been compared between the period 2000–2004 with that for 1980–1999 for different drainage basins (Peterson et al., 2006). The result of this study is shown in Table 2.4. The last 5 years were characterized by an increase of total discharge to the Arctic Ocean, mainly due to a contribution from Asian rivers. The mean 2000–2004 discharge from Asia was 110 km<sup>3</sup> (5%) higher than for the previous 20 years. The mean discharge to the ocean from North America and Europe for 2000–2004 was practically unchanged relative to 1980–1999. Adjacent territories such as Bering Strait, Hudson Bay, and Hudson Strait drainage basins had insignificantly higher discharges in 2000–2004 compared with the previous 20 years.

Table 2.4 Characteristics of the annual inflow to the Arctic Ocean for 1980 – 2004 (from R-ArcticNet database ([www.R-ArcticNet.sr.unh.edu](http://www.R-ArcticNet.sr.unh.edu))).

Basin	Mean discharge 2000-2004	Mean discharge 1980-1999	Change in mean discharge	Maximum annual inflow 1980-2004		Minimum annual inflow 1980-2004	
	km <sup>3</sup> /year	km <sup>3</sup> /year	%	km <sup>3</sup>	year	km <sup>3</sup>	year
Bering Strait*	311	301	3.3	362	1990	259	1999
Hudson Bay and Strait	920	905	1.7	1020	1992	770	1981
North America	1170	1170	0	1350	1996	990	1995
North America with Hudson B. & Str	2090	2080	0.5	2310	1996	1810	1981
Europe	708	708	0	790	1993	590	1980
Asia	2560	2450	4.5	2780	2002	2150	1982
Arctic Ocean Basin	4440	4330	2.5	4770	1997	3870	1982
Arctic Basin, Hudson Bay and Str. Basins	5670	5530	2.5	6040	1997	5070	1982

\* including Norton Sound, Yukon River and Anadyrsky basins

A consistent increase in river discharge is observed from Eurasia for a longer time interval as well. Most of the rivers show an increasing trend in annual river discharge over the observational periods. The mean discharge over 2000–2004 for the large Eurasian rivers was 3–9% higher than the discharge over 1936–2004. Thus, the contemporary data further confirm the presence of a significant increasing trend in the freshwater discharge to the Arctic Ocean from Eurasia documented earlier by Peterson *et al.* (2002) (Fig. 2.50). The maximum total discharge of the six largest Eurasian rivers over 1936–2004 was observed in 2002, at 2080 km<sup>3</sup>/year (Fig. 2.50). There is no clear picture for the North American rivers; they generally have both positive and negative insignificant long-term discharge trends. The discharge of the Yukon and Mackenzie Rivers during the last 5 years was higher than normal, although the estimated total discharge to the ocean from North America has not changed significantly.

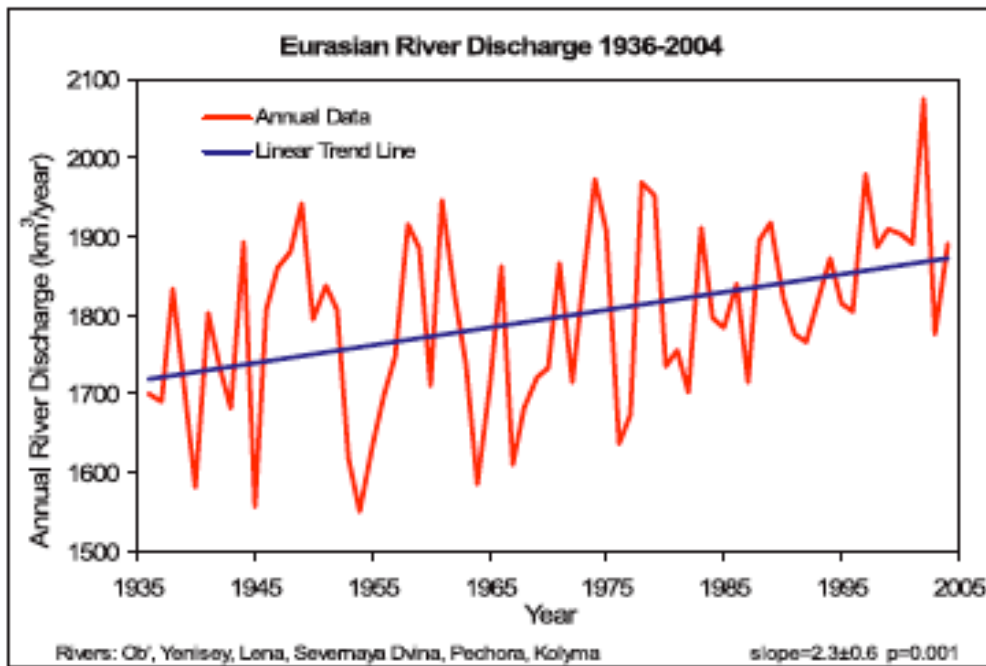


Figure 2.50: Total annual discharge to the Arctic Ocean from the six largest rivers in the Eurasian pan-Arctic for 1936–2004. The least-squares linear increase was 2.3 km<sup>3</sup> per year. (Updated from Peterson *et al.*, 2002.)

The Arctic glaciers have, in general, retreated over the same period (Dyurgerov and Meier, 2000; Rignot *et al.*, 2004), whereas less is known about the Greenland ice sheet, one of the wildcards of the climate system. The latter has been the subject of increased attention for two important reasons: Melting of the Greenland ice sheet will add fresh water to the North Atlantic Ocean which have been theorized to weaken or even destroy the Atlantic MOC (Stouffer *et al.*, 2006). Secondly, the Greenland ice sheet stores a freshwater amount equivalent to an increase of the global sea level of 7 meters, implying that even partial melting will influence the global sea level in dramatic ways. Recent observation-based studies of the surface elevation of the Greenland ice sheet diverge; reporting that the interior of the Greenland ice sheet has increased during 1992-2003 (Johannessen *et al.*, 2005), that there is a net positive mass balance for the whole ice sheet for the same period (Zwally *et al.*, 2005), and that there has been a dramatic glacier acceleration between 1996-2005 (Rignot and Kanagaratnam, 2006).

The contribution of glaciers to the freshwater inflow to the Arctic and world oceans has been increasing as a result of climate warming and will affect many aspects of the Arctic climate system. This comes primarily from glaciers in the Canadian, Russian, and Svalbard archipelagos and from individual ice caps around the Greenland Ice Sheet (GRIS) (Dyurgerov and Meier, 2005). New and more precise measurements show surface thinning along the southwestern and southeastern coasts of Greenland and a substantial increase in surface melting and water concentration on the surface in the ablation zone of GRIS (Abdalati *et al.*, 2001; Box *et al.*, 2004, 2006; Krabill *et al.*, 2004; Thomas, 2004). Large tidewater glaciers have nearly doubled in surface velocity, and basal melting has increased (Krabill *et al.*, 2004; Thomas, 2004; Joughin *et al.*, 2004; Steffen *et al.*, 2004). These observations and an analysis of climate change suggest that GRIS dynamics has responded with no delay to recent climate and mass balance changes, at least along the coast. While there are clear thinning and accelerated outflows near the edges, there is a debate about the mass balance for Greenland as a whole (Johannessen *et al.*, 2005; Rignot and Kanagaratnam, 2006). The fresh water discharges create the East Greenland Coastal Current (Wilkinson and Bacon, 2005), corresponding to at least 30 % of the total Arctic freshwater gain. Clearly, both the

fresh water from the Greenland Ice Sheet and the freshwater transport out of the Arctic are of key importance for the Arctic and global climate system. Some examples of mass balance studies of the Greenland ice sheet are presented in Fig. 2.51.

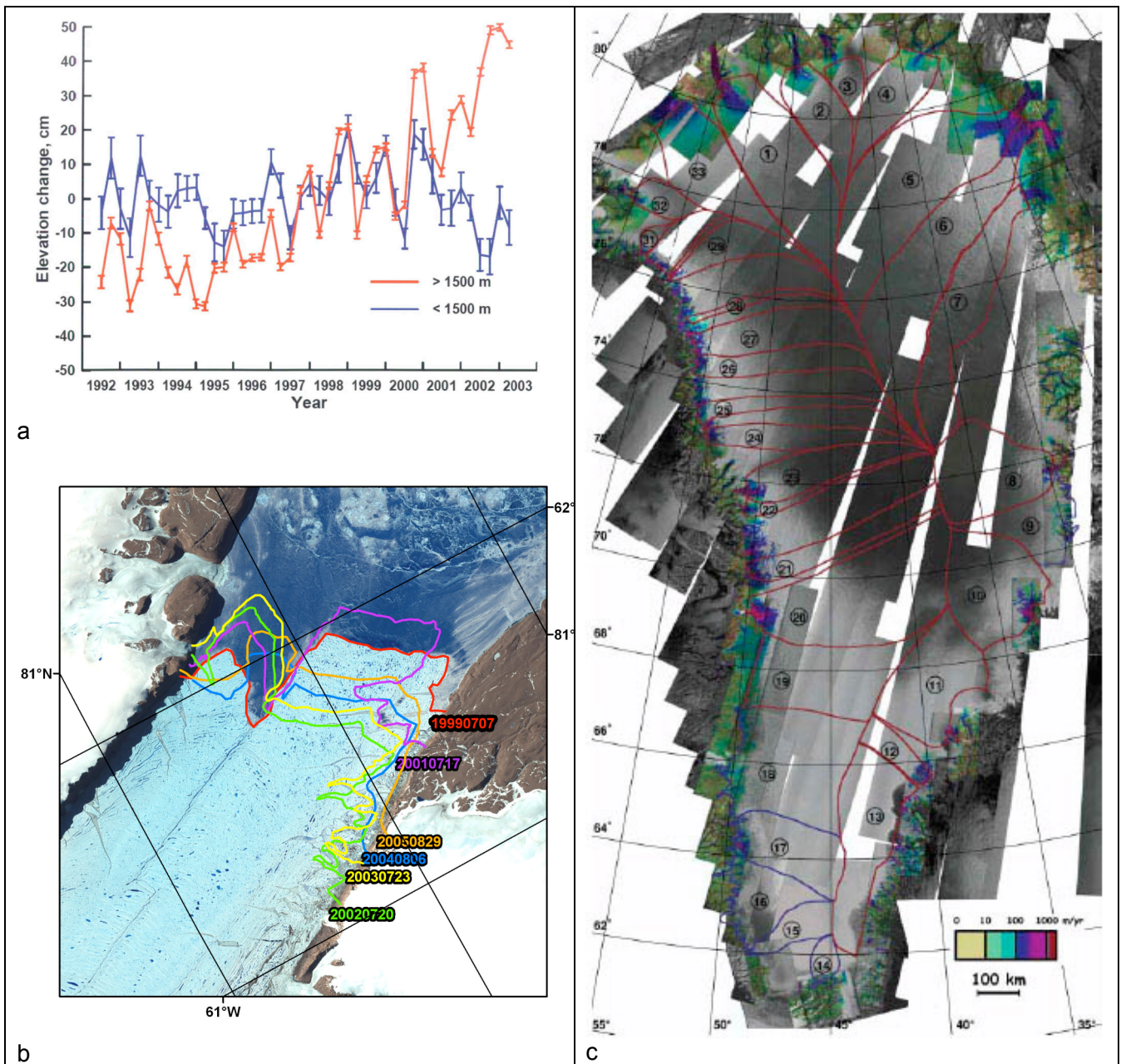


Figure 2.51 (a) Surface elevation of Greenland ice sheet from radar altimeter data (Johannessen et al., 2005), (b) change in ice front from the Patermann glacier in north Greenland based on analysis of satellite images between 1999 and 2005 provided by NERSC, (c) mass loss of Greenland outlet glaciers estimated from SAR interferometry (Rignot and Kanagaratnam, 2006). The colour code indicate the areas and magnitude of the mass loss around the edges of the Greenland ice sheet.

Freshwater inflow from Arctic mountain glaciers, icecaps, and GRIS has been rising over the last several decades. This rise has been especially fast since the end of the 1980s and mid-1990s. It is likely that freshwater inflow to the Arctic Ocean from glaciers will continue to rise as a result of climate warming. Although many small glaciers will disappear, the large glaciers in Canadian,



Russian, the Svalbard archipelagos, and the Greenland ice sheet will add to the hydrological cycle as cold glaciers warm and begin producing more runoff. Peterson et al (2006) have reported many changes in the freshwater cycle of high-latitude lands and oceans in the past few decades. A synthesis of these changes in freshwater sources and in ocean freshwater storage illustrates the complementary and synoptic temporal pattern and magnitude of these changes over the past 50 years (Fig. 2.52).

Increasing river discharge anomalies and excess net precipitation on the ocean contributed about 20,000 cubic kilometers of fresh water to the Arctic and high-latitude North Atlantic oceans from lows in the 1960s to highs in the 1990s. Sea ice attrition provided another 15,000 cubic kilometers, and glacial melt added about 2000 cubic kilometers. The sum of anomalous inputs from these freshwater sources matched the amount and rate at which fresh water accumulated in the North Atlantic during much of the period from 1965 through 1995. The changes in freshwater inputs and ocean storage occurred in conjunction with the amplifying North Atlantic Oscillation and rising air temperatures. Freshwater may now be accumulating in the Arctic Ocean and will likely be exported southward if and when the North Atlantic Oscillation enters into a new high phase. The freshwater changes are summarized in Table 2.5.

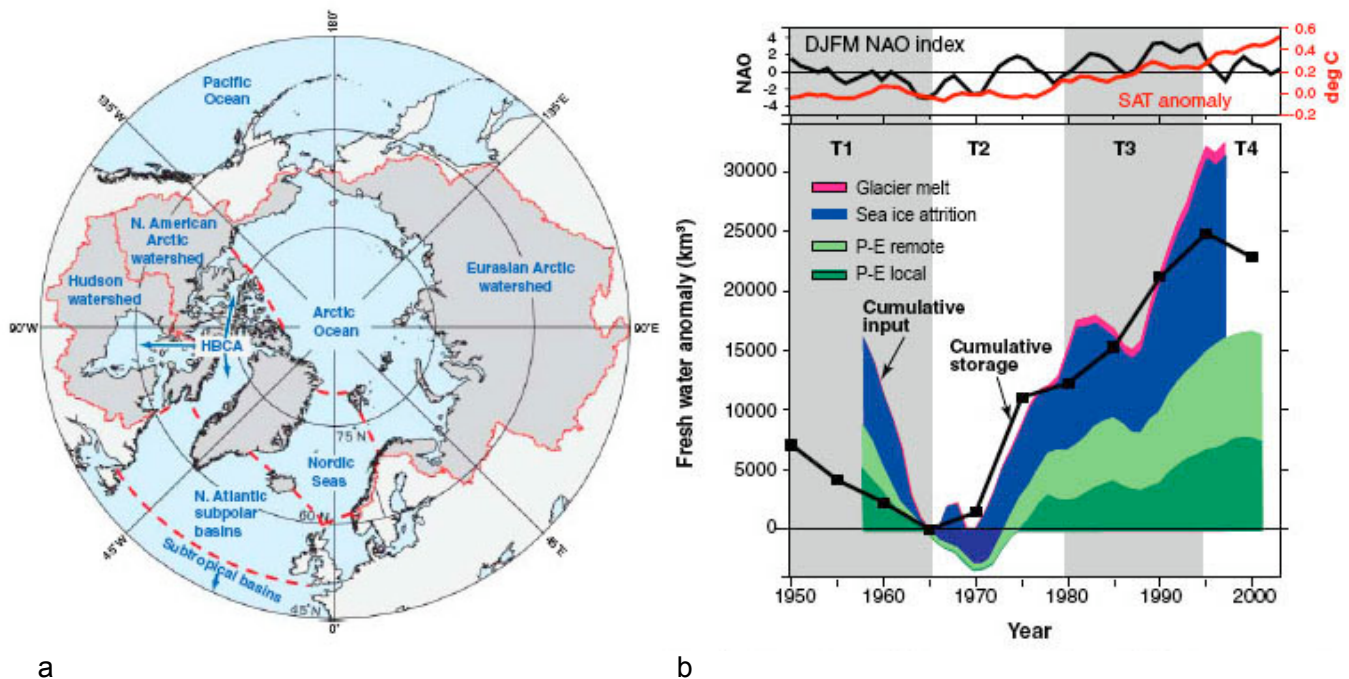


Figure 2.52 (a) Map of the watershed and ocean domains used for estimates of freshwater anomalies by Peterson et al., (2006). Solid red lines delineate watershed boundaries used for calculations of river discharge anomalies. Dashed lines separate regions of the ocean surface used for calculations of precipitation minus evaporation (P-E) anomalies and define the boundaries used for freshwater storage analysis in the Nordic Seas and the North Atlantic Subpolar Basins; (b) Comparison of freshwater (FW) source anomalies and FW storage anomalies relative to 1965 (units are km<sup>3</sup>). Black curve is cumulative Nordic Seas and Subpolar Basins (NSSB) ocean FW storage. Colored areas represent cumulative FW contributions from P-E local (Subpolar plus Nordic Seas, dark green), P-E remote (Arctic Ocean, Hudson Bay and Canadian Archipelago, and river discharge, light green), sea ice attrition (blue), and glacier melt (red). Source contributions are stacked to show total FW source input.



Table 2.5. Contemporary anomalies for major FW sources to the Arctic Ocean, Hudson Bay and Canadian Archipelago (HBCA), Nordic Seas, and Atlantic Subpolar Basins (Peterson et al., 2006).

Freshwater sources	References	Years covered in references	Average anomaly $\pm$ SE for 1990s (km <sup>3</sup> /year)	% relative to 1936-1955 baseline
Rivers flowing into the Arctic Ocean	Peterson et al. (2002)	1936-1999	163 $\pm$ 34	+ 5.3
	R-ArcticNET v3.0	2000-2003		
	Wu et al. (2005)	1900-2050		
Rivers flowing into Hudson Bay	Dery et al. (2005)	1964-2000	- 59 $\pm$ 16	- 8.0
Small glaciers, ice caps	Dyurgerov and Carter (2004)	1961-2001	38 $\pm$ 13	
Greenland Ice Sheet	Box et al., (2004)	1991-2000	81 $\pm$ 38	
P-E Arctic Ocean	ERA-40 (Uppala et al., 2005)	1958-2001	124 $\pm$ 72	+ 7.6
P-E HBCA	ERA-40 (Uppala et al., 2005)	1958-2001	81 $\pm$ 33	+ 15.6
P-E Nordic Seas	ERA-40 (Uppala et al., 2005)	1958-2001	67 $\pm$ 28	+ 17.8
P-E Subpolar Basin	ERA-40 (Uppala et al., 2005)	1958-2001	336 $\pm$ 73	+ 16.8
Sea Ice	Rothrock et al. (2003)*	1987-1997	817 $\pm$ 339	
<b>TOTAL</b>			<b>1649</b>	

\* Rothrock et al. reported observed changes in sea ice thickness annually from 1987 – 1997 and also modeled changes over a wider time frame (1951-1999). Thickness has been converted to freshwater volume following Wadhams and Munk (2004).

In Table 2.5 the anomalies for river discharge and P-E are relative to a 1936–1955 baseline. Anomalies for small glaciers and ice caps include melt from the pan-Arctic watershed, Arctic and subarctic islands, and ice caps around but not connected to the Greenland Ice Sheet. Anomalies for sea ice focus specifically on melting of stocks in the Arctic Ocean. Anomalies for small glaciers and ice caps, the Greenland Ice Sheet, and sea ice are relative to a water balance of zero (no net change in volume). In all cases, positive values indicate excess FW inputs to the ocean. Dashed entries indicate no estimates. R-ArcticNET v3.0 is a river discharge archive, and ERA-40 is a reanalysis of atmospheric observations.

## 2.6 Permafrost

Observations show a general increase in permafrost temperatures during the last several decades in Alaska (Osterkamp and Romanovsky, 1999; Romanovsky *et al.*, 2002; Clow and Urban, 2003; Osterkamp, 2003), northwest Canada (Couture *et al.*, 2003; Smith *et al.*, 2005), Siberia (Pavlov, 1994; Romanovsky *et al.*, 2001; Pavlov and Moskalenko, 2002), and northern Europe (Isaksen *et al.*, 2000; Harris and Haerberli, 2003). Uninterrupted permafrost temperature records for more than 20 years have been obtained by the University of Alaska Fairbanks along the International Geosphere- Biosphere Programme Alaskan transect, which spans the entire continuous permafrost zone in the Alaskan Arctic. All of the observatories show a substantial warming during the last 20 years. The amount of warming was different at different locations, but it was typically 0.5–2°C at the depth of zero seasonal temperature variations in permafrost (Fig. 2.53).

These data also indicate that the increase in permafrost temperatures is not monotonic. During the observational period, relative cooling has occurred in the mid-1980s, in the early 1990s, and then again in the early 2000s. As a result, permafrost temperatures at 20 m deep experienced stabilization and even a slight cooling during these periods. An even more significant cooling of permafrost was observed during the very late 1990s and the early 2000s in interior Alaska (not shown). A significant portion of this cooling is related to a shallower-than-normal winter snow cover during this period. During the last three years, there was a sign of recovery in mean annual temperatures at shallow depths. In 2005, soil temperatures in interior Alaska reached the temperatures of the early to mid-1990s, which were the warmest during the last 70 years.

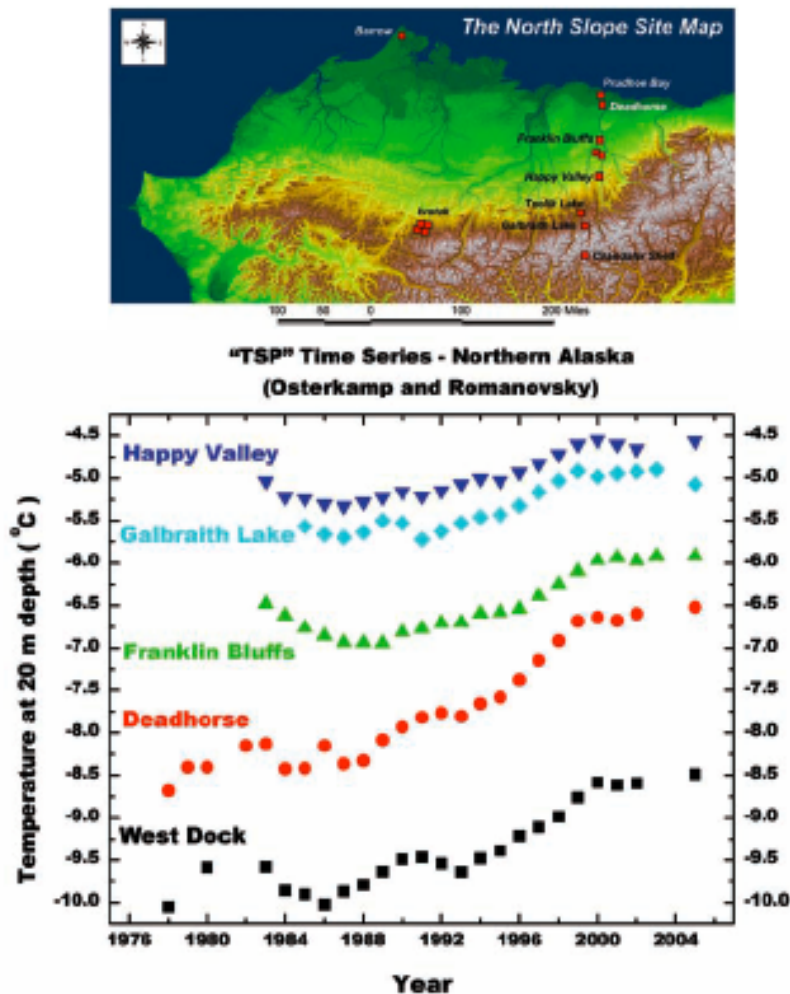


Figure 2.53: Top: Locations of the long-term University of Alaska permafrost observatories in northern Alaska. Bottom: Changes in permafrost temperatures at a depth of 20 m over the last 20–25 years. (Updated from Osterkamp, 2003.)

Data on changes in the active layer thickness in the Arctic lowlands are less conclusive. In the North American Arctic, the active layer thickness experiences a large interannual variability, with no discernible trends; this is likely because of the short length of historical data records (Brown *et al.*, 2000). A noticeable increase in the active layer thickness was reported for the Mackenzie Valley (Nixon *et al.*, 2003). However, this positive trend reversed to a negative trend at most of these sites after 1998 (Tarnocai *et al.*, 2004). An increase in thickness of more than 20 cm between the mid-1950s and 1990, derived from the historical data collected at the Russian meteorological stations, was reported for the continuous permafrost regions of the Russian Arctic (Frauenfeld *et al.*, 2004; Zhang *et al.*, 2005). At the same time, reports from several specialized permafrost research sites in central Yakutia showed no significant changes in the active layer thickness (Varlamov *et al.*, 2001; Varlamov, 2003). The active layer was especially deep in 2005 in interior Alaska. Around Fairbanks the 2005 active layer depth was the deepest observed in the past 10 years. Data from many of these sites show that the active layer that developed during the summer of 2004 (one of the warmest summers in Fairbanks on record) did not completely freeze during the 2004–2005 winter; a thin layer just above the permafrost table was unfrozen during the entire winter.

The long-term thawing of permafrost starts when the soil layer that was unfrozen during the summer above the permafrost does not refreeze completely, even during the most severe winter. The residual unfrozen layer is termed “talik,” and the process is often being referred to as “talik formation.” The cause of this event could be climate warming and/or an increase in snow accumulation (for any reason) at the ground surface. Changes in the surface hydrology could also trigger long-term permafrost thawing. However, a more common cause of increased thawing has been disturbances of the ground surface above the permafrost, both natural (forest fire, flood) and human-made (agricultural activities, roads and building construction, etc.). There are a very limited number of localities within the permafrost zone where talik formation has been carefully documented. One of the best examples is the Tanana River Flats near Fairbanks, Alaska, where naturally occurring long-term permafrost thawing was studied and documented by Jorgenson *et al.* (2001). This study revealed widespread and rapid permafrost thawing that caused a shift in ecosystems from birch forest to fens and bogs. Similar processes were reported by Osterkamp *et al.* (2000) for the Tok area in Alaska. Deepening of the permafrost table from 3.5 m in 1989 to 5 m in 2004 was reported for some areas at the Gakona Permafrost Observatory in Alaska (Romanovsky *et al.*, 2005).

There is also evidence that the recent warming has already resulted in permafrost thawing and talik formation at some sites in northern Eurasia. For example, during the 1960s and early 1970s, ground temperatures at 3.2 m at Khoseda-Khard, in the European North of Russia, were at or below 0°C, with some years also showing the 1.6 and 2.4 m levels perennially frozen. Conditions changed drastically during the latter part of the twentieth century (Fig. 2.54). In the relatively cold year of 1964, 3.2-m ground temperatures were at 0°C year-round, suggesting a phase transition (the 2.4-m level thawed out during fall). In the relatively warm year of 1989, fall temperatures at 3.2 m reached 3.3°C. Thawing of permafrost as a result of forest fires and agricultural activities in Alaska has been reported by Osterkamp and Romanovsky (1999), Romanovsky and Osterkamp (2000), and Yoshikawa *et al.* (2003).

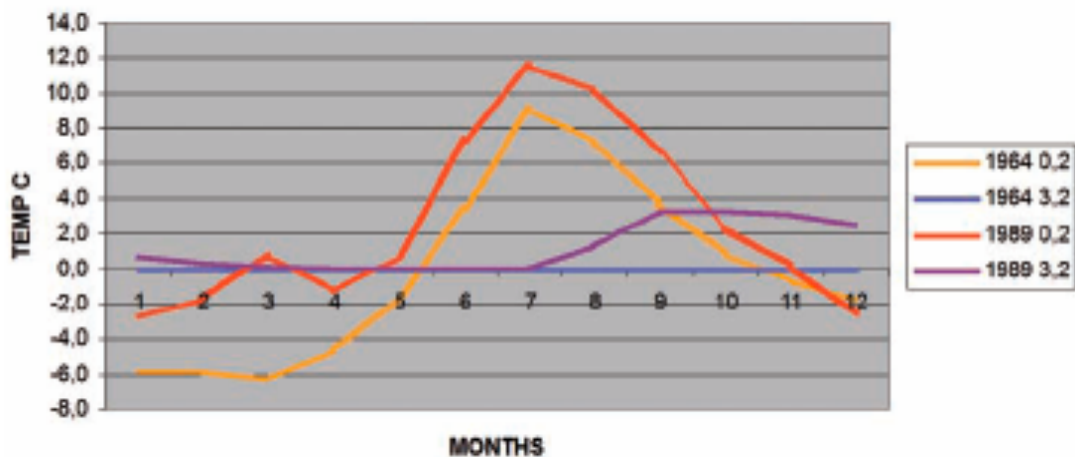


Figure 2.54 Monthly ground temperature records at 0.2 m and 3.2 m in 1964 (a cold year) and 1989 (a warm year) at the weather station Khoseda-Khard, in northeast European Russia. (From *Klimatologicheskii spravochnik SSSR, 1961–1992.*)

Romanovsky *et al.* (2002) have provided an overview of permafrost changes in different parts of the Arctic in Table 2.6.

Table 2.6. Overview of permafrost temperature trends in different Arctic regions (Romanovsky et al., 2002)

Country	Region	Permafrost temperature trends	Reference
USA	Trans-Alaska pipeline route (20 m), 1983-2000	+0.6 to +1.5°C	Osterkamp and Romanovsky, 1999; Romanovsky and Osterkamp, 2001
	Barrow Permafrost Observatory (15 m), 1950-2001	+1°C	UAF Geophysical Institute ongoing research
Russia	East Siberia (1.6-3.2 m), 1960-1992	+0.03°C/year	UAF Geophysical Institute ongoing research
	North of West Siberia (10 m), 1980-1990	+0.3 to +0.7°C	Pavlov, 1994
	European North of Russia, continuous permafrost zone (6 m), 1973-1992	+1.6 to +2.8°C	Pavlov, 1994
	European North of Russia, discontinuous permafrost zone (6 m), 1970-1995	up to +1.2°C	Oberman and Mazhitova, 2001
Canada	Alert, Nunavut (15 m), 1995-2000	+0.15°C/year	Geological Survey of Canada ongoing research
	Northern Mackenzie basin, NWT (28 m), 1990-2000	+0.1°C/year	Geological Survey of Canada ongoing research
	Central Mackenzie basin, NWT (15 m), 1985-2000	+0.03°C/year	Geological Survey of Canada ongoing research
	Northern Quebec (10 m), late 1980s – mid 1990s	-0.1°C/year	Allard et al., 1995



### 3. Sea ice model simulations and satellite analysis for the Arctic regions

#### 3.1 Introduction

Sea ice is an important component of the climate system. Its presence in the Arctic and Antarctic has a strong impact on the fluxes of momentum, moisture and heat from the ocean to the atmosphere. The strong impact of sea ice is perhaps best demonstrated in the way it affects the heat fluxes. In the Arctic it is not uncommon to have heat fluxes close to a kilowatt between the ocean and atmosphere when ice is absent. The presence of ice, on the other hand, can reduce this flux by two orders of magnitude (Maykut and Untersteiner, 1971). Although the presence or absence of ice is perhaps the most important effect when it comes to insulating the ocean from the atmosphere, the thickness of ice is important as well. The thicker the ice is, the stronger will its insulating effect be. As described in section 2.3 sea ice in the Arctic has been observed to undergo severe change in the last few decades, where the trend shows a significant reduction in both ice area and ice thickness. For sea ice modelling it is a major challenge to simulate the observed seasonal and interannual variability as well as the decadal trends of ice extent, thickness and other ice variables.

The most common sea-ice model formulations use a simple two-category ice thickness formulation, where the grid cell is divided into a fraction with open water, and a remaining fraction consisting of ice of thickness  $hi$ . This formulation has proven to give good results, but it misses some important properties of the ice cover, properties which are important for the seasonal evolution of the ice cover. As an example, lateral melt parameterizations are needed to account for thinner ice melting quicker than thick ice (Hakkinen and Mellor, 1992). Such parameterizations can have a strong effect on the seasonal variations of the ice cover, and associated ocean-atmosphere heat exchange (Mellor and Kantha, 1989; Harvey, 1990).

Sea ice models that describe the ice thickness distribution do not need such parameterizations if the thin ice is sufficiently resolved by the model. To properly account for these effects, a sea-ice model describing the ice thickness distribution has been developed at the Nansen Center. This is done by estimating the areal coverage of ice within different ice thickness categories, using the theory from Thorndike et al. (1975). The model used in this report calculates the ice coverage in the following ice thickness intervals; 0.0-0.5 meters, 0.5-1.0 meters, 1.0-2.0 meters, 2.0-5.0 meters and the last ice thickness interval is for ice thicker than 5 meters. This makes it possible to get good estimates of how much thick ice is present in a given region. In particular, the volume of ice constituting ridges and ice keels can be estimated from the deformed ice, represented by thickness above 2.0 m. Such information can for instance be important for operations which need to operate within the ice pack.

The multi-category sea-ice model at NERSC has been coupled to the HYCOM ocean model (Bleck, 2002) and the Elastic-Viscous-Plastic sea ice rheology model of Hunke and Dukowicz (1997), which is used to calculate the sea-ice drift. The latter is important to determine the evolution of the ice thickness distribution. For instance, in regions where ice is converging, the ice thickness must increase when the ice concentration is close to 100%. This increase in ice thickness is effectively done by changing the ice thickness distribution; the amount of thin ice in the region decreases, and the amount of thick ice in the region increases.

We have used this ice-ocean model system to calculate ice coverage statistics for several regions in the Arctic Ocean (Fig. 3.1). These regions are set up to cover most of the regional seas, where ice is of a seasonal nature, and two regions in the central Arctic Ocean, where the ice is usually present all year-round. We have compiled a set of regionally and seasonally averaged quantities which we think compresses the massive amount of information from the model, into a more manageable, and hopefully comprehensible, data set.

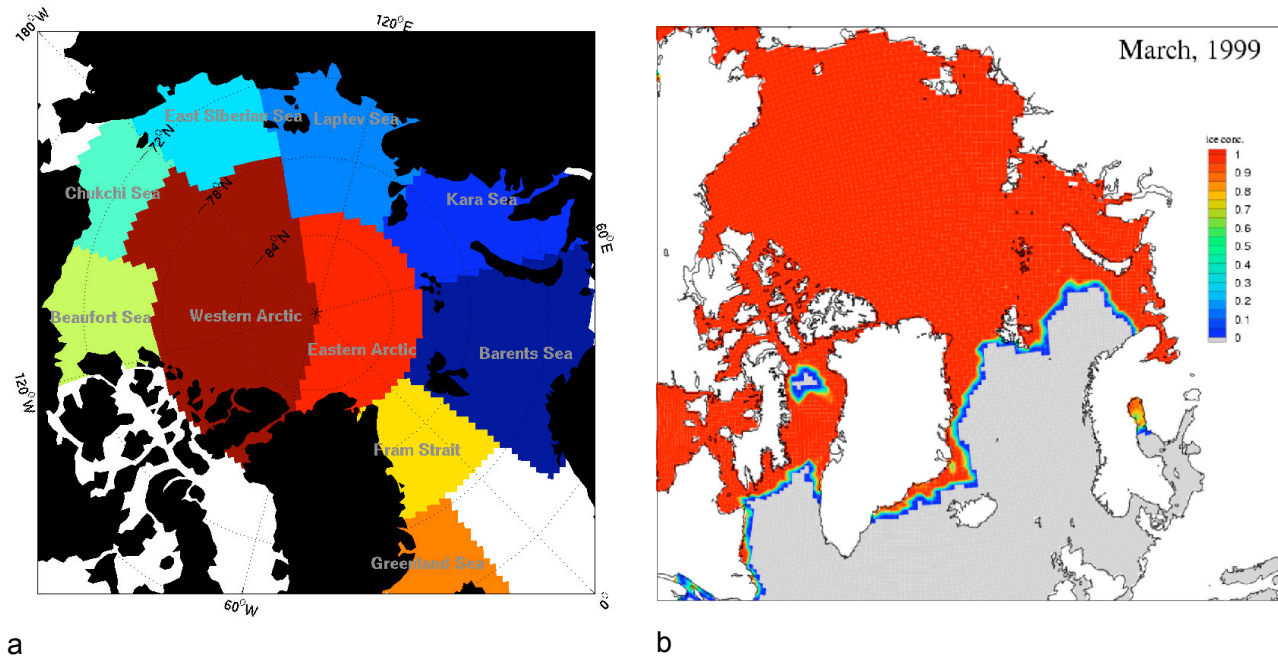


Figure 3.1. (a) The regions where sea-ice statistics are calculated from model simulations and from the satellite data; (b) ice extent in the Arctic for March 1999 produced by the coupled ice-ocean model at NERSC.

This chapter consists of a brief description of the model system (section 3.2), validation of the model against some of the in-situ data in the Arctic (section 3.3), some regional statistics from the model (section 3.4), and the conclusions of the modeling study (section 3.5).

## 3.2 Model description and setup

### 3.2.1 Ice thickness distribution

The model system consists of the HYbrid Coordinate Ocean Model (HYCOM; Bleck, 2002), the Elastic-Viscous-Plastic (EVP) ice dynamics model (Hunke and Dukowicz, 1997) coupled with a multi-category sea ice model describing the thermodynamic and kinematic evolution of the sea-ice cover. The multi-category sea-ice model closely follows the delta-function based description of Bitz et al. (2001), and is briefly described in the next section. The coupling of the ice model with the EVP ice dynamics model and the HYCOM ocean model is then described in Section 3.2.2.

The model describes the ice thickness distribution as discrete ice thicknesses, each having an associated area coverage. This is achieved by using  $d$ -functions, and the theory of redistribution follows that of Thorndike et al. (1975), outlined for  $d$ -function based ice thickness distributions by Bitz et al. (2001). The distribution  $g(h)$  is given as

$$g(h) = c_0\delta(h) + \sum_{i=1}^N c_i\delta(h - h_i), \quad (1)$$

where  $N$  is the number of ice categories used in the model. The variables  $c_i$  are the fractions of the different sea-ice categories, and  $c_0$  is the fraction of open water. Due to ridging and rafting of sea-ice, new ice thickness delta-functions will be created. In order to limit the number of ice categories,

a procedure is needed to merge new ice categories which are created by ridging processes. This is done, following Bitz et al. (2001), by prescribing fixed ice thickness limits ( $H_i, H_{i+1}$ ) wherein only one ice category is allowed to exist. The evolution of the ice concentration and ice volume adhere to the following continuity equations,

$$\frac{\partial c_i}{\partial t} = -\nabla \cdot (u_i c_i) + \Psi_i + \mathcal{G}_i, \quad (2)$$

$$\frac{\partial v_i}{\partial t} = -\nabla \cdot (u_i v_i) + \Theta_i + \mathcal{V}_i, \quad (3)$$

following the notation of Bitz et al. (2001). Here,  $v_i = c_i h_i$  is the ice volume per unit area for category  $i$ ,  $\psi_i$  and  $\Theta_i$  are contributions from sea ice ridging on ice concentration and ice volume, respectively, while  $\mathcal{G}_i$  and  $\mathcal{V}_i$  are the thermodynamic growth contributions to ice concentration and ice volume, respectively. Similar equations apply for the snow thickness, the amount of latent heat stored in the brine heat storage (Semtner Jr., 1976), and the heat content of the ice.

### 3.2.2 Thermodynamic model

The thermodynamic contribution to the ice thickness and ice concentration evolution is calculated using heat budget balances on the ice or snow interface to the atmosphere, and between the ice-ocean interface. Each ice category is treated independently, so in the following we drop the subscript indicating which category is treated. The thermodynamic model describes the heat fluxes which arise over water and ice, and also describes the heat fluxes acting within the ice and the heat fluxes between ice and the ocean. The model includes a snow cover and it has a snow albedo parameterization following that of Douville et al. (1995). The model also allows the creation of snow-ice. If the snow-ice interface is depressed below sea-level, an amount of snow is converted to ice to ensure that the snow-ice interface is again above the sea-level. A brief description of some of the elements of the model is given in the following section, including the internal heat fluxes in the ice, and the heat budgets. The parameterization of heat fluxes from the atmosphere and ocean follows those in Drange and Simonsen (1996).

#### Internal heat flux in the ice

The internal heat fluxes in the ice arise due to vertical heat conduction, a brine heat storage parameterization following Semtner Jr. (1976) and Grenfell and Maykut (1977), and a simple parameterization of thermal inertia, described below. The heat equation in the ice and snow is given as

$$c_{p\{i,s\}} \rho_{i,s} \frac{\partial T_{i,s}}{\partial t} = k_{i,s} \frac{\partial^2 T_{i,s}}{\partial z^2}, \quad (4)$$

where  $c_{p\{i,s\}}$  is the heat capacity of ice or snow,  $\rho_{i,s}$  is the density of ice or snow,  $k_{i,s}$  is the conductivity  $T_{i,s}$  is the temperature and  $z$  is the vertical coordinate. The heat capacity of snow is set to zero. This equation can be solved in different ways, depending on the ice category. For "thick" ice, the equation is solved with a forward in time-centered in space numerical scheme, following Semtner Jr. (1976). This approach uses a single snow layer, and a specified number of ice layers. For "thin" ice, the "0-layer" approximation of Semtner Jr. (1976) is used, which neglects the heat capacity of the ice. The delineation between thin and thick ice depends on the specific setup of ice thickness categories. The "0-layer" approximation gives the following conductive heat flux in the ice

$$F_c = -k_{\text{eff}} \frac{T_{\text{surf}} - T_f(S_w)}{h + h_s}, \quad k_{\text{eff}} = \frac{(h + h_s)k_s k_i}{h k_s + h_s k_i}. \quad (5)$$

In this equation,  $T_f(S_w)$  is the freezing point temperature of sea water with salinity  $S_w$ ,  $T_{\text{surf}}$  is the temperature of the surface substance (ice or snow), and  $h_s$  is the snow thickness. We also include a thermal inertia heat flux  $F_{\text{int}}$ . Since the "0-layer" conductive heat flux has the same value at the top and bottom of the ice, the internal heat of the ice cannot change due to this. The inertia heat

flux comes in addition to the conductive heat flux in order to simulate the effect the changes in heat in the ice has on the surface budget, and to keep track of the changes to heat stored in the ice. The inertia heat flux is given by connecting the ice bulk temperature ( $T_{i,blk}$ ) to the surface temperature of the ice or snow ( $T_{srf}$ ). The conductive heat flux must satisfy

$$F_c = -k_{eff} \frac{T_{srf} - T_f(S_w)}{h + h_s}, \quad (6)$$

$$F_c = -k_i \frac{T_{i/s} - T_f(S_w)}{h} = -2k_i \frac{T_{i,blk} - T_f(S_w)}{h}, \quad (7)$$

where  $T_{i/s}$  is the ice temperature at the snow/ice interface. The final result in Eq. (7) is obtained by relating the bulk temperature to the ice temperature at the snow/ice interface, where a linear ice temperature profile is assumed. The connection between ice bulk temperature and surface temperature becomes

$$T_{i,blk} = \frac{hk_{eff}}{2k_i(h + h_s)} (T_{srf} - T_f(S_w)) + T_f(S_w). \quad (8)$$

The heat required to increase the internal energy of the ice is then related to the change of surface temperature. This heat flux is applied at the top surface

$$F_{inrt} = -c_{pi}\rho_i h \frac{\partial T_{i,blk}}{\partial t} = -c_{pi}\rho_i h \frac{hk_{eff}}{2k_i(h + h_s)} \frac{\partial T_{srf}}{\partial t}. \quad (9)$$

Figure 3.2 illustrates the effect of this parameterization. A simple test case is used where a constant atmospheric heat flux of  $-20\text{Wm}^{-2}$  is enforced on 0.7m thick ice. The initial temperature of the ice is set to the freezing point of sea water, and the system is allowed to adjust to the atmospheric heat flux.

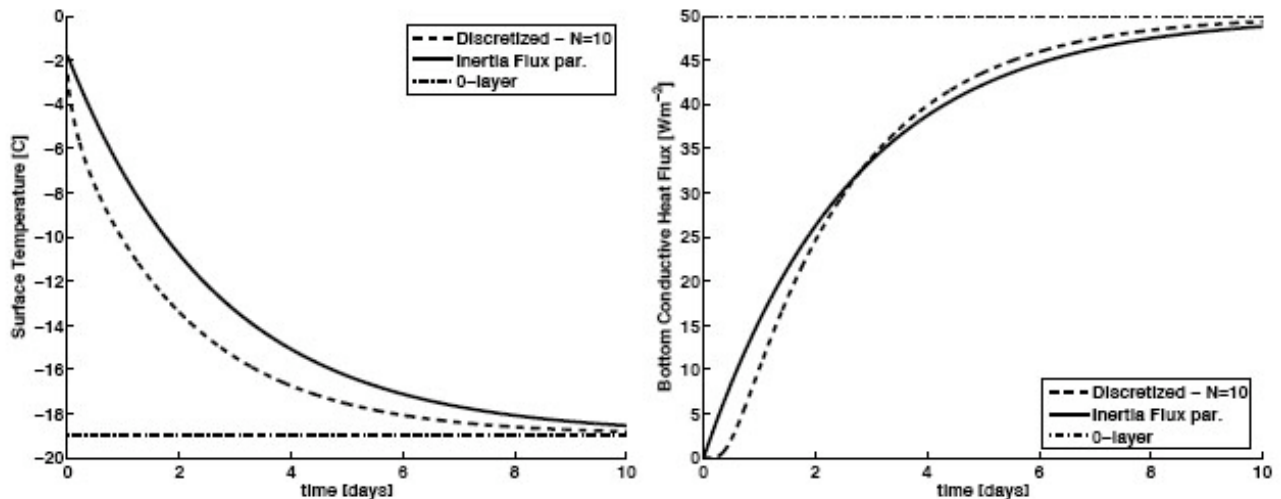


Figure 3.2: Illustration the inertia heat flux parameterization, Eq. (9). The left panel shows the surface temperature evolution and the right panel shows the evolution of the conductive heat flux at the bottom of the ice floe for the case described in the text. The dashed line shows the reference solution, where the heat equation is solved using 10 vertical layers in the ice. The solid line is the evolution when using the inertia heat flux parameterization, while the dash-dotted line is the solution using the “0-layer” approximation.



Figure 3.2 illustrates how the evolution of the surface temperature and the conductive heat flux at the bottom of the ice floe react to abrupt changes in the surface heat flux. A reference solution is also shown, which is the heat equation solved using a discretization of 10 vertical layers in the ice. Whereas the “0-layer” approximation adjusts immediately to changes in the heat flux, the use of the inertia heat flux parameterization leads to an evolution which more closely matches the reference solution, both for bottom conductive heat flux and for surface temperature. Finally, it should be mentioned that the  $F_{\text{inrt}}$  parameterization is also used for the surface layer when Eq. (4) is solved for thick ice with more than one vertical layer. The surface boundary condition for the discretized Eq. (4) then becomes the conductive heat flux  $F_c$  plus the inertia heat flux  $F_{\text{inrt}}$ . It can be shown that as the vertical discretization increases,  $F_{\text{inrt}} \rightarrow 0$ , so for “thick ice” its purpose is mainly to correct for low vertical resolution.

## Heat budgets

### Ice surface heat budget

The heat budget on the top of the ice/snow system is given as

$$F_{\text{net}}^{\text{top}} = -L_{\text{srf}} \rho_{\text{srf}} \min \left( 0, \frac{dh_{\text{srf}}}{dt} \right) = F_c^{\text{top}} + F_{\text{brine}} + F_{\text{inrt}} - F_{L,\text{srf}} - F_{r,\text{srf}} - F_{s,\text{srf}} - F_{e,\text{srf}}, \quad (10)$$

where the surface material (subscript srf) is either snow or ice. The heat fluxes from the atmosphere are the latent ( $F_{e,\text{srf}}$ ), sensible ( $F_{s,\text{srf}}$ ), long wave ( $F_{L,\text{srf}}$ ), and short wave ( $F_{r,\text{srf}}$ ) heat fluxes, their parameterizations are given as in Drange and Simonsen (1996).  $L_{\text{srf}}$  is the latent heat of the surface material, where the latent heat of ice is modified following Semtner Jr. (1976). The brine heat reservoir is restricted to 30% of the energy needed to melt the ice cover. The surface temperature is calculated using Eq. (10), where the heat fluxes are already linearly dependent on surface temperature, or are discretized to be so. The exception is the latent heat flux and the brine storage heat flux, which uses surface temperatures at the previous time step, and the procedure of Semtner Jr. (1976), respectively. Whenever Eq. (10) predicts  $T_{\text{srf}}$  to be higher than the melting point of sea-ice or snow,  $T_{\text{srf}}$  is set to the melting point, and balance is sought by melting the surface material. In typical wintertime conditions  $F_{\text{net}}^{\text{top}}$  is zero, so  $T_{\text{srf}}$  is given by the flux balance on the r.h.s of Eq. (10).

### Heat budget for the ice/ocean interface

The heat balance given at the bottom of the ice is

$$F_w + F_{\text{rw}} - F_c^{\text{bot}} = F_{\text{net}}^{\text{bot}} = -L_i \rho_i \frac{dh_i}{dt}. \quad (11)$$

The heat flux from the ocean ( $F_w$ ) is given in Holland and Jenkins (1999). The short wave heat flux going through the ice ( $F_{\text{rw}}$ ) is modeled following Grenfell and Maykut (1977) in conjunction with the brine heat storage parameterization of Semtner Jr. (1976). The flux  $F_c^{\text{bot}}$  is the conductive heat flux at the bottom of the ice.

### Heat budget for the open water fraction

The heat budget for open water is given as

$$-F_{L,w} - F_{s,w} - F_{e,w} - F_{r,w} = F_{\text{net},w}, \quad (12)$$

where the net heat flux at the ocean surface is introduced,  $F_{\text{net},w}$ . Depending on the state of the ocean surface, different approaches are followed. If the ocean temperature is above the freezing point, the heat flux entering the open water fraction is used entirely to cool or heat the ocean. If the ocean surface is at the freezing point, further cooling of the ocean surface is compensated by

latent heat loss due to freezing ice. The new ice introduced in this manner is set to have a thickness  $h_0$ , which means that the growth of new ice depends on the lateral growth of the ice. In the multi-category ice model, newly frozen ice of thickness  $h_0$  and accumulated over a time step will be added to an already existing ice category. Which category depends on the discretization of the ice thickness and the choice of  $h_0$ , but it is usually the category with lowest ice thickness range. Finally, we mention that no lateral melting parameterization is applied in the simulations.

### 3.2.3 Coupling with HYCOM and the EVP rheology

The sea-ice model has been coupled to the HYCOM ocean model, which can use a mixture of sigma, z and isopycnic coordinates to describe the ocean in the vertical, and has several options for vertical mixing schemes. HYCOM, as set up here has z-layers with five meter resolution near the surface. Deeper in the water column the z-layers revert to isopycnal layers in the ocean interior. The model uses 22 layers in the vertical with densities ranging from 1021.00 to 1028.11  $\text{kgm}^{-3}$  referenced to potential density at the surface, where the lightest layers usually become z-layers in the hybrid coordinate formulation. For vertical mixing the K-Profile Parameterization scheme of Large et al. (1994) is used. The model grid is set up using the conformal mapping tools of Bentsen et al. (1999), with a grid size ranging from 50 to 80 km in the North Atlantic and Arctic regions. The bathymetry and grid cell size used in the model are shown in Fig. 3.3.

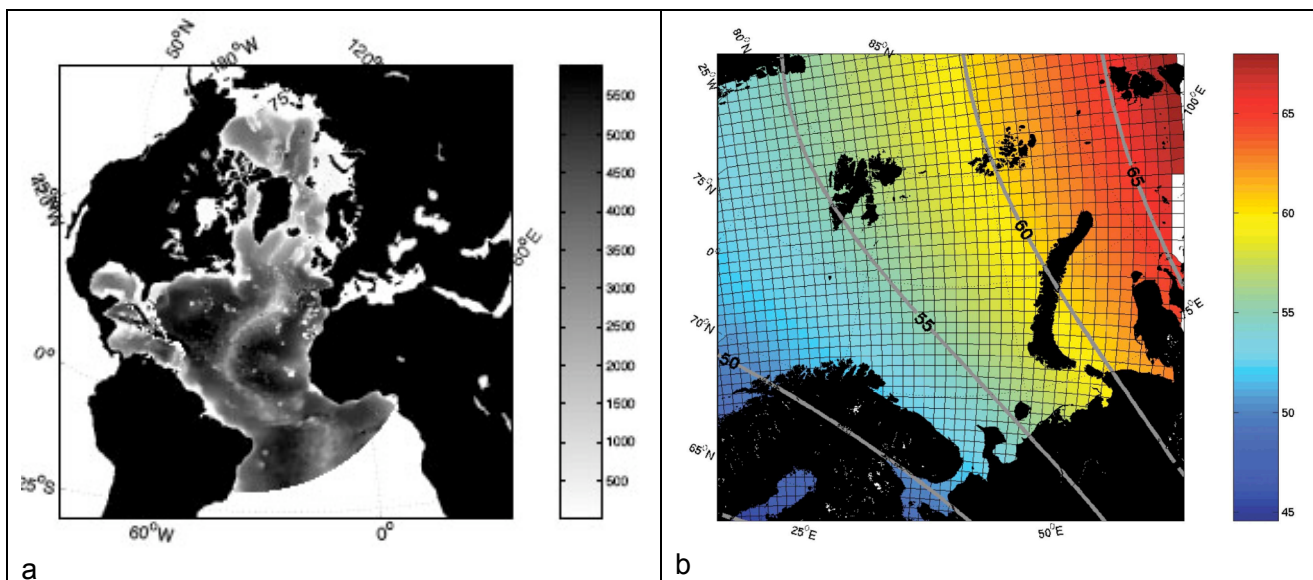


Figure 3.3. (a) Bathymetry for the model domain covering the North Atlantic and Arctic ocean presented in greyscale; (b) illustration of the model grid size for the Arctic region varying between 50-80 km.

The ocean model time step was set to 20 minutes in the simulations. To calculate heat fluxes the simulation uses reanalyzed data (ERA40) from the European Center for Medium-Range Weather Forecasts (ECMWF). Data used from ERA40 are temperature at 2 meters, dew-point temperature at 2 meters, winds at 10 meters, clouds and precipitation with a temporal resolution of 6 hours. River climatologies are included and added to the model fields as a negative salinity flux. The ice model uses the ice thickness distribution and thermodynamic model given in sections 3.2.1 and 3.2.2. The dynamic part of the ice model uses the EVP formulation of Hunke and Dukowicz (1997). The coupling between the ice model and HYCOM involves the transfer of ocean heat and salinity fluxes calculated from the ice model to HYCOM. In addition there is a two-way exchange of drag forces acting between the ice and the ocean. The drag from the ocean on the ice, and from the atmosphere on ice is given by quadratic bulk formulas as

$$\tau_{i,o} = \rho_w C_{D,o} (v_o - v_i) |v_o - v_i|, \quad (13)$$

$$\tau_{i,a} = \rho_a C_{D,a} v_a |v_a|, \quad (14)$$

where the drag coefficients are set to  $C_{D,o} = 5.5 \times 10^{-3}$  and  $C_{D,a} = 2.2 \times 10^{-3}$ . A zero turning angle is assumed since the upper ocean model layer is only 5m thick. The EVP model is set up with the ice strength parameterization of Hibler (1980), given as

$$P = P^* c h e^{-C^*(1-c)}, \quad (15)$$

where  $P^* = 27500 \text{Nm}^{-2}$ , and  $C^* = 20$ . The sea ice model thermodynamics are tightly coupled to the ocean model, and the ice model calculates the heat fluxes to the ocean model for every ocean model time step. The EVP model, ridging, and advection of sea-ice parameters is done every two hours. Sea ice shear does not contribute to ridging in the simulations. Also, it should be mentioned that the model at present has no separation between ridged or level ice when it comes to material properties. The mechanical and thermodynamic properties of the ice are the same for ice that has undergone ridging as for level ice.

The ocean model was initialized from the Generalized Digital Environment Model (GDEM, Teague et al., 1990) climatology, and run with ERA40 6-hourly forcing from 1958 until 2002 after a 10 year spin-up using an ERA40-based climatology. This climatology consists of monthly averages of the ERA40 fields over the period 1958–2002. During the integration the model was run using surface salinity and temperature relaxation with an e-folding time scale of 150 days. This relaxation was only applied in ice-free areas. Along the model boundaries (Bering Strait, South Atlantic ocean) the model was relaxed towards the GDEM climatology. In addition, the model was set up with a 0.8 Sv barotropic transport into the Arctic from the Bering Strait (Woodgate et al., 2005).

In the experiment, a total of 5 ice thickness categories are used to account for the different ice thicknesses encountered in the Arctic ocean, see Table 3.1. The thickness classes are closer for the thin end of the thickness distribution, whereas ice thickness greater than 5 meters makes up the last class.

*Table 3.1. Number of ice categories used in the model, the ice thickness limits for each class and the number of vertical layers used when solving the thermodynamics.*

Ice thickness class	1	2	3	4	5
Ice thickness limits (m)	0.0 – 0.5	0.5 – 1.0	1.0 – 2.0	2.0 – 5.0	> 5.0
Vertical layers	1	1	3	4	5

The thickness limit used to delimit “thick” and “thin” ice in the thermodynamic model ( $h_L$ ) is set to 1.0 meters. In ice classes 3-5 the heat equation is solved explicitly, whereas for class 1-2 it is solved using the parameterizations given for “thin ice”. The coupling between the ice model and HYCOM involves the transfer of ocean heat and salinity fluxes calculated from the ice model to HYCOM. In addition there is a two-way exchange of drag forces acting between the ice and the ocean.

### 3.3 Model validation

The mean summer (July-September) and mean winter (January-March) ice thickness fields were calculated for the time period 1958–2002 and are shown in Figures 3.4b and 3.4a. The ice thickness fields are reasonable, increasing in thickness from the Siberian Coast towards the Canadian Arctic Archipelago and the northern coast of Greenland. Thick ice is present in the Beaufort Sea, and the East Siberian Sea also has relatively thick ice. Sea ice transport through the

Fram Strait is illustrated by the tongue of thicker ice being advected from the Arctic Basin into the Greenland Sea. Ice concentration is not shown, but at times the ice extent can be excessive in the peripheral seas of the Arctic, such as the Barents Sea and the Greenland Sea. The overestimated ice extent in these seas is partly connected to too low inflow of Atlantic Water into the Nordic Seas. The inflow of warm Atlantic water into the Nordic Seas is about 6 Sv, which is lower than estimates from models (Nilsen et al., 2003) and observations (Østerhus et al., 2005) of 8 Sv. Another possible mechanism could be too high transport of sea ice from the Arctic into the Greenland Sea, but ice transport estimates shown later on show that this is probably not the case.

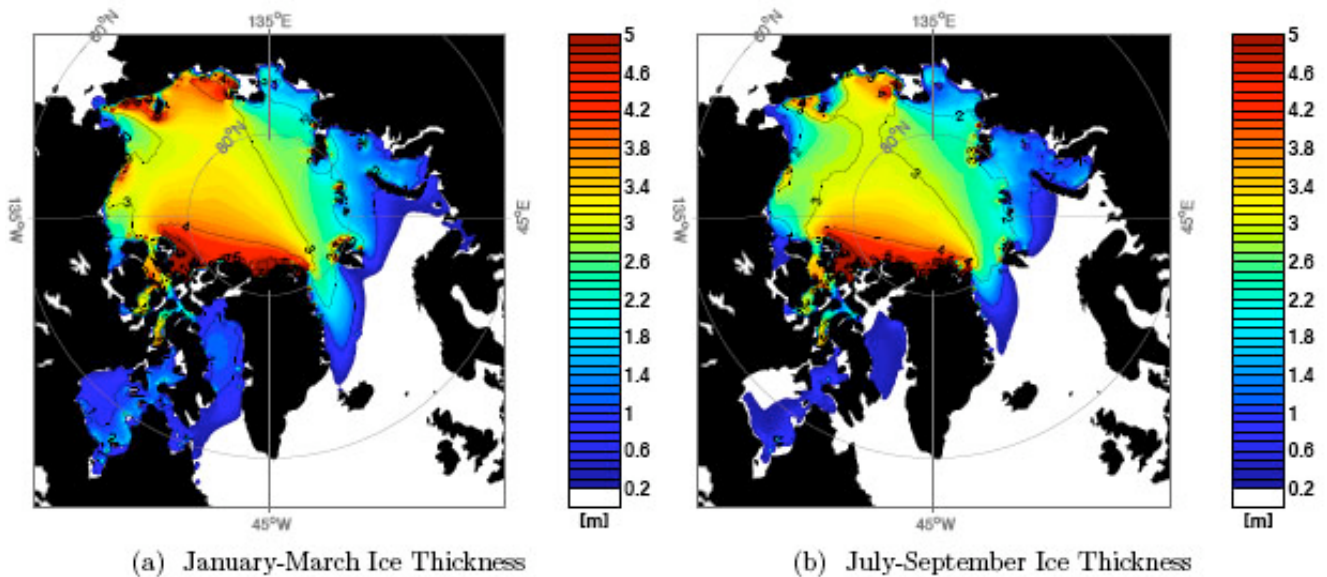


Figure 3.4: Mean ice thickness for the period 1958–2002 from the NERSC ice-ocean model.

### 3.3.1 Comparison with ULS data

A more rigorous look at the modeled ice thickness fields can be done by comparing with data gathered from Upward Looking Sonars (ULS) carried on board British and American submarines. The sea ice draft data gathered from submarines is provided by the National Snow and Ice Data Center (NSIDC) for several cruises from the 1970s up until the 1990s. The ULS data consists of a collection of files where each file provides a “track”. This is a collection of ice draft measurements over a given track length, typically 50 km, although this length can vary. Track lengths from the “SCICEX” cruises, for instance, are typically of 12 km length. Averaged ULS ice draft is calculated for a track and is compared to the model mean ice draft estimate, where the model ice draft  $h_d$  is calculated as

$$h_d = \frac{\sum_{j=1}^N c_j (\rho_i h_j + \rho_{s,j} h_{s,j})}{\rho_w} \quad (16)$$

The ice draft from the model is based on weekly averages of ice and snow thickness, and snow density. The model fields are interpolated to the positions of the observed tracks, to create “simulated” cruise tracks. Three example cruises illustrating the difference between model and ULS draft measurements are shown in Figures 3.5a, 3.5d and 3.5g for the submarine cruises denoted “1986a”, “1991” and “1993” respectively. These figures illustrate that the model gives a favorable description of the sea ice draft. Cruises “1986a” and “1993” show the best correspondence between model and data. The short scale variability is not captured by the model, nor do we expect it to be due to low spatial and temporal resolution, but the large scale variations



in sea ice draft correspond well with the ULS data. On the other hand, data from the cruise “1991” shows a situation where the model does not capture the large scale variability that well. In this case there is a positive bias in the ice draft field when considering the thickness field along the entire track. Table 3.2 shows the RMS errors and the bias of the model when compared with all the available ULS data. From the table the ice thickness bias is positive for some cruises and negative for others, there is no strong overall bias in either direction. Some cruises stand out in the table, the cruise “1986b” has a draft underestimate which is consistent for the entire cruise track, giving a negative bias and a RMS error of nearly one meter. The cruise “scicex97” also has relatively high errors, due a positive bias for that cruise.

*Table 3.2: Difference between simulated tracks and the tracks provided by the NSIDC. The table show the Root-Mean-Square (RMS) difference and the average difference between tracks.*

Cruise	UK76	1986a	1986b	1987	UK87	1988a	1988b
RMS error	0.54	0.23	0.98	0.74	2.06	0.23	0.91
Bias	0.66	-0.03	-0.83	-0.63	0.21	0.09	-0.85
Cruise	1989b	1990	1991	UK91	1992a	1992b	L2-92
RMS Error	0.46	0.18	0.49	0.80	0.47	0.31	0.65
Bias	0.13	0.14	0.42	-0.36	-0.29	0.34	0.58
Cruise	grayling92	1993	scicex93	1994	scicex96	scicex97	scicex98
RMS Error	0.64	0.16	0.58	0.20	0.40	0.83	0.45
Bias	-0.52	0.21	0.60	0.24	0.30	0.70	0.17

The cruise “UK87” also stands out in Table 3.2, having a small bias, but a very large RMS error. It turns out that this RMS error stems from a very high track-to-track variability in the ice field for this cruise, this variability is not captured by the model, Figure 3.6a. The “UK87” cruise was carried out in the Fram Strait as was the “UK91” cruise, Figure 3.6b. The UK91 cruise shows much lower short-scale variability than the “UK87” Cruise, and the model does well in simulating the UK91 cruise. It should be noted that the track lengths of the ULS data are the same in both the “UK87” and “UK91” cruises, so the differences in track-to-track variability point to changes in the ice field which are not captured by the model. One reason for this could be low spatial resolution in the model and sub-grid scale processes.

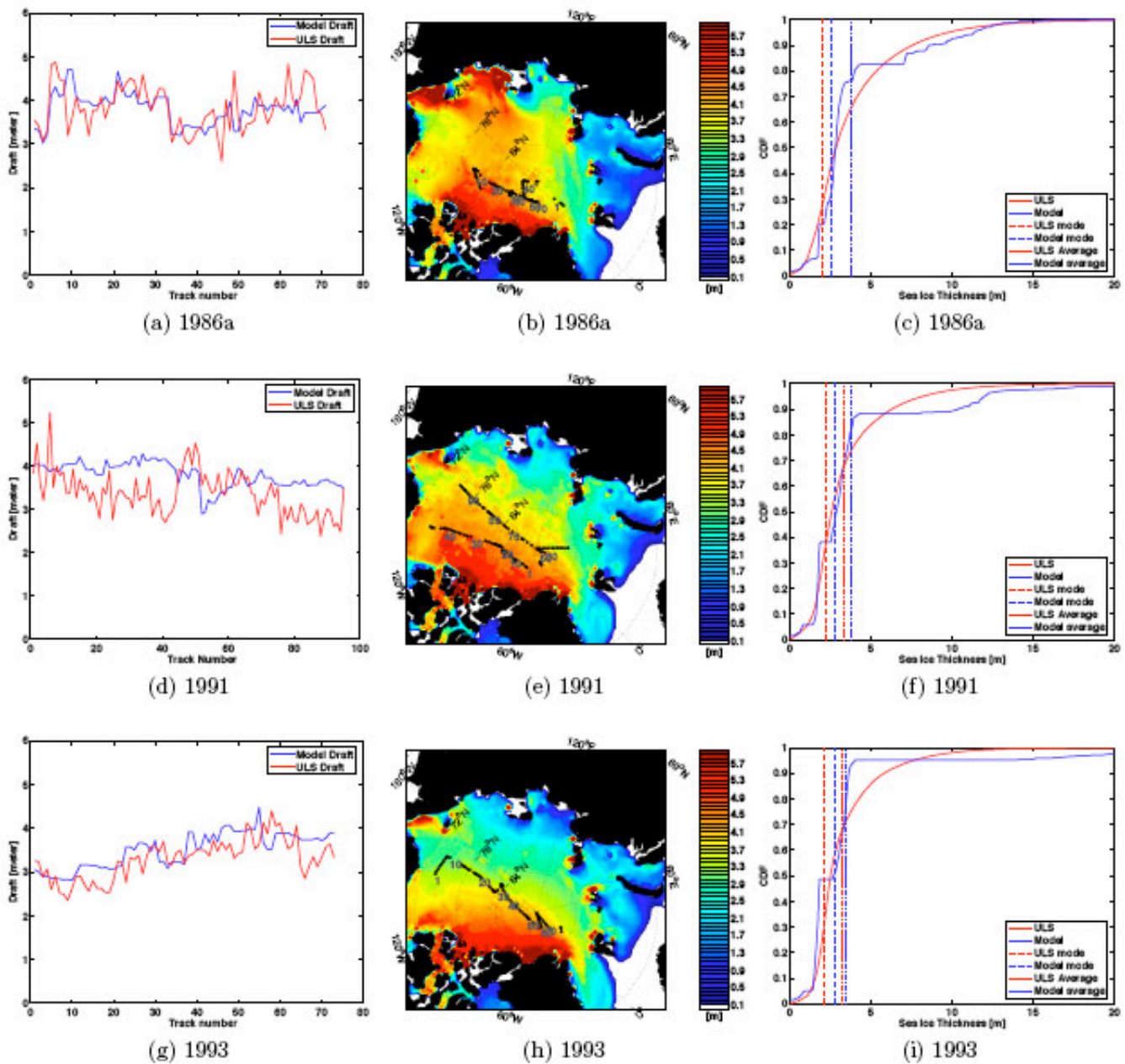


Figure 3.5: Left panel shows the ice draft from model (red) and data (blue) for three different tracks. Right panel shows spatial location where color indicates difference (model - data). From top to bottom the cruises are: “1986a”, “1991”, and “1993”.

To sum up all the different comparisons of ice draft a scatter plot for the ULS draft vs. model draft is shown in Figure 3.7 for all available cruises. The color indicator denotes the month of the measurement. Again, the model is able to reproduce the ULS ice thickness data for most of the cruises seen here. It should be noted, however, that the model has a tendency to produce too thick ice in the ULS 1-2m thickness range. This appears mainly due to summer cruises, most noticeably the “scicex97” cruise.

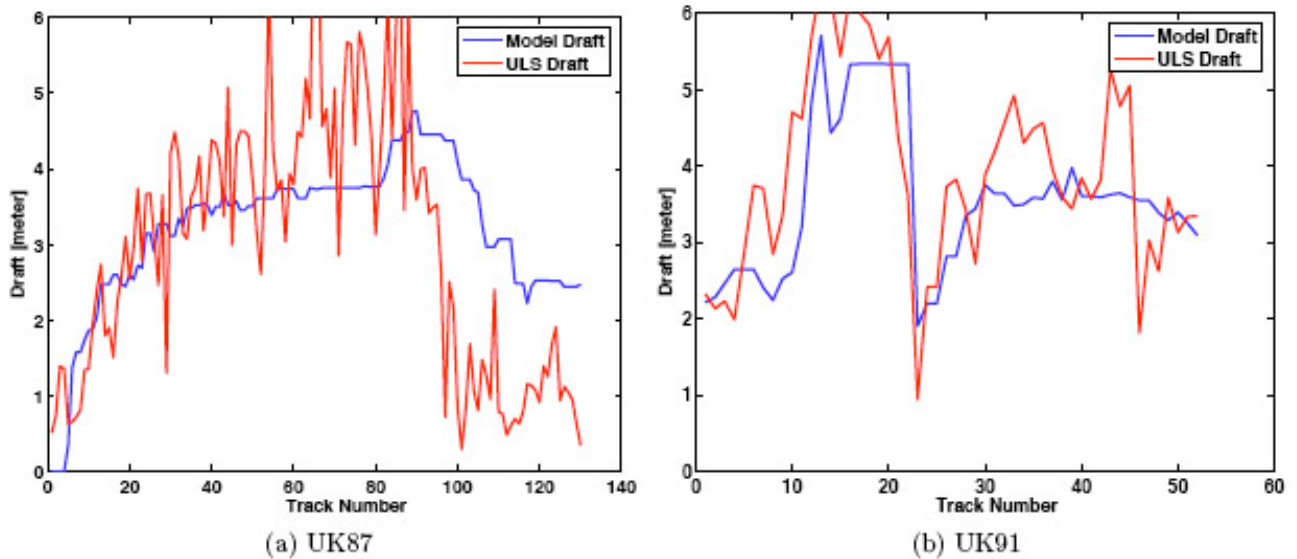


Figure 3.6: Ice draft from model (red) and data (blue) for two cruises carried out in the vicinity of the Fram Strait.

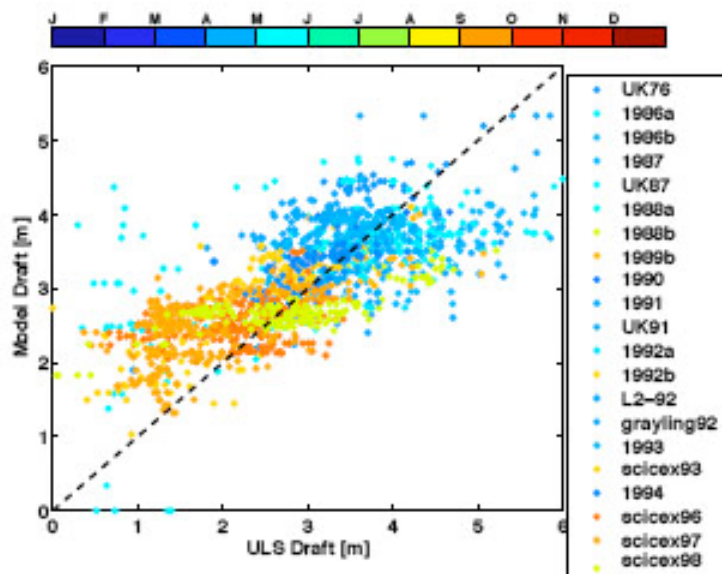


Figure 3.7: Scatter plot of ice draft from ULS measurements (horizontal axes) versus model estimated draft (vertical axes). Color code denotes month of measurements.

The ice draft distribution is readily obtained from the ULS data. To compare this with the model data, it is convenient to change this to a cumulative ice draft distribution function (CDF). The average cumulative draft distributions for the cruises “1986a”, “1991” and “1993” are shown in Figures 3.5c, 3.5f and 3.5i respectively. Although the model CDF is smoothed over several tracks (several grid cells), the staircase-like behavior which is expected for a single model CDF is still visible. This is most pronounced for the “1991” and “1993” cruises. Nonetheless, the model CDF corresponds quite well when compared to the ULS-derived CDF. From the comparison it can be seen that the model in some cases puts too much ice in the thick end of the CDF, this is best seen for tracks “1991” and “1993”. The amount of thick ice produced by the ridging process can be tuned to improve the results, but this has not been done yet.

### 3.3.2 SSM/I comparison

From passive microwave sensors carried onboard satellites, it is possible to estimate the sea-ice concentration, or the percentage of the ocean surface covered by sea-ice. Measurements are available from 1978 to present, but here we use the period 1979-2001 for comparison. In Fig. 3.8, we have illustrated the sea-ice concentration from the model (black line with "+" marks) and observations (grey line). This contour line denotes the 70 % concentration contour in the model. Fig. 3.8 illustrates how the sea-ice model tends to overestimate the sea-ice concentration in many regions in the Arctic. In winter, there is too much ice in the Greenland and Barents Sea, while in summer the sea-ice is overestimated in the Kara Sea, Laptev Sea and the Beaufort Sea. The reason for this underestimate may be connected to the lack of a lateral melt parameterization in the multicategory model. For multi-category sea-ice models, the effect of lateral melt is believed to be of smaller importance relative to single-category models, which is why it is not used here. The results do indicate, however, that using it in these simulations could be beneficial. Another effect which can impact the results is the short-wave radiative fluxes which are obtained from the ERA40 forcing fields. No separate validation has been performed on these fields.

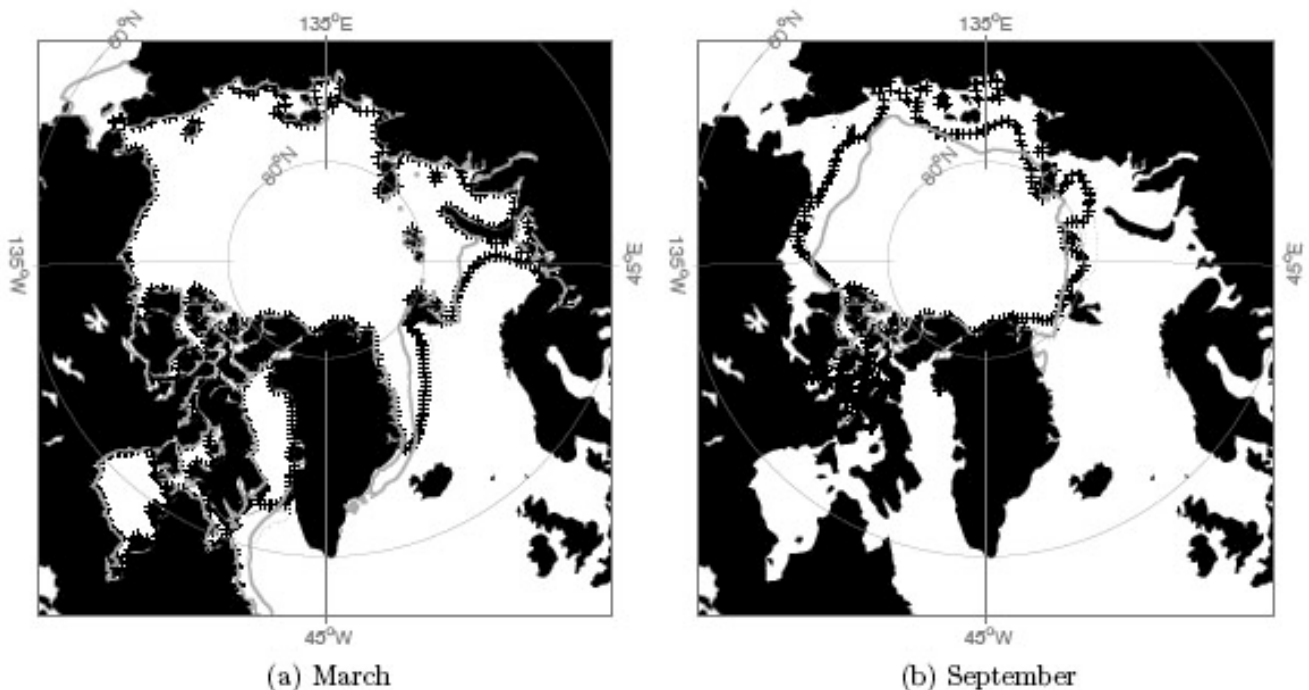


Figure 3.8: Comparison of satellite-derived sea-ice concentration 70% contour line (grey lines) and model (black with "+" marks). The comparisons for 1979-2001 are shown for March (left) and September (right).

### 3.4 Ice cover statistics

This section presents statistics and time series from the different regions shown in Figure 3.1a. For each region we produce time series of the following quantities:

- total ice volume
- total ice area
- area having ice thicker than 2 meters
- area having ice thicker than 4 meters
- area having ice thicker than 6 meters



In addition to this, we have split the time series into seasonal averages. For instance, the total ice area is presented as four different time series, one for the months January to March, one for the month of April to June, one for the month of July to September, and one for the months of October to December. An example of this type of plot is seen in Figure 3.9a. The same procedure is done for all the quantities in the list above. Statistical properties of these quantities are also summarized in tables, giving standard deviation, minimum, maximum and mean values of the quantities for the seasonal averages. Finally, we have produced a plot to illustrate in more detail how the composition of the ice cover changes from season to season, and from year to year. For each season a stacked bar chart is presented, which separates the ice cover into 1-meter bins. Each such bin (for instance; 3-4 meters) has a different color code, and the height of the bar-portion with this color illustrates how much of the ice is in the range 3-4 meters. Note that an "open water" category is also included in this plot. This property denotes the amount of open water in the region relative to the maximum total ice coverage over the time period 1958–2001. Figure 3.10a is an example of this type of plot for the Barents Sea, averaged over the region and the time January to March. In the last year of this time series (2001), the ice in the thickness range 1-2 meter covers approximately 0.1 million sq. km of the Barents Sea Region. The amount of open water, however, is relatively large, approximately 4 million sq. km.

### 3.4.1 Barents Sea region

Tables 3.3-3.6: Sea ice area and sea ice volume statistics for the Barents Sea region, including the area coverage of ice thicker than 2, 4 and 6 meters.

	Mean	Standard Deviation	Minimum	Maximum
Ice Area [ $10^6\text{km}^2$ ]	0.95	0.12	0.75	1.20
Ice Volume [ $10^3\text{km}^3$ ]	1.41	0.32	0.77	2.19
Area $h > 2$ [ $10^6\text{km}^2$ ]	0.11	0.04	0.03	0.20
Area $h > 4$ [ $10^6\text{km}^2$ ]	0.03	0.01	0.01	0.06
Area $h > 6$ [ $10^6\text{km}^2$ ]	0.03	0.01	0.01	0.06

Table 3.3: January – March

	Mean	Standard Deviation	Minimum	Maximum
Ice Area [ $10^6\text{km}^2$ ]	0.96	0.13	0.66	1.21
Ice Volume [ $10^3\text{km}^3$ ]	1.67	0.31	1.14	2.33
Area $h > 2$ [ $10^6\text{km}^2$ ]	0.13	0.05	0.05	0.25
Area $h > 4$ [ $10^6\text{km}^2$ ]	0.03	0.01	0.01	0.09
Area $h > 6$ [ $10^6\text{km}^2$ ]	0.03	0.01	0.01	0.06

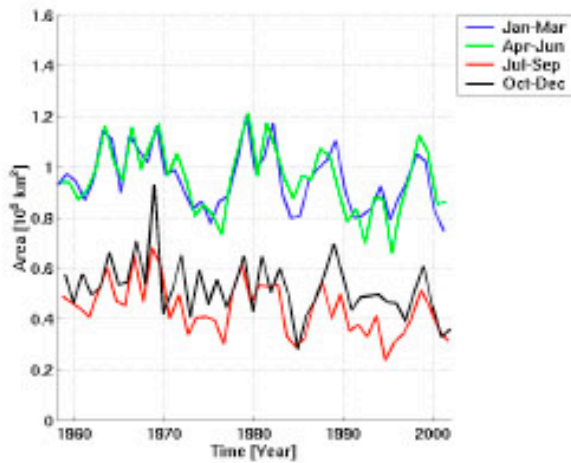
Table 3.4: April – June

	Mean	Standard Deviation	Minimum	Maximum
Ice Area [ $10^6\text{km}^2$ ]	0.44	0.10	0.24	0.68
Ice Volume [ $10^3\text{km}^3$ ]	1.00	0.28	0.54	1.88
Area $h > 2$ [ $10^6\text{km}^2$ ]	0.09	0.04	0.04	0.22
Area $h > 4$ [ $10^6\text{km}^2$ ]	0.03	0.01	0.01	0.06
Area $h > 6$ [ $10^6\text{km}^2$ ]	0.03	0.01	0.01	0.06

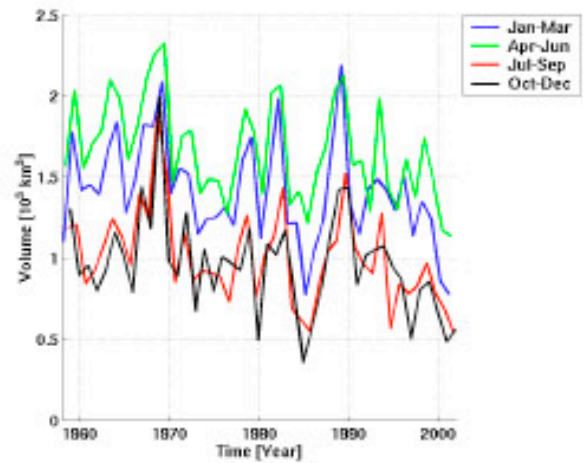
Table 3.5: July-September

	Mean	Standard Deviation	Minimum	Maximum
Ice Area [ $10^6\text{km}^2$ ]	0.52	0.11	0.28	0.93
Ice Volume [ $10^3\text{km}^3$ ]	0.96	0.30	0.36	2.00
Area $h > 2$ [ $10^6\text{km}^2$ ]	0.08	0.04	0.02	0.22
Area $h > 4$ [ $10^6\text{km}^2$ ]	0.03	0.01	0.01	0.06
Area $h > 6$ [ $10^6\text{km}^2$ ]	0.03	0.01	0.01	0.06

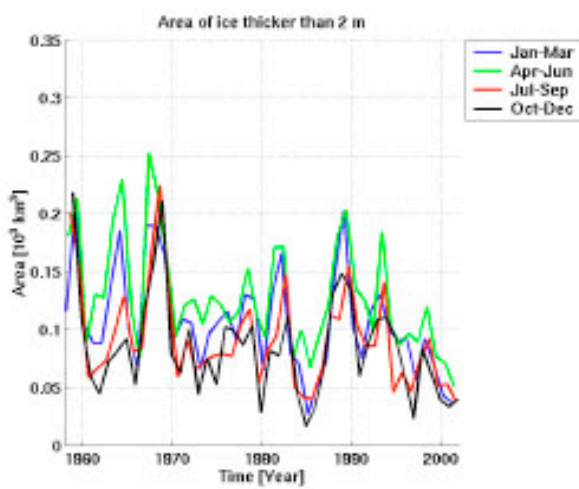
Table 3.6: October - December



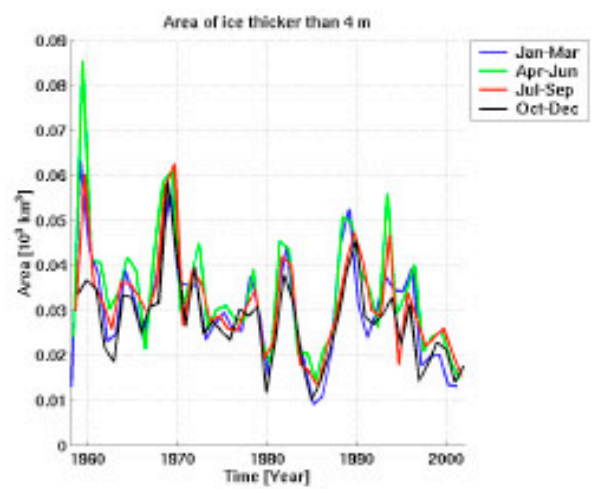
(a) Ice Area



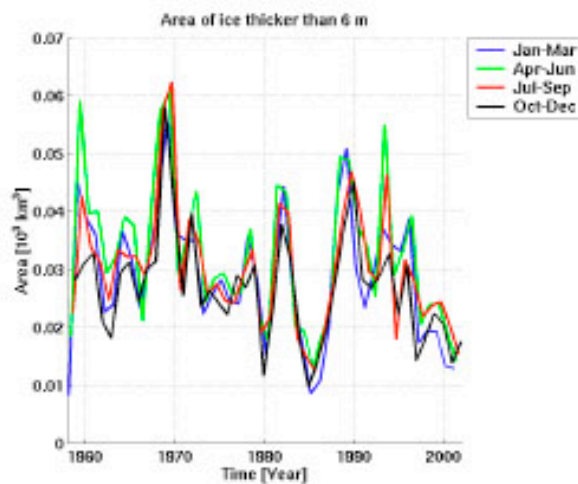
(b) Ice Volume



(c) Ice Area where  $h > 2$  meter



(d) Ice Area where  $h > 4$  meter



(e) Ice Area where  $h > 6$  meter

Figure 3.9: Ice Area and ice Volume for the Barents Sea region. Also shown are the areas covered by ice thicker than 2, 4 and 6 meters

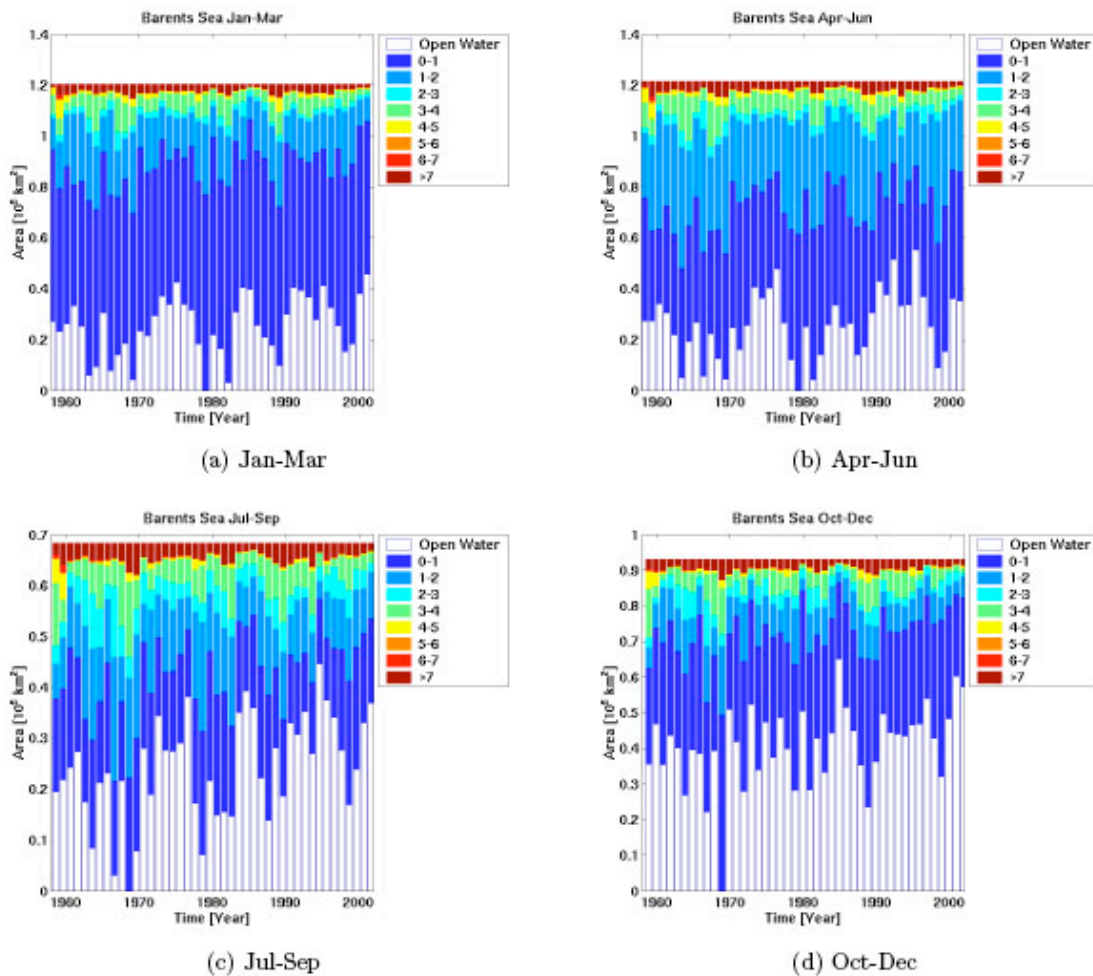


Figure 3.10: The area covered by ice in different sea-ice thickness ranges, for different seasons. Note that "Open Water" is relative to the maximum ice coverage in the time period 1958–2002.

### 3.4.2 Beaufort Sea region

Tables 3.7-3.10: Sea ice area and sea ice volume statistics for the Beaufort Sea region, including the area coverage of ice thicker than 2, 4 and 6 meters.

	Mean	Standard Deviation	Minimum	Maximum
Ice Area [ $10^6 \text{km}^2$ ]	0.67	0.00	0.66	0.67
Ice Volume [ $10^3 \text{km}^3$ ]	2.08	0.42	1.35	3.03
Area $h > 2$ [ $10^6 \text{km}^2$ ]	0.18	0.07	0.06	0.34
Area $h > 4$ [ $10^6 \text{km}^2$ ]	0.05	0.02	0.01	0.13
Area $h > 6$ [ $10^6 \text{km}^2$ ]	0.05	0.02	0.01	0.12

Table 3.7: January – March

	Mean	Standard Deviation	Minimum	Maximum
Ice Area [ $10^6 \text{km}^2$ ]	0.52	0.10	0.16	0.63
Ice Volume [ $10^3 \text{km}^3$ ]	1.71	0.54	0.27	2.90
Area $h > 2$ [ $10^6 \text{km}^2$ ]	0.14	0.06	0.01	0.31
Area $h > 4$ [ $10^6 \text{km}^2$ ]	0.06	0.03	0.01	0.13
Area $h > 6$ [ $10^6 \text{km}^2$ ]	0.06	0.02	0.01	0.12

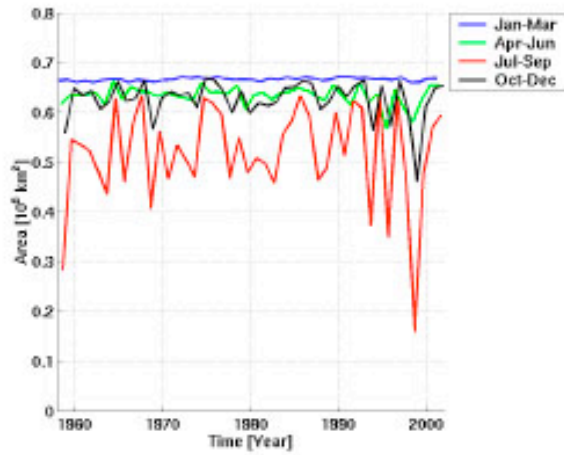
Table 3.9: July - September

	Mean	Standard Deviation	Minimum	Maximum
Ice Area [ $10^6 \text{km}^2$ ]	0.63	0.02	0.57	0.66
Ice Volume [ $10^3 \text{km}^3$ ]	2.18	0.44	1.12	3.27
Area $h > 2$ [ $10^6 \text{km}^2$ ]	0.21	0.08	0.05	0.46
Area $h > 4$ [ $10^6 \text{km}^2$ ]	0.06	0.02	0.02	0.12
Area $h > 6$ [ $10^6 \text{km}^2$ ]	0.05	0.02	0.01	0.12

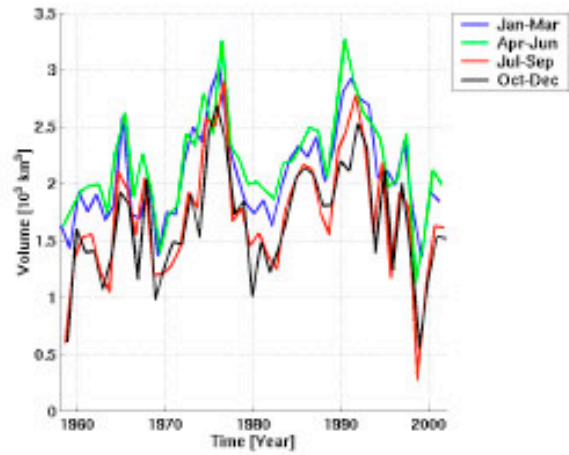
Table 3.8: April-June

	Mean	Standard Deviation	Minimum	Maximum
Ice Area [ $10^6 \text{km}^2$ ]	0.63	0.04	0.46	0.67
Ice Volume [ $10^3 \text{km}^3$ ]	1.65	0.49	0.56	2.68
Area $h > 2$ [ $10^6 \text{km}^2$ ]	0.12	0.05	0.02	0.23
Area $h > 4$ [ $10^6 \text{km}^2$ ]	0.05	0.02	0.01	0.13
Area $h > 6$ [ $10^6 \text{km}^2$ ]	0.05	0.02	0.01	0.13

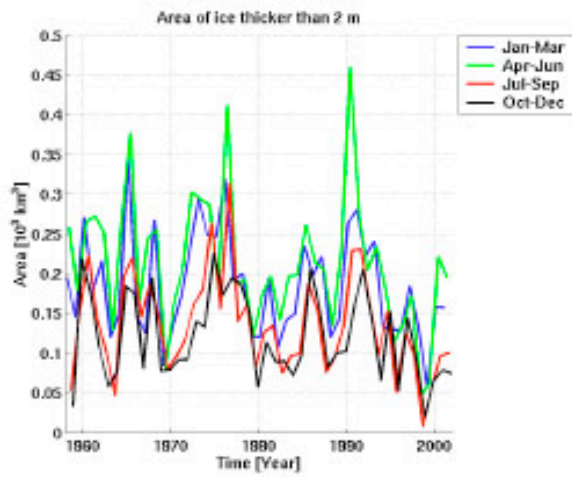
Table 3.10: October - December



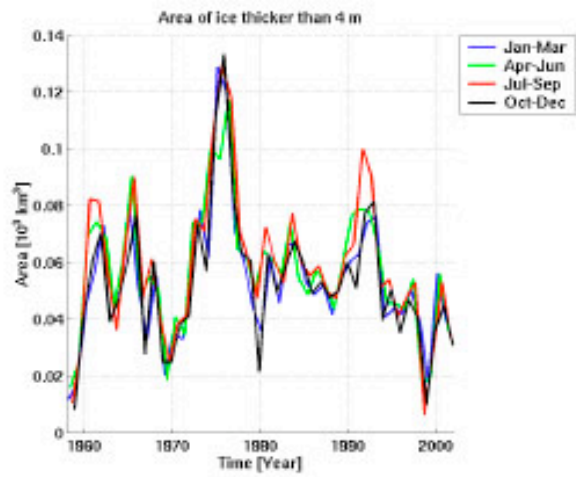
(a) Ice Area



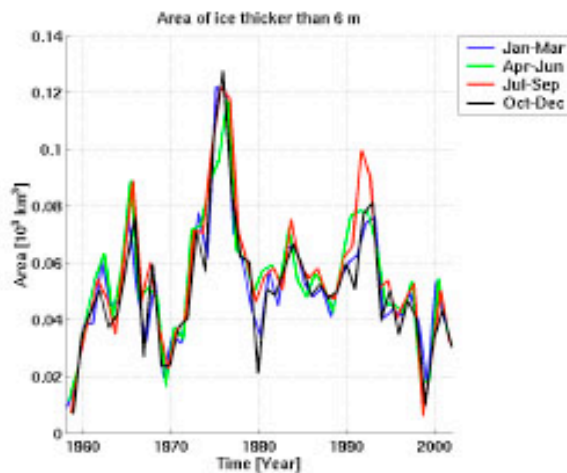
(b) Ice Volume



(c) Ice Area where  $h > 2$  meter



(d) Ice Area where  $h > 4$  meter



(e) Ice Area where  $h > 6$  meter

Figure 3.11: Ice Area and ice Volume for the Beaufort Sea region. Also shown are the areas covered by ice thicker than 2, 4 and 6 meters



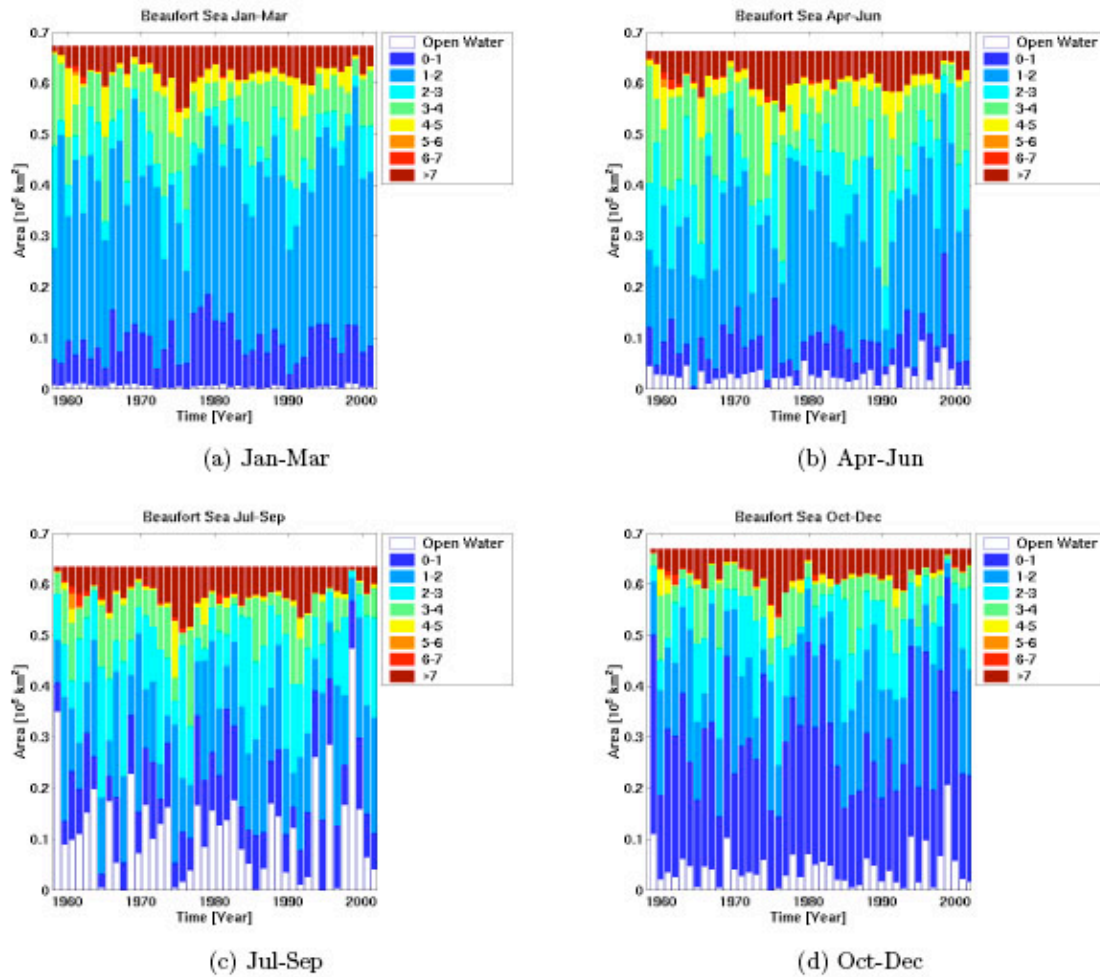


Figure 3.12: The area covered by ice in different sea-ice thickness ranges, for different seasons. Note that "Open Water" is relative to the maximum ice coverage in the time period 1958–2002.

### 3.4.3 Chukchi Sea region

Tables 3.11-3.14: Sea ice area and sea ice volume statistics for the Chukchi Sea region, including the area coverage of ice thicker than 2, 4 and 6 meters.

	Mean	Standard Deviation	Minimum	Maximum
Ice Area [ $10^6 \text{km}^2$ ]	0.52	0.00	0.51	0.53
Ice Volume [ $10^3 \text{km}^3$ ]	1.70	0.34	1.03	2.58
Area $h > 2$ [ $10^6 \text{km}^2$ ]	0.18	0.05	0.07	0.33
Area $h > 4$ [ $10^6 \text{km}^2$ ]	0.06	0.03	0.01	0.12
Area $h > 6$ [ $10^6 \text{km}^2$ ]	0.05	0.03	0.01	0.11

Table 3.11: January – March

	Mean	Standard Deviation	Minimum	Maximum
Ice Area [ $10^6 \text{km}^2$ ]	0.51	0.01	0.49	0.52
Ice Volume [ $10^3 \text{km}^3$ ]	1.89	0.34	1.24	2.68
Area $h > 2$ [ $10^6 \text{km}^2$ ]	0.21	0.06	0.11	0.32
Area $h > 4$ [ $10^6 \text{km}^2$ ]	0.06	0.03	0.02	0.13
Area $h > 6$ [ $10^6 \text{km}^2$ ]	0.06	0.03	0.01	0.13

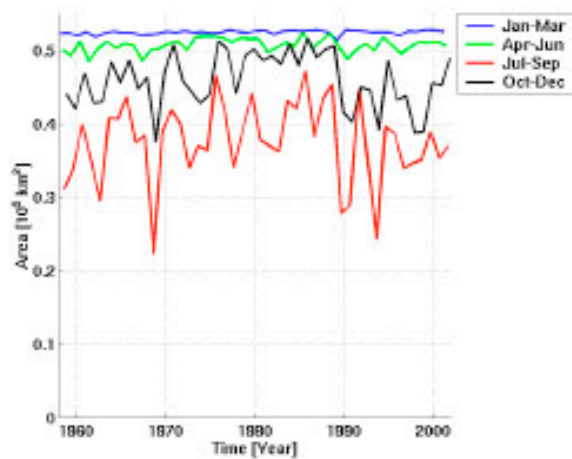
Table 3.12: April-June

	Mean	Standard Deviation	Minimum	Maximum
Ice Area [ $10^6 \text{km}^2$ ]	0.38	0.06	0.22	0.47
Ice Volume [ $10^3 \text{km}^3$ ]	1.29	0.35	0.63	1.88
Area $h > 2$ [ $10^6 \text{km}^2$ ]	0.11	0.04	0.04	0.21
Area $h > 4$ [ $10^6 \text{km}^2$ ]	0.06	0.03	0.01	0.13
Area $h > 6$ [ $10^6 \text{km}^2$ ]	0.05	0.02	0.01	0.10

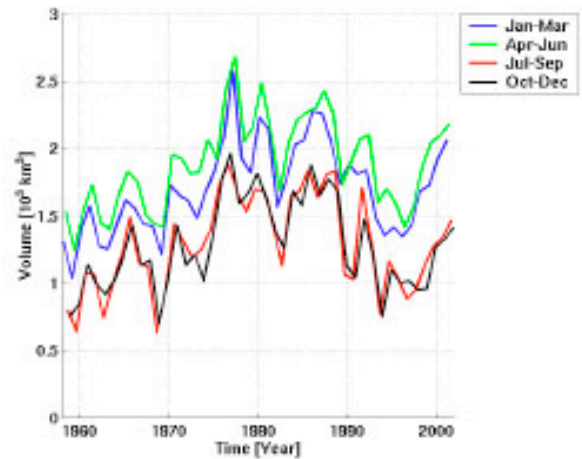
Table 3.13: July - September

	Mean	Standard Deviation	Minimum	Maximum
Ice Area [ $10^6 \text{km}^2$ ]	0.46	0.04	0.38	0.52
Ice Volume [ $10^3 \text{km}^3$ ]	1.28	0.33	0.70	1.96
Area $h > 2$ [ $10^6 \text{km}^2$ ]	0.11	0.05	0.03	0.23
Area $h > 4$ [ $10^6 \text{km}^2$ ]	0.05	0.02	0.01	0.13
Area $h > 6$ [ $10^6 \text{km}^2$ ]	0.05	0.02	0.01	0.10

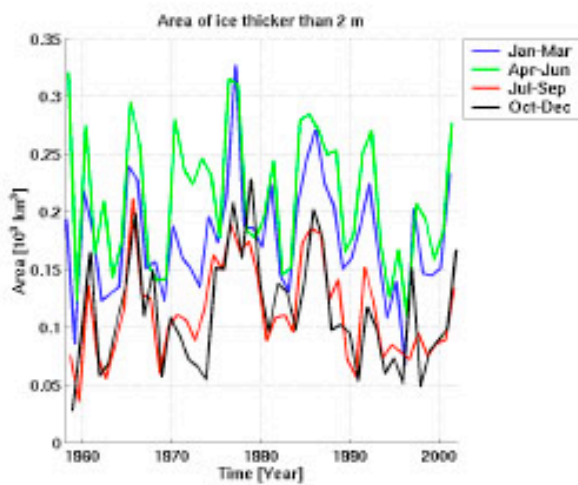
Table 3.14: October - December



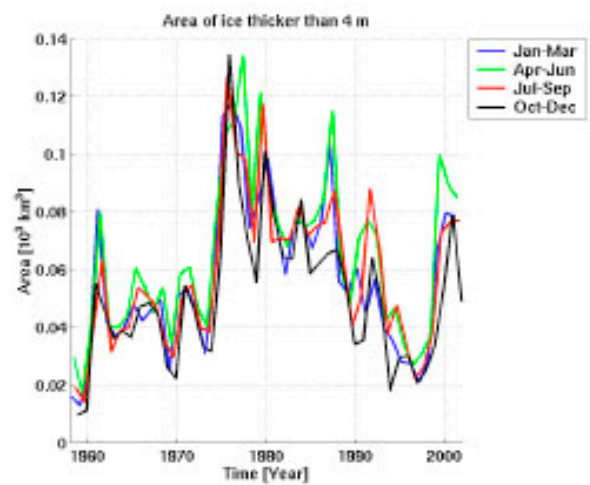
(a) Ice Area



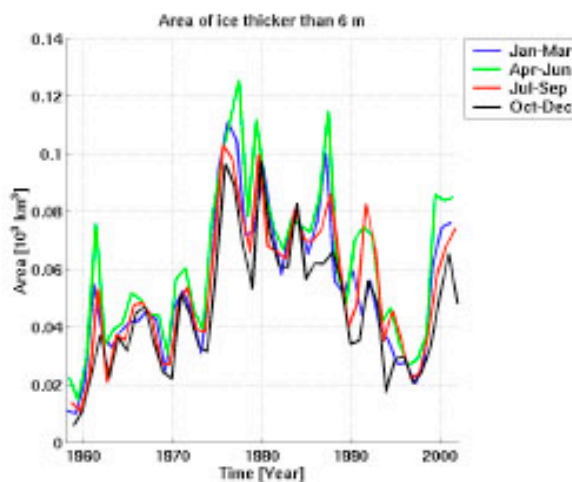
(b) Ice Volume



(c) Ice Area where  $h > 2$  meter



(d) Ice Area where  $h > 4$  meter



(e) Ice Area where  $h > 6$  meter

Figure 3.13: Ice Area and ice Volume for the Chukchi Sea region. Also shown are the areas covered by ice thicker than 2, 4 and 6 meters

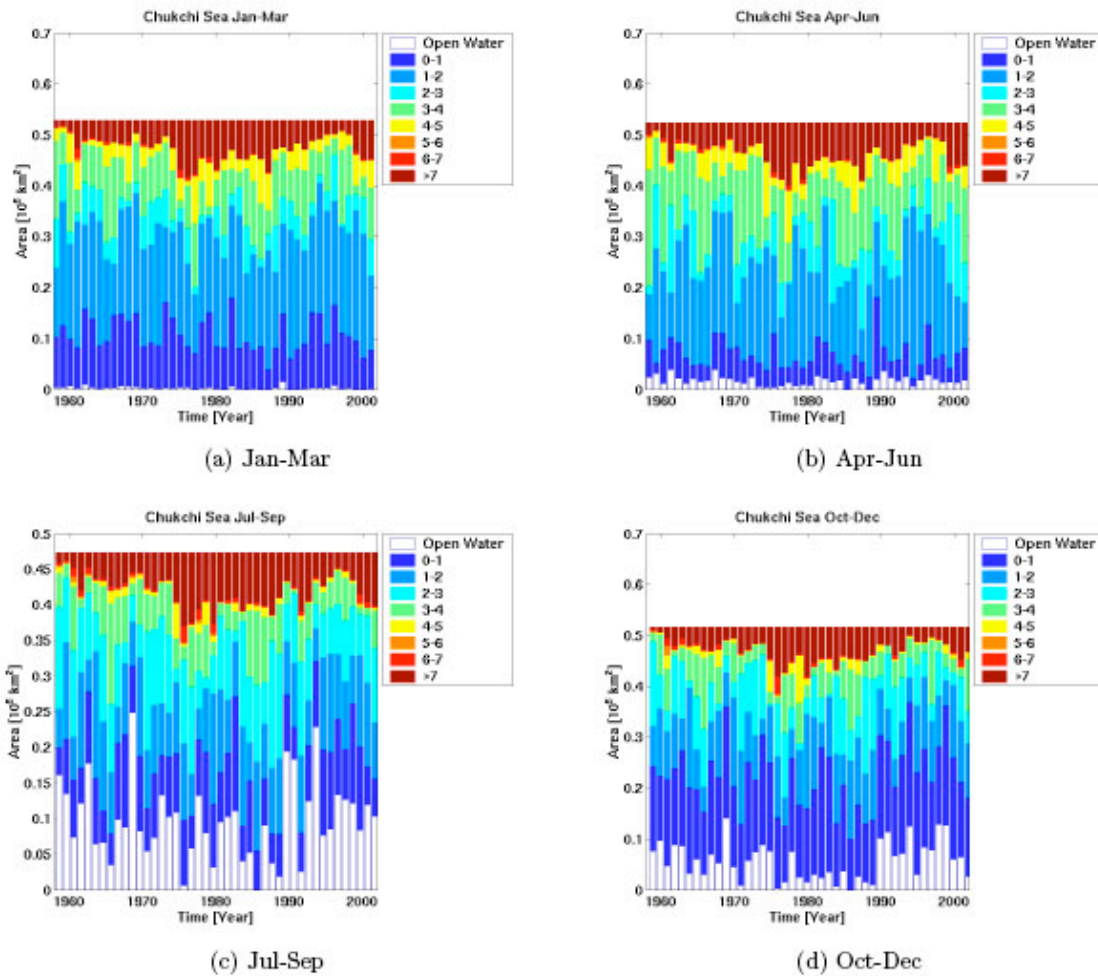


Figure 3.14: The area covered by ice in different sea-ice thickness ranges, for different seasons. Note that "Open Water" is relative to the maximum ice coverage in the time period 1958–2002.

### 3.4.4 East Siberian Sea region

Tables 3.15-3.18: Sea ice area and sea ice volume statistics for the East Siberian Sea region, including the area coverage of ice thicker than 2, 4 and 6 meters.

	Mean	Standard Deviation	Minimum	Maximum
Ice Area [ $10^6 \text{km}^2$ ]	0.66	0.00	0.66	0.66
Ice Volume [ $10^3 \text{km}^3$ ]	2.35	0.53	1.44	3.49
Area $h > 2$ [ $10^6 \text{km}^2$ ]	0.23	0.09	0.07	0.49
Area $h > 4$ [ $10^6 \text{km}^2$ ]	0.08	0.03	0.02	0.16
Area $h > 6$ [ $10^6 \text{km}^2$ ]	0.07	0.03	0.01	0.16

Table 3.15: January – March

	Mean	Standard Deviation	Minimum	Maximum
Ice Area [ $10^6 \text{km}^2$ ]	0.64	0.02	0.53	0.66
Ice Volume [ $10^3 \text{km}^3$ ]	2.46	0.54	1.35	3.74
Area $h > 2$ [ $10^6 \text{km}^2$ ]	0.25	0.09	0.04	0.45
Area $h > 4$ [ $10^6 \text{km}^2$ ]	0.08	0.04	0.02	0.19
Area $h > 6$ [ $10^6 \text{km}^2$ ]	0.08	0.03	0.02	0.19

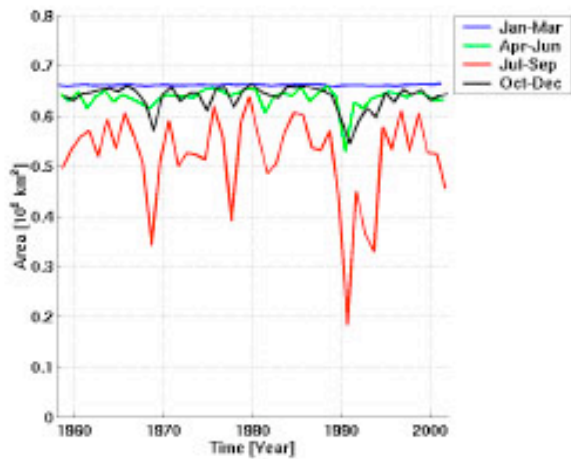
Table 3.16: April-June

	Mean	Standard Deviation	Minimum	Maximum
Ice Area [ $10^6 \text{km}^2$ ]	0.52	0.09	0.18	0.64
Ice Volume [ $10^3 \text{km}^3$ ]	1.97	0.60	0.61	3.22
Area $h > 2$ [ $10^6 \text{km}^2$ ]	0.18	0.08	0.02	0.33
Area $h > 4$ [ $10^6 \text{km}^2$ ]	0.08	0.04	0.01	0.19
Area $h > 6$ [ $10^6 \text{km}^2$ ]	0.08	0.04	0.01	0.19

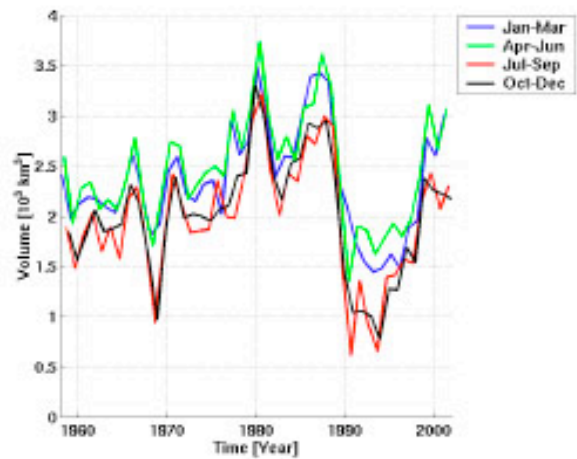
Table 3.17: July - September

	Mean	Standard Deviation	Minimum	Maximum
Ice Area [ $10^6 \text{km}^2$ ]	0.64	0.03	0.54	0.66
Ice Volume [ $10^3 \text{km}^3$ ]	2.01	0.58	0.77	3.31
Area $h > 2$ [ $10^6 \text{km}^2$ ]	0.17	0.08	0.01	0.38
Area $h > 4$ [ $10^6 \text{km}^2$ ]	0.08	0.04	0.01	0.16
Area $h > 6$ [ $10^6 \text{km}^2$ ]	0.07	0.04	0.01	0.16

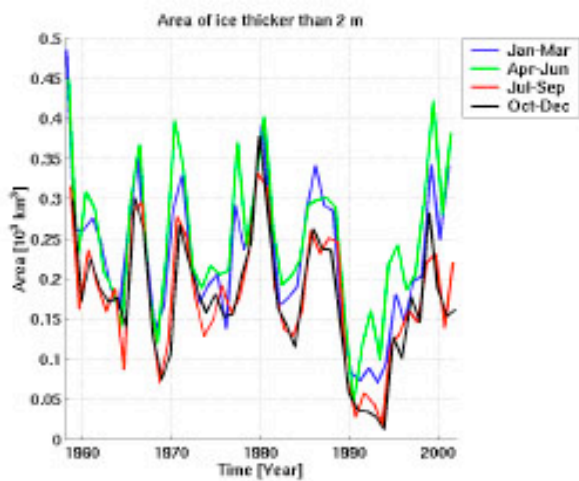
Table 3.18: October - December



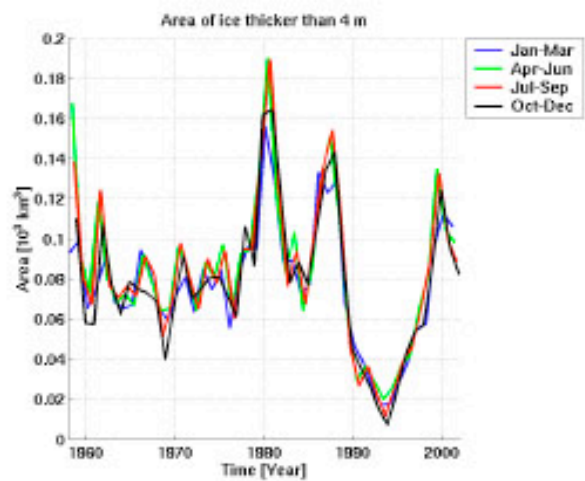
(a) Ice Area



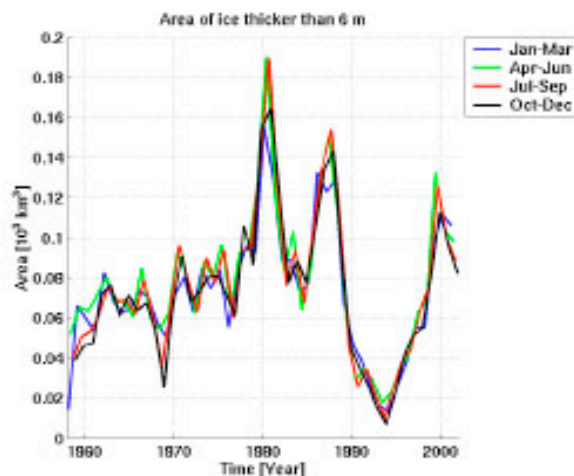
(b) Ice Volume



(c) Ice Area where  $h > 2$  meter



(d) Ice Area where  $h > 4$  meter



(e) Ice Area where  $h > 6$  meter

Figure 3.15: Ice Area and ice Volume for the East Siberian Sea region. Also shown are the areas covered by ice thicker than 2, 4 and 6 meters



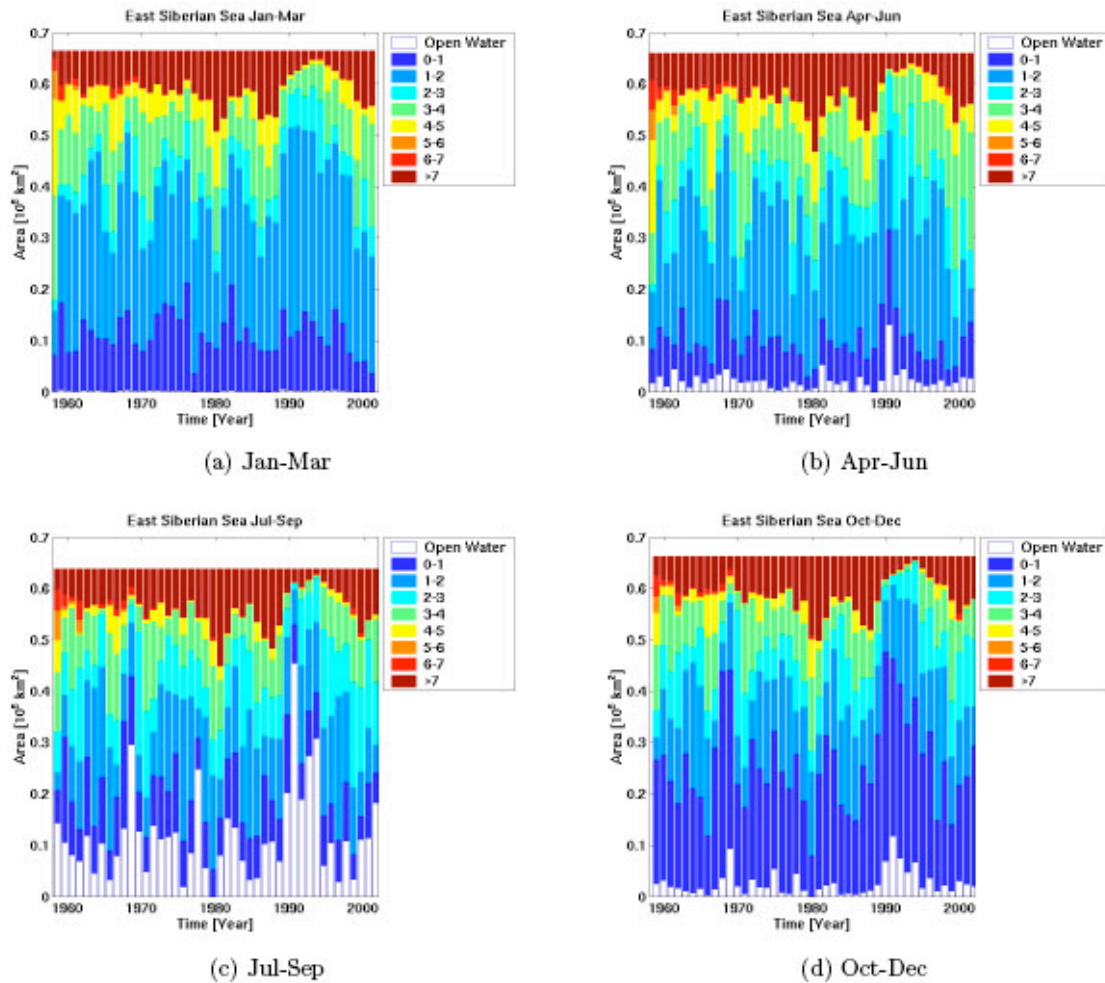


Figure 3.16: The area covered by ice in different sea-ice thickness ranges, for different seasons. Note that "Open Water" is relative to the maximum ice coverage in the time period 1958–2002.

### 3.4.5 Eastern Arctic region

Tables 3.19-3.22: Sea ice area and sea ice volume statistics for the Eastern Arctic region, including the area coverage of ice thicker than 2, 4 and 6 meters.

	Mean	Standard Deviation	Minimum	Maximum
Ice Area [ $10^6 \text{km}^2$ ]	1.33	0.00	1.33	1.34
Ice Volume [ $10^3 \text{km}^3$ ]	4.38	0.36	3.51	5.22
Area $h > 2$ [ $10^6 \text{km}^2$ ]	0.55	0.12	0.33	0.94
Area $h > 4$ [ $10^6 \text{km}^2$ ]	0.12	0.04	0.05	0.22
Area $h > 6$ [ $10^6 \text{km}^2$ ]	0.11	0.04	0.02	0.20

Table 3.19: January – March

	Mean	Standard Deviation	Minimum	Maximum
Ice Area [ $10^6 \text{km}^2$ ]	1.31	0.01	1.29	1.32
Ice Volume [ $10^3 \text{km}^3$ ]	4.67	0.33	4.03	5.42
Area $h > 2$ [ $10^6 \text{km}^2$ ]	0.60	0.12	0.33	0.94
Area $h > 4$ [ $10^6 \text{km}^2$ ]	0.13	0.05	0.06	0.34
Area $h > 6$ [ $10^6 \text{km}^2$ ]	0.12	0.03	0.03	0.20

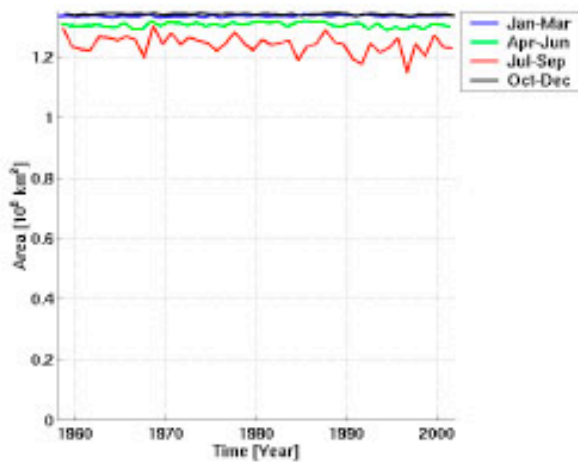
Table 3.20: April-June

	Mean	Standard Deviation	Minimum	Maximum
Ice Area [ $10^6 \text{km}^2$ ]	1.24	0.03	1.15	1.30
Ice Volume [ $10^3 \text{km}^3$ ]	4.22	0.41	3.28	5.28
Area $h > 2$ [ $10^6 \text{km}^2$ ]	0.50	0.13	0.20	0.97
Area $h > 4$ [ $10^6 \text{km}^2$ ]	0.14	0.05	0.06	0.32
Area $h > 6$ [ $10^6 \text{km}^2$ ]	0.12	0.04	0.03	0.25

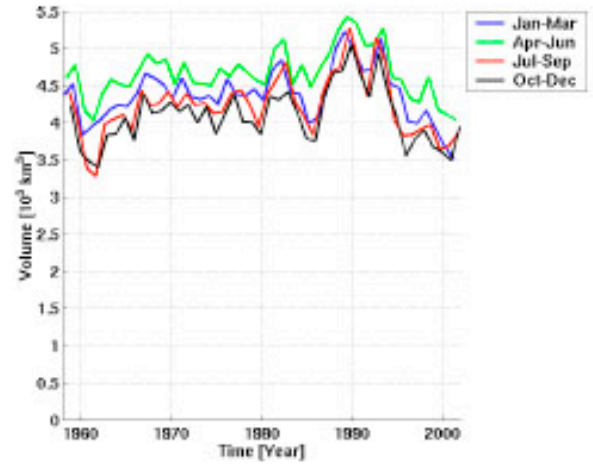
Table 3.21: July - September

	Mean	Standard Deviation	Minimum	Maximum
Ice Area [ $10^6 \text{km}^2$ ]	1.34	0.00	1.33	1.34
Ice Volume [ $10^3 \text{km}^3$ ]	4.09	0.38	3.39	5.04
Area $h > 2$ [ $10^6 \text{km}^2$ ]	0.47	0.13	0.22	0.85
Area $h > 4$ [ $10^6 \text{km}^2$ ]	0.13	0.04	0.06	0.24
Area $h > 6$ [ $10^6 \text{km}^2$ ]	0.11	0.04	0.04	0.23

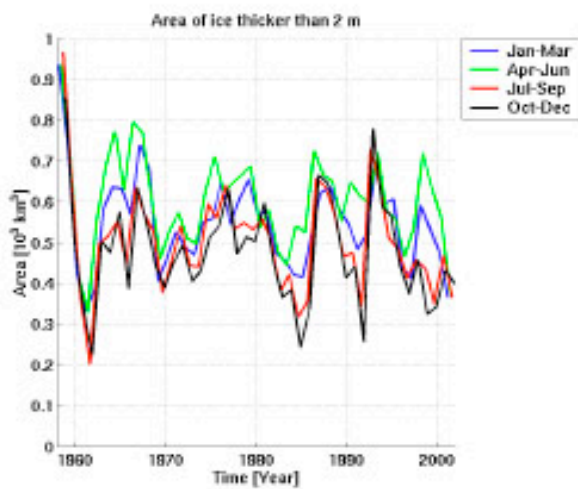
Table 3.22: October - December



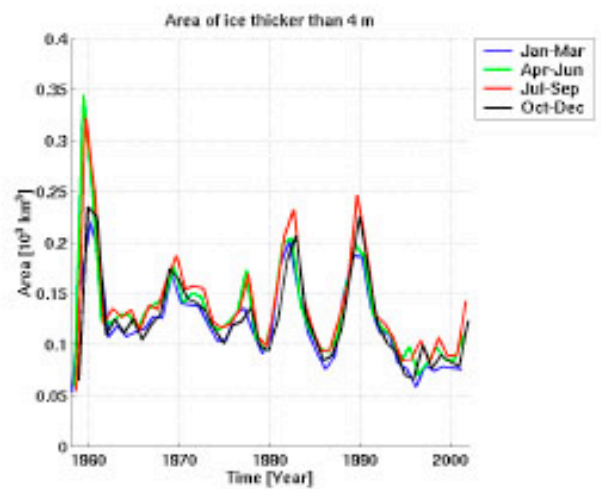
(a) Ice Area



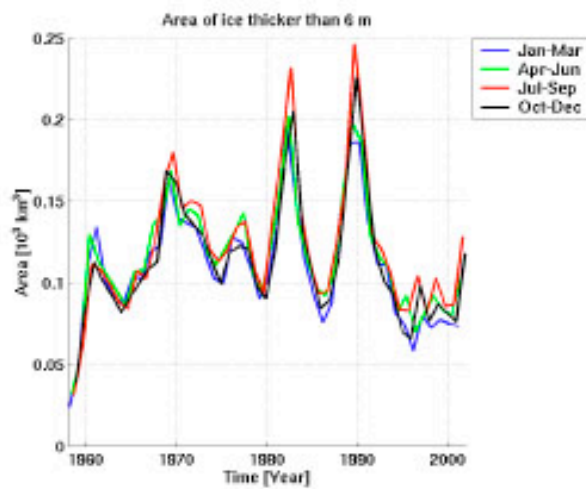
(b) Ice Volume



(c) Ice Area where  $h > 2$  meter



(d) Ice Area where  $h > 4$  meter



(e) Ice Area where  $h > 6$  meter

Figure 3.17: Ice Area and ice Volume for the Eastern Arctic region. Also shown are the areas covered by ice thicker than 2, 4 and 6 meters

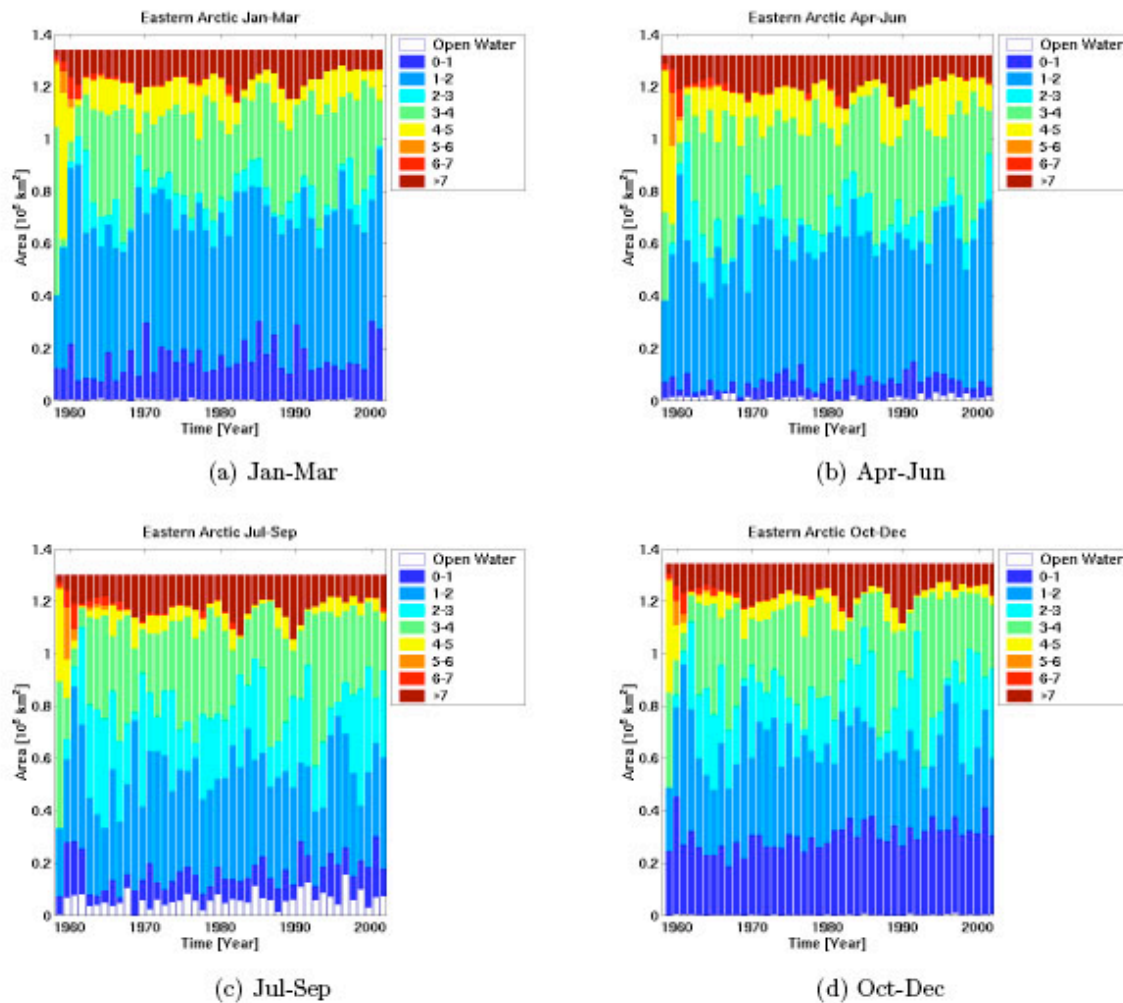


Figure 3.18: The area covered by ice in different sea-ice thickness ranges, for different seasons. Note that "Open Water" is relative to the maximum ice coverage in the time period 1958–2002.

### 3.4.6 Fram Strait region

Tables 3.23-3.26: Sea ice area and sea ice volume statistics for the Fram Strait region, including the area coverage of ice thicker than 2, 4 and 6 meters.

	Mean	Standard Deviation	Minimum	Maximum
Ice Area [ $10^6 \text{km}^2$ ]	0.51	0.05	0.41	0.64
Ice Volume [ $10^3 \text{km}^3$ ]	1.17	0.19	0.64	1.52
Area $h > 2$ [ $10^6 \text{km}^2$ ]	0.13	0.03	0.07	0.20
Area $h > 4$ [ $10^6 \text{km}^2$ ]	0.04	0.01	0.01	0.06
Area $h > 6$ [ $10^6 \text{km}^2$ ]	0.03	0.01	0.00	0.06

Table 3.23: January – March

	Mean	Standard Deviation	Minimum	Maximum
Ice Area [ $10^6 \text{km}^2$ ]	0.47	0.05	0.34	0.59
Ice Volume [ $10^3 \text{km}^3$ ]	1.27	0.20	0.75	1.69
Area $h > 2$ [ $10^6 \text{km}^2$ ]	0.15	0.03	0.08	0.23
Area $h > 4$ [ $10^6 \text{km}^2$ ]	0.04	0.02	0.02	0.08
Area $h > 6$ [ $10^6 \text{km}^2$ ]	0.04	0.01	0.01	0.07

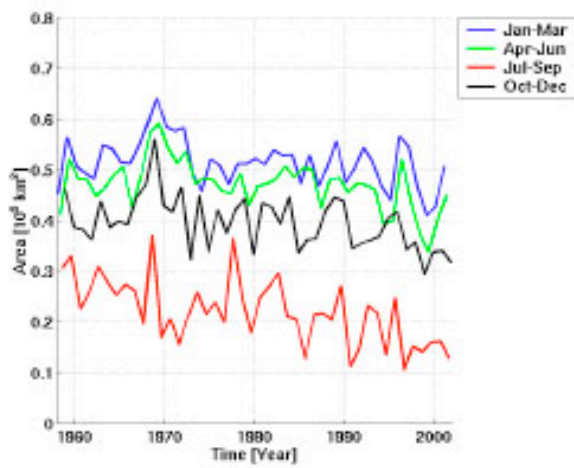
Table 3.24: April-June

	Mean	Standard Deviation	Minimum	Maximum
Ice Area [ $10^6 \text{km}^2$ ]	0.22	0.06	0.11	0.37
Ice Volume [ $10^3 \text{km}^3$ ]	0.73	0.22	0.34	1.27
Area $h > 2$ [ $10^6 \text{km}^2$ ]	0.08	0.04	0.03	0.20
Area $h > 4$ [ $10^6 \text{km}^2$ ]	0.04	0.02	0.01	0.08
Area $h > 6$ [ $10^6 \text{km}^2$ ]	0.03	0.01	0.01	0.06

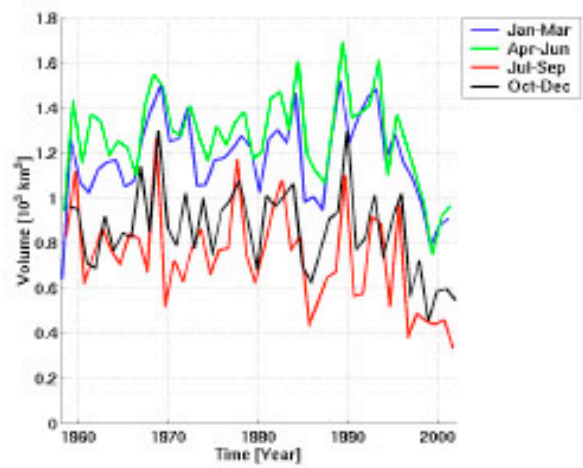
Table 3.25: July - September

	Mean	Standard Deviation	Minimum	Maximum
Ice Area [ $10^6 \text{km}^2$ ]	0.40	0.05	0.29	0.56
Ice Volume [ $10^3 \text{km}^3$ ]	0.86	0.19	0.45	1.30
Area $h > 2$ [ $10^6 \text{km}^2$ ]	0.09	0.04	0.03	0.17
Area $h > 4$ [ $10^6 \text{km}^2$ ]	0.03	0.01	0.02	0.07
Area $h > 6$ [ $10^6 \text{km}^2$ ]	0.03	0.01	0.01	0.07

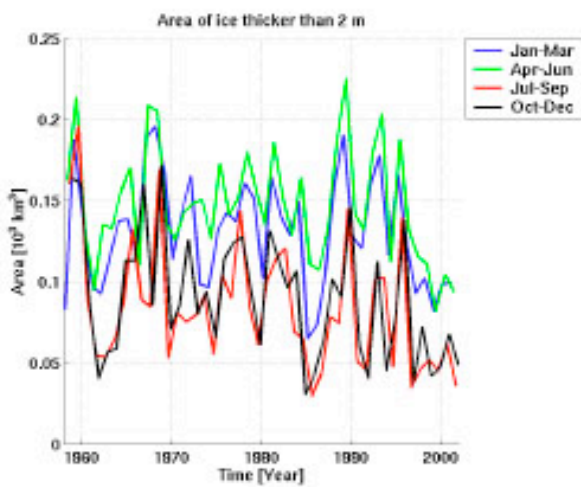
Table 3.26: October - December



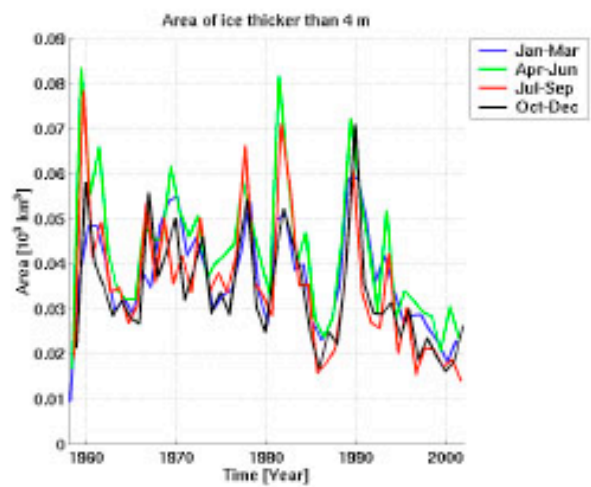
(a) Ice Area



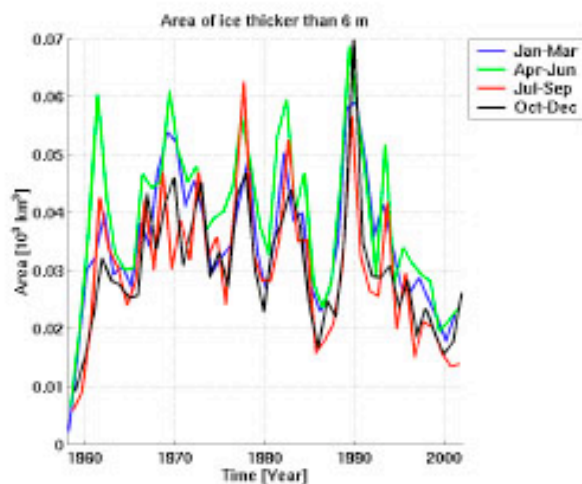
(b) Ice Volume



(c) Ice Area where  $h > 2$  meter



(d) Ice Area where  $h > 4$  meter



(e) Ice Area where  $h > 6$  meter

Figure 3.19: Ice Area and ice Volume for the Fram Strait region. Also shown are the areas covered by ice thicker than 2, 4 and 6 meters



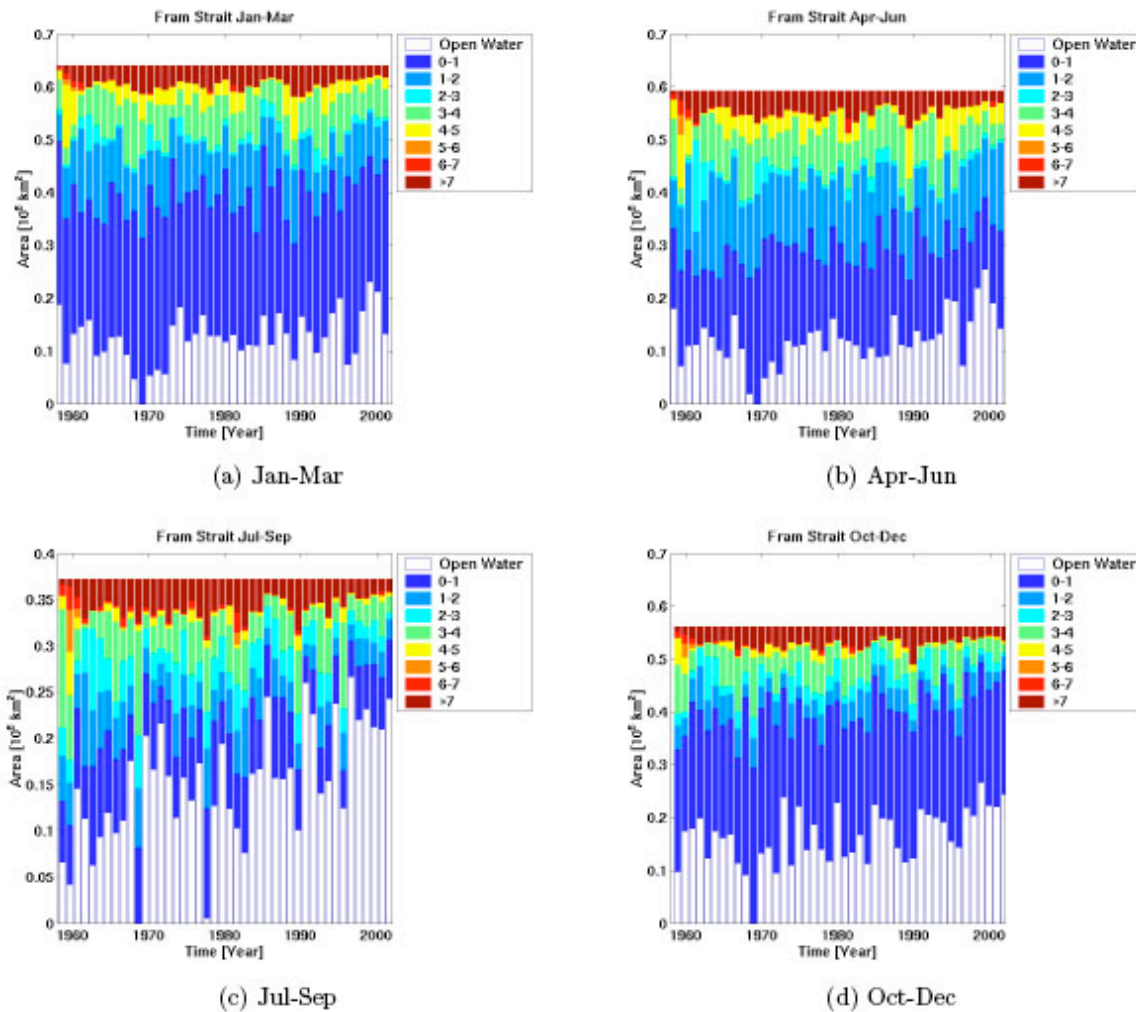


Figure 3.20: The area covered by ice in different sea-ice thickness ranges, for different seasons. Note that "Open Water" is relative to the maximum ice coverage in the time period 1958–2002.

### 3.4.7 Greenland Sea region

Tables 3.27-3.30: Sea ice area and sea ice volume statistics for the Greenland Sea region, including the area coverage of ice thicker than 2, 4 and 6 meters.

	Mean	Standard Deviation	Minimum	Maximum
Ice Area [ $10^6 \text{km}^2$ ]	0.15	0.05	0.03	0.24
Ice Volume [ $10^3 \text{km}^3$ ]	0.18	0.10	0.02	0.46
Area $h > 2$ [ $10^6 \text{km}^2$ ]	0.01	0.01	0.00	0.05
Area $h > 4$ [ $10^6 \text{km}^2$ ]	0.01	0.00	0.00	0.02
Area $h > 6$ [ $10^6 \text{km}^2$ ]	0.00	0.00	0.00	0.02

Table 3.27: January – March

	Mean	Standard Deviation	Minimum	Maximum
Ice Area [ $10^6 \text{km}^2$ ]	0.01	0.01	0.00	0.05
Ice Volume [ $10^3 \text{km}^3$ ]	0.03	0.03	0.00	0.19
Area $h > 2$ [ $10^6 \text{km}^2$ ]	0.00	0.00	0.00	0.02
Area $h > 4$ [ $10^6 \text{km}^2$ ]	0.00	0.00	0.00	0.01
Area $h > 6$ [ $10^6 \text{km}^2$ ]	0.00	0.00	0.00	0.01

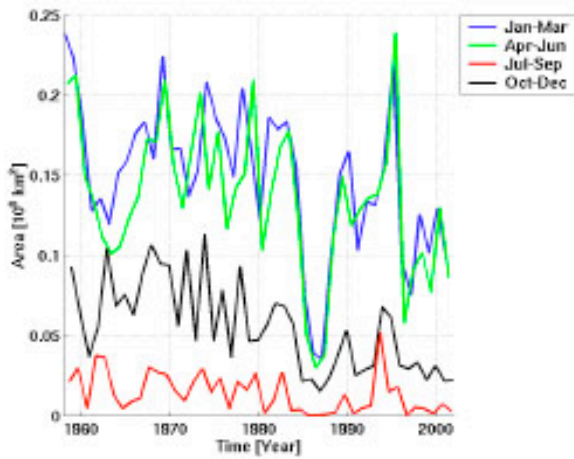
Table 3.29: July - September

	Mean	Standard Deviation	Minimum	Maximum
Ice Area [ $10^6 \text{km}^2$ ]	0.14	0.05	0.03	0.24
Ice Volume [ $10^3 \text{km}^3$ ]	0.22	0.11	0.03	0.58
Area $h > 2$ [ $10^6 \text{km}^2$ ]	0.02	0.02	0.00	0.07
Area $h > 4$ [ $10^6 \text{km}^2$ ]	0.01	0.00	0.00	0.01
Area $h > 6$ [ $10^6 \text{km}^2$ ]	0.01	0.00	0.00	0.01

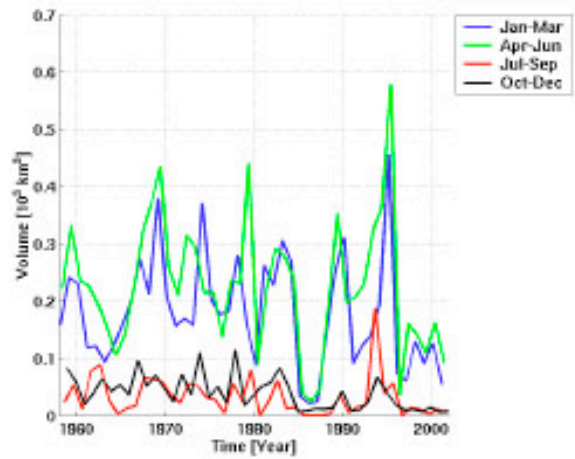
Table 3.28: April-June

	Mean	Standard Deviation	Minimum	Maximum
Ice Area [ $10^6 \text{km}^2$ ]	0.06	0.03	0.02	0.11
Ice Volume [ $10^3 \text{km}^3$ ]	0.04	0.03	0.01	0.11
Area $h > 2$ [ $10^6 \text{km}^2$ ]	0.00	0.00	0.00	0.01
Area $h > 4$ [ $10^6 \text{km}^2$ ]	0.00	0.00	0.00	0.01
Area $h > 6$ [ $10^6 \text{km}^2$ ]	0.00	0.00	0.00	0.01

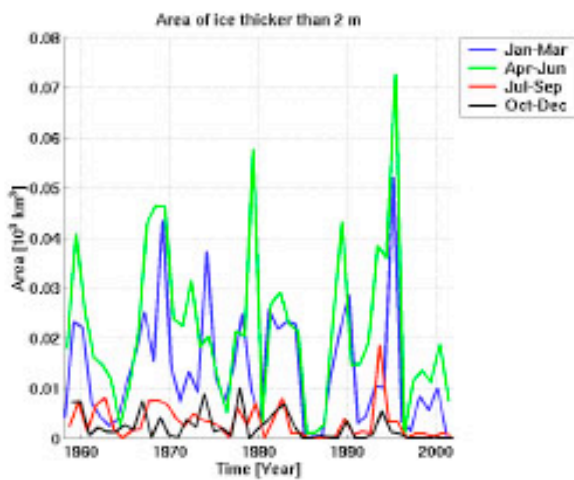
Table 3.30: October - December



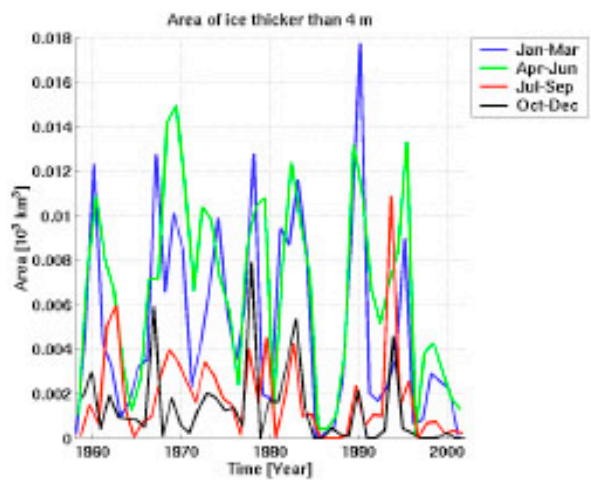
(a) Ice Area



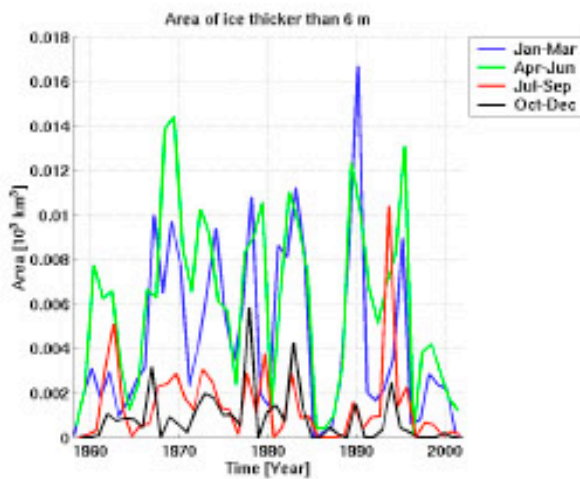
(b) Ice Volume



(c) Ice Area where  $h > 2$  meter



(d) Ice Area where  $h > 4$  meter



(e) Ice Area where  $h > 6$  meter

Figure 3.21: Ice Area and ice Volume for the Greenland Sea region. Also shown are the areas covered by ice thicker than 2, 4 and 6 meters

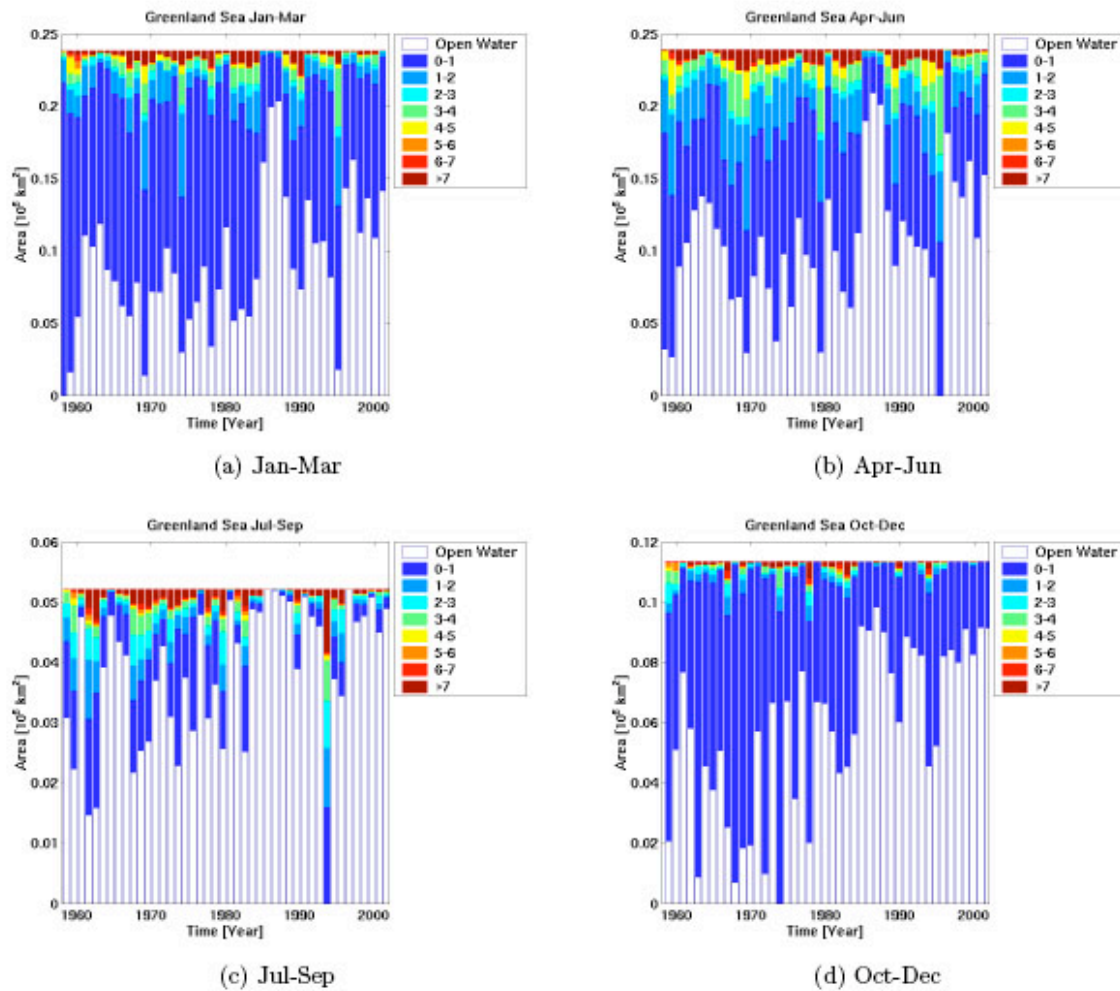


Figure 3.22: The area covered by ice in different sea-ice thickness ranges, for different seasons. Note that "Open Water" is relative to the maximum ice coverage in the time period 1958–2002.

### 3.4.8 Kara Sea region

Tables 3.31-3.34: Sea ice area and sea ice volume statistics for the Kara Sea region, including the area coverage of ice thicker than 2, 4 and 6 meters.

	Mean	Standard Deviation	Minimum	Maximum
Ice Area [ $10^6 \text{km}^2$ ]	0.80	0.00	0.79	0.81
Ice Volume [ $10^3 \text{km}^3$ ]	1.42	0.24	0.98	1.86
Area $h > 2$ [ $10^6 \text{km}^2$ ]	0.10	0.05	0.03	0.26
Area $h > 4$ [ $10^6 \text{km}^2$ ]	0.03	0.02	0.01	0.09
Area $h > 6$ [ $10^6 \text{km}^2$ ]	0.03	0.01	0.01	0.05

Table 3.31: January – March

	Mean	Standard Deviation	Minimum	Maximum
Ice Area [ $10^6 \text{km}^2$ ]	0.77	0.02	0.72	0.79
Ice Volume [ $10^3 \text{km}^3$ ]	1.61	0.24	1.21	2.09
Area $h > 2$ [ $10^6 \text{km}^2$ ]	0.13	0.05	0.06	0.25
Area $h > 4$ [ $10^6 \text{km}^2$ ]	0.04	0.02	0.02	0.09
Area $h > 6$ [ $10^6 \text{km}^2$ ]	0.03	0.01	0.01	0.06

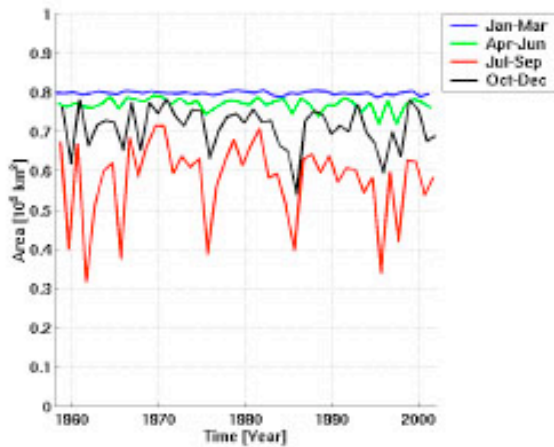
Table 3.32: April-June

	Mean	Standard Deviation	Minimum	Maximum
Ice Area [ $10^6 \text{km}^2$ ]	0.58	0.10	0.32	0.71
Ice Volume [ $10^3 \text{km}^3$ ]	1.27	0.34	0.55	1.96
Area $h > 2$ [ $10^6 \text{km}^2$ ]	0.11	0.05	0.04	0.25
Area $h > 4$ [ $10^6 \text{km}^2$ ]	0.04	0.02	0.02	0.10
Area $h > 6$ [ $10^6 \text{km}^2$ ]	0.04	0.01	0.01	0.06

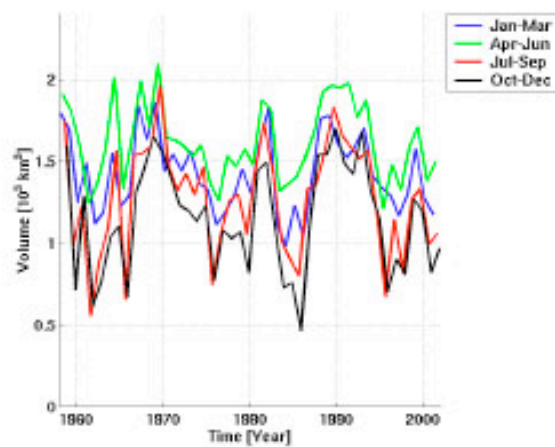
Table 3.33: July - September

	Mean	Standard Deviation	Minimum	Maximum
Ice Area [ $10^6 \text{km}^2$ ]	0.71	0.05	0.54	0.78
Ice Volume [ $10^3 \text{km}^3$ ]	1.14	0.33	0.46	1.70
Area $h > 2$ [ $10^6 \text{km}^2$ ]	0.09	0.04	0.02	0.21
Area $h > 4$ [ $10^6 \text{km}^2$ ]	0.03	0.02	0.01	0.10
Area $h > 6$ [ $10^6 \text{km}^2$ ]	0.03	0.01	0.01	0.06

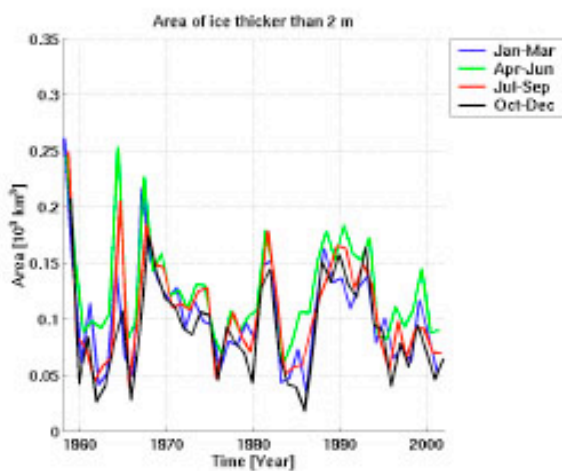
Table 3.34: October - December



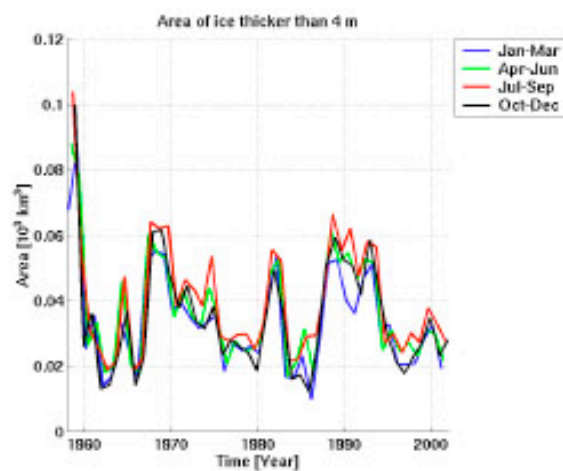
(a) Ice Area



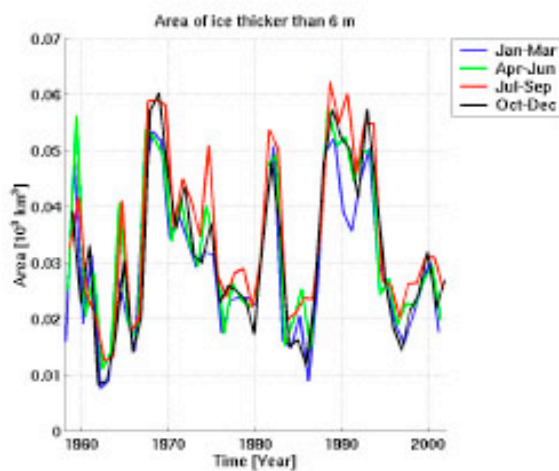
(b) Ice Volume



(c) Ice Area where  $h > 2$  meter



(d) Ice Area where  $h > 4$  meter



(e) Ice Area where  $h > 6$  meter

Figure 3.23: Ice Area and ice Volume for the Kara Sea region. Also shown are the areas covered by ice thicker than 2, 4 and 6 meters



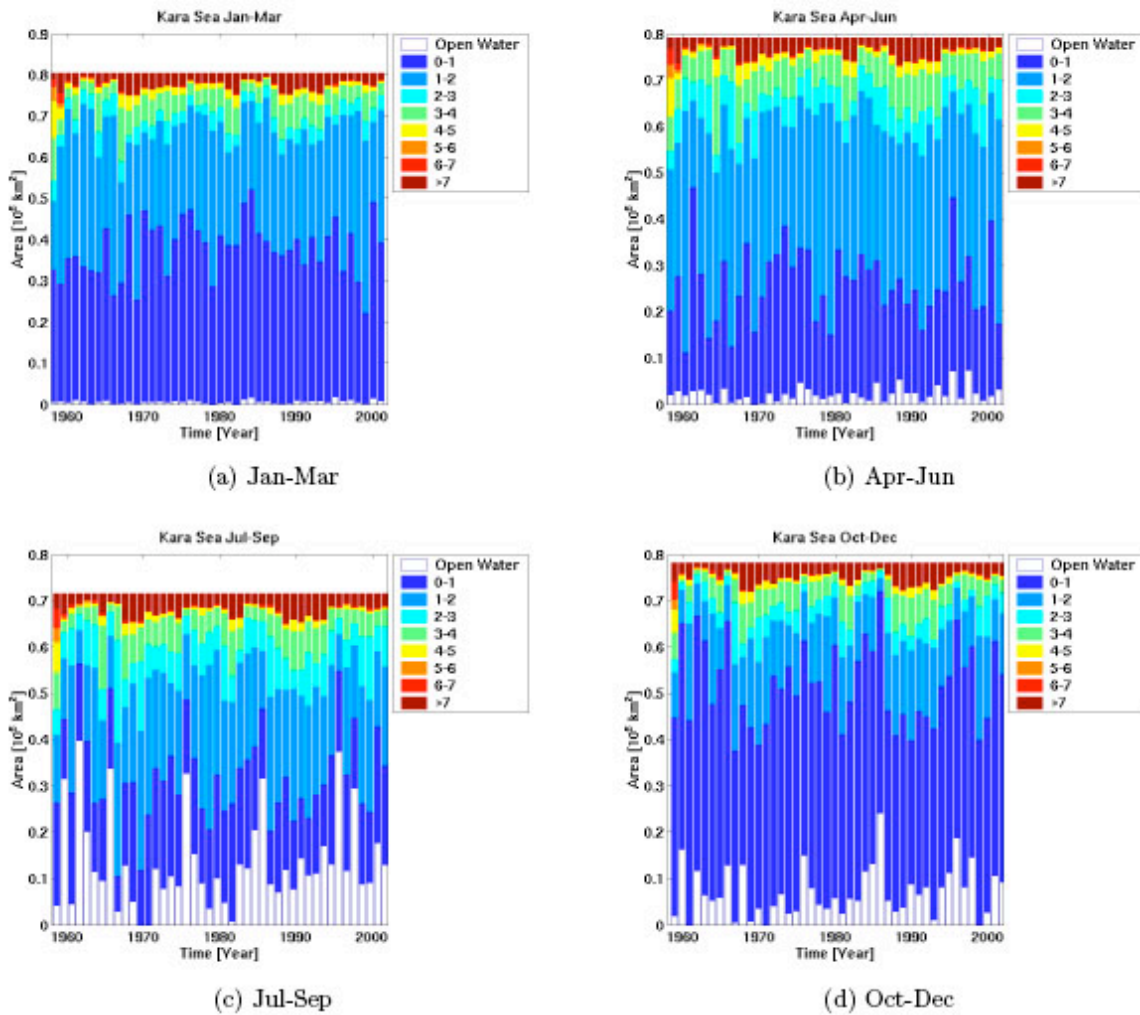


Figure 3.24: The area covered by ice in different sea-ice thickness ranges, for different seasons. Note that "Open Water" is relative to the maximum ice coverage in the time period 1958–2002.

### 3.4.9 Laptev Sea region

Tables 3.35-3.38: Sea ice area and sea ice volume statistics for the Laptev Sea region, including the area coverage of ice thicker than 2, 4 and 6 meters.

	Mean	Standard Deviation	Minimum	Maximum
Ice Area [ $10^6 \text{km}^2$ ]	0.87	0.00	0.86	0.88
Ice Volume [ $10^3 \text{km}^3$ ]	2.00	0.38	1.34	2.75
Area $h > 2$ [ $10^6 \text{km}^2$ ]	0.17	0.09	0.04	0.54
Area $h > 4$ [ $10^6 \text{km}^2$ ]	0.05	0.02	0.02	0.10
Area $h > 6$ [ $10^6 \text{km}^2$ ]	0.04	0.02	0.01	0.09

Table 3.35: January – March

	Mean	Standard Deviation	Minimum	Maximum
Ice Area [ $10^6 \text{km}^2$ ]	0.84	0.01	0.81	0.87
Ice Volume [ $10^3 \text{km}^3$ ]	2.15	0.36	1.54	2.99
Area $h > 2$ [ $10^6 \text{km}^2$ ]	0.19	0.08	0.08	0.44
Area $h > 4$ [ $10^6 \text{km}^2$ ]	0.05	0.02	0.02	0.09
Area $h > 6$ [ $10^6 \text{km}^2$ ]	0.04	0.02	0.02	0.09

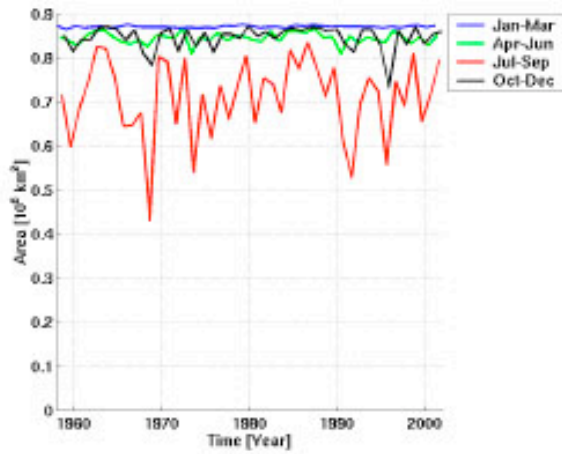
Table 3.36: April-June

	Mean	Standard Deviation	Minimum	Maximum
Ice Area [ $10^6 \text{km}^2$ ]	0.71	0.09	0.43	0.83
Ice Volume [ $10^3 \text{km}^3$ ]	1.78	0.43	0.78	2.77
Area $h > 2$ [ $10^6 \text{km}^2$ ]	0.14	0.07	0.04	0.40
Area $h > 4$ [ $10^6 \text{km}^2$ ]	0.06	0.02	0.02	0.12
Area $h > 6$ [ $10^6 \text{km}^2$ ]	0.05	0.02	0.02	0.11

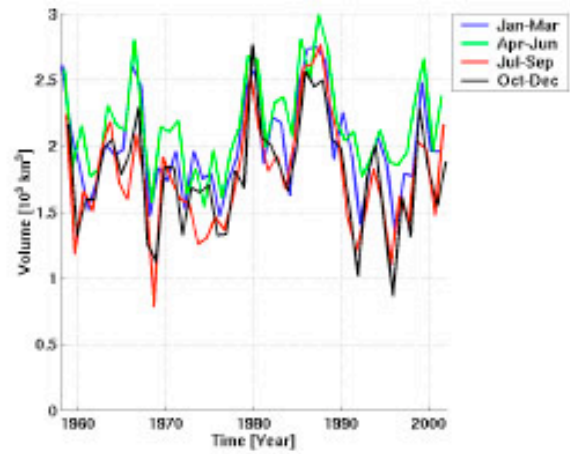
Table 3.37: July - September

	Mean	Standard Deviation	Minimum	Maximum
Ice Area [ $10^6 \text{km}^2$ ]	0.85	0.03	0.73	0.87
Ice Volume [ $10^3 \text{km}^3$ ]	1.78	0.41	0.86	2.76
Area $h > 2$ [ $10^6 \text{km}^2$ ]	0.14	0.06	0.04	0.35
Area $h > 4$ [ $10^6 \text{km}^2$ ]	0.05	0.02	0.02	0.11
Area $h > 6$ [ $10^6 \text{km}^2$ ]	0.05	0.02	0.02	0.10

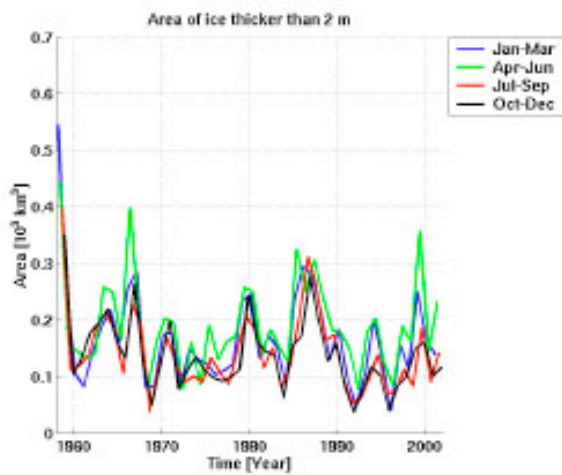
Table 3.38: October - December



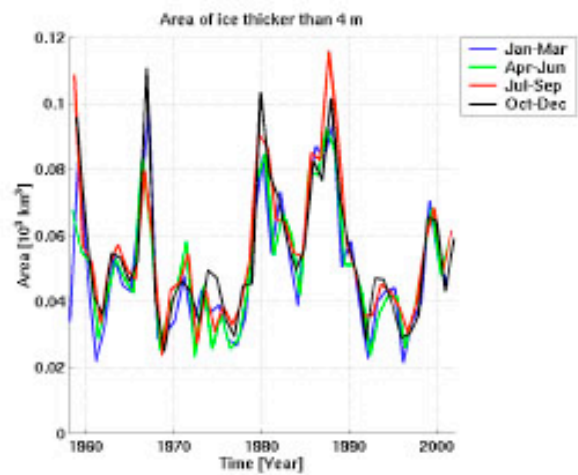
(a) Ice Area



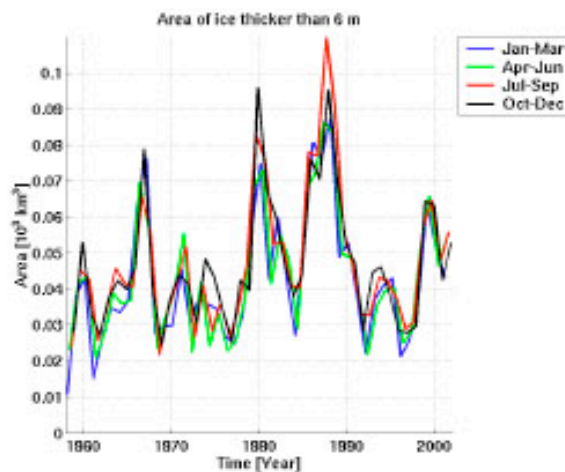
(b) Ice Volume



(c) Ice Area where  $h > 2$  meter



(d) Ice Area where  $h > 4$  meter



(e) Ice Area where  $h > 6$  meter

Figure 3.25: Ice Area and ice Volume for the Laptev Sea region. Also shown are the areas covered by ice thicker than 2, 4 and 6 meters

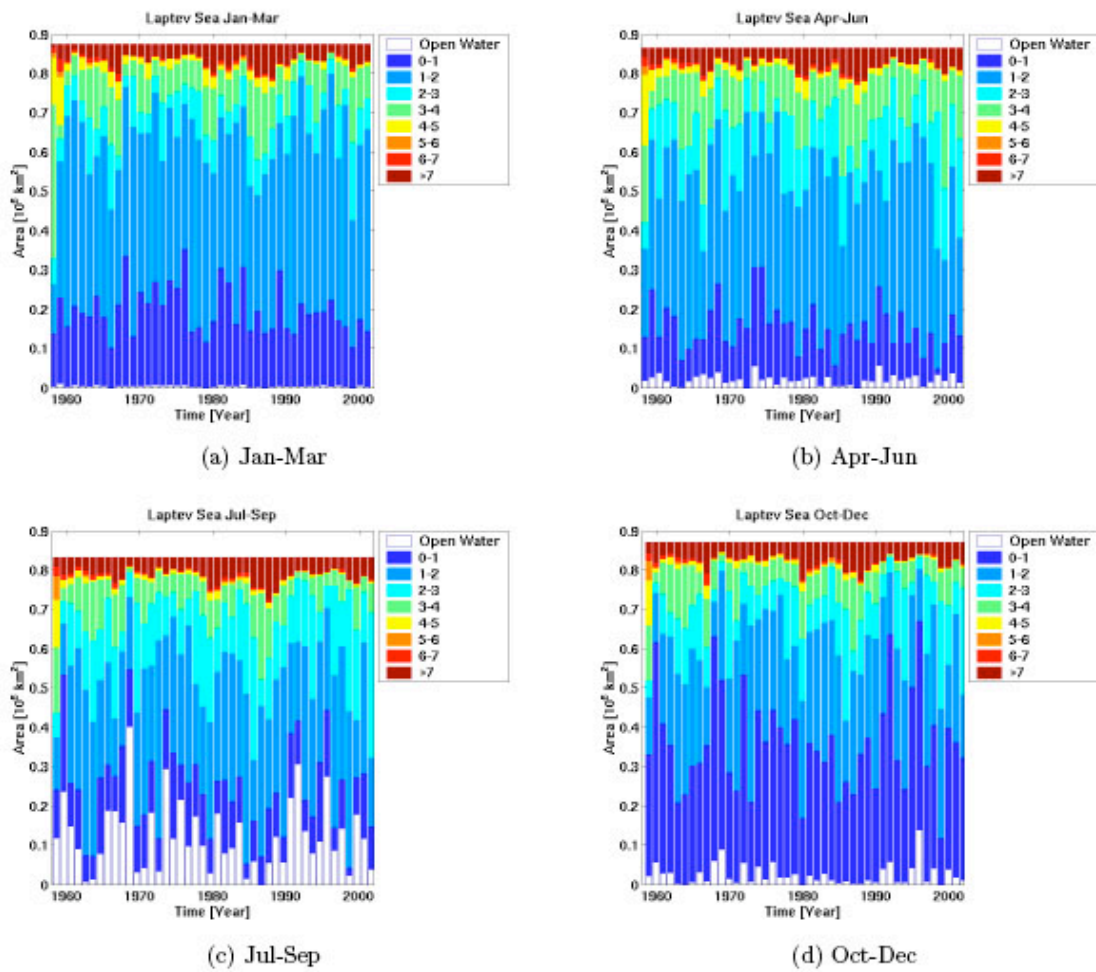


Figure3. 26: The area covered by ice in different sea-ice thickness ranges, for different seasons. Note that "Open Water" is relative to the maximum ice coverage in the time period 1958–2002.

3.4.10 Western Arctic region

Tables 3.39-3.42: Sea ice area and sea ice volume statistics for the Western Arctic region, including the area coverage of ice thicker than 2, 4 and 6 meters.

	Mean	Standard Deviation	Minimum	Maximum
Ice Area [ $10^6 \text{km}^2$ ]	2.53	0.00	2.52	2.54
Ice Volume [ $10^3 \text{km}^3$ ]	9.36	0.77	8.11	10.84
Area $h > 2$ [ $10^6 \text{km}^2$ ]	1.28	0.20	0.87	1.87
Area $h > 4$ [ $10^6 \text{km}^2$ ]	0.28	0.08	0.06	0.47
Area $h > 6$ [ $10^6 \text{km}^2$ ]	0.25	0.09	0.03	0.47

Table 3.39: January – March

	Mean	Standard Deviation	Minimum	Maximum
Ice Area [ $10^6 \text{km}^2$ ]	2.47	0.01	2.44	2.50
Ice Volume [ $10^3 \text{km}^3$ ]	10.00	0.80	8.73	11.50
Area $h > 2$ [ $10^6 \text{km}^2$ ]	1.46	0.21	0.97	2.00
Area $h > 4$ [ $10^6 \text{km}^2$ ]	0.31	0.09	0.09	0.54
Area $h > 6$ [ $10^6 \text{km}^2$ ]	0.28	0.10	0.03	0.53

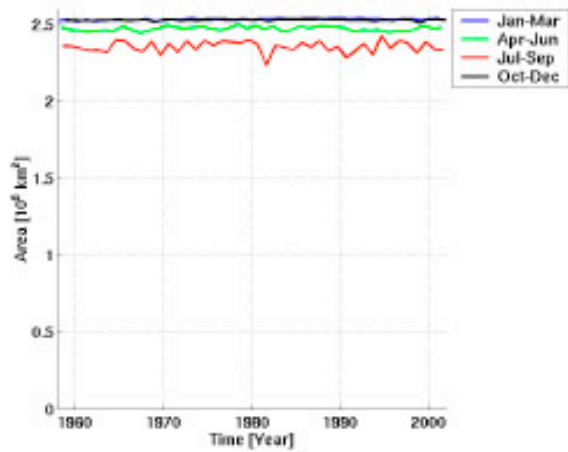
Table 3.40: April-June

	Mean	Standard Deviation	Minimum	Maximum
Ice Area [ $10^6 \text{km}^2$ ]	2.35	0.04	2.24	2.42
Ice Volume [ $10^3 \text{km}^3$ ]	8.90	0.83	7.49	10.44
Area $h > 2$ [ $10^6 \text{km}^2$ ]	1.16	0.23	0.64	1.71
Area $h > 4$ [ $10^6 \text{km}^2$ ]	0.31	0.09	0.09	0.55
Area $h > 6$ [ $10^6 \text{km}^2$ ]	0.27	0.09	0.04	0.54

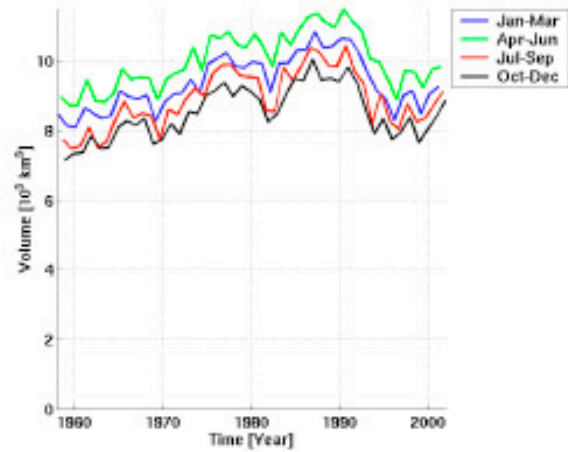
Table 3.41: July - September

	Mean	Standard Deviation	Minimum	Maximum
Ice Area [ $10^6 \text{km}^2$ ]	2.53	0.01	2.51	2.54
Ice Volume [ $10^3 \text{km}^3$ ]	8.50	0.75	7.15	10.05
Area $h > 2$ [ $10^6 \text{km}^2$ ]	1.07	0.23	0.60	1.50
Area $h > 4$ [ $10^6 \text{km}^2$ ]	0.28	0.08	0.08	0.50
Area $h > 6$ [ $10^6 \text{km}^2$ ]	0.25	0.08	0.05	0.50

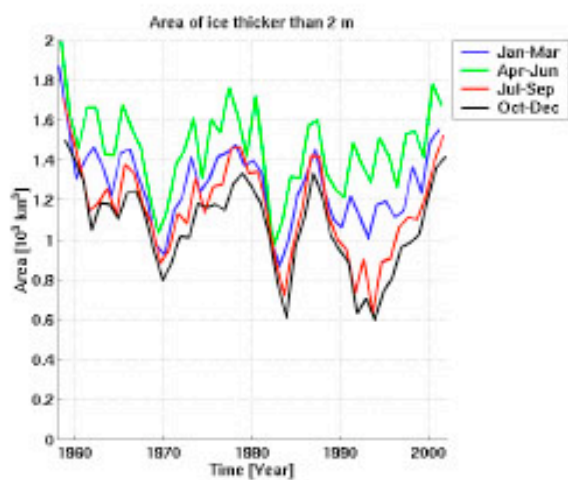
Table 3.42: October - December



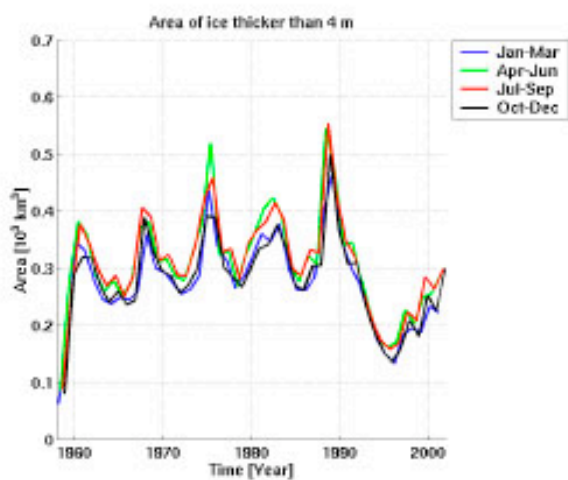
(a) Ice Area



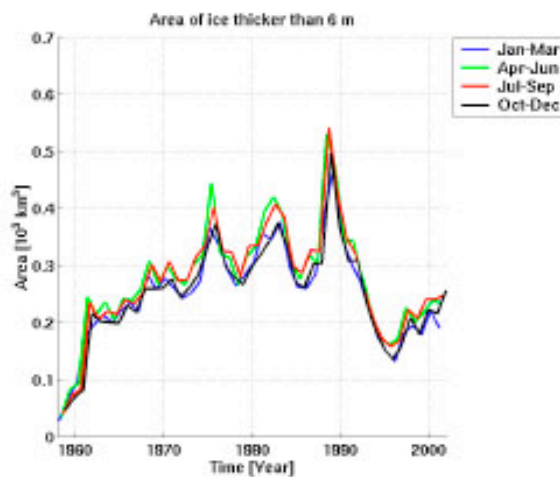
(b) Ice Volume



(c) Ice Area where  $h > 2$  meter



(d) Ice Area where  $h > 4$  meter



(e) Ice Area where  $h > 6$  meter

Figure 3.27: Ice Area and ice Volume for the Western Arctic region. Also shown are the areas covered by ice thicker than 2, 4 and 6 meters



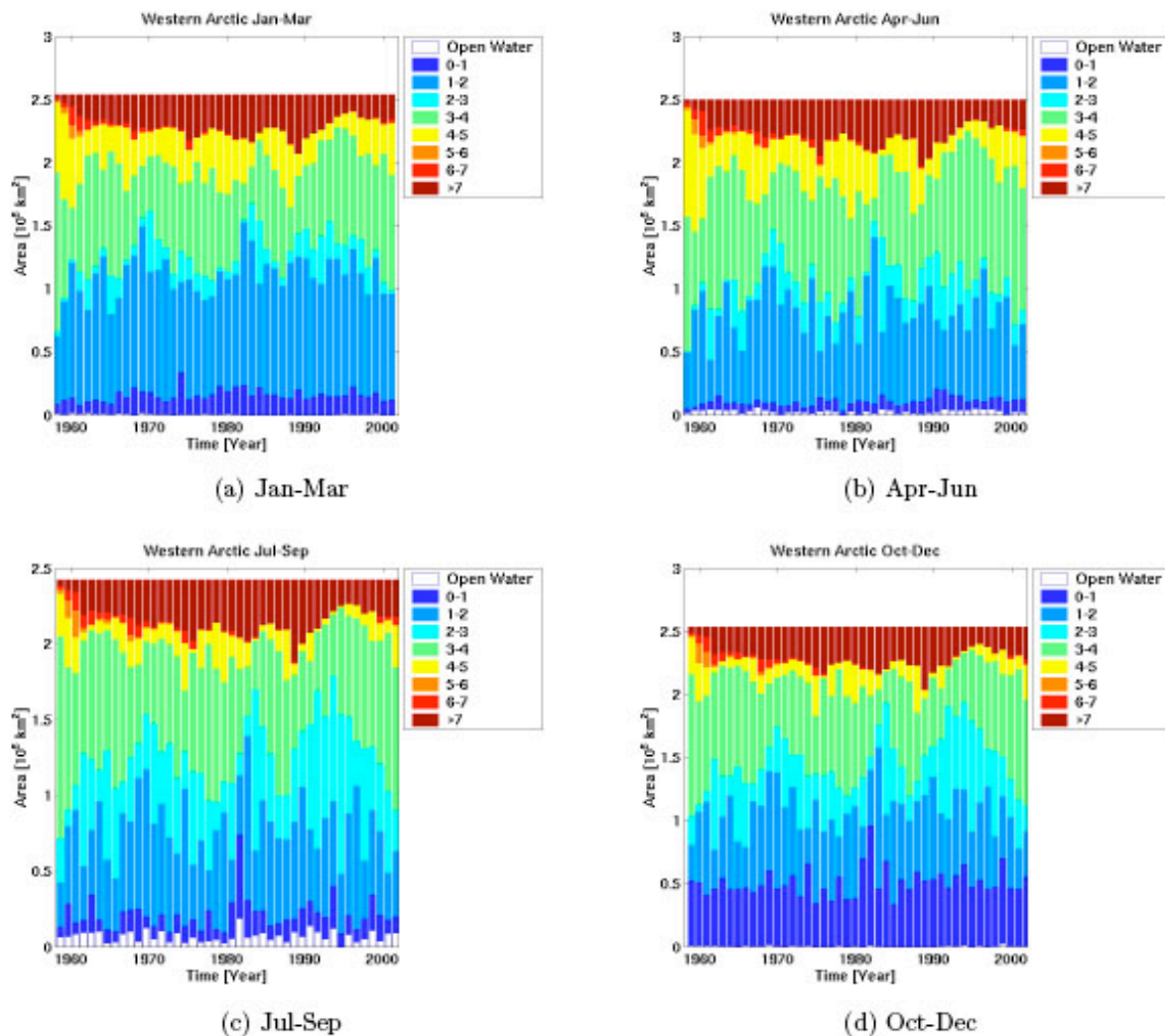


Figure 3.28: The area covered by ice in different sea-ice thickness ranges, for different seasons. Note that "Open Water" is relative to the maximum ice coverage in the time period 1958–2002.

### 3.5 Regional analysis of satellite data 1978-2005

#### 3.5.1 Satellite data description

Passive microwave satellite data have been continuously available since 1978, providing valuable data to observe variability and trend in sea extent and concentration. From 1978 to 1987 the Scanning Multichannel Microwave Radiometer (SMMR) on Nimbus-7 produced the first time series of multichannel data. From 1987 to present the Special Sensor Microwave/Imager (SSM/I), mounted on a series of satellites operated by the Defense Meteorological Satellite Program (DMSP) have continued to produce global daily passive microwave data. SSM/I is a seven-channel, four-frequency, linearly polarized passive microwave radiometric system. Channels are 85.5 GHz, 37.0 GHz, 22.2 GHz, and 19.3 GHz. Instrument coverage is global except for circular sectors centered over the pole, 280 km in radius, located poleward of 87°N and 87°S, which are never measured due to orbit inclination. Orbital data for each 24-hour period are mapped to a selected grid cells using a simple "drop in the bucket" sum and average method. The measurement footprint size (effective field of view) is as follows:

19.3 GHz: 70x45 km; 22.2 GHz: 60x40 km; 37.0 GHz: 38x30 km; and 85.5 GHz: 16x14 km

These footprints are mapped to a 12.5 km grid spacing at 85.5 GHz, and 25 km at the lower frequencies. All SSM/I  $T_B$  gridded data are stored as scaled 2-byte integers. F8 data are band interleaved by pixel, in binary format. F11 and F13 data are in Hierarchical Data Format (HDF4). The data are produced and distributed by the National Snow and Ice Data Center (NSIDC), Boulder, Colorado, USA.

### 3.5.2 Algorithm for sea ice concentration

To produce ice concentration maps we use the NORSEX algorithm (Svendsen et al., 1983) that calculates concentrations of first-year (FY) ice, multi-year (MY) ice and the percentage of the area of open water (OW) at the Arctic surface. According to this algorithm the brightness temperature from a three-component footprint is assumed to be the sum of individual emitted brightness temperatures, weighted by the concentration of every fraction:

$$T_B = C_{MY}e_{MY}T_{MY} + C_{FY}e_{FY}T_{FY} + C_{OW}e_{OW}272$$

where  $C_{MY}, C_{FY}, C_{OW}$  are concentrations of multi-year ice, first-year ice and open water, respectively, covering the field of view of the instrument.  $e_{MY}, e_{FY}, e_{OW}$  are emissivities of the respective components and  $T_{MY}$  and  $T_{FY}$  are temperatures of two types of ice, which are calculated using monthly averaged atmospheric surface temperature and effective temperature of the open water (272 K). Temperatures are measured in Kelvins. The algorithm uses SSM/I brightness temperature measurements at 19 and 37 GHz, vertical polarizations. The weather effects, including roughening of the sea surface by near surface winds, cloud liquid water and atmospheric water vapor, all increase the radiance measured by a satellite sensor and may cause the appearance of false sea ice concentrations. They are minimized using weather filters suggested by Cavalieri et al. (1991) and Gloersen and Cavalieri (1986).

### 3.5.3 Trend analysis of ice area in each region

All ice concentration data from 1979 to 2004 have been used to calculate monthly mean ice area for each of the study regions defined in Fig.3.1. The monthly mean values are compiled into three-monthly averaged ice areas shown in the upper graphs in Figs 3.29 – 3.36. A trend analysis has been performed using the monthly ice areas in each region. The results of the error analysis for the Barents Sea is shown in Table 3.43, where the trend value is shown in the first row and the error value in the second row. These parameters are plotted in the lower graphs in Figs 3.29-3.36. The trend is generally negative (blue bars), which means that the ice area has been reduced. For example, in January the ice area has been reduced by 7750 km<sup>2</sup> in the period 1979 – 2004 (Table 3.43). The third row shows  $r$ , which is the coefficient for determination of the error. If it is 1, there is a perfect correlation in the sample. This means there is no difference between the estimated using linear function  $y$ -value and the actual  $y$ -value. The fourth row shows the  $F$  statistics, determining whether the observed relationship between the dependent and independent variables occurs by chance. When the trend is significant to 95 % confidence level the  $F$ -statistic is indicated in red. In the Barents Sea data, the trend is not significant for August, September, October and November. Similar analysis has been performed for all the regions and the results are presented in the lower graphs of Figs. 3.29-3.36. Note that the two regions representing the interior of the Arctic are not included in the analysis because these areas are fully ice-covered throughout the year and no change in ice area is therefore observed.

Table 3.43. Trend and error analysis for the ice area data in the Barents Sea.

Month	jan	feb	mar	apr	may	jun	jul	aug	sep	oct	nov	dec
Trend value (km <sup>2</sup> )	-7750	-7988	-6701	-9312	-8465	-8065	-4443	-2267	-1093	-1752	-2510	-7241
Error value (km <sup>2</sup> )	3136	3799	3180	3736	3857	2732	1612	1375	1687	2604	2776	2484
$r$	0.19	0.15	0.15	0.19	0.16	0.25	0.23	0.09	0.01	0.01	0.03	0.25
$F$ statistic	6.10	4.41	4.43	6.21	4.81	8.71	7.59	2.71	0.41	0.45	0.81	8.49

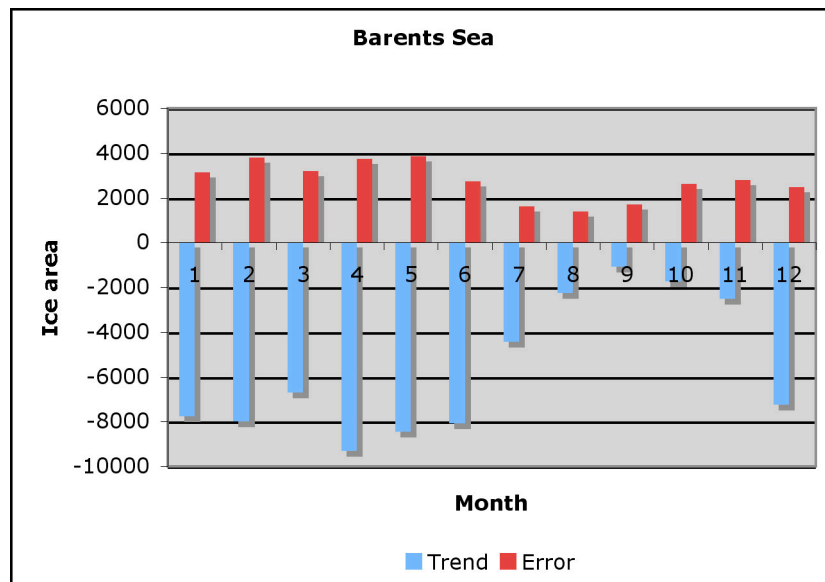
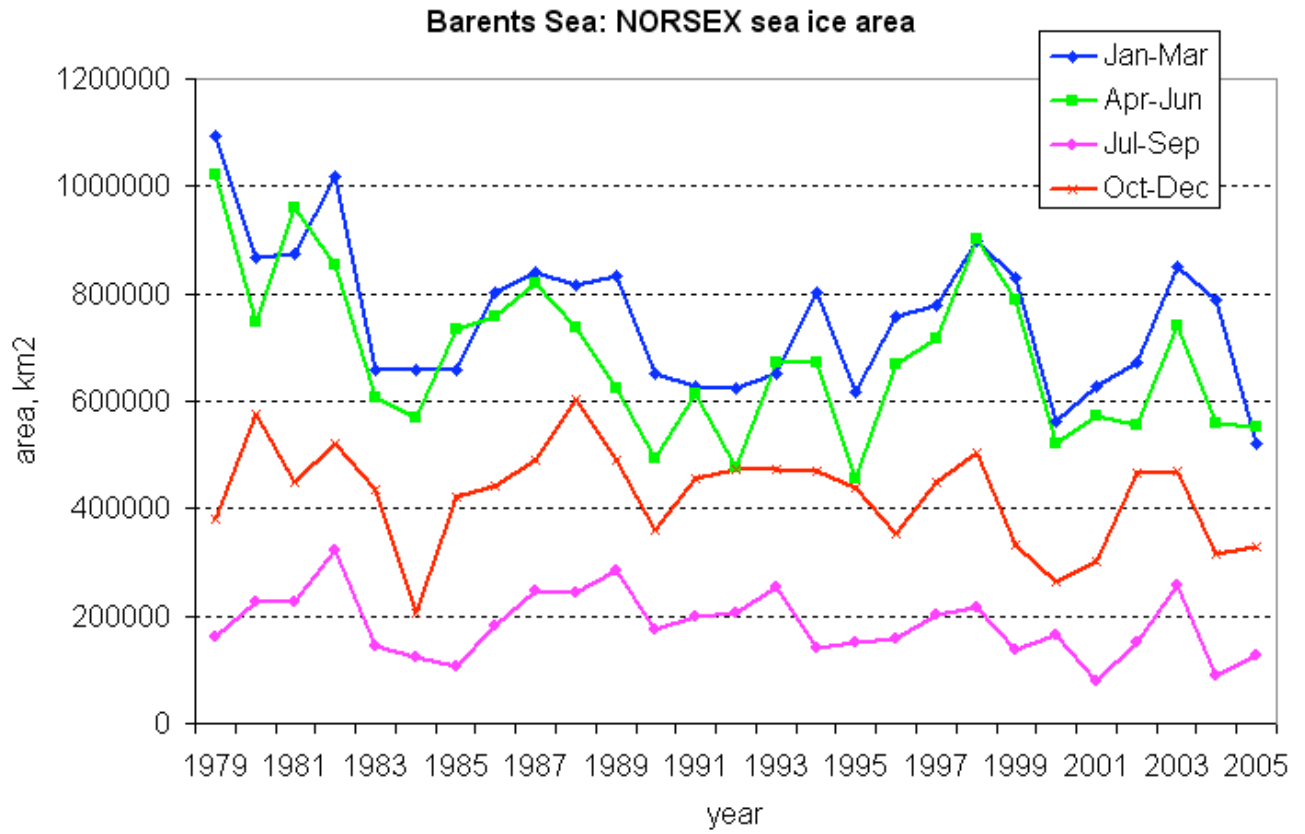


Figure 3.29. Upper graph: time series of monthly mean ice area in the Barents Sea from SSM/I data, lower graph: trend and error in ice area (in km<sup>2</sup>) for each month

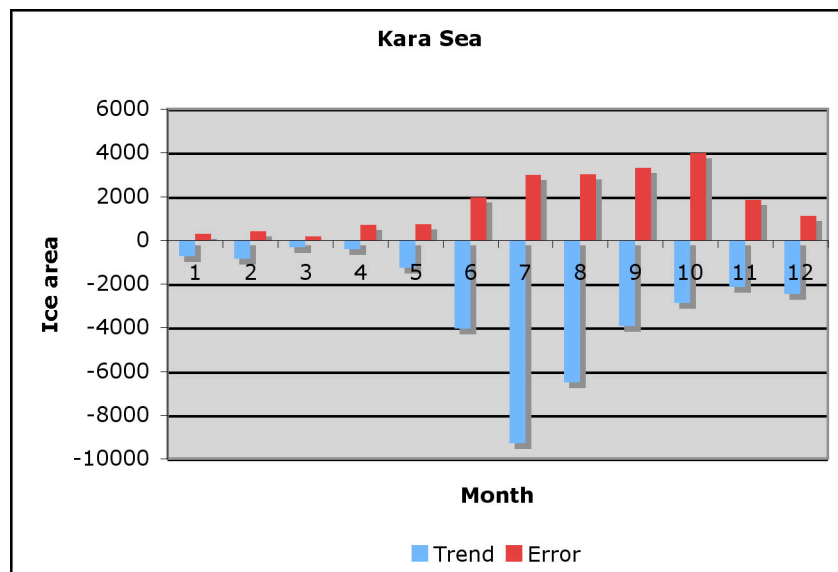
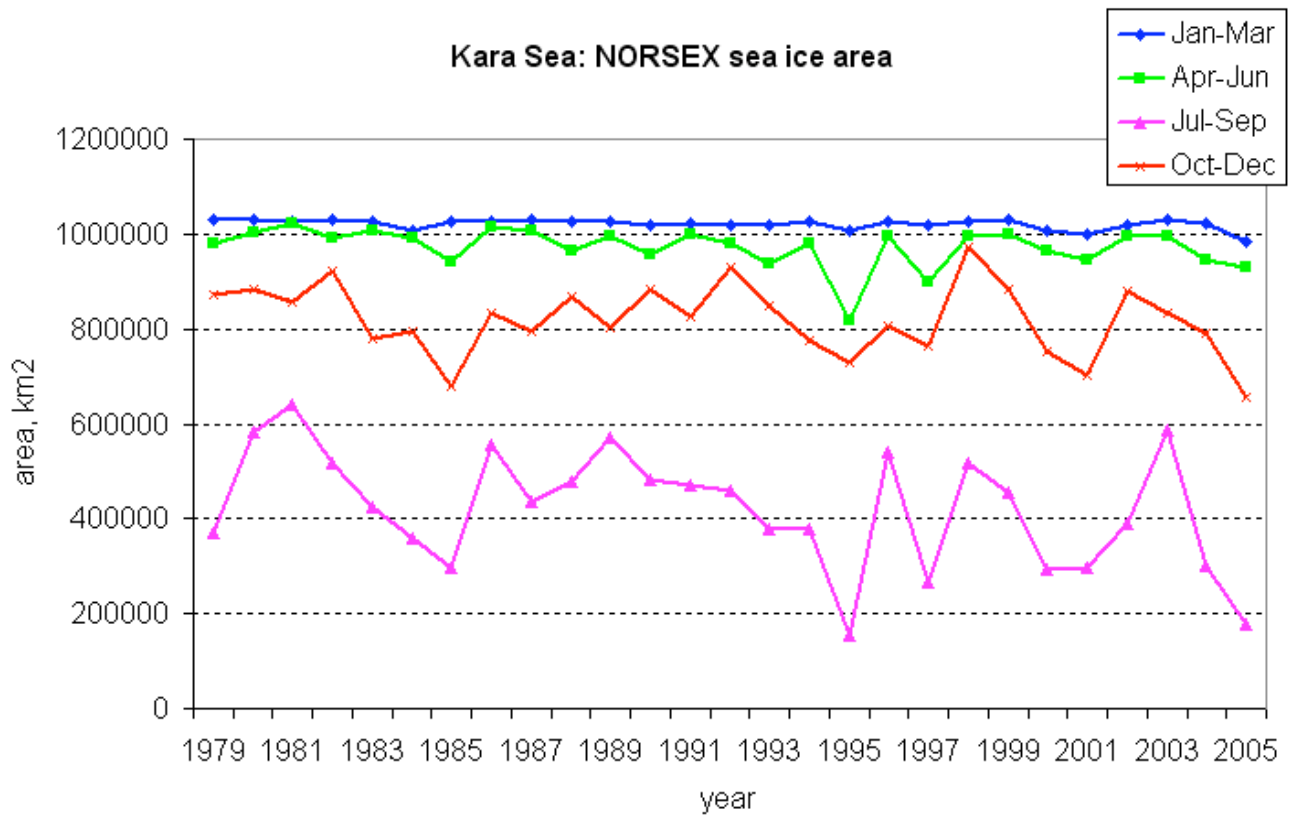


Figure 3.30. Upper graph: time series of monthly mean ice area in the Kara Sea Sea from SSMI data, lower graph: trend and error in ice area (in km<sup>2</sup>) for each month



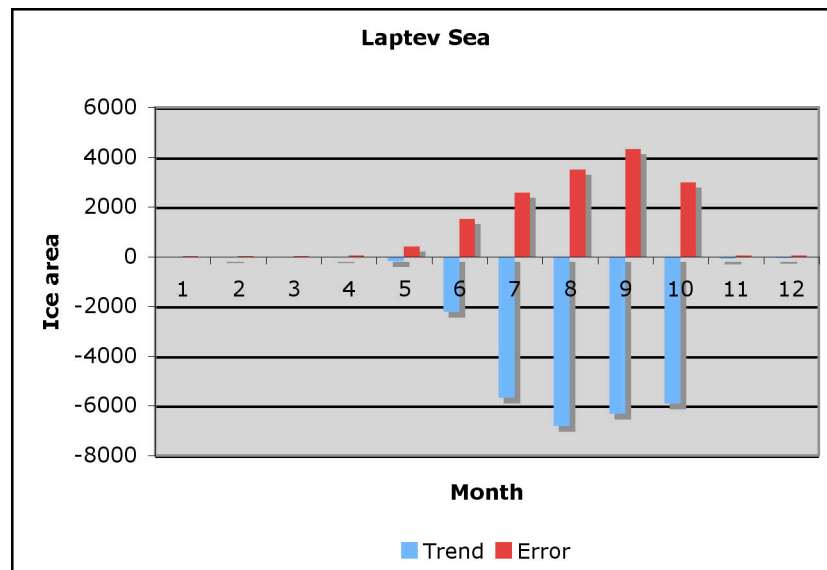
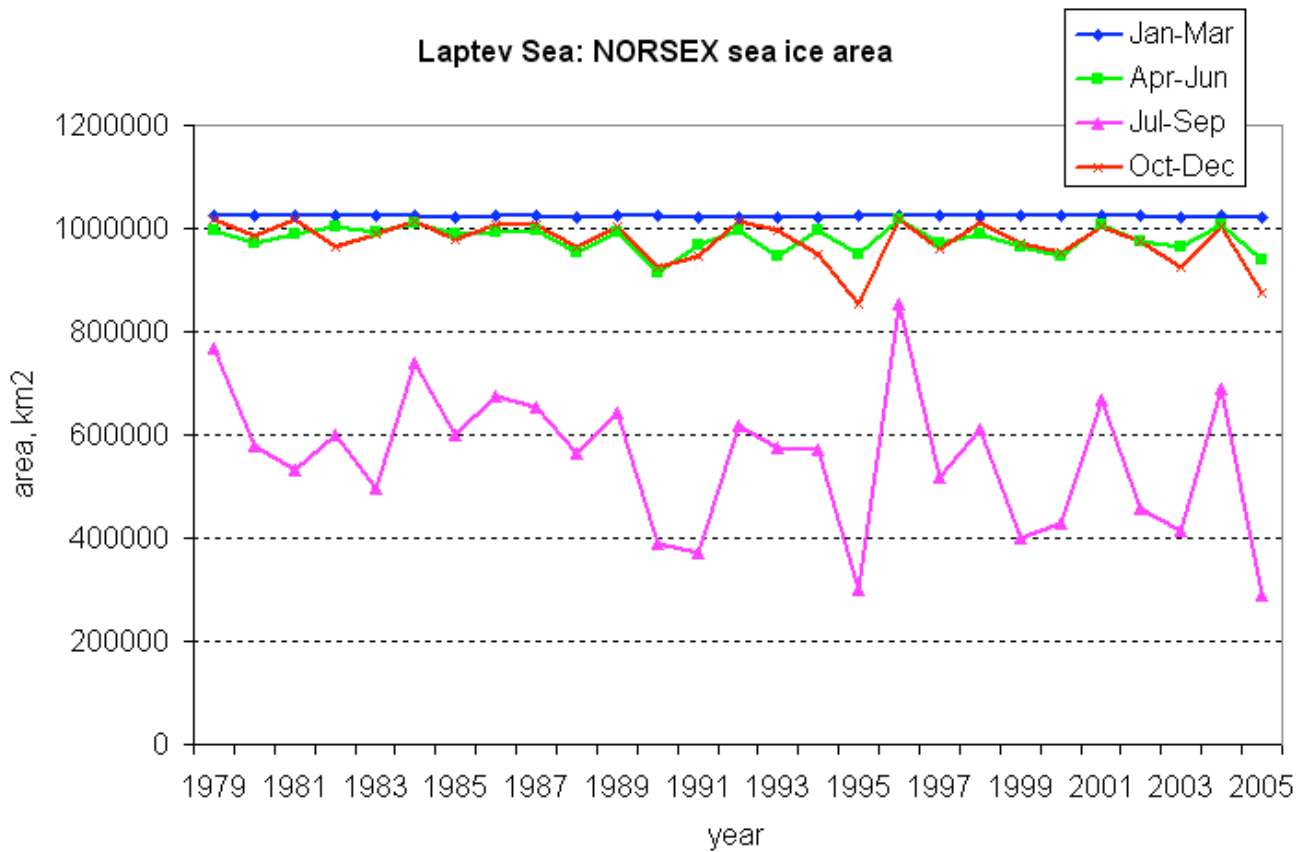


Figure 3.31. Upper graph: time series of monthly mean ice area in the Laptev Sea Sea from SSMI data, lower graph: trend and error in ice area (in km<sup>2</sup>) for each month

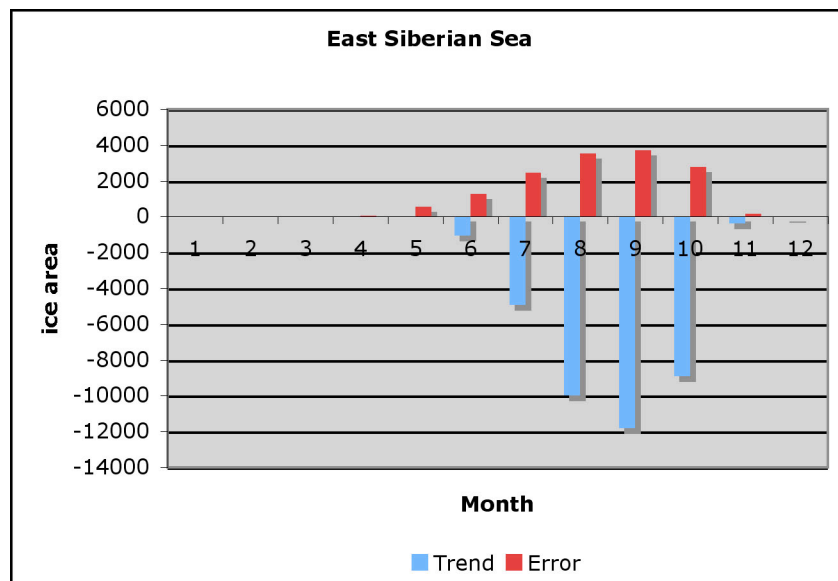
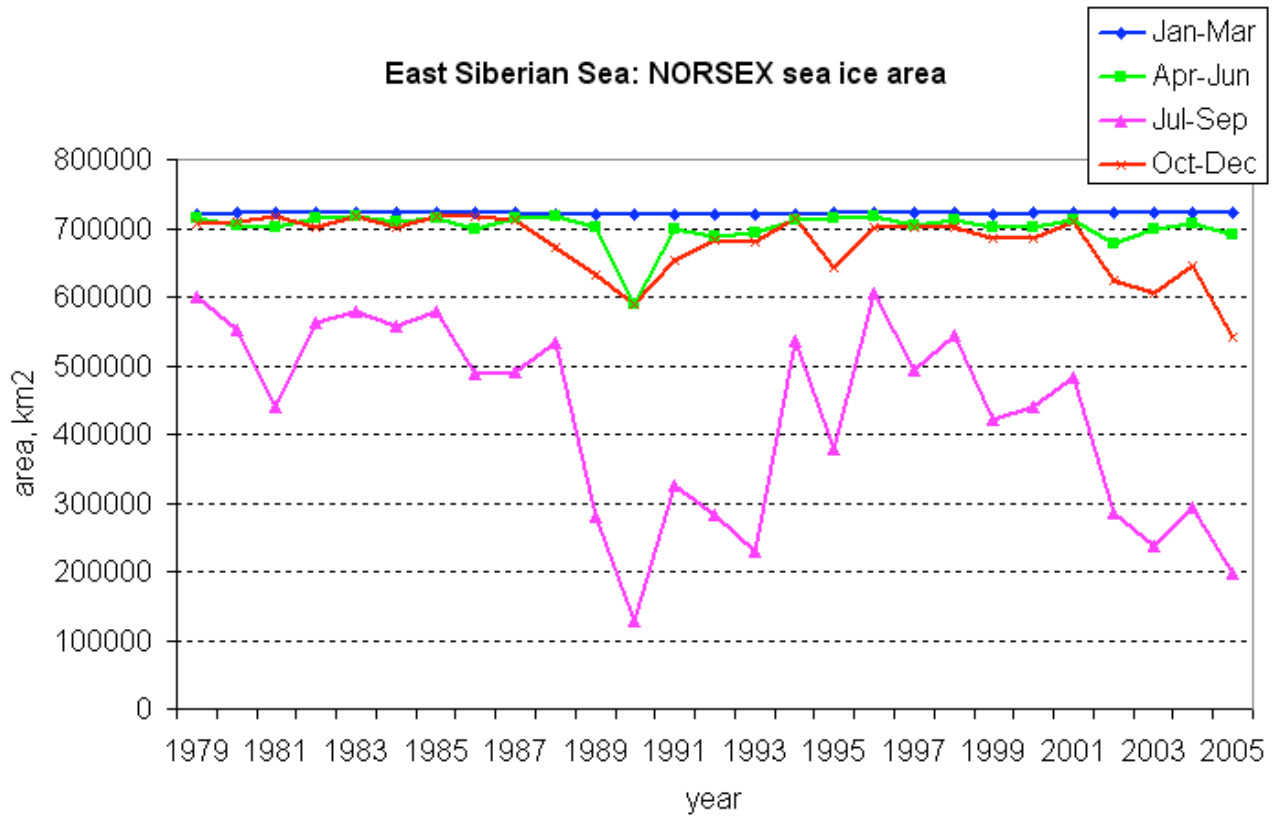


Figure 3.32. Upper graph: time series of monthly mean ice area in the East Siberian Sea from SSMI data, lower graph: trend and error in ice area (in km<sup>2</sup>) for each month

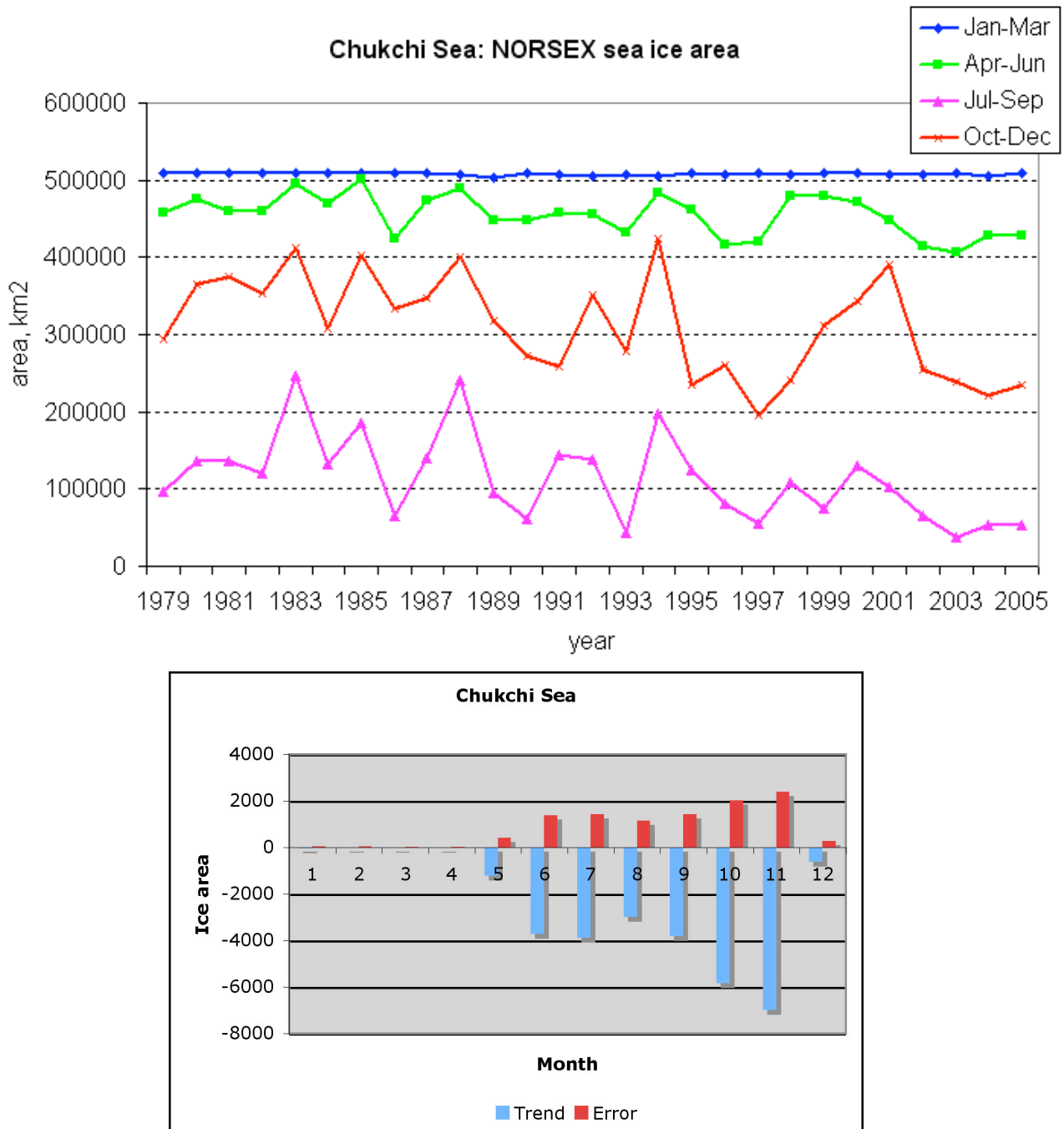


Figure 3.33. Upper graph: time series of monthly mean ice area in the Chukchi Sea from SSMI data, lower graph: trend and error in ice area (in km<sup>2</sup>) for each month

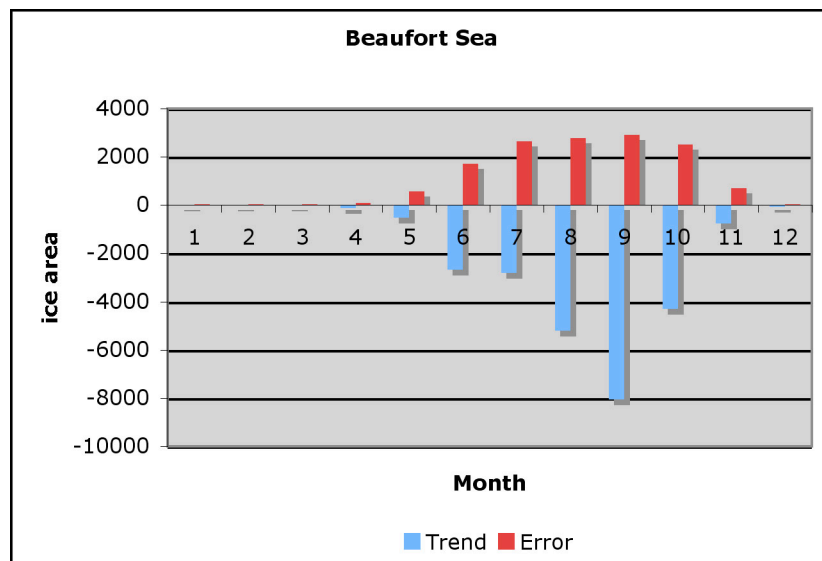
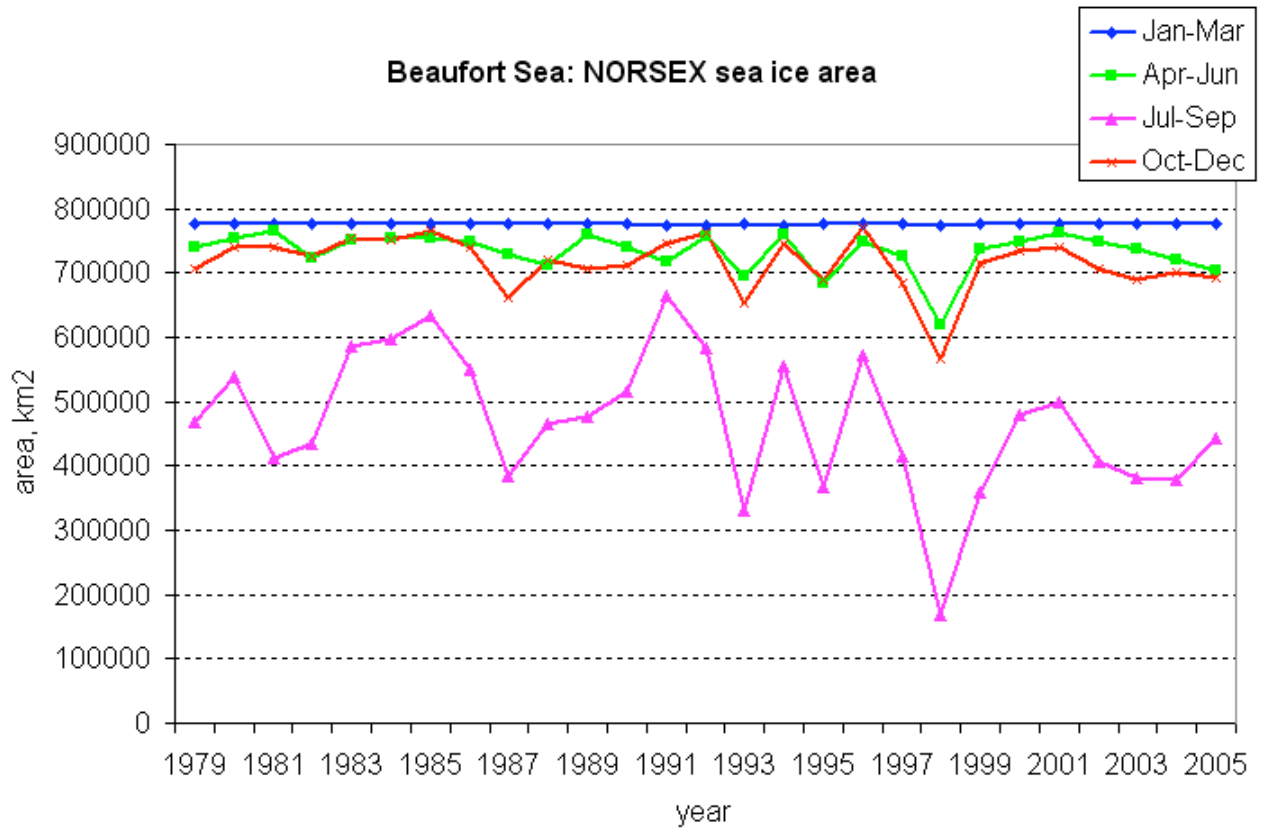


Figure 3.34. Upper graph: time series of monthly mean ice area in the Beaufort Sea from SSM/I data, lower graph: trend and error in ice area (in km<sup>2</sup>) for each month



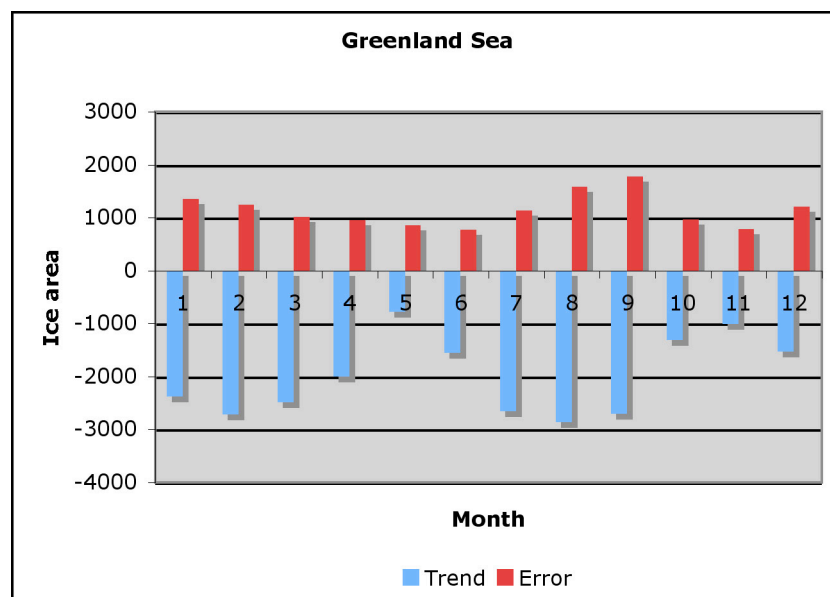
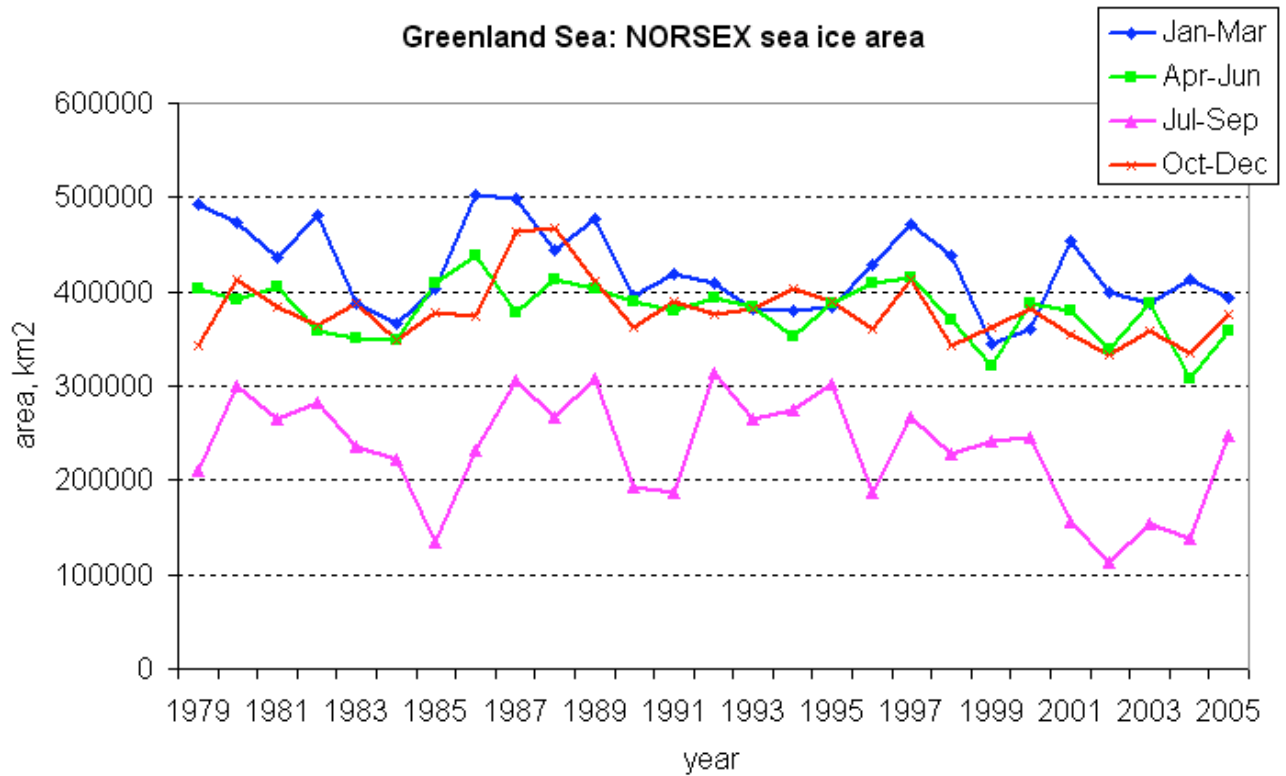


Figure 3.35. Upper graph: time series of monthly mean ice area in the Greenland Sea from SSM/I data, lower graph: trend and error in ice area (in km<sup>2</sup>) for each month

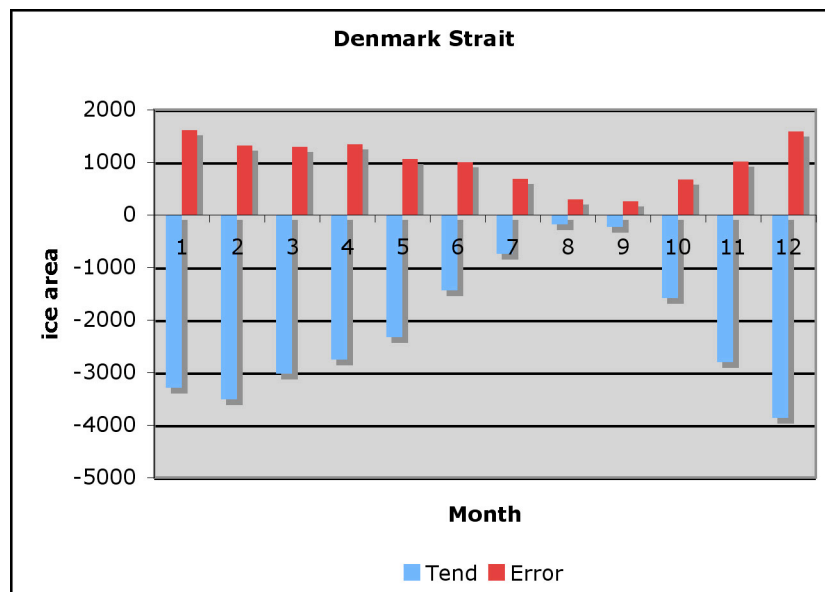
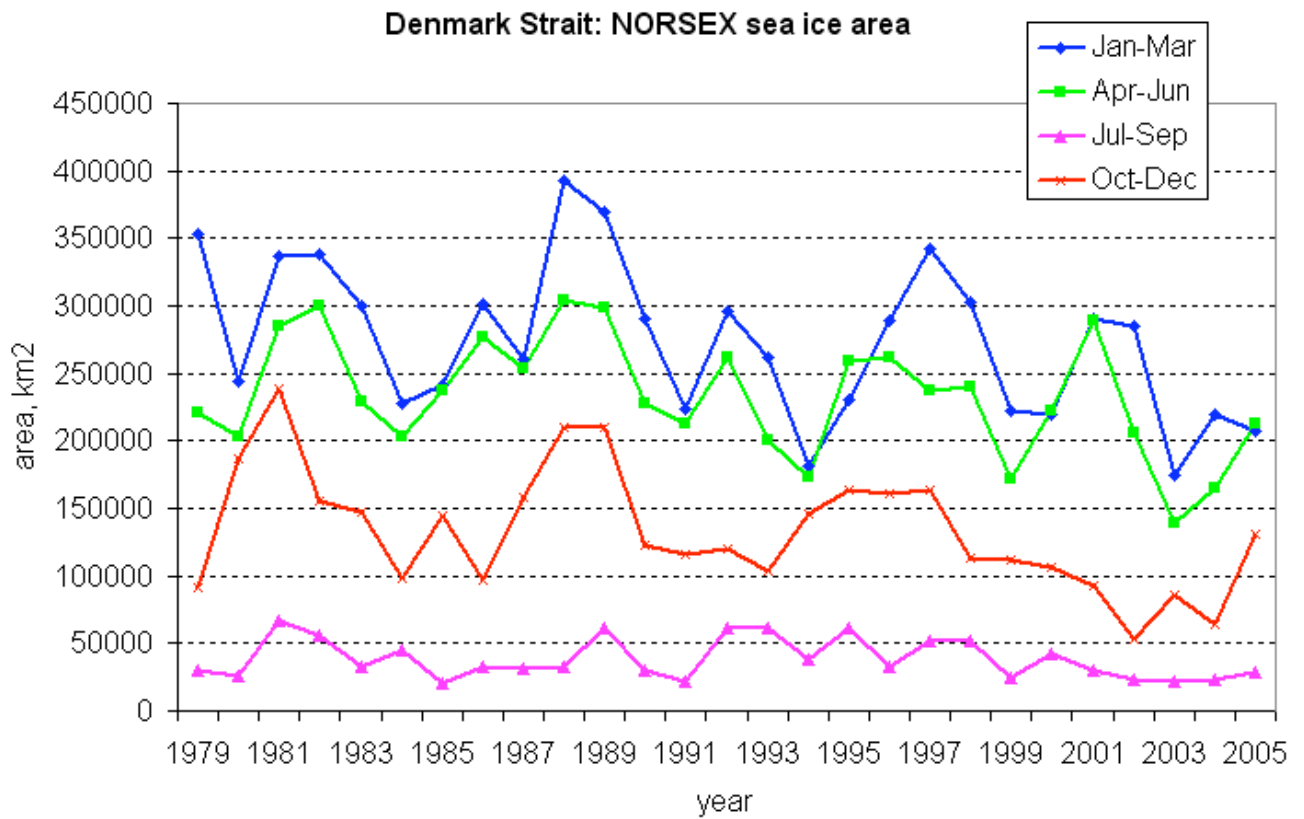


Figure 3.36. Upper graph: time series of monthly mean ice area in the Denmark Strait from SSM/I data, lower graph: trend and error in ice area (in km<sup>2</sup>) for each month

### 3.6 Conclusions

In this chapter we have used a multi-category sea-ice model to derive statistics of ice area, ice thickness and ice volume for different regions in the Arctic. Due to the large amount of data produced by the coupled ice-ocean model system, the model data has been aggregated to seasonal and regional quantities for different areas in the Arctic. As with any model data set, the realism of the model output must be validated. We have tried to demonstrate the strength and weaknesses of the model output by comparing model fields with some of the available sea-ice data in the Arctic. Comparisons of the model data with ice draft estimates from Upward Looking Sonar data, illustrate that the average ice thickness gives a good description of this quantity. The model bias is usually low, whereas the RMS errors can be high. However, it should be taken into account that the model is relatively coarse compared to the scale of the observations. The high RMS-errors can come from unresolved scales in the sea-ice model. In addition, the cumulative ice thickness distribution from the model has been compared with the cumulative ice thickness distribution from the ULS observations. The comparison illustrates how the model tends to put too much ice in the thickest sea-ice categories. We have also compared the model with estimates from passive microwave sensors. The comparison shows how the model tends to overestimate the ice concentration, especially in the regional seas. In winter, this is evident in the Barents Sea and the Greenland Sea. In summer there is also an overestimate of the sea-ice concentration in the Kara Sea, the Beaufort Sea and in the Laptev Sea. The regional breakdown of the data set is done for the sub-regions shown in Figure 3.1, where seasonal statistics have been produced. The total ice area and volume of sea-ice in each region have been estimated and plotted as a time series. In addition, we have plotted the area coverage of ice thicker than a threshold limit, the limits used here are 2, 4, and 6 meters. These statistics can give an indication of how severe the ice is in a given region. For instance, the higher ice coverage of +6 meter ice, the more difficult the navigation of ships will become. All these quantities are summarized in a table, showing the mean, standard deviation and minimum and maximum values in the period 1958–2001.

The main conclusions for the satellite data analysis based on passive microwave data from 1979 to present are the following:

- Satellite-derived ice concentrations demonstrate negative trend in ice area in almost all the regional seas of the Arctic, but all regions show considerable interannual variability of the ice cover
- Ice retreat with confidence at 95% level is found for the Denmark Strait, Greenland Sea, Barents Sea and Kara Sea in the late winter (February – March). In the Barents Sea alone the negative trend is significant (95%) for the months December-July
- In the opposite side of the Arctic, the negative trend is significant during summer months and early winter. It is significant in September in the East Siberian, Chukchi and Beaufort Seas, in August-November in the East Siberian Sea and in May-December in the Chukchi Sea.
- There is an opposite tendency in the variations of the ice concentration in different parts of the Arctic: in the late winter the negative trend is more significant in the part of the Arctic that is close to the Atlantic Ocean and in summer and early winter the negative trend is more significant in the part close to Pacific Ocean.
- Denmark Strait: The maximum ice area is observed usually in March-April. During summer months (August-September) the ice area is very small. The difference between maximum and minimum ice cover is 6 – 8 times.
- Greenland Sea: Maximum ice cover can be observed in any winter month: from December to March and even April. The minimum ice cover is observed in August-September. The average difference between maximum and minimum ice cover is 2 times but can be up to 4 times in some years.
- Barents Sea: Negative trends in the ice area is significant for 8 months of the year. The decrease is most pronounced in winter. The minimum ice cover is observed usually in September and there has been a record low extent of ice in the last 5 summers.

- Kara Sea: The sea is totally covered by ice during winter (January-May). The minimum ice cover is observed usually in September and can be more than 5 times smaller than the maximum ice cover. In recent years, we observe very little ice in this sea in August-September (record minimum in 2005).



## 4. Review of recent climate model projections

Recent results of Atmosphere-Ocean General Circulation Model (AOGCM) model simulations from the IPCC 2007 report have been reviewed, focusing on simulations results for the Arctic. Fully coupled atmosphere-ice-ocean models is a key tool to study the spatial-temporal variability of climate processes over decades and centuries. In the Arctic there is lack of systematic observations of meteorological and oceanographic variables. Climate model simulations are therefore important to cover the whole Arctic with synoptic simulated data of atmosphere, sea ice and ocean, but accuracy and reliability of the models need to be improved. Climate model simulations are used to produce scenarios of future changes of atmosphere, ocean and sea ice conditions. The Arctic Climate Impact Assessment (ACIA, 2005) has made a general overview of status and projected changes for all the major climate parameters. The most recent assessment of climate change has been published by IPCC (in May, 2007) in the Fourth Assessment Report. This report is over 900 pages and represents a significant progress in understanding climate changes compared to the Third Assessment Report (TAR) from IPCC in 2001. The Technical Summary gives an overview of the results of the Fourth Assessment Report (Solomon et al., 2007). The whole report is available at <http://ipcc-wg1.ucar.edu/wg1/wg1-report.html>.

### 4.1 Global warming under different emission scenarios

The model prediction of global warming from the previous IPCC reports (1990, 1996 and 2001) has been compared with observed global warming since 1990 (Fig. 4.1a). The observed temperature anomalies are presented as annual (black dots) and decadal average values (black line) from Fig. 4.1b. Projected trends and their ranges from the IPCC First (FAR) and Second (SAR) Assessment Reports are shown as green and magenta solid lines and shaded areas, and the projected range from the TAR is shown by vertical blue bars. These projections were adjusted to start at the observed decadal average value in 1990.

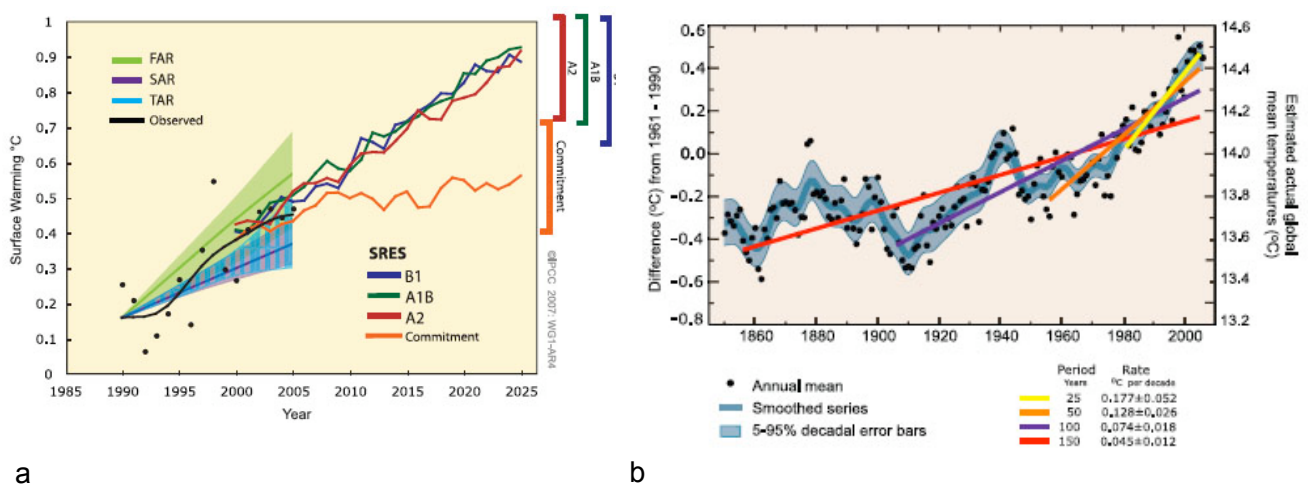


Figure 4.1 (a) Shaded areas show projections of global warming from the previous IPCC reports (1990, 1996, 2001) compared to observed warming between 1990 and 2005 (black line and dots). The multimodel projections from the IPCC 2007 report for 2000 – 2025 are shown by the colored lines; (b) observed global mean temperature from 1850 to 2005.

The multi-model mean projections for the SRES B1, A1B and A2 scenarios<sup>1</sup>, as in Figure 4.1a, are shown for the period 2000 to 2025 as blue, green and red curves with uncertainty ranges indicated against the right-hand axis. The orange curve shows model projections of warming if greenhouse gas and aerosol concentrations were held constant from the year 2000 (Commitment scenario).

<sup>1</sup> SRES scenarios are *emission scenarios* developed by Nakićenović and Swart (2000) and used, among others, as a basis for some of the *climate projections* presented in the IPCC 2007 report.

Projections for 1990 to 2005 carried out for the First Assessment Report (FAR) and the Second Assessment Report (SAR) suggested global mean temperature increases of about 0.3°C and 0.15°C per decade, respectively. The difference between the two was due primarily to the inclusion of aerosol cooling effects in the SAR, whereas there was no quantitative basis for doing so in the FAR. Projections given in the TAR were similar to those of the SAR. These results are comparable to observed values of about 0.2°C per decade, providing broad confidence in such short-term projections. The warming from the three scenarios, A2, A1B and B1 are consistent on short time scale (the next two decades) but varies on longer time scales (to the end of this century). Figure 4.2 (left panel) illustrates the relative probability of global mean temperature change for the three different scenarios on short and long time scale.

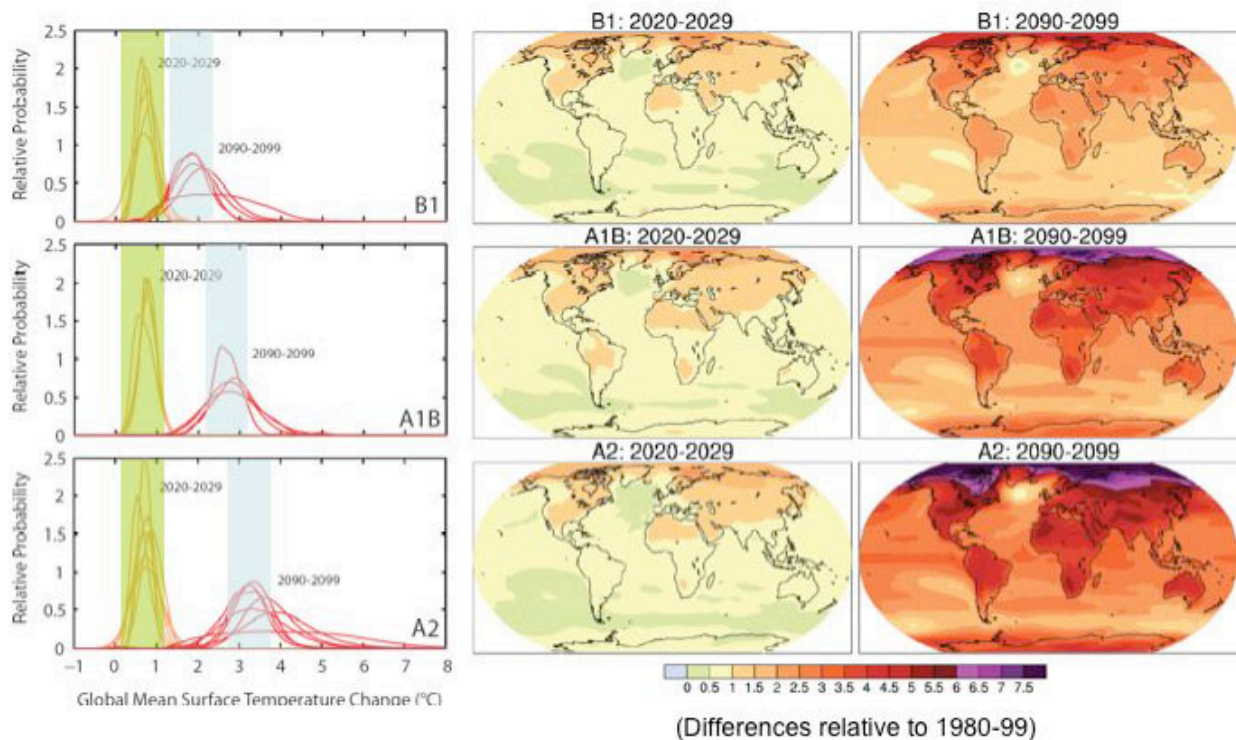


Figure 4.2. Projected surface temperature changes for the early and late 21st century relative to the period 1980 to 1999. The central and right panels show the AOGCM multi-model average projections (°C) for the B1 (top), A1B (middle) and A2 (bottom) SRES scenarios averaged over the decades 2020 to 2029 (centre) and 2090 to 2099 (right). The left panel shows corresponding uncertainties as the relative probabilities of estimated global average warming from several different AOGCM and EMIC<sup>2</sup> studies for the same periods. Some studies present results only for a subset of the SRES scenarios, or for various model versions. Therefore the difference in the number of curves, shown in the left-hand panels, is due only to differences in the availability of results.

The pattern of global warming is different between land and oceans and between low and high latitudes. In IPCC 2007 this has been better quantified from the new multi-model mean in terms of zonal averages where land and ocean values are separated. Figure 4.3 illustrates the late-century A2 case, with all values shown both in absolute terms and relative to the global mean warming. Warming over land is greater than the mean except in the southern mid-latitudes, where the warming over ocean is a minimum. Warming over ocean is smaller than the mean except at high latitudes, where sea ice changes have an influence.

<sup>2</sup> EMIC: Earth System Model of Intermediate Complexity

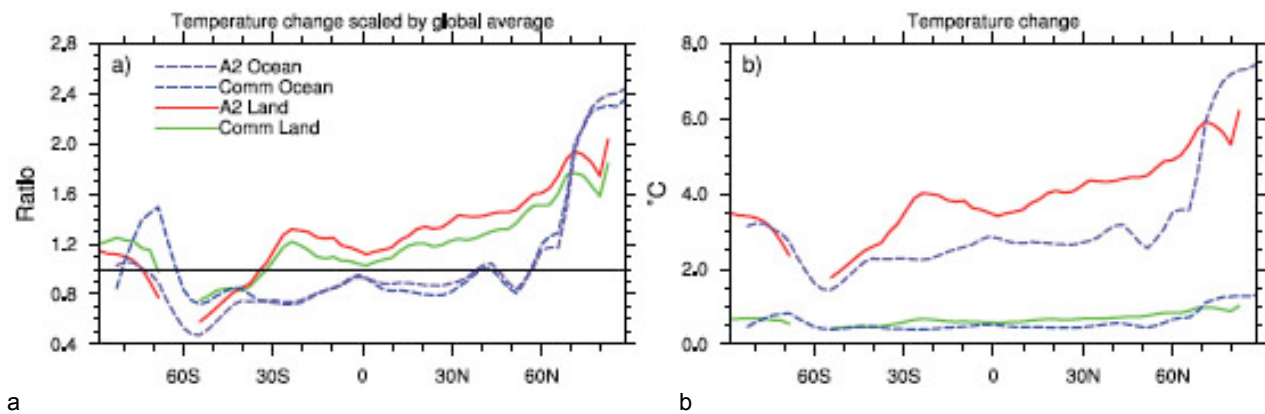


Figure 4.3 Zonal means over land and ocean separately, for annual mean surface warming, shown as ratios scaled with the global mean warming (a) and not scaled (b). Multi-model mean results are shown for two scenarios, A2 and Commitment, for the period 2080 to 2099 relative to the zonal means for 1980 to 1999. The Commitment scenario of warming is the case where greenhouse gas and aerosol concentrations are held constant from the year 2000.

The zonal mean warming for the A1B scenario at each latitude from the bottom of the ocean to the top of the atmosphere is shown in Fig. 4.4 for three periods of the 21st-century. To produce this ensemble mean, the model data were first interpolated to standard ocean depths and atmospheric pressures. Consistent with the global transfer of excess heat from the atmosphere to the ocean, and the difference between warming over land and ocean, there is some discontinuity between the plotted means of the lower atmosphere and the upper ocean. The relatively uniform warming of the troposphere and cooling of the stratosphere in this multi-model mean are consistent with the changes reported in TAR, but now its evolution during the 21st century under this scenario can also be seen.

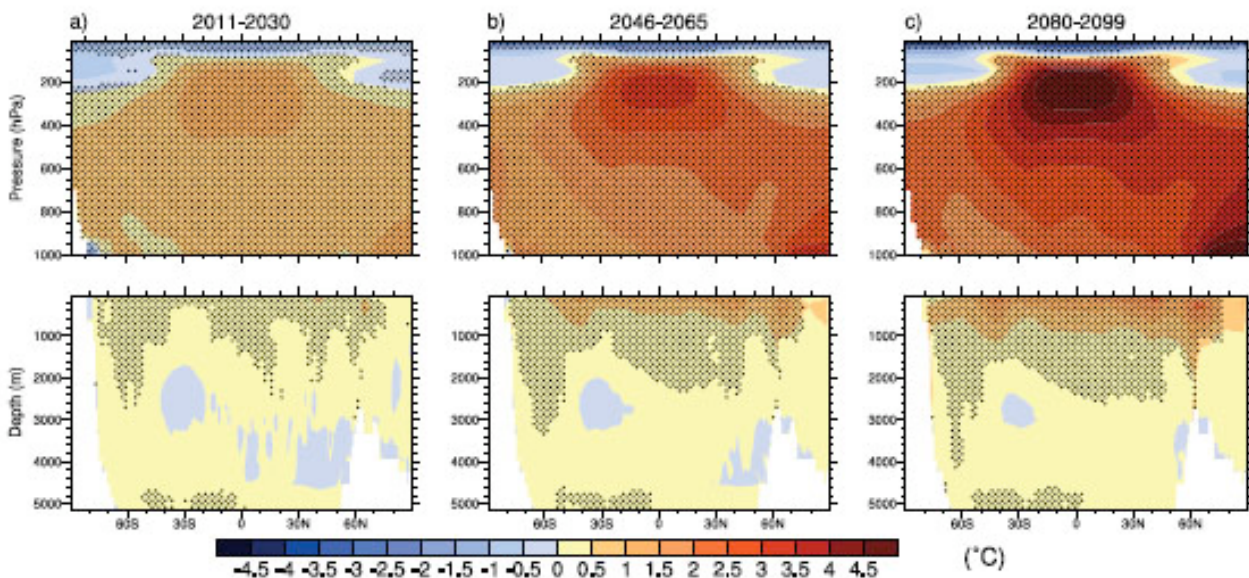


Figure 4.4 Zonal means of change in atmospheric (top) and oceanic (bottom) temperatures ( $^{\circ}\text{C}$ ), shown as south-north cross sections. Values are the multi-model means for the A1B scenario for three periods (a–c). Stippling denotes regions where the multi-model ensemble mean divided by the multi-model standard deviation exceeds 1.0 (in magnitude). Anomalies are relative to the average of the period 1980 to 1999.

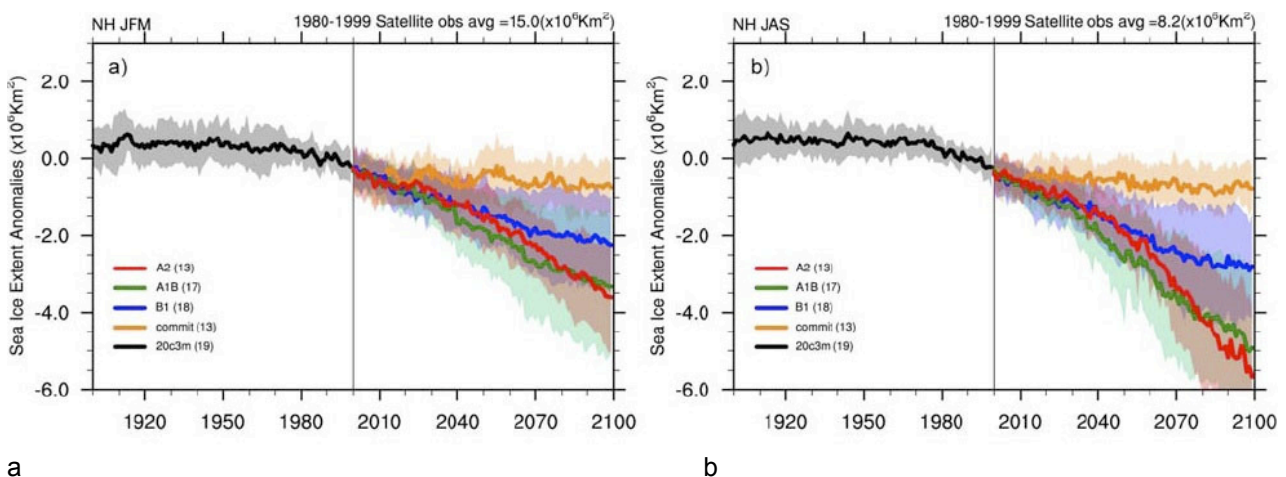


The upper-tropospheric warming reaches a maximum in the tropics and is seen even in the early-century time period. The pattern is very similar over the three periods, consistent with the rapid adjustment of the atmosphere to the forcing. These changes are simulated with good consistency among the models. The larger values of both signs are stippled, indicating that the ensemble mean is larger in magnitude than the inter-model standard deviation. The ratio of mean to standard deviation can be related to formal tests of statistical significance and confidence intervals, if the individual model results were to be considered a sample.

The ocean warming evolves more slowly. There is initially little warming below the mixed layer, except at some high latitudes. Even as a ratio with mean surface warming, later in the century the temperature increases more rapidly in the deep ocean, consistent with results from individual models (e.g., Watterson, 2003; Stouffer, 2004). This rapid warming of the atmosphere and the slow penetration of the warming into the ocean has implications for the time scales of climate change commitment.

## 4.2 Changes in Arctic sea ice cover

Models of the 21st century project that future warming is amplified at high latitudes resulting from positive feedbacks involving snow and sea ice, and other processes. The warming is particularly large in autumn and early winter (i.e. Holland and Bitz, 2003) when sea ice is thinnest and the snow depth is insufficient to blur the relationship between surface air temperature and sea ice thickness (Maykut and Untersteiner, 1971). As shown by Zhang and Walsh (2006), the coupled models show a range of responses in NH sea ice areal extent ranging from very little change to a strong and accelerating reduction over the 21st century (Figure 4.5).



**a** **b**  
 Figure 4.5 Multi-model simulated anomalies in Arctic sea ice extent for the 20th and 21st century using the SRES A2, A1B and B1 as well as the commitment scenario for (a) January to March (JFM), and (b) July to September (JAS). The solid lines show the multi-model mean, shaded areas denote  $\pm 1$  standard deviation. Sea ice extent is defined as the total area where sea ice concentration exceeds 15%. Anomalies are relative to the period 1980 to 2000. The number of models is given in the legend and is different for each scenario.

An important characteristic of the projected change is for summer ice area to decline far more rapidly than winter ice area, and hence sea ice rapidly approaches a seasonal ice cover (Figures 4.5b and 4.6b). Seasonal ice cover is, however, rather robust and persists to some extent throughout the 21st century in most (if not all) models. Bitz and Roe (2004) note that future projections show that arctic sea ice thins fastest where it is initially thickest, a characteristic that future climate projections share with sea ice thinning observed in the late 20th century (Rothrock et al., 1999). Consistent with these results, a projection by Gregory et al. (2002b) shows that arctic sea ice volume decreases more quickly than sea ice area (because trends in winter ice area are low) in the 21st century.



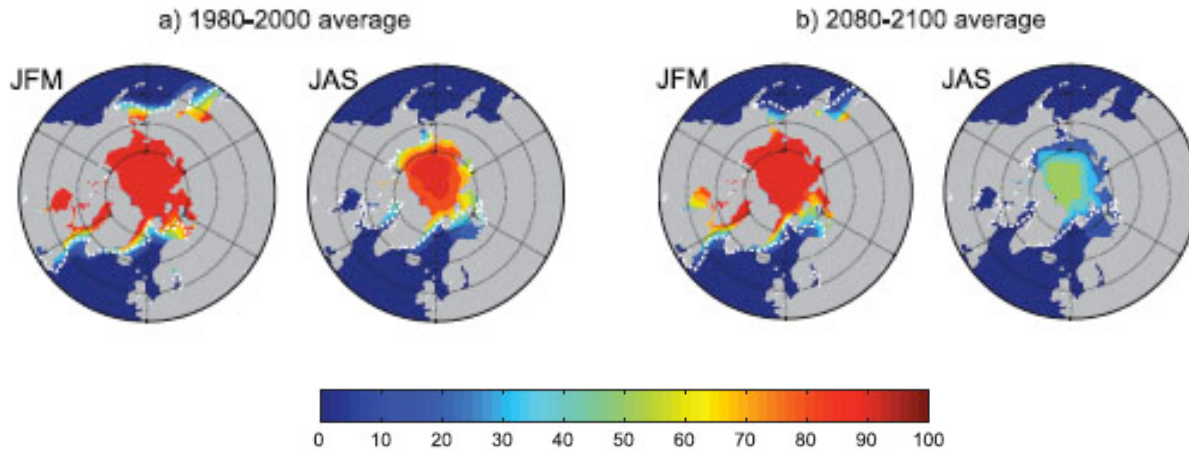


Figure 4.6 Multi-model mean sea ice concentration (%) for January to March (JFM) and June to September (JAS), in the Arctic for the periods (a) 1980 to 2000 and b) 2080 to 2100 for the SRES A1B scenario. The dashed white line indicates the present-day 15% average sea ice concentration limit. Modified from Flato et al. (2004).

Most climate models share common characteristics such as peak surface warming in autumn and early winter, sea ice rapidly becomes seasonal, arctic ice decays faster than antarctic ice, and northward ocean heat transport increases into the northern high latitudes. However, the models have poor agreement on the amount of thinning of sea ice (Flato et al., 2004; Arzel et al., 2006) and the overall climate change in the polar regions (IPCC, 2001; Holland and Bitz, 2003). Flato et al. (2004) show that the basic state of the sea ice and the reduction in thickness and/or extent have little to do with sea ice model physics among CMIP2<sup>3</sup> models. Holland and Bitz (2003) and Arzel et al. (2006) find serious biases in the basic state of simulated sea ice thickness and extent. Further, Rind et al. (1995), Holland and Bitz (2003) and Flato (2004) show that the basic state of the sea ice thickness and extent have a significant influence on the projected change in sea ice thickness in the Arctic and extent in the Antarctic.

#### 4.3 Sea ice reduction is faster than the IPCC models

Recent results from satellite and other observations presented by the National Snow and Ice Data Center (NSIDC) and the National Center for Atmospheric Research (NCAR) show that the Arctic ice cover is retreating more rapidly than estimated by any of the eighteen computer models used by the Intergovernmental Panel on Climate Change (IPCC) in preparing its 2007 assessments (Fig. 4.7). This suggests that current model projections may in fact provide a conservative estimate of future Arctic change, and that the summer Arctic sea ice may disappear considerably earlier than IPCC projections (Stroeve et al., 2007). By analyzing the IPCC computer model runs, Stroeve et al., (2007) found that, on average, the models simulated a loss in September ice cover of 2.5 percent per decade from 1953 to 2006. The fastest rate of September retreat in any individual model simulation was 5.4 percent per decade. September marks the yearly minimum of sea ice in the Arctic. But newly available data sets, blending early aircraft and ship reports with more recent satellite measurements, show that the September ice actually declined at a rate of about 7.8 percent per decade during the 1953 to 2006 period.

Stroeve et al (2007) speculate that the computer models may fail to capture the full impact of increased carbon dioxide and other greenhouse gases in the atmosphere. Whereas the models indicate that about half of the ice loss from 1979 to 2006 was caused by increased greenhouse

<sup>3</sup> CMIP2: Coupled Model Intercomparison Project (<http://www-pcmdi.llnl.gov/projects/cmip/announ.php>)

gases, and the other was half caused by natural variations in the climate system, the new study indicates that greenhouse gases may be playing a significantly higher role. There are a number of factors that may lead to the low rates of simulated sea ice loss. Several models overestimate the thickness of the present day sea ice and the models may also fail to capture changes in atmosphere and ocean circulation that transport heat to polar regions. Although the loss of ice for March is far less dramatic than the September loss, the models underestimate it by a wide margin, as well. The actual rate of sea ice loss in March, about  $-1.8$  percent per decade in the 1953 to 2006 period, was three times larger than the mean from the computer models.

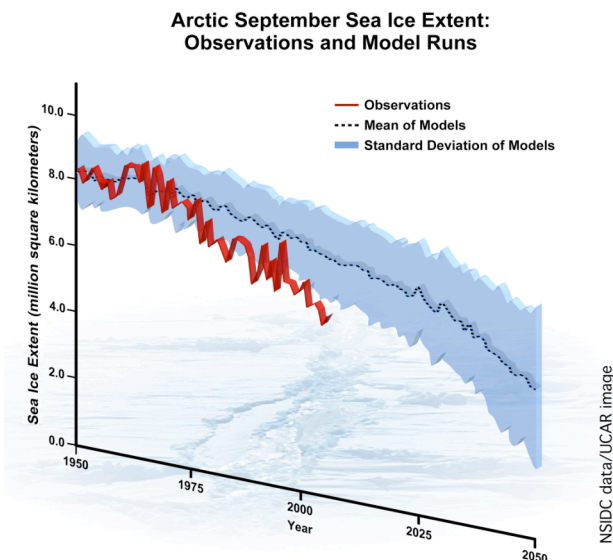


Figure 4.7. Actual observations of September Arctic sea ice, in red, show a more severe decline than any of the eighteen computer models, averaged in a dashed line, that the 2007 IPCC reports reference (Stroeve et al., 2007).

#### 4.4 Precipitation

Models simulate that global mean precipitation increases with global warming. However, there are substantial spatial and seasonal variations in this field even in the multi-model means depicted in Figure 4.8. A feature common to all climate model projections is the increase in high-latitude temperature as well as an increase in high-latitude precipitation. Since the TAR, there is an improved understanding of projected patterns of precipitation (Fig. 4.8).

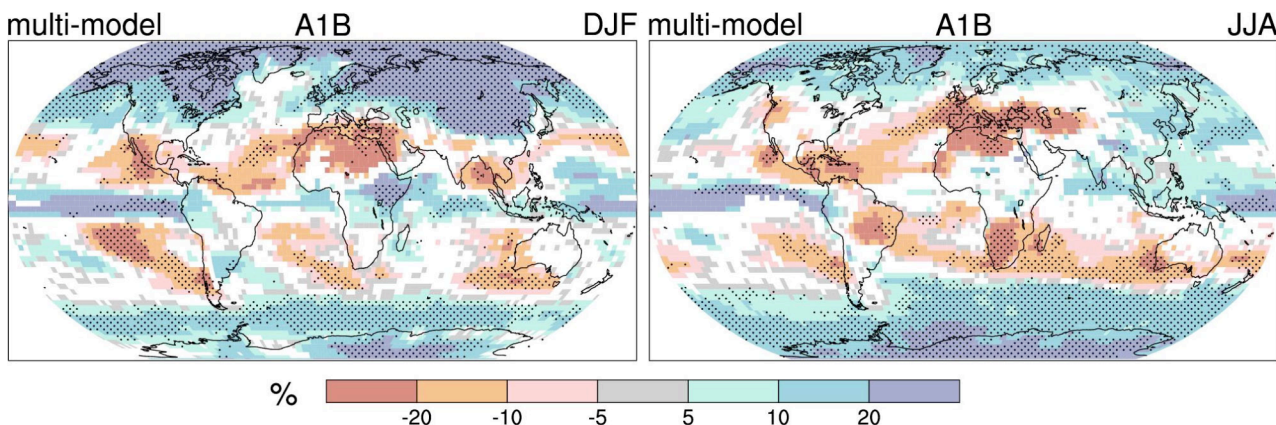


Figure 4.8 Spatial patterns of the multi-model mean precipitation changes (in %) for the period 2090 to 2099 relative to 1980 to 1999 (% change) based on the SRES A1B scenario. December to February means are in the left column, June to August means in the right column. The changes are plotted only where more than 66% of the models agree on the sign of the change. The

*stippling indicates areas where more than 90% of the models agree on the sign of the change.*

Increases in the amount of precipitation are *very likely* at high latitudes while decreases are *likely* in most subtropical land regions (by as much as about 20% in the A1B scenario in 2100). Poleward of 50°, mean precipitation is projected to increase due to the increase in water vapour in the atmosphere and the resulting increase in vapour transport from lower latitudes. The increase in high northern latitudes is most pronounced in the winter months.

#### 4.5 Atlantic Meridional Overturning Circulation

Both of the effects of warming and increased precipitation tend to make the high-latitude surface waters less dense and hence increase their stability, thereby inhibiting convective processes. As more coupled models have become available since the TAR, the evolution of the Atlantic Meridional Overturning Circulation (MOC) can be more thoroughly assessed. Figure 4.9 shows simulations from 19 coupled models integrated from 1850 to 2100 under SRES A1B atmospheric CO<sub>2</sub> and aerosol scenarios up to year 2100, and constant concentrations thereafter.

Generally, the simulated late-20th century Atlantic MOC shows a spread ranging from a weak MOC of about 12 Sv to over 20 Sv (Figure 4.9). When forced with the SRES A1B scenario, the models show a reduction in the MOC of up to 50% or more, but in one model, the changes are not distinguishable from the simulated natural variability. The reduction in the MOC proceeds on the time scale of the simulated warming because it is a direct response to the increase in buoyancy at the ocean surface. A positive North Atlantic Oscillation (NAO) trend might delay this response by a few decades but not prevent it (Delworth and Dixon, 2000). Such a weakening of the MOC in future climate causes reduced sea surface temperature (SST) and salinity in the region of the Gulf Stream and North Atlantic Current (Dai et al., 2005). This can produce a decrease in northward heat transport south of 60°N, but increased northward heat transport north of 60°N (A. Hu et al., 2004). No model shows an increase in the MOC in response to the increase in greenhouse gases, and no model simulates an abrupt shut-down of the MOC within the 21st century.

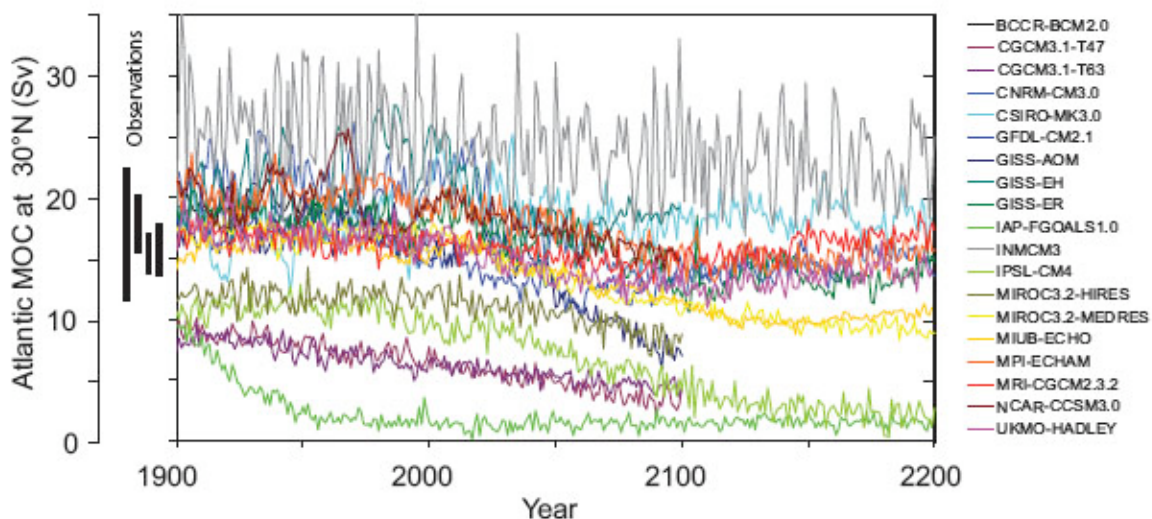


Figure 4.9 Evolution of the Atlantic meridional overturning circulation (MOC) at 30°N in simulations with the suite of comprehensive coupled climate models from 1850 to 2100 using 20th Century Climate in Coupled Models (20C3M) simulations for 1850 to 1999 and the SRES A1B emissions scenario for 1999 to 2100. Observationally based estimates of late-20th century MOC are shown as vertical bars on the left. Three simulations show a steady or rapid slow down of the MOC that is unrelated to the forcing; a few others have late-20th century simulated values that are inconsistent with observational estimates. Of the model simulations consistent with the late-20th century observational estimates, no simulation shows an increase in the MOC during the 21st century; reductions range from indistinguishable within the simulated natural variability to over 50% relative to the 1960 to 1990 mean; and none of the models projects an abrupt transition to an off state of



the MOC. Adapted from Schmittner et al. (2005) with additions.

The reduction in MOC strength associated with increasing greenhouse gases represents a negative feedback for the warming in and around the North Atlantic. That is, through reducing the transport of heat from low to high latitudes, SSTs are cooler than they would otherwise be if the MOC was unchanged. As such, warming is reduced over and downstream of the North Atlantic. Various simulations using coupled models of different complexity find significant reductions in convection in the GIN Sea in response to warming (Schaeffer et al., 2004; Bryan et al., 2006). Presumably, a delicate balance exists in the GIN Sea between the circum-arctic river runoff, sea ice production and advection of saline waters from the North Atlantic, and on a longer time scale, the inflow of freshwater through Bering Strait. The projected increases in circum-arctic river runoff (Wu et al., 2005) may enhance the tendency towards a reduction in GIN Sea convection (Stocker and Raible, 2005; Wu et al., 2005).

In conclusion, it is very likely that the MOC, based on currently available simulations, will decrease, perhaps associated with a significant reduction in Labrador Sea Water formation, but very unlikely that the MOC will undergo an abrupt transition during the course of the 21st century. At this stage, it is too early to assess the likelihood of an abrupt change of the MOC beyond the end of the 21st century, but the possibility cannot be excluded.

#### 4.6 Greenland ice sheet melting

A consistent feature of all climate models is that projected 21st-century warming is amplified in northern latitudes. This suggests continued melting of the Greenland Ice Sheet, since increased summer melting dominates over increased winter precipitation in model projections of future climate. Ridley et al. (2005) coupled UKMO-HadCM3 to an ice sheet model to explore the melting of the Greenland Ice Sheet under elevated (four times pre-industrial) levels of atmospheric CO<sub>2</sub> (Figure 4.10). While the entire Greenland Ice Sheet eventually completely ablated (after 3 kyr), the peak rate of melting was 0.06 Sv corresponding to about 5.5 mm yr<sup>-1</sup> global sea level rise. Toniazzo et al. (2004) further show that in UKMO-HadCM3, the complete melting of the Greenland Ice sheet is an irreversible process even if pre-industrial levels of atmospheric CO<sub>2</sub> are re-established after it melts.

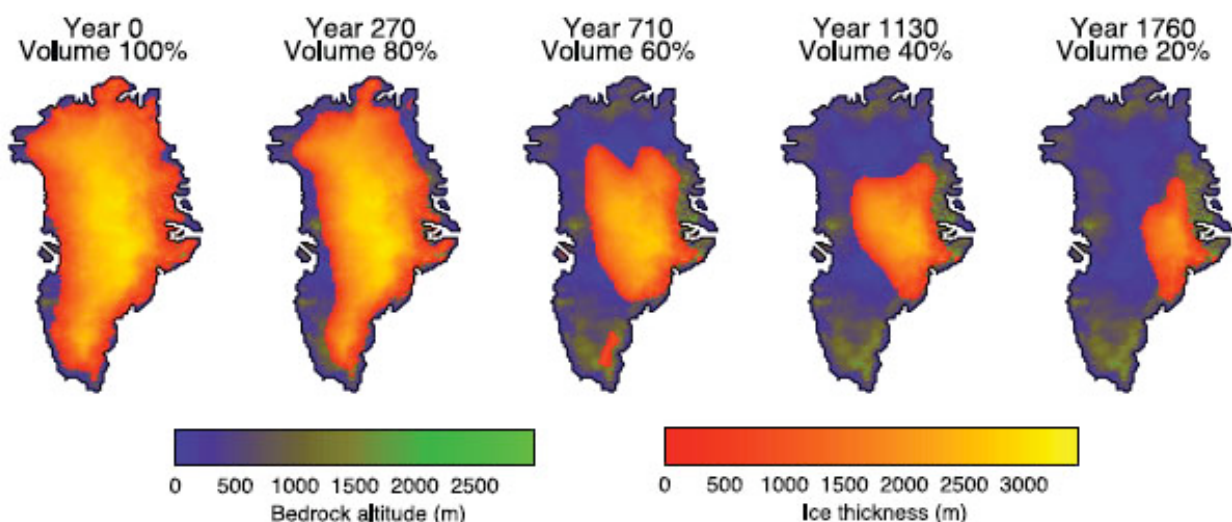


Figure 4.10 Evolution of Greenland surface elevation and ice sheet volume versus time in the experiment of Ridley et al. (2005) with the UKMO-HadCM3 AOGCM coupled to the Greenland Ice Sheet model of Huybrechts and De Wolde (1999) under a climate of constant quadrupled pre-industrial atmospheric CO<sub>2</sub>.



#### 4.7 Sea level rise

Sea level is projected to rise between the present (1980–1999) and the end of this century (2090–2099) under selected SRES scenarios as shown in Fig. 4.11a. These are 5 to 95% ranges based on the spread of AOGCM results, not including uncertainty in carbon cycle feedbacks. For each scenario, the midpoint of the range is within 10% of the TAR model average for 2090–2099. The ranges are narrower than in the TAR mainly because of improved information about some uncertainties in the projected contributions. In all scenarios, the average rate of rise during the 21st century *very likely* exceeds the 1961 to 2003 average rate ( $1.8 \pm 0.5$  mm yr<sup>-1</sup>). During 2090 to 2099 under A1B, the central estimate of the rate of rise is 3.8 mm yr<sup>-1</sup>. For an average model, the scenario spread in sea level rise is only 0.02 m by the middle of the century, and by the end of the century it is 0.15 m.

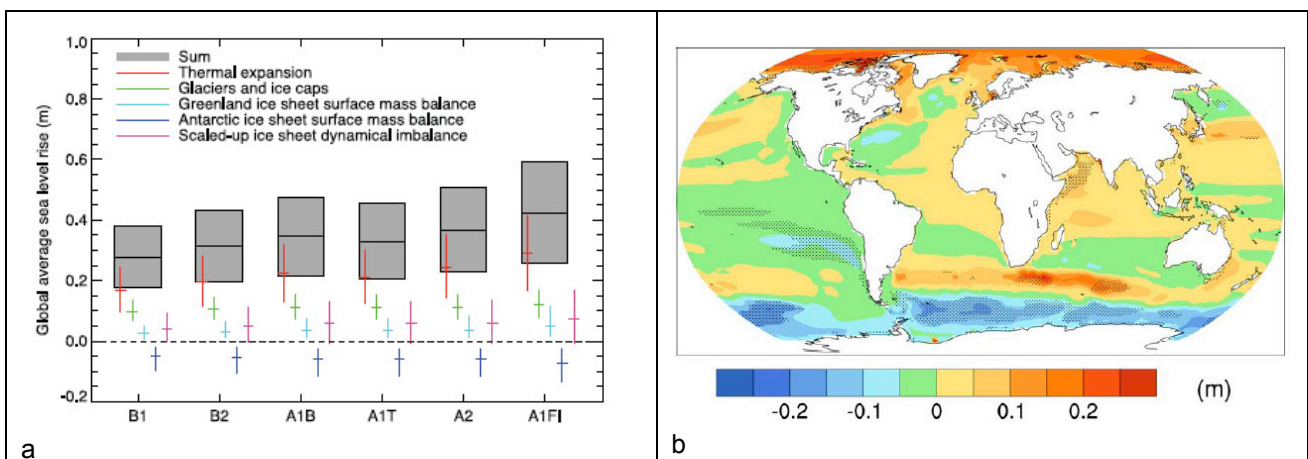


Figure 4.11. (a) Projections and uncertainties (5 to 95% ranges) of global average sea level rise and its components in 2090 to 2099 (relative to 1980 to 1999) for the six SRES marker scenarios. The projected sea level rise assumes that the part of the present-day ice sheet mass imbalance that is due to recent ice flow acceleration will persist unchanged. It does not include the contribution shown from scaled-up ice sheet discharge, which is an alternative possibility. It is also possible that the present imbalance might be transient, in which case the projected sea level rise is reduced by 0.02 m. It must be emphasized that we cannot assess the likelihood of any of these three alternatives, which are presented as illustrative. (b) Local sea level change (m) due to ocean density and circulation change relative to the global average (i.e., positive values indicate greater local sea level change than global) during the 21st century, calculated as the difference between averages for 2080 to 2099 and 1980 to 1999, as an ensemble mean over 16 AOGCMs forced with the SRES A1B scenario. Stippling denotes regions where the magnitude of the multi-model ensemble mean divided by the multi-model standard deviation exceeds 1.0.

Thermal expansion is the largest component, contributing 70 to 75% of the central estimate in these projections for all scenarios. Glaciers, ice caps and the Greenland Ice Sheet are also projected to contribute positively to sea level. General Circulation Models indicate that the Antarctic Ice Sheet will receive increased snowfall without experiencing substantial surface melting, thus gaining mass and contributing negatively to sea level. Further accelerations in ice flow of the kind recently observed in some Greenland outlet glaciers and West Antarctic ice streams could substantially increase the contribution from the ice sheets. For example, if ice discharge from these processes were to scale up in future in proportion to global average surface temperature change (taken as a measure of global climate change), it would add 0.1 to 0.2 m to the upper bound of sea level rise by 2090 to 2099. In this example, during 2090 to 2099 the rate of scaled-up Antarctic discharge would roughly balance the expected increased rate of Antarctic

accumulation, being under A1B a factor of 5 to 10 greater than in recent years. Understanding of these effects is too limited to assess their likelihood or to give a best estimate. Sea level rise during the 21st century is projected to have substantial geographical variability. The model median spatial standard deviation is 0.08 m under A1B. The patterns from different models are not generally similar in detail, but have some common features, including smaller than average sea level rise in the Southern Ocean, larger than average in the Arctic, and a narrow band of pronounced sea level rise stretching across the southern Atlantic and Indian Oceans.

#### 4.8 Snow cover and frozen ground

Snow cover is an integrated response to both temperature and precipitation and exhibits strong negative correlation with air temperature in most areas with a seasonal snow cover. Because of this temperature association, the simulations project widespread reductions in snow cover over the 21st century (Fig. 4.12). For the Arctic Climate Impact Assessment (ACIA) model mean, at the end of the 21st century the projected reduction in the annual mean NH snow cover is 13% under the B2 scenario (ACIA, 2005). The individual model projections range from reductions of 9 to 17%. The actual reductions are greatest in spring and late autumn/early winter, indicating a shortened snow cover season (ACIA, 2005). The beginning of the snow accumulation season (the end of the snowmelt season) is projected to be later (earlier), and the fractional snow coverage is projected to decrease during the snow season (Hosaka et al., 2005).

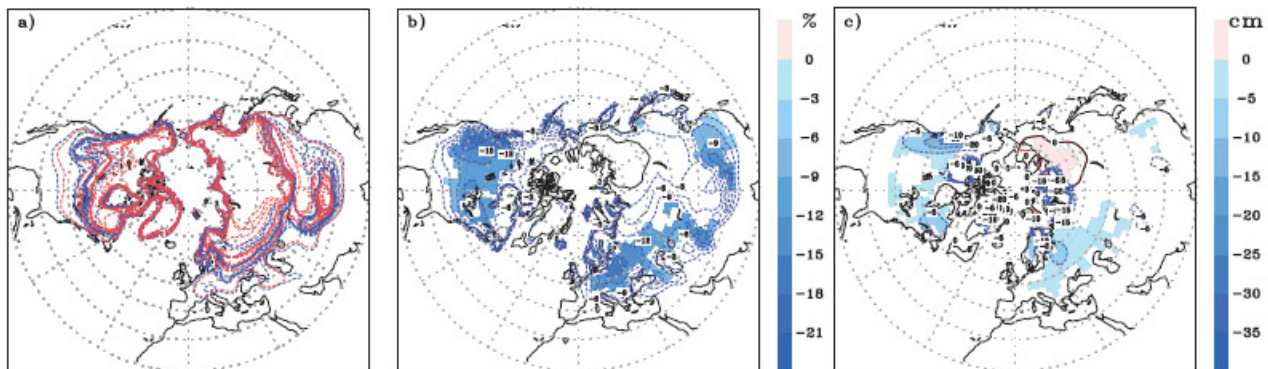


Figure 4.12. Multi model mean snow cover and projected changes over the 21st century from 12 (a and b) and 11 (c) AOGCMs, respectively. a) Contours mark the locations where the December to February (DJF) snow area fraction exceeds 50%, blue for the period 1980–1999, and red for 2080–2099, dashed for the individual models and solid for the multi model mean. b) Projected multi model mean change in snow area fraction over the period 2080–2099, relative to 1980–1999. Shading denotes regions where the ensemble mean divided by the ensemble standard deviation exceeds 1.0 (in magnitude), c) as b) but changes in snow depth (in cm).

Warming at high northern latitudes in climate model simulations is also associated with large increases in simulated thaw depth over much of the permafrost regions (Lawrence and Slater, 2005; Yamaguchi et al., 2005; Kitabata et al., 2006). Yamaguchi et al. (2005) show that initially soil moisture increases during the summer. In the late 21st century when the thaw depth has increased substantially, a reduction in summer soil moisture eventually occurs (Kitabata et al., 2006). Stendel and Christensen (2002) show poleward movement of permafrost extent, and a 30 to 40% increase in active layer thickness for most of the permafrost area in the NH, with the largest relative increases concentrated in the northernmost locations.

Regionally, the changes are a response to both increased temperature and increased precipitation (changes in circulation patterns) and are complicated by the competing effects of warming and increased snowfall in those regions that remain below freezing. In general, snow amount and snow coverage decreases in the NH. However, in a few regions (e.g., Siberia), snow amount is projected to increase. This is attributed to the increase in precipitation (snowfall) from autumn to

winter (Meleshko et al., 2004; Hosaka et al., 2005).

#### 4.9 Sea level pressure and atmospheric circulation

As a basic component of the mean atmospheric circulations and weather patterns, projections of the mean sea level pressure for the medium scenario A1B are considered. Seasonal mean changes for DJF and JJA are shown in Figure 4.13. Sea level pressure differences show decreases at high latitudes in both seasons in both hemispheres. The compensating increases are predominantly over the mid-latitude and subtropical ocean regions in DJF. Many of these increases are consistent across the models.

Sea level pressure is projected to increase over the subtropics and mid-latitudes, and decrease over high latitudes (order several millibars by the end of the 21st century) associated with a poleward expansion and weakening of the Hadley Circulation and a poleward shift of the storm tracks of several degrees latitude with a consequent increase in cyclonic circulation patterns over the high-latitude arctic and antarctic regions. Thus, there is a projected positive trend of the Northern Annular Mode (NAM) and the closely related North Atlantic Oscillation (NAO). This helps explain, in part, the increases in precipitation at high latitudes and decreases in the subtropics and parts of the mid-latitudes. The pattern of pressure change implies increased westerly flows across the western parts of the continents. These contribute to increases in mean precipitation (Fig. 4.8) and increased precipitation intensity (Meehl et al., 2005a).

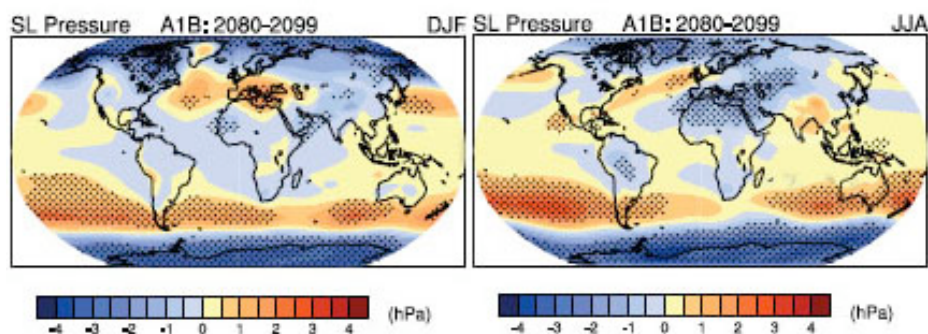


Figure 4.13. Multi-model mean changes in sea level pressure for boreal winter (DJF, left) and summer (JJA, right). Changes are given for the SRES A1B scenario, for the period 2080 to 2099 relative to 1980 to 1999. Stippling denotes areas where the magnitude of the multi-model ensemble mean exceeds the inter-model standard deviation.

#### 4.10 Extreme weather and climate events

In a warmer future climate, there will be an increased risk of more intense, more frequent and longer-lasting heat waves. The European heat wave of 2003 is an example of the type of extreme heat event lasting from several days to over a week that is likely to become more common in a warmer future climate. Also hurricanes in the north Atlantic have been more frequent and intense in the last ten years (Fig. 4.14). A related aspect of temperature extremes is that there is likely to be a decrease in the daily (diurnal) temperature range in most regions. It is also likely that a warmer future climate would have fewer frost days (i.e., nights where the temperature dips below freezing). Growing season length is related to number of frost days, and has been projected to increase as climate warms. There is likely to be a decline in the frequency of cold air outbreaks (i.e., periods of extreme cold lasting from several days to over a week) in NH winter in most areas. Exceptions could occur in areas with the smallest reductions of extreme cold in western North America, the North Atlantic and southern Europe and Asia due to atmospheric circulation changes.

In a warmer future climate, most Atmosphere-Ocean General Circulation Models project increased



summer dryness and winter wetness in most parts of the northern middle and high latitudes. Summer dryness indicates a greater risk of drought. Along with the risk of drying, there is an increased chance of intense precipitation and flooding due to the greater water-holding capacity of a warmer atmosphere. This has already been observed and is projected to continue because in a warmer world, precipitation tends to be concentrated into more intense events, with longer periods of little precipitation in between. Therefore, intense and heavy downpours would be interspersed with longer relatively dry periods. Another aspect of these projected changes is that wet extremes are projected to become more severe in many areas where mean precipitation is expected to increase, and dry extremes are projected to become more severe in areas where mean precipitation is projected to decrease.

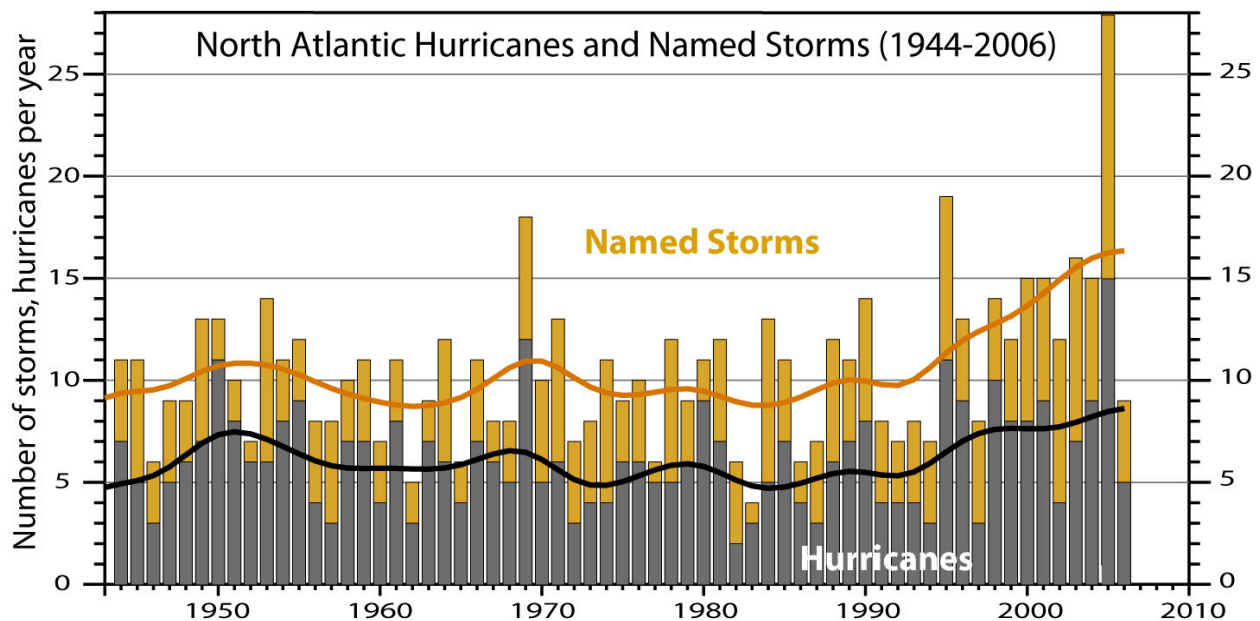


Figure 4.14. Annual number of hurricanes and named storms in the North Atlantic from 1944 to 2006.

In concert with the results for increased extremes of intense precipitation, even if the wind strength of storms in a future climate did not change, there would be an increase in extreme rainfall intensity. In particular, over NH land, an increase in the likelihood of very wet winters is projected over much of central and northern Europe due to the increase in intense precipitation during storm events, suggesting an increased chance of flooding over Europe and other mid-latitude regions due to more intense rainfall and snowfall events producing more runoff. Similar results apply for summer precipitation, with implications for more flooding in the Asian monsoon region and other tropical areas. The increased risk of floods in a number of major river basins in a future warmer climate has been related to an increase in river discharge with an increased risk of future intense storm-related precipitation events and flooding. Some of these changes would be extensions of trends already underway.

There is evidence from modelling studies that future tropical cyclones could become more severe, with greater wind speeds and more intense precipitation. Studies suggest that such changes may already be underway; there are indications that the average number of Category 4 and 5 hurricanes per year has increased over the past 30 years. Some modelling studies have projected a decrease in the number of tropical cyclones globally due to the increased stability of the tropical troposphere in a warmer climate, characterised by fewer weak storms and greater numbers of intense storms. A number of modelling studies have also projected a general tendency for more intense but fewer storms outside the tropics, with a tendency towards more extreme wind events and higher ocean waves in several regions in association with those deepened cyclones. Models also project a poleward shift of storm tracks in both hemispheres by several degrees of



latitude (Fig. 4.15).

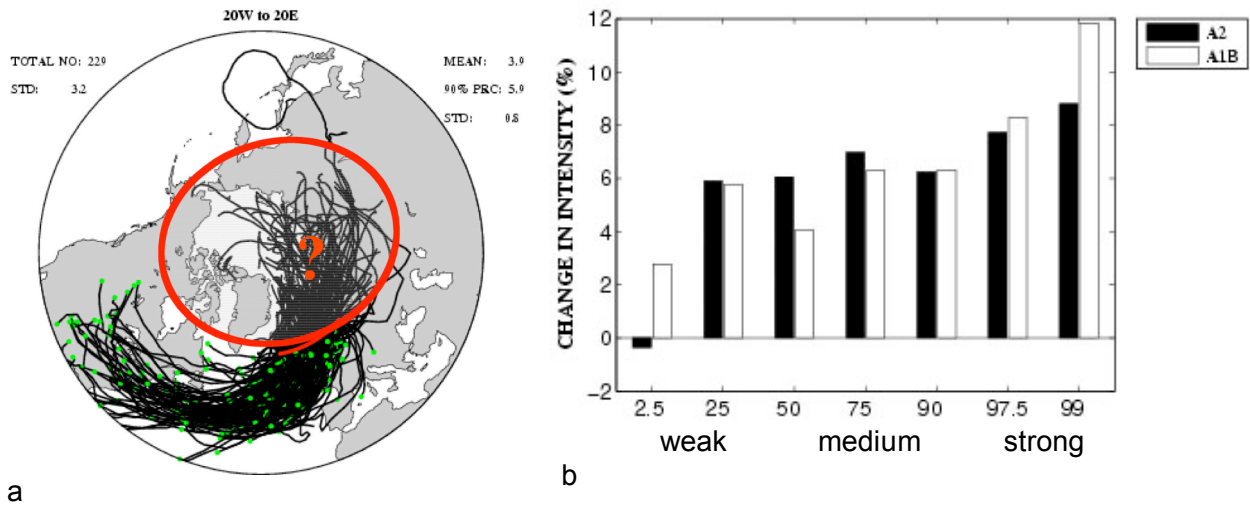


Figure 4.15. (a) Low pressure paths from the North Atlantic to the Arctic region from Bergen Climate Model simulations; (b) Percentage change in low pressure intensity for weak, medium and strong low pressures based on scenarios A2 and A1B. Courtesy: A. Sorteberg.

## 5. Conclusions and impact on Arctic design and operations

It is reasonable to characterize the Arctic climate change as a combination of natural variability on interannual and decadal scale and a long term warming trend due to greenhouse gas emissions. Such a scenario is at least partly in agreement with time series of the Arctic Oscillation (AO) and the North Atlantic Oscillation (NAO), which are often used as indices of Arctic climate variability. The conclusions in the last IPCC 2007 report are more definite about the climate change in the Arctic regions compared to earlier assessments: The IPCC 2007 report states the following about the projected climate change in the 21st century:

- *The Arctic is very likely to warm during this century in most areas, and the annual mean warming is very likely to exceed the global mean warming. Warming is projected to be largest in winter and smallest in summer.*
- *Annual arctic precipitation is very likely to increase. It is very likely that the relative precipitation increase will be largest in the winter and smallest in summer.*
- *Arctic sea ice is very likely to decrease in extent and thickness. It is uncertain how the Arctic Ocean circulation will change.*

Increased air temperature may lead to enhanced hydrological cycle and greater moisture convergence into the Arctic Ocean providing increased stratification in the upper ocean. Melting of large amounts of sea ice must also lead to dramatic increases in the fresh water flux out from the Arctic Ocean. The Great Salinity Anomaly of the late 1960s and 1970s is a good example of such an extreme event. An excess of fresh water exported from the Arctic into the Nordic and Labrador seas can alter or stop convection there, thus strongly affecting the formation of North Atlantic Deep Water and the global thermohaline circulation.

Regional models of the Arctic Ocean have increased their spatial resolution by an order of magnitude, from the order of 100 km to 10 km, during the last decade. As a result, many important (and commonly neglected) small-scale bathymetric and geographic features have been included in such models. This allows more realistic representation of circulation and water mass and properties exchanges within the Arctic Ocean and its interactions with the global ocean. High model resolution also allows to better address new tactical requirements of operational ice prediction models, such as ice edge position, lead orientation, and sea ice thickness and concentration.

The large scale drift of sea ice and its properties as well as the fresh water export from the Russian shelves and the Atlantic Water circulation within the Arctic Basins change in the recent decades. The most significant changes in Atlantic water masses has been observed in the Eurasian and Makarov basins, over the Chukchi/Beaufort shelves and slopes and in the Canadian Archipelago. Results from both observations and models indicate that a continuation of large scale measurements including repeated basin-wide hydrographic transects and focused process studies in the above mentioned regions should be of highest priority. This would allow evaluation of what may be an inherent cyclicity in Arctic climate and understanding and possibly more reliable predictions of future climate change in the Arctic Ocean.

**Scenario for sea ice changes:** Several scenarios suggest that the observed trend of reduced ice extent will continue and that summer ice extent may nearly disappear towards the end of the 21<sup>st</sup> century. This means that the multiyear ice will be absent, leaving the Arctic Ocean with only a seasonal ice cover. For volume and thickness, a conservative estimate is obtained by extrapolating model forecasts which are not contradicted by sparse observations. Thinning of the ice cover will continue, but the rate of thinning and its geographical distribution is difficult to estimate. Observations of ice thickness are sparse, and model simulations show highly variable

prediction of ice thickness change. The melt seasons will be longer and reductions in multiyear ice have key operational implications, leading to greater access and longer navigation season for shipping around the Arctic basin.

**Scenario for changing weather regimes:** Recent scenarios of climate change in the Arctic produced by state-of-the-art global climate models (GCMs) suggest that the Arctic/subArctic will experience substantial warming compared to the present situation. The temperature in many models shows a 6-8°C warming over the ocean during winter, with a less dramatic change in terrestrial regions. With higher temperature and reduction of the ice cover, the marginal ice zone will migrate considerably polewards throughout the year. Less sea ice will clearly lead to much greater latent and sensible surface heat fluxes into the Arctic boundary layer (BL). A warmer and moister BL would most likely produce greater BL cloudiness, perhaps extending the current observed summer cloud fractional coverage maximum on both ends of the warm season. This would result in poorer surface visibility for a greater portion of the year, and in the winter could also increase the likelihood of freezing mist and drizzle. Since the temperature of the continental Arctic away from the coastal regions will continue to be modulated largely by radiative energy loss (assuming that seasonal snow cover still pertains), the temperature differences between land and ocean will likely be more pronounced, creating more localized baroclinicity to the coastal regions in the cold season. Given the ingredients of greater baroclinicity, a BL environment with significantly enriched latent energy, and the strong planetary vorticity implicit in the high latitude setting, it seems reasonable for Arctic cyclogenesis of so-called polar lows to be more common than currently observed during much of the year. The current tendency of poleward-propagating extratropical cyclones to decay in cooler sub-Arctic waters (for example as currently happens in the Aleutians/Bering Sea) might be diminished, causing stronger and more frequent storm events in the sub-Arctic coastal areas. Vessel icing could also increase in these areas, especially during outbreak of cold Arctic continental air masses. With more mixed-phase precipitation through a much greater portion of the year, the threat of aircraft icing would also be greatly enhanced.

How can the climate change in the Arctic effect the various sub-Arctic regions where offshore operations are foreseen? During winter, the central Arctic and all peripheral seas including the Greenland Sea, Bering Sea, and Gulf of St. Lawrence will continue to have significant ice cover. Ice extent and thickness will generally be reduced. The Sea of Okhotsk and Sea of Japan will be ice-free for the entire year. In late summer, the entire Russian coast will be ice free, allowing navigation through the Barents, Kara, Laptev and East Siberian Seas along the entire Northern Sea Route. This situation has already been observed in the last couple of summers. The Northwest Passage through the Canadian Archipelago and along the coast of Alaska will in general be ice free and navigable in summer by non-icebreaking ships. Ice will be present all year along the eastern and northern coasts of Greenland. Ice will also remain throughout the summer within and adjacent to the northern Canadian Archipelago. However, severe winters with more ice than average may also be expected due to the natural variability of the climate system. The effect of more wind and waves in ice-covered areas will be increased ridging and stamukhas in near coastal regions. This means that vessels and installations must be designed to meet extreme ice forcing.

The main elements of Arctic climate change with impact on offshore industry can be summarized as follows:

- The climate of the Arctic will have interannual and decadal scale natural variability, expressed by indices such as Arctic Oscillation (AO) and the North Atlantic Oscillation (NAO). This means that there will relatively warmer and colder periods superimposed on a long-term trend of warming.
- Model studies indicate that temperatures in the Arctic region will increase by mid-century with summer temperature (Jun-Aug) increasing by 1-2 deg. C, autumn (Sep-Nov) by 7-8 deg. C, winter (Dec-Feb) by 8-9 deg. C and spring (Mar-May) by about 5 deg. C. Variations between model predictions are of the order of 1-2 deg. C in summer and 5-6 deg. C in

winter. The most pronounced warming is expected in the European sector of the Arctic, according to the Bergen Climate Model (Fig. 5.1a).

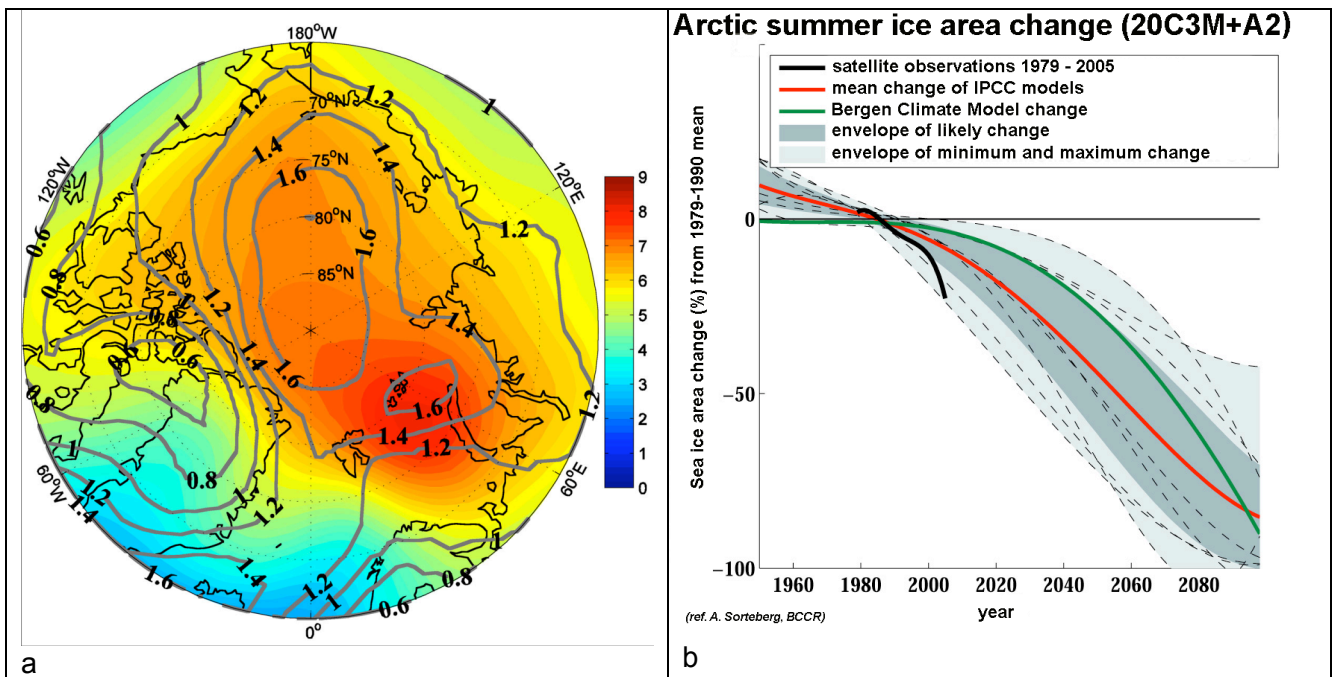


Figure 5.1 (a) Predicted ensemble mean increase (colours) in surface temperature by the end of the 21<sup>st</sup> century compared to 1980-2000, from BCM simulations (Sorteberg et al., 2005). The contours indicate the maximum difference between the ensemble members; (b) Predicted (colored lines) and observed (thick solid line) decrease of Arctic sea ice area from IPCC models, Bergen Climate Model (BCM) and satellite data from 1979-2005.

- In the winter the entire Arctic Basin will be ice covered. Model studies suggest that summer ice extent will decrease by roughly 30% and ice volume by roughly 40%. A conservative consideration of model results suggests summer ice extent will decrease by only 15% and that ice volume will decrease by 40% leading to an increase in the relative abundance of thin, first-year ice. Recent observations show, however, that the decrease in sea ice extent can be faster than the IPCC models predict (Fig. 5.1b and Fig. 4.7).
- In the atmosphere, the Arctic boundary layer will be warmer and wetter. Cloudiness will increase, extending the summer cloudy regime into earlier onset and later decline. The likelihood of freezing mist and drizzle will increase as a result.
- Polar low pressure systems will become more common and boundary layer forced convection will increase mixed phase (ice-water) precipitation. Vessel and aircraft icing will be more common.
- Sea level will increase more in the high northern latitudes compared to most other regions of the world. Along the Norwegian coast the mean sea level is predicted to increase from 0.50 to 0.80 m during the 21<sup>st</sup> century.
- Arctic warming will affect permafrost. The active (seasonally melted) layer will thicken and permafrost extent in the discontinuous permafrost region (along the borders of permafrost stability) will decrease. The inner and outer boundaries of the discontinuous zone will move to the North.



- Changes in timing and composition of river runoff will affect surface seawater. Increased sediment loads in spring runoff will spread out at sea affecting optical transparency.
- Increased melting of glaciers and ice sheet will transport more freshwater to the ocean, with impact on water mass and circulation
- Less sea ice will increase trafficability in the Northern Sea Route and other Arctic sailing routes.
- The Sea of Okhotsk and the Sea of Japan will remain ice-free throughout the year. The Russian coast and the Canadian Archipelago will be ice free and open to navigation by non-ice-strengthened ships in summer.
- Icing of ships and aircraft will require accommodation in ship/aircraft design and operation. Weapons systems will also be affected by icing conditions.
- Climate warming is likely to bring extensive fishing activity to the Arctic, particularly in the Barents Sea and Beaufort/Chukchi region where commercial operations have been minimal in the past. In addition, Bering Sea fishing opportunities will increase as sea ice cover begins later and ends sooner in the year.
- Ecological disruption due to climate induced separation of essential habitats can be expected with particular effects on marine mammal populations.
- The exploration, development, production and transportation of petroleum in the Arctic will expand with or without climate change as prices continue to rise due to the decreasing rate of discovery of reserves elsewhere. Climate warming and reduction in ice cover will facilitate and perhaps accelerate the process.

Even if the general long-term trends seem to be clear regarding sea ice and air temperatures, it is important to be aware of the decadal variability in the Arctic climate system. The understanding of the polar climate system and its variability is still incomplete due to its complex atmosphere-land-cryosphere-ocean interactions. The global models used to simulate the climate change are not representing processes such as clouds, planetary boundary layer processes and sea ice very well. Additionally, the resolution of global models is still not adequate to resolve important processes in the polar seas. All this contributes to a rather large range of present-day and future simulations, which may reduce confidence in the future projections. A serious problem is the lack of observations in the polar regions against which to assess models, and for developing process knowledge. Planning of offshore operations in the Arctic need to consider that there is considerable uncertainty in the predictions of atmosphere, sea ice and ocean changes for the different regions of Arctic for the next decades.

## 6. References

- Abdalati, W., W. Krabill, E. Frederick, S. Manizade, C. Martin, J. Sonntag, R. Swift, R. Thomas, W. Wright, and J. Yungel (2001). Outlet glacier and margin elevation changes: Near-coastal thinning of the Greenland ice sheet, 2001. *J. Geophys. Res.*, 106(D24), 33,729–33,742.
- Abramov, V. and G. K. Zubakin (1992). Russian iceberg observations 1970-1989, OKN IDAP report, December 1992, 37 pp.
- Abramov, V. (1996). Atlas of Arctic Icebergs. Backbone Publishing Company, 70 pp.
- ACIA (2005). *Arctic Climate Impact Assessment*. Cambridge University Press. 1042 p.
- Alekseev, G. V., O. M. Johannessen, A. A. Korablev and A. Y. Proshutinsky (2004). Arctic Ocean and sea ice, In *Arctic Environment Variability in the Context of Global Change* (eds. L. P. Bobylev, K. Ya Kondratyev and O. M. Johannessen), Springer Praxis Publishing, Chichester, UK, 471 pp.
- Arzel, O., T. Fichefet and H. Goosse (2006). Sea ice evolution over the 20<sup>th</sup> and 21<sup>st</sup> centuries as simulated by current AOGCMs. *Ocean Modelling* 12, pp 401-415.
- Bengtsson, L., V.A. Semenov, and O.M. Johannessen (2004). The early century warming in the Arctic - A possible mechanism, *Journal of Climate*, 17(20), 4045-4057
- Bengtsson, L., K.I. Hodges, E. Roeckner, and R. Brokopf (2006). On The Natural Variability of the Pre-Industrial European Climate, *Journal of Climate*.
- Bentsen, M., Evensen, G., Drange, H., Jenkins, A. D. (1999). Coordinate transform on a sphere using conformal mapping. *Mon. Wea. Rev.* 127, 2733–2740.
- Bitz, C. M., Holland, M. M., Weaver, A. J., Eby, M. (2001). Simulating the ice-thickness distribution in a coupled climate model. *J. Geophys. Res.* 106 (C2), 2441–2461.
- Bitz, C.M., and G.H. Roe, 2004: A mechanism for the high rate of sea-ice thinning in the Arctic Ocean. *J. Clim.*, 18, 3622–3631
- Bleck, R. (2002). An oceanic circulation model framed in hybrid isopycnic–cartesian coordinates. *Ocean Modelling* 1, 55–88.
- Bobylev, L.P., K.Y. Kondratyev, and O.M. Johannessen, eds (2003) *Arctic Environment Variability in the Context of Global Change*, Springer - Praxis Publishing. 470 p.
- Box, J.E., D.H. Bromwich, and Le-Sheng Bai (2004). Greenland ice sheet mass balance 1991–2000: Application of polar MM5 mesoscale model and in situ data. *J. Geophys. Res.*, 109, D16105, doi: 10.1029/2003JD004451.
- Brown, J., K.M. Hinkel, and F.E. Nelson (2000). The Circumpolar Active Layer Monitoring (CALM) Program: Research designs and initial results. *Polar Geog.*, 24(3), 165–258.
- Bryan, F.O., et al., 2006: Response of the North Atlantic thermohaline circulation and ventilation to increasing carbon dioxide in CCSM3. *J. Clim.*, 19, 2382–2397.
- Cavalieri, D., J. Crawford, M. Drinkwater, D. Eppler, L.Farmer, R. Jentz, C. Wackerman (1991). Aircraft active and passive- microwave validation of sea ice concentration from the DMSP SSMI. *J.Geophys.Res.*, Vol.96, pp.21989-22008,
- Cavalieri, D.J., Parkinson, C.L., Vinnikov, K.Y. (2003). 30-year satellite record reveals contrasting Arctic and Antarctic decadal sea ice variability. *Geophysical Research Letters* 30 (18). doi:10.1029/2003GL018931.
- Clow, G.D., and F.E. Urban (2003). GTN-P Monitoring Network: Detection of a 3 K permafrost warming in northern Alaska during the 1990's. First Study of Environmental Arctic Change (SEARCH) Open Science Meeting, 27–30 October 2003, Seattle, WA.
- CMIP2 (2003). Coupled Model Intercomparison Project (CMIP2), (<http://www-pcmdi.llnl.gov/cmip>)
- Couture, R., S. Smith, S.D. Robinson, M.M. Burgess, and S. Solomon (2003). On the hazards to infrastructure in the Canadian North associated with thawing of permafrost. Proceedings of Geohazards 2003, 3rd Canadian Conference on Geotechnique and Natural Hazards, Edmonton, Alberta, Canada, The Canadian Geotechnical Society, 97–104.
- Dai, A., et al., 2005: Atlantic thermohaline circulation in a coupled general circulation model: Unforced variations versus forced changes. *J. Clim.*, 18, 3270–3293.
- Delworth, T.L., and K.W. Dixon, 2000: Implications of the recent trend in the Arctic/North Atlantic Oscillation for the North Atlantic thermohaline circulation. *J. Clim.*, 13, 3721–3727
- De'ry, S. J., M. Stieglitz, E. C. McKenna, E. F. Wood (2005). *J. Climate*, 18, 2540.

- Deser, C., J. E. Walsh and M. S. Timlin (2000). Arctic Sea Ice Variability in the Context of Recent Atmospheric Circulation Trends, *Journal of Climate*, DOI: 10.1175/1520-0442(2000)
- Dickson, R.R. (1999) All change in the Arctic, *Nature*, **397**, 389-391.
- Dickson, R. R., Yashayaev, I., Meincke, J., Turrell, B., Dye S. and Holfort, J. (2003). Rapid freshening of the deep North Atlantic Ocean over the past four decades. *Nature*, **416**, pp. 832–837
- Douville, H., Royer, J.-F., Mahfouf, J.-F. (1995). A new snow parametrization for the Météo France climate model, part I: validation in stand-alone experiments. *Clim. Dyn.* **12**, 21–35.
- Dyurgerov, M.B. and M.F. Meier (2000). Twentieth century climate change: Evidence from small glaciers, *PNAS*, **97**(4), 1406-1411.
- Dyurgerov, M. B., C. L. Carter (2004). *Arct. Antarct. Alp. Res.* **36**, 117
- Environmental Working Group (EWG), Arctic Climatology Project (1997). Environmental Working Group joint U.S.-Russian atlas of the Arctic Ocean— Winter period. L. Timokhov, and F. Tanis (eds.), Ann Arbor, Michigan, Environmental Research Institute of Michigan, in association with the National Snow and Ice Data Center, CD-ROM.
- Environmental Working Group (EWG), Arctic Climatology Project (1998). Environmental Working Group joint U.S.-Russian atlas of the Arctic Ocean— Summer period. L. Timokhov, and F. Tanis (eds.), Ann Arbor, Michigan, Environmental Research Institute of Michigan, in association with the National Snow and Ice Data Center, CD-ROM.
- Flato, G.M., Boer, G.J. (2001). Warming asymmetry in climate change simulations. *Geophysical Research Letters* **28**, 195–198.
- Flato, G.M., and Participating CMIP Modeling Groups, 2004: Sea-ice and its response to CO2 forcing as simulated by global climate change studies. *Clim. Dyn.*, **23**, 220–241.
- Frauenfeld, O.W., T. Zhang, R.G. Barry, and D. Gilichinsky (2004). Interdecadal changes in seasonal freeze and thaw depths in Russia. *J. Geophys. Res.*, **109**, D05101, doi: 10.1029/2003JD004245.
- Gloersen, P., D. Cavalieri (1986). “Reduction of weather effects in the calculation of sea ice concentration from microwave radiances”. *J. Geophys. Res.*, Vol.91, pp.3913-3919.
- Goosse, H., Renssen, H., (2001). A two-phase response of the Southern Ocean to an increase in greenhouse gas concentration. *Geophysical Research Letters* **28**, 3469–3472.
- Goosse, H., Renssen, H., (2005). A simulated reduction in Antarctic sea-ice area since 1750: implications of the long memory of the ocean. *International Journal of Climatology* **25**, 569–579. doi:10.1002/joc.1139.
- Gregory, J.M., et al., 2002b: Recent and future changes in Arctic sea ice simulated by the HadCM3 AOGCM. *Geophys. Res. Lett.*, **29**, 2175.
- Haas, C., and H. Eicken (2001). Interannual variability of summer sea ice thickness in the Siberian and Central Arctic under different atmospheric circulation regimes, *J. Geophys. Res.*, **106**(C3), 4449-4462.
- Haas, C. (2004). Late-summer sea ice thickness variability in the Arctic Transpolar Drift 1991–2001 derived from ground-based electromagnetic sounding. *Geophys. Res. Lett.*, **31**, L09402, doi: 10.1029/2003GL019394.
- Hansen, J. (2006) Global temperature trends: 2005 summation. <http://data.giss.nasa.gov/gistemp/2005/>
- Häkkinen, S., Mellor, G. L. (1992). Modeling the seasonal variability of a coupled Arctic ice–ocean system. *J. Geophys. Res.* **97** (C12), 20285–20304.
- Häkkinen, S. (2002). Surface salinity variability in the northern North Atlantic during recent decades. *J. Geophys. Res.*, **107**, (C12), doi:10.1029/2001JC000812
- Hansen, B and S. Østerhus (2000). North Atlantic - Nordic Seas exchanges. *Prog. Oceanogr.* **45**,109.
- Harris, C., and W. Haeberli (2003). Warming permafrost in European mountains. *World Meteorol. Org. Bull.*, **52**(3), 6 pp. See also *Global Planet. Change*, **39**, (2003), 215–225.
- Harvey, L. D. D. (1990). Testing alternative parametrizations of lateral melting and upward basal heat flux in a thermodynamic sea ice model. *J. Geophys. Res.* **95**, 7359–7365.
- Hibler, III, W. D. (1980). Modeling a variable thickness ice cover. *Mon. Wea. Rev.* **108**, 1943–1973.
- Hilmer, M. and P. Lemke (2000). On the decrease of Arctic sea ice volume, *Geophysical Research Letters*, **27**, pp. 3751-3754.
- Holland, M.M., and C.M. Bitz, 2003: Polar amplification of climate change in the Coupled Model Intercomparison Project. *Clim. Dyn.*, **21**, 221–232.
- Holloway, G. and T. Sou (2002). Has arctic sea ice rapidly thinned? *J. Clim.*, **15**, 1691–1698.
- Houghton, J.T., Ding, Y., Griggs, D.J., Noguer, M., van der Linden, P.J., Dai, X., Maskell, K., Johnson, C.A. (2001).

- Climate change 2001. The scientific basis. Contribution of Working Group I to the Third Assessment Report of the Intergovernmental Panel on Climate Change. Cambridge University Press, Cambridge, UK.
- Hosaka, M., D. Nohara, and A. Kitoh, 2005: Changes in snow coverage and snow water equivalent due to global warming simulated by a 20km-mesh global atmospheric model. *Scientific Online Letters on the Atmosphere*, **1**, 93–96.
- Hu, Z.-Z., E.K. Schneider, U.S. Bhatt, and B.P. Kirtman, 2004: Potential mechanism for response of El Niño–Southern Oscillation variability to change in land surface energy budget. *J. Geophys. Res.*, **109**, D21113, doi:10.1029/2004JD004771.
- Hunke, E. C., Dukowicz, J. K. (1997). An elastic-viscous-plastic model for sea ice dynamics. *J. Phys. Oceanogr.* **27**, 1849–1867.
- Hurrell, J. W. (1995). Decadal trends in the North Atlantic oscillation regional temperatures and precipitation. *Science*, **269**, 676–679.
- Huybrechts, P., and J. De Wolde, 1999: The dynamic response of the Greenland and Antarctic ice sheets to multiple-century climatic warming. *J. Clim.*, **12**, 2169–2188.
- Isaksen, K., D. Vonder Mühll, H. Gubler, T. Kohl, and J.L. Sollid (2000). Ground surface temperature reconstruction based on data from a deep borehole in permafrost at Janssonhaugen, Svalbard. *Annals Glaciol.*, **31**, 287–294.
- IPCC First Assessment Report. 1990 (see <http://www.ipcc.ch/pub/reports.htm>)
- IPCC Second Assessment Report: Climate Change 1995 (see <http://www.ipcc.ch/pub/reports.htm>)
- IPCC, 2001: *Climate Change 2001: The Scientific Basis. Contribution of Working Group I to the Third Assessment Report of the Intergovernmental Panel on Climate Change* [Houghton, J.T., et al. (eds.)]. Cambridge University Press, Cambridge, United Kingdom and New York, NY, USA, 881 pp.
- Johannessen, O.M., E.V. Shalina, and M.W. Miles (1999). Satellite evidence for an Arctic sea ice cover in transformation, *Science*, **286**, 1937–1939.
- Johannessen, O.M., L. Bengtsson, M.W. Miles, S.I. Kuzmina, V.A. Semenov, G.V. Alekseev, A.P. Nagurnyi, V.F. Zakharov, L.P. Bobylev, L.H. Pettersson, K. Hasselmann, and H.P. Cattle (2004). Arctic climate change - observed and modeled temperature and sea ice variability, *Tellus*, **56A**, 328–341.
- Johannessen, O.M., K. Khvorostovsky, M.W. Miles, and L.P. Bobylev (2005). Recent ice-sheet growth in the interior of Greenland, *Science*, **310**, 1013–1016.
- Jorgenson, M.T., C.H. Racine, J.C. Walters, and T.E. Osterkamp (2001). Permafrost degradation and ecological changes associated with a warming climate in central Alaska. *Climatic Change*, **48**(4), 551–571.
- Joughin, I., W. Abdalati, and M. Fahnestock (2004). Large fluctuations in speed on Greenland's Jakobshavn Isbrae glacier. *Nature*, **432**, 608–610.
- Karcher, M. J., R. Gerdes, F. Kauker, and C. Koberle (2003). Arctic warming: Evolution and spreading of the 1990s warm event in the Nordic seas and the Arctic Ocean, *J. Geophys. Res.*, **108**(C2), 3034, doi:10.1029/2001JC001265.
- Kitabata, H., K. Nishizawa, Y. Yoshida, and K. Maruyama, 2006: Permafrost thawing in circum-Arctic and highland under climatic change scenarios projected by CCSM3. *Scientific Online Letters on the Atmosphere*, **2**, 53–56.
- Klimatologicheskii spravochnik SSSR (1961–1992). Meteorologicheskie ezhesemyachnie dannye za 1961–1992, chast' II, VII, *Temperatura pochvy, tumany, grozy, meteli i grad*, Gidrometeoizdat, Leningrad (in Russian).
- Krabil, W., W. Abdalati, E.B. Frederick, S. Manizade, C. Martin, J. Sonntag, R. Swift, R. Thomas, W. Wright, and J. Yungel (2004). Greenland ice sheet: High-elevation balance and peripheral thinning. *Science*, **289**, 428–430.
- Kvingedal, B. (2005). *Sea-Ice Extent and Variability in the Nordic Seas, 1967–2002*, in *The Nordic Seas: An Integrated Perspective*, H. Drange, T.M.F. Dokken, T. Furevik, R. Gerdes, and W. Berger, eds, AGU.
- Kwok, R., G.F. Cunninham, H.J. Zwally, and D. Yi (2006). ICESat over Arctic sea ice: Interpretation of altimetric and reflectivity profiles. *J. Geophys. Res.*, **111**, C06006, doi: 10.1029/2005JC003175
- Large, W. C., McWilliams, J. C., Doney, S. C., (1994). Oceanic vertical mixing: A review and a model with a nonlocal boundary layer parametrization. *Rev. Geophys.* **32** (4), 363–403.
- Lawrence, D.M., and A.G. Slater, 2005: A projection of severe near-surface permafrost degradation during the 21st century. *Geophys. Res. Lett.*, **32**, L24401, doi:10.1029/2005GL025080.
- Laxon, S., N. Peacock, and D. Smith (2003). High interannual variability of sea ice thickness in the Arctic Region. *Nature*, **425**, 947–950.
- Levitus, S., Antonov, J. and Boyer, D. (2005). The warming of the world ocean, 1955–2003. *Geophys. Res. Lett.*, **32**, L0264, doi:10.1029/2004GL021592



- Lindsay, R.W. and J. Zhang (2005). The thinning of Arctic sea ice, 1988-2003: Have we passed a tipping point? *Journal of Climate*, **18**, 4879-4897.
- Maykut, G. A., Untersteiner, N. (1971). Some results from a time-dependent thermodynamic model of sea ice. *J. Geophys. Res.* 76 (6), 1550-1575.
- Meehl, G.A., J.M. Arblaster, and C. Tebaldi, 2005a: Understanding future patterns of precipitation extremes in climate model simulations. *Geophys. Res. Lett.*, **32**, L18719, doi:10.1029/2005GL023680.
- Meleshko, V.P., et al., 2004: Anthropogenic climate change in 21st century over Northern Eurasia. *Meteorol. Hydrol.*, **7**, 5-26.
- Mellor, G. L., Kantha, L., (1989). An ice-ocean coupled model. *J. Geophys. Res.* 10937-10954.
- Moritz, R.E., C.M. Bitz, and E.J. Steig (2002). Dynamics of recent climate change in the Arctic, *Science*, **297**, 1497-1502.
- Maslowski, W., B. Newton, P. Schlosser, A.J. Semtner, and D.G. Martinson (2000). Modeling Recent Climate Variability in the Arctic Ocean, *Geophys. Res. Lett.*, V. 27(22), pp. 3743-3746,
- Maslowski, W., J.L. Clement, W. Walzowski, J.S. Dixon, J. Jakacki, and T.P. McNamara (2006). Oceanic forcing of Arctic sea ice at gateways and margins of Pacific and Atlantic water inflow. *Eos, Trans. AGU*, 87(36), Ocean Sci. Meet. Suppl., Abstract OS32P-05.
- McCartney, Michael S. and Talley, L. D. (1982). The Subpolar Mode Water of the North Atlantic Ocean. *J. Phys. Oceanog.*, **12**, pp.1169-1188
- McLaughlin, F., E. Carmack, R.W. MacDonald, A.J. Weaver, and J. Smith (2003). The Canada Basin 1989-1995: Upstream events and far-field effects of the Barents Sea. *J. of Geophys. Res.*, 107(C7), 3233, doi: 10.1029/2002JC001537.
- Melling, H., D.A. Riedel, and Z. Gedalof (2005). Trends in the draft and extent of seasonal pack ice, Canadian Beaufort Sea. *Geophys. Res. Lett.*, **32**, L24501, doi: 10.1029/2005GL024483.
- Morison, J., M. Steele, and R. Andersen (1998). Hydrography of the upper Arctic Ocean measured from the nuclear submarine USS Pargo, *Deep Sea Research Part I: Oceanographic Research Papers*, **45**, 15-38.
- Morison, J. H., K. Aagaard and M. Steele (2000). Recent Environmental Changes in the Arctic: A review. *Arctic*, 53, 4.
- Morison, J.H., K. Aagaard, K.K. Falkner, K. Hatakeyama, R. Moritz, J.E. Overland, D. Perovich, K. Shimada, M. Steele, T. Takizawa, and R. Woodgate (2002). North Pole environmental observatory delivers early results. *Eos, Trans. AGU*, 83(33), 357, doi: 10.1029/2002EO000259.
- Morison J., M. Steele, T. Kikuchi, K. Falkner, and W. Smethie (2006). Relaxation of central Arctic Ocean hydrography to pre-1990s climatology. *Geophys. Res. Lett.*, **33**, L17604, doi:10.1029/2006GL026826.
- Mynemi, R.B., C.D. Keeling, C.J. Tucker, G. Asrar, and R.R. Nemani (1997). Increased plant growth in the northern high latitudes from 1981 to 1991, *Nature*, **386**, 698-702.
- Nagurnyi, A.P., V.G. Korostelev and V.V. Ivanov (1994). Multiyear variability of sea ice thickness in the arctic basin measured by elastic-gravity waves on the ice surface, *Meteorol. Hydrol.*, **3**, pp. 72-78 (in Russian).
- Nakićenović, N., and R. Swart (eds.), 2000: *Special Report on Emissions Scenarios. A Special Report of Working Group III of the Intergovernmental Panel on Climate Change*. Cambridge University Press, Cambridge, United Kingdom and New York, NY, USA, 599 pp.
- Nilsen, J., Gao, Y., Drange, H., Furevik, T., Bentsen, M. (2003). Simulated North Atlantic-Nordic Seas water mass exchanges in an isopycnic coordinate OGCM. *Geophys. Res. Lett.* 30 (10), 1536, doi:10.1029/2002GL016597.
- Nixon, F.M., C. Tarnocai, and L. Kutny (2003). Long-term active layer monitoring: Mackenzie Valley, northwest Canada. In *Permafrost*, Phillips, M., Springman, S. and L. U. Arenson (eds.), Swets & Zeitlinger, Lisse, 821-826.
- Oberman, N.G., and G.G. Mazhitova (2001) Permafrost dynamics in the northeast of European Russia at the end of the 20th century. *Norweg. J. Geog.*, **55**, 241-244.
- Nordic Council (2002). Review of Ocean Climate Research. Role of the Nordic countries in global ocean climate research. Report by the Nordic Council of Ministers, Copenhagen, 68 pp.
- Osterkamp, T.E. (2003). A thermal history of permafrost in Alaska. Proceedings of the 8th International Conference on Permafrost, July 21-25, 2003, Zurich, Switzerland, M. Phillips, S.M. Springman, and L.U. Arenson (eds.). Lisse, The Netherlands, A.A. Balkema, vol. 2, 863-868.
- Osterkamp, T.E., and V.E. Romanovsky (1999). Evidence for warming and thawing of discontinuous permafrost in Alaska. *Permafrost Periglac. Proc.*, 10(1), 17-37.
- Osterkamp, T.E., L. Viereck, Y. Shur, M.T. Jorgenson, C. Racine, A. Doyle, and R.D. Boone (2000). Observations of thermokarst and its impact on boreal forests in Alaska, U.S.A. *Arc. Antarc. Alp. Res.*, **32**, 303-315.

- Overland, J. E., C. H. Pease, R. W. Preisendorfer, and A. L. Comisky (1986). Prediction of vessel icing, *J. of Climate and Applied Meteorology*, 25, 1793-1806.
- Pavlov, A.V. (1994). Current changes of climate and permafrost in the Arctic and sub-Arctic of Russia. *Permafrost Periglac. Proc.*, 5, 101–110.
- Pavlov, A.V., and N.G. Moskalenko (2002). The thermal regime of soils in the north of western Siberia. *Permafrost Periglac. Proc.*, 13(1), 43–51.
- Peltier, W. R. (2002). Global glacial isostatic adjustment: Paleogeodetic and space-geodetic tests of the ICE-4G (VM2) model, *J. Quat. Sci.*, 17, 491–510.
- Peterson, B.J., R.M. Holmes, J.W. McClelland, C.J. Vorosmarty, R.B. Lammers, A.I. Shiklomanov, I.A. Shiklomanov, and S. Rahmstorf (2002). Increasing river discharge to the Arctic Ocean, *Science*, 298, 2171-2173.
- Peterson, B. J., J. McClelland, R. Curry, R. M Holmes, J. E Walsh and K. Aagaard (2006). Trajectory Shifts in the Arctic and Subarctic Freshwater Cycle. *Science*, Vol. 313, 25.
- Pfirman, S., W.F. Haxby, R. Colony, and I. Rigor (2004). Variability in Arctic sea ice drift. *Geophys. Res. Lett.*, 31, L16402, doi: 10.1029/2004GL020063.
- Polyakov, I., G.V. Alekseev, R.V. Bekryaev, U. Bhatt, R. Colony, M.A. Johnson, V.P. Karklin, D. Walsh, and A.V. Yulin (2003). Long-term ice variability in Arctic marginal seas. *J. Climate*, 16(12), 2078–2085.
- Polyakov, I.V., et al. (2005). One more step toward a warmer Arctic. *Geophys. Res. Lett.*, 32, L17605. doi: 10.1029/2005GL023740.
- Prinsenber, S. J., I. K. Peterson, S. Narayanan, and J. U. Umoh (1997). Interaction between atmosphere, ice cover, and ocean off Labrador and Newfoundland from 1962–1992. *Can. J. Aquat. Sci.*, 54, 30–39..
- Proshutinsky, A.Y., and M.A. Johnson (1997). Two circulation regimes of the winddriven Arctic Ocean. *J. Geophys. Res.*, 102(C6), 12,493–12,514. Przybylak, R. (2002) *Variability of Air Temperature and Atmospheric Precipitation in the Arctic*. Dordrecht, The Netherlands, Kluwer, 330 pp.
- Proshutinsky, T, and T. Weingarten (1998). INSROP Phase 2 project: Natural Conditions and Ice Navigation, (<http://www.ims.uaf.edu/insrop-2>)
- Proshutinsky, A., R.H. Bourke, and F.A. McLaughlin (2002). The role of the Beaufort Gyre in Arctic climate variability: Seasonal to decadal time scales. *Geophys. Res. Lett.*, 29(23), 2100, doi: 10.1029/2002GL015847.
- Proshutinsky A., I.M. Ashik, E.N. Dvorkin, S. Häkkinen, R.A. Krishfield, and W.R. Peltier (2004). Secular sea level change in the Russian sector of the Arctic Ocean. *J. Geophys. Res.*, 109, C03042, doi: 10.1029/2003JC002007.
- Proshutinsky, A., J. Yang, R. Krishfield, R. Gerdes, M. Karcher, F. Kauker, C. Koeberle, S. Hakkinen, W. Hibler, D. Holland, M. Maqueda, G. Holloway, E. Hunke, W. Maslowski, M. Steele, and J. Zhang (2005). Arctic Ocean Study: Synthesis of model results and observations. *Eos, Trans. AGU*, 86(40), 368, 10.1029/2005EO400003.
- Raisanen, J. (2002). CO<sub>2</sub>-induced changes in inter-annual temperature and precipitation variability in 19 CMIP2 experiments, *Journal of Climate*, 15, 2395-2411.
- Rawlins, M.A., R.B. Lammers, S. Frolking, B. Fekete, and C.J. Vorosmarty (2003). Simulating pan-Arctic runoff with a macro-scale terrestrial water balance model. *Hydrol. Proc.*, 17, 2521–2539.
- Ridley, J.K., P. Huybrechts, J.M. Gregory, and J.A. Lowe, 2005: Elimination of the Greenland ice sheet in a high CO<sub>2</sub> climate. *J. Clim.*, 17, 3409–3427.
- Rignot, E.J., D. Braaten, S.P. Gogineni, W.B. Krabill, and J.R. McConnell (2004). Rapid ice discharge from southeast Greenland glaciers, *Geophysical Research Letters*, 31(L10401), doi:10.1029/2004GL019474.
- Rignot, E. and P. Kanagaratnam (2006). Changes in the Velocity Structure of the Greenland Ice Sheet, *Science*, 311(5763), 986-990.
- Rigor, I., and J.M. Wallace (2004). Variations in the age of Arctic sea-ice and summer sea-ice extent. *Geophys. Res. Lett.*, 31, L09401, doi: 10.1029/ 2004GL019492
- Romanov, I.P. (1995). *Atlas of Ice and Snow of the Arctic Basin and Siberian Shelf Seas*, edited by A. Tunik, Backbone Publishing, Elmwood Park, USA, 277 pp
- Romanovsky, V.E., and T.E. Osterkamp (2000). Effects of unfrozen water on heat and mass transport processes in the active layer and permafrost. *Permafrost Periglac. Proc.*, 11, 219–239.
- Romanovsky, V.E., M. Burgess, S. Smith, K. Yoshikawa, and J. Brown (2002). Permafrost temperature records: Indicator of climate change. *Eos, Trans. AGU*, 83(50), 589, 593–594.
- Romanovsky, V.E., N.I. Shender, T.S. Sazonova, V.T. Balobaev, G.S. Tipenko, and V.G. Rusakov (2001). Permafrost temperatures in Alaska and East Siberia: Past, present and future. *Proceedings of the Second Russian*

*Conference on Geocryology (Permafrost Science)*, Moscow, June 6–8, p. 301–314.

- Romanovsky, V., K. Yoshikawa, D. Sergueev, and Y. Shur (2005). Permafrost observatory near Gakona, Alaska. Local-scale features in permafrost distribution and temperatures. *Eos, Trans. AGU*, **86**, Fall Meet. Suppl.
- Rothrock, D.A., Y. Yu, and G.A. Maykut (1999). Thinning of the Arctic sea-ice cover, *Geophysical Research Letters*, **26**(23), 3469–3472.
- Rothrock, D.A., Zhang, J., Yu, Y. (2003). The Arctic ice thickness anomaly of the 1990s: a consistent view from observations and models. *Journal of Geophysical Research* 108 (C3). doi:10.1029/2001JC001208.
- SEARCH, *SEARCH: Study of Environmental Arctic Change, Science Plan*. 2001, Polar Sciences Center, University of Washington: Seattle.
- Rudels, B., E.P. Jones, L.G. Anderson, and G. Kattner (1994). On the intermediate depth waters of the Arctic Ocean. In *The Polar Oceans and Their Role in Shaping the Global Environment: The Nansen Centennial Volume*, O.M. Johannessen, R.D. Muench, and J.E. Overland (eds.), Washington, D.C., American Geophysical Union, 33–46.
- Rudels et al., (2002)
- Schaeffer, M., F.M. Seltin, J.D. Opsteegh, and H. Goosse, 2004: The influence of ocean convection patterns on high-latitude climate projections. *J. Clim.*, **17**, 4316–4329
- Schmittner, A., M. Latif, and B. Schneider, 2005: Model projections of the North Atlantic thermohaline circulation for the 21st century assessed by observations. *Geophys. Res. Lett.*, **32**, L23710, doi:10.1029/2005GL024368.
- Schweiger, A.J. (2004). Changes in seasonal cloud cover over the Arctic seas from satellite and surface observations, *Geophysical Research Letters*, Vol. 31, L2207, doi:10.1029/2004GL020067, 2004.
- Semtner Jr., A. J. (1976). A model for the thermodynamic growth of sea ice in numerical investigations of climate. *J. Phys. Oceanogr.* 6 (3), 379–389.
- Serreze, M.C., J.E. Walsh, F.S. Chapin III, T.E. Osterkamp, M.B. Dyrugerov, V.E. Romanovsky, W.C. Oechel, J. Morison, T. Zhang, and R.G. Barry (2000). Observational evidence for recent change in the northern high-latitude environment, *Climatic Change*, **46**, 159–206.
- Serreze, M.C., J.A. Maslanik, T.A. Scambos, F. Fetterer, J. Stroeve, K. Knowles, C. Fowler, S.D. Drobot, R.G. Barry, and T.M. Haran (2003). A record minimum Arctic sea ice extent and area in 2002, *Geophysical Research Letters*, **30**(3), 1110, doi:10.1029/2002GL016406.
- Shiklomanov, I., A. I. Shiklomanov, R. B. Lammers, B. J. Peterson, and C. J. Vörösmarty (2000). In *The Freshwater Budget of the Arctic Ocean* (Ed. E. L. Lewis), Kluwer Academic, Dordrecht, Netherlands, 2000, pp. 281–296.
- Shimada, K., E.C. Carmack, K. Hatakeyama, and T. Takizawa (2001). Varieties of shallow temperature maximum waters in the western Canadian Basin of the Arctic Ocean. *Geophys. Res. Lett.*, **28**(18), 3441–3444.
- Shimada, K., F. McLaughlin, E. Carmack, A. Proshutinsky, S. Nishino, and M. Itoh (2004) Penetration of the 1990s warm-temperature anomaly of Atlantic Water in the Canada Basin. *Geophys. Res. Lett.*, **31**, L20301, doi: 10.1029/2004GL020860.
- Shimada, K., T. Kamoshida, M. Itoh, S. Nishino, E. Carmack, F. McLaughlin, S. Zimmermann, and A. Proshutinsky (2006). Influence of Pacific summer water on the recent anomalous reduction of ice cover in the Arctic Ocean. *Eos, Trans. AGU*, **87**(36), Ocean Sci. Meet. Suppl., Abstract OS33N-01.
- Smith, S.L., M.M. Burgess, D. Riseborough, and F.M. Nixon (2005). Recent trends from Canadian permafrost thermal monitoring network sites. *Permafrost Periglac. Proc.*, **16**, 19–30.
- Solomon, S., D. Qin, M. Manning, R.B. Alley, T. Berntsen, N.L. Bindoff, Z. Chen, A. Chidthaisong, J.M. Gregory, G.C. Hegerl, M. Heimann, B. Hewitson, B.J. Hoskins, F. Joos, J. Jouzel, V. Kattsov, U. Lohmann, T. Matsuno, M. Molina, N. Nicholls, J. Overpeck, G. Raga, V. Ramaswamy, J. Ren, M. Rusticucci, R. Somerville, T.F. Stocker, P. Whetton, R.A. Wood and D. Wratt, 2007: Technical Summary. In: *Climate Change 2007: The Physical Science Basis. Contribution of Working Group I to the Fourth Assessment Report of the Intergovernmental Panel on Climate Change* [Solomon, S., D. Qin, M. Manning, Z. Chen, M. Marquis, K.B. Averyt, M. Tignor and H.L. Miller (eds.)]. Cambridge University Press, Cambridge, United Kingdom and New York, NY, USA.
- Sorteberg, A., T. Furevik, H. Drange, and N.-G. Kvamstø (2005). Effects of simulated natural variability on Arctic temperature projections, *Geophysical Research Letters*, **32**(L18708), doi:10.1029/2005GL023404.
- Steele, M. and T. Boyd (1998). Retreat of the cold halocline layer in the Arctic Ocean. *J. Geophys. Res.* 103, p. 10419–10435
- Steele, M., J. Morison, W. Ermold, I. Rigor, M. Ortmeyer, and K. Shimada (2004). Circulation of summer Pacific

- halocline water in the Arctic Ocean. *J. Geophys. Res.*, **109**, C02027, doi: 10.1029/2003JC002009.
- Steffen, K., N. Cuillen, R. Huff, C. Stewart, and E. Rignot (2004). Petermann Gletscher's floating tongue in northwestern Greenland: Peculiar surface features, bottom melt channels and mass balance assessment. Paper presented at the 34th International Arctic Workshop, Institute of Arctic and Alpine Research, Boulder, Colorado, March 10–13.
- Stendel, M., and J.H. Christensen, 2002: Impact of global warming on permafrost conditions in a coupled GCM. *Geophys. Res. Lett.*, **29**, 1632.
- Stocker, T.F., and C.C. Raible, 2005: Climate change - Water cycle shifts gear. *Nature*, **434**, 830–833.
- Stouffer, R.J., 2004: Time scales of climate response. *J. Clim.*, **17**, 209–217.
- Stouffer, R.J., J. Yin, J.M. Gregory, K.W. Dixon, M.J. Spelman, W. Hurlin, A.J. Weaver, M. Eby, G.M. Flato, H. Hasumi, A. Hu, J.H. Jungclaus, I.V. Kamenkovich, A. Levermann, M. Montoya, S. Murakami, S. Nawrath, A. Oka, W.R. Peltier, D.Y. Robitaille, A. Sokolov, G. Vettoretti, and S.L. Weber (2006). Investigating the causes of the response of the thermohaline circulation to past and future climate changes, *Journal of Climate*.
- Stroeve, J.C., M.C. Serreze, F. Fetterer, T. Arbetter, W. Meier, J. Maslanik, and K. Knowles (2005). Tracking the Arctic's shrinking ice cover: Another extreme September minimum in 2004. *Geophys. Res. Lett.*, **32**(4), L04501, doi: 10.1029/2004GL021810.
- Stroeve, J., M. M. Holland, W. Meier, T. Scambos, and M. Serreze (2007), Arctic sea ice decline: Faster than forecast, *Geophys. Res. Lett.*, **34**, L09501, doi:10.1029/2007GL029703.
- Svendsen, E., K. Kloster, B. Farrelly, O. Johannessen, J. Johannessen, W. Campbell, P. Gloersen, D. Cavalieri, C. Matzler (1983). Norwegian Remote Sensing Experiment: Evaluation of the Nimbus-7 SMMR for sea ice research. *J. Geophys. Res.*, **88**(C5), pp.2781-2791,
- Swift, J.H., K. Aagaard, L. Tomikhov, and E.G. Nikiforov (2005). Long-term variability of Arctic Ocean waters: Evidence from a reanalysis of the EWG data set, *Journal of Geophysical Research*, **110**(C03012), doi:10.1029/2004JC002312.
- Tarnocai, C., F.M. Nixon, and L. Kutny (2004). Circumpolar-Active-Layer-Monitoring (CALM) sites in the Mackenzie Valley, northwestern Canada. *Permafrost Periglac. Proc.*, **15**, 141–153.
- Teague, W., M.J., C., P.J., H. (1990). A comparison between the Generalized Digital Environmental Model and Levitus climatologies. *J. Geophys. Res.* **95** (C5), 7167–7183.
- Thomas, R.H. (2004). Greenland: Recent mass balance observations. In *Mass Balance of the Cryosphere: Observations and Modeling of Contemporary and Future Changes*. J. Bamber, and A. Payne (eds.), Cambridge, Cambridge University Press, 393–436.
- Thompson, D.W.J., and M. Wallace (1998). The Arctic Oscillation signature in the wintertime geopotential height and temperature fields. *Geophys. Res. Lett.*, **25**(9), 1297–1300.
- Thompson, D. W. J., J. M. Wallace, and G. Hegerl (2000). Annular modes in the extratropical circulation. Part II: Trends, *J. Climate*, **13**, 1018-1036.
- Thorndike, A. S., Rothrock, D. A., Maykut, G. A., Colony, R. (1975). The thickness distribution of sea ice. *J. Geophys. Res.* **80** (33), 4501–4513.
- Toniazzo, T., J.M. Gregory, and P. Huybrechts, 2004: Climatic impact of Greenland deglaciation and its possible irreversibility. *J. Clim.*, **17**, 21–33.
- Uppala, S. M. et al., (2005). *Q. J. R. Meteorol. Soc.* **131**, 2961
- Varlamov, S.P. (2003) Variations in the thermal state of the lithogenic base of landscapes in central Yakutia. *Proceedings of the Second International Conference, The Role of Permafrost Ecosystems in Global Climate Change*, 12–17 August 2002, Yakutsk, Russia, 52–56.
- Varlamov, S.P., Yu.B. Skachkov, P.N. Skryabin, and N.I. Shender (2001). Thermal response of the lithogenic base of permafrost landscapes to recent climate change in central Yakutia. *Proceedings of the International Conference, The Role of Permafrost Ecosystems in Global Climate Change*, 3–5 May 2000, Yakutsk, Russia, 44–45.
- Vinnikov, K.Y., Robbock, A., Stou (1999). Global warming and northern hemisphere sea ice extent. *Science* **286**, 1934–1937.
- Wadhams, P. and W. Munk (2004). *Geophys. Res. Lett.* **31**, L11311 10.1029/2004GL020039
- Walsh, J. E., and C. M. Johnson (1979). An analysis of arctic sea ice fluctuations, 1953–77. *J. Phys. Oceanogr.*, **9**, 580–591.
- Walsh, J. E., W. L. Chapman and T. L. Shy (1996). Recent decrease of sea level pressure in the central Arctic. *J. Climate*, **9**, 480-486.



- Wang, M. and J.E. Overland (2004). Detecting Arctic climate change using Koppen climate classification, *Climatic Change*, **67**, 43-62.
- Watterson, I.G., 2003: Effects of a dynamic ocean on simulated climate sensitivity to greenhouse gases. *Clim. Dyn.*, **21**, 197–209
- Wilkinson, D. and S. Bacon (2005). The spatial and temporal variability of the East Greenland Coastal Current from historic data, *Geophysical Research Letters*, **32**(L24618), doi:10.1029/2005GL024232.
- Woodgate, R. A., Aagaard, K., Weingartner, T. J. (2005). Monthly temperature, salinity, and transport variability of the Bering Strait through flow. *Geophys. Res. Lett.* **32**, L04601, doi:10.1029/2004GL021880.
- Woodgate R.A., K. Aagaard, T.J. Weingartner (2006). Interannual changes in the Bering Strait fluxes of volume, heat and freshwater between 1991 and 2004, *Geophys. Res. Lett.*, **33**, L15609, doi: 10.1029/2006GL026931.
- Wu, P., R. Wood, and P. Stott, 2005: Human influence on increasing Arctic river discharge. *Geophys. Res. Lett.*, **32**, L02703, doi:10.1029/2004GL021570.
- Yamaguchi, K., A. Noda, and A. Kitoh, 2005: The changes in permafrost induced by greenhouse warming: A numerical study applying multiple-layer ground model. *J. Meteorol. Soc. Japan*, **83**, 799–815.
- Yoshikawa, K., W.R. Bolton, V.E. Romanovsky, M. Fukuda, and L.D. Hinzman (2003). Impacts of wildfire on the permafrost in the boreal forests of interior Alaska. *J. Geophys. Res.*, **107**, 8148. doi: 10.1029/2001JD000438, 2002. (Printed 108(D1), 2003.)
- Yu, Y., G.A. Maykut, and D.A. Rothrock (2004). Changes in the thickness distribution of Arctic sea ice between 1958-1970 and 1993-1997, *Journal of Geophysical Research*, **109**(C08004), doi:10.1029/2003JC001982.
- Zhang, T., O.W. Frauenfeld, M.C. Serreze, A.J. Etringer, C. Oelke, J.L. McCreight, R.G. Barry, D. Gilichinsky, D. Yang, H. Ye, F. Ling, and S. Chudinova (2005). Spatial and temporal variability of active layer thickness over the Russian Arctic drainage basin. *J. Geophys. Res.*, **110**, D16101, doi: 10.1029/2004JD005642.
- Zhang, X.D., and J.E. Walsh, 2006: Toward a seasonally ice-covered Arctic Ocean: Scenarios from the IPCC AR4 model simulations. *J. Clim.*, **19**, 1730–1747.
- Zubakin, G. K., A. K. Naumov and I. V. Buzin (2004). Estimates of ice and icebergs spreading in the Barents Sea. Paper no. 2004-JSC-381, 8 pp.
- Zwally, H.J., M.B. Giovinetto, J. Li, H.G. Cornejo, M.A. Beckley, A.C. Brenner, J.L. Saba, and D. Yi (2005) Mass changes of the Greenland and Antarctic ice sheets and shelves and contributions to sea-level rise: 1992-2002, *Journal of Glaciology*, **51**(175), 509-527.
- Østerhus, S., Turrell, W. R., Jonsson, S., and Hansen, B. (2005). Measured volume, heat, and salt fluxes from the Atlantic to the Arctic Mediterranean. *Geophys. Res. Lett.* **32** (7), L07603, doi:10.1029/2004GL022188.